สำนักหอสมุดกลาง พระจอมเกล้าลาดกระบัง

THE STUDY OF ELECTRONIC STATES OF HETEROSTRUCTURE SEMICONDUCTORS BY PHOTOLUMINESCENCE AND PHOTOCURRENT SPECTROSCOPIES

WISANU PECHARAPA

เลขหมู่ QC
เลขทะเบียน 50171
วัน,เดือน,ปี 23 พ.ค. 2551

.b.............................
.i.............................

A THESIS SUBMITTED IN FULFILLMENT
OF THE REQUIREMENT FOR THE DEGREE OF
DOCTOR OF PHILOSOPHY IN APPLIED PHYSICS
SCHOOL OF GRADUATE STUDIES
KING MONGKUT'S INSTITUTE OF TECHNOLOGY LADKRABANG
2007

This material is reserved for educational use only, not allowed for commercial use.
Forbidden to modify the content, and cite the document when use.

COPYRIGHT 2007

SCHOOL OF GRADUATE STUDIES

KING MONGKUT'S INSTITUTE OF TECHNOLOGY LADKRABANG

This material is reserved for educational use only, not allowed for commercial use.

Forbidden to modify the content, and cite the document when use.

หัวข้อวิทยานิพนธ์	การศึกษาสถานะพลังงานไฟฟ้าของสารกึ่งตัวนำโครงสร้างเฮทเทอโรโดยโฟโตลูมิเนสเซนต์และโฟโตเคอเรนต์สเปกโตรสโคปี
นักศึกษา	นายวิษณุ เพชรภา
รหัสนักศึกษา	43065904
ปริญญา	ปรัชญาดุษฎีบัณฑิต
สาขาวิชา	ฟิสิกส์ประยุกต์
อาจารย์ผู้ควบคุมวิทยานิพนธ์	รศ.ดร. จิติ หนูแก้ว

บทคัดย่อ

วิทยานิพนธ์นี้เป็นการตรวจสอบสถานะพลังงานไฟฟ้าของสารกึ่งตัวนำโครงสร้างเฮทเทอโรมิติต่ำโดยโฟโตเคอเรนต์และโฟโตลูมิเนสเซนต์สเปกโตรสโคปี อาทิเช่น โครงสร้างบ่อควอนตัม โครงสร้างเดลตาโดปของธาตุหายาก โครงสร้างบ่อควอนตัมระหว่างสารกึ่งตัวนำอินทรีย์และอนินทรีย์ เป็นต้น

สารกึ่งตัวนำโครงสร้างบ่อควอนตัมของธาตุกลุ่ม III-V ถูกตรวจสอบโดยระบบวัดโฟโตลูมิเนสเซนต์สเปกโตรสโคปี โครงสร้างดังกล่าวประกอบด้วย สารกึ่งตัวนำบ่อควอนตัมเดี่ยวของ InGaAs/InP ที่มีความกว้างบ่อแคบมากที่ปลูกโดยกระบวนการปลูกแบบ organometallic vapor phase epitaxy และสารกึ่งตัวนำบ่อควอนตัมแบบพหุของ InGaAs/GaAs โดยกระบวนการปลูกแบบ molecular beam epitaxy สัญญาณโฟโตลูมิเนสเซนต์ของทั้งสองตัวอย่างสามารถบอกคุณภาพการก่อตัวของโครงสร้างดังกล่าวและสถานะพลังงานไฟฟ้าในบ่อควอนตัม ซึ่งเกิดจากการรวมตัวของอิเล็กตรอนและโฮลในระดับพลังงานย่อยที่ 1 ในบ่อควอนตัม สัญญาณโฟโตลูมิเนสเซนต์ของโครงสร้างดังกล่าวที่ขึ้นกับอุณหภูมิสามารถนำไปศึกษาผลกระทบของอุณหภูมิ และสามารถนำไปหาค่าที่เกี่ยวข้องได้ เช่น พลังงานที่ใช้ในการกระตุ้นในกระบวนการยับยั้งการเปล่งแสง (Photoluminescence Quenching) และกระบวนการขยายของสัญญาณ (Broadening Mechanism) สถานะพลังงานไฟฟ้าและโครงสร้างของสารกึ่งตัวนำเดลตาโดปของเออเบียม (Erbium delta-doped) ใน InP ที่ปลูกโดยกระบวนการปลูกแบบ organometallic vapor phase epitaxy ถูกตรวจสอบโดยระบบวัดโฟโตเคอเรนต์สเปกโตรสโคปี สัญญาณโฟโตเคอเรนต์ที่ชัดเจนของตัวอย่างที่ถูกเจือทำให้ทราบถึงการก่อตัวที่ดีของชั้น ErP ในสารกึ่งตัวนำ InP และจำนวนเกาะ ErP เพิ่มขึ้นเมื่อเวลาในการเจือเพิ่มขึ้น ระบบวัดโฟโตเคอเรนต์สเปกโตรสโคปีใช้นำไปตรวจสอบสมบัติของสารกึ่งตัวนำโครงสร้าง NC-ZnSe/p-Si ที่มีความหนาของชั้น ZnSe แตกต่างกัน พบว่ารูปร่างของสัญญาณกว้างขึ้น ช่วงการตอบสนองต่อแสงของตัวอย่างเลื่อนไปทางแสงสีน้ำเงินเมื่อความหนาของชั้น ZnSe เพิ่มขึ้น สารกึ่งตัวนำโครงสร้าง ZnSe/Alq_3/TPD ที่ปลูกบนฐานรองซิลิกอน

This material is reserved for educational use only, not allowed for commercial use.

Forbidden to modify the content, and cite the document when use.

ถูกตรวจสอบโดยระบบวัดโฟโตเคอเรนต์และอิเล็กโตรรีเฟลกแตนท์สเปกโตรสโคปี สัญญาณที่ได้จากระบบวัดทั้งสองบอกถึงการเปลี่ยนระดับพลังงานแสงภายในบ่อควอนตัมเดี่ยว โดยที่ค่าพลังงานนี้ลดลงตามความหนาของชั้น Alq_3 ที่เพิ่มขึ้น

This material is reserved for educational use only, not allowed for commercial use.
Forbidden to modify the content, and cite the document when use.

Thesis Title	The Study of Electronic States of Heterostructure Semiconductors by Photoluminescence and Photocurrent Spectroscopies
Student	Mr. Wisanu Pecharapa
Student ID	43065904
Degree	Doctor of Philosophy
Program	Applied Physics
Thesis Advisor	Associate Professor Dr. Jiti Nukeaw

ABSTRACT

In this thesis, the electronic states of the low-dimensional heterostructure semiconductors are investigated by photocurrent and photoluminescence spectroscopies. Spectroscopic studies of heterostructure semiconductors such as quantum wells, rare earth delta-doped structure, and organic/inorganic quantum well are presented.

The III-V compound quantum well structure is extensively investigated by photoluminescence spectroscopy. These structures include InGaAs/InP single quantum well with extremely thin well width grown by organometallic vapor phase epitaxy, and an InGaAs/GaAs multiple quantum wells structure grown by molecular beam epitaxy. Photoluminescence signal of both samples confirm the high quality formation of quantum structure. The spectra can also reveal the electronic state in the well: i.e., the first electron subband and the first heavy-hole subband in the quantum wells. Temperature-dependent photoluminescence was carried out in order to study the effect of temperature on the electronic state in the well. Important parameters such as activation energies responsible for the photoluminescence quenching and broadening mechanisms are achieved. Electronic structure of Erbium delta-doped InP grown by organometallic vapor phase epitaxy is investigated by photocurrent spectroscopy. The clear photocurrent spectra of the doped samples reflect the high quality formation of ErP layer in InP. The total number of ErP islands increase with increasing exposure time. Photocurrent spectroscopy on NC-ZnSe/p-Si heterostructure with different ZnSe layer thickness was conducted. The shape of photocurrent spectra is widened and the response wavelength has significant blue shift to lower wavelength as the ZnSe layer thickness increases. ZnSe/Alq_3/TPD heterostructure on Si substrate was investigated by photocurrent and electroreflectance spectroscopies. Both photocurrent and

This material is reserved for educational use only, not allowed for commercial use.
Forbidden to modify the content, and cite the document when use.

electroreflectance spectra show the optical transition energies in single quantum well. The optical transition energy decreases with increasing in Alq_3 well thickness.

This material is reserved for educational use only, not allowed for commercial use.
Forbidden to modify the content, and cite the document when use.

ACKNOWLEDGEMENT

Firstly, I would like to express my highest respect and appreciation to my advisor, Associate Professor Dr. Jiti Nukeaw whose guidance, enthusiastic advice and encouragement directed me to the accomplishment of this work. I also appreciate his effort and time devoted to giving advice and discussion throughout this works. I am highly grateful to be one of his students.

This work would not be successful without the appropriate help from these people, to whom I would like to appreciate:

I would particularly like to thank Dr. Prasert Kraisingdecha at Department of Physics, Silprakorn University, for his help on photoluminescence measurement.

I would like to give a special thank to Professor Y.Takada and his research group at Department of Material Science and Engineering, Nagoya University, Japan for providing the samples of Er delta-doped InP to be characterized.

I would like to give my thanks to all people in Quantum and Optical Semiconductor Laboratory for providing not only willing help, but also friendly social atmosphere.

Thanks are also given to S. Rahong, K. Upprakhot, A. Keawprajak, N. Kayunkid for preparing organic/inorganic heterostructure samples.

I would like to acknowledge Department of Applied Physics, KMITL, for allowing me to study for Doctoral degree.

Finally, I would like to express my thanks to my parent, my sisters, my wife and my sons for making my life meaningful and their willing help.

Wisanu Pecharapa

This material is reserved for educational use only, not allowed for commercial use.

Forbidden to modify the content, and cite the document when use.

LIST OF PUBLICATIONS

The following publications and conference presentations have resulted from the research works associated to this thesis.

Publications:

1. W. Pecharapa and J. Nukeaw, **"Photocurrent Study of Erbium Delta-Doped InP Grown by Organometallic Vapor Phase Epitaxy"**, International Journal of Modern Physics B, Vol. 16, No. 28&29, pp. 4436-4440, Nov 20, 2002.
2. W. Pecharapa and J. Nukeaw, **"Study of Interband Transition in Single Quantum Well of Er δ-doped InP by Photocurrent Spectroscopy"**, NECTEC Technical Journal, Vol. 3, No. 11, pp. 98-103, July-Oct 2001.
3. W. Pecharapa, W. Techitheera, P. Kraisingdecha, and J. Nukeaw, **"Photoluminescence of extremely thin InGaAs/InP Single Quantum Wells grown by Organometallic Vapor Phase Epitaxy"**, Journal of Metals, Materials and Minerals, Vol. 13, No.1, pp. 1-5, 2003.
4. W. Pecharapa, A. Keawprajak, N. Kayunkid, S. Rahong, W. Yindeesuk, and J. Nukeaw, **"Electroreflectance and Photocurrent measurement on ZnSe/Alq3/TPD heterostructure on Si-substrate"**, Material Science and Engineering B, Vol. 123, pp. 163-166, 2005.
5. W. Pecharapa, A. Keawprajak, N. Kayunkid, S. Rahong, W. Yindeesuk, and J. Nukeaw, **"Growth and characterization of novel optoelectronic materials based on II-VI inorganic/organic heterostructures"**, ScienceAsia, Vol. 32 No. 3, pp. 223-229, 2006.

This material is reserved for educational use only, not allowed for commercial use.
Forbidden to modify the content, and cite the document when use.

Conference Presentations:

1. W. Pecharapa and J. Nukeaw, **"Formation of ErP/InP single quantum well affected by erbium delta-doping on InP"**, The 8th International Conference on Electronic Materials (ICEM2002), Xi'an, China, June 10-14, 2002.
2. W. Pecharapa and J. Nukeaw, **"Observation of interband transitions in ErP/InP single quantum well affected by erbium delta-doping InP"**, The 26th International Conference on the Physics of Semiconductors (ICPS2002), Edinburgh, Scotland, July 29- August 2, 2002.
3. W. Pecharapa, K. Upprakhot, W. Techitdheera, and J. Nukeaw, **"Photocurrent study of nanocrystal ZnSe/p-Si heterostructure grown by electron beam evaporator"**, The International Workshop on Optical Science and Technology, Bangkok, Thailand, August 21-22, 2003.

This material is reserved for educational use only, not allowed for commercial use.
Forbidden to modify the content, and cite the document when use.

TABLE OF CONTENTS

PAGE

ABSTRACT (THAI) I
ABSTRACT (ENGLISH) III
ACKNOWLEDGEMENT V
LIST OF PUBLICATIONS VI
TABLE OF CONTENTS VIII
LIST OF TABLES XII
LIST OF FIGURES XIII
CHAPTER 1 INTRODUCTION 1
1.1 Motivation 1
1.2 Objective 1
1.3 Scope of Study 2
1.4 Expected Results 2

CHAPTER 2 THEORETICAL BACKGROUND 3
2.1 Photoluminescence Spectroscopy 3
2.1.1 Photoluminescence Process in Semiconductor 3
2.1.2 Photoluminescence Spectrum 6
2.1.3 Photoluminescence Intensity 7
2.1.4 Luminescence from Quantum Well Structures 8
2.2 Photocurrent Spectroscopy 10
2.2.1 Photocurrent Process 10
2.2.2 Photocurrent in Quantum Wells 14
2.2.3 Metal-Semiconductor Junctions 15
2.2.3.1 Schottky Junctions or Rectifying Junctions 15
2.2.3.2 Ohmic Contacts or Nonrectifying Junctions 21
2.3 Band Theory of Semiconductor 22
2.3.1 Band Structure in One Dimension 22
2.3.2 Motion of Electrons in Bands 25

This material is reserved for educational use only, not allowed for commercial use.
Forbidden to modify the content, and cite the document when use.

TABLE OF CONTENTS (cont.)

PAGE

2.3.3 Band Structure in Two and Three Dimension 26

2.3.4 Modification of Band Structure 31

2.3.4.1 Modification of Band Structure by Alloying 32

2.3.4.2 Modification of Band Structure by Heterostructures 33

2.4 Molecular Orbital Theory 34

2.4.1 σ-Bond and π-Bonds 34

2.4.2 Electronic States and Excitation of Organic Semiconductor 35

2.5 Heterostructure Semiconductors 40

2.5.1 Quantum Wells and Low-Dimensional Structure 42

2.5.2 Superlattice 43

2.5.3 Doped Heterostructure 44

2.5.3.1 Delta-Doped Structure 44

2.5.3.2 Modulated Doped Structure 48

2.6 Quantum Theory for Semiconductor 49

2.6.1 Infinite Square Well 49

2.6.2 Finite Square Well 52

2.6.3 Parabolic Well 54

2.6.4 Triangular Well 56

2.6.5 Perturbation Theory 59

CHAPTER 3 EXPERIMENTS SET UP 64

3.1 Photoluminescence Spectroscopy Set Up 64

3.2 Photocurrent Spectroscopy Set Up 65

3.3 Contact Growth Processes 66

3.3.1 Surface Cleaning Process 66

3.3.2 Growth of Indium Tin Oxide Contact 66

3.3.3 Growth of Gold Contact 67

3.4 Equipment for Photoluminescence and Photocurrent Spectroscopy 68

This material is reserved for educational use only, not allowed for commercial use.

Forbidden to modify the content, and cite the document when use.

TABLE OF CONTENTS (cont.)

PAGE

3.4.1 Temperature Controller and Vacuum Unit 68

3.4.2 Light Sources 71

3.4.3 Optical Equipment 71

3.4.4 Signal Acquisition Equipment 73

CHAPTER 4 PHOTOLUMINESCENCE AND PHOTOCURRENT OF BULK SEMICONDUCTOP. 76

4.1 Photoluminescence of Bulk Semiconductor 76

4.2 Current – Voltage Characteristics of Bulk GaAsP 85

4.3 Photocurrent of Bulk Semiconductor 86

References 90

CHAPTER 5 PHOTOLUMINESCENCE OF NARROW WELL WIDTH InP/InGaAs/InP SINGLE QUANTUM WELL GROWN BY OMVPE 91

5.1 Literature Review 91

5.2 Sample Structure 92

5.3 Results and Discussion 93

5.4 Gas Source Supply Interruption Effect During Growth on quantum Well Structure of Narrow-Well Width $In_{0.53}Ga_{0.47}As$/InP SQWs 103

5.5 Summary 107

References 108

CHAPTER 6 PHOTOCURRENT OF ERBIUM DELTA-DOPED InP STRUCTURE 110

6.1 Literature Review 110

6.2 Sample Structure 111

6.3 Results and Discussion 112

6.3.1 Quantum Island Model 113

6.3.2 Quantum Well Model 115

This material is reserved for educational use only, not allowed for commercial use.

Forbidden to modify the content, and cite the document when use.

TABLE OF CONTENTS (cont.)

PAGE

6.3.3 Quantum Confined Stark Effects 118

6.4 Summary 121

References 122

CHAPTER 7 PHOTOCURRENT OF NANOCRYSTAL ZnSe and

$ZnSe/Alq_3/TPD$ HETEROSTRUCTURE ON SILICON SUBSTRATE 125

7.1 Literature Review 125

7.2 Sample Structure 127

7.2.1 Sample Structure of Nanocrystal ZnSe/p-Si 127

7.2.2 Sample Structure of $ZnSe/Alq_3/TPD/Si$ 127

7.3 Results and Discussion 129

7.3.1 Nanocrystal ZnSe/p-Si 129

7.3.2 $ZnSe/Alq_3/TPD/Si$ 132

7.4 Summary 140

References 141

CHAPTER 8 PHOTOLUMINESCENCE OF InGaAs/GaAs MULTIPLE

QUANTUM WELL STRUCTURE GROWN BY

MOLECULAR BEAM EPITAXY 145

8.1 Literature Review 145

8.2 Sample Structure 145

8.3 Results and Discussion 146

8.4 Summary 156

References 157

CHAPTER 9 CONCLUSION 159

This material is reserved for educational use only, not allowed for commercial use.

Forbidden to modify the content, and cite the document when use.

LIST OF TABLES

TABLE **PAGE**

4.1 Full width at half maximum of PL spectra, Energy gap and the maximum amplitude of PL peak of GaAsP by the best fitting. 78

4.2 fitted parameters of GaAsP from frequency sensitive photocurrent measurement. 88

8.1 Parameters obtained by fitting equation (4.2) to the peak energy versus temperature data in Fig. 8.4 148

This material is reserved for educational use only, not allowed for commercial use.
Forbidden to modify the content, and cite the document when use.

LIST OF FIGURES

FIGURE **PAGE**

2.1 Schematic representation of the basic processes involved in a typical photoluminescence process in semiconductors. 5

2.2 (a-c) Radiative recombination paths: (a) band-to-band; (b) donor to valence band; (c) conduction band to acceptor; (d) Nonradiative recombination via an intermediate state (E_i). 7

2.3 Photoluminescence for a InGaAs/InP quantum well sample with five quantum wells with different thickness, the inset shows the electronic structure and the nature of the optical transitions. 9

2.4 Photocurrent in semiconductor........10

2.5 Energy band diagrams for a metal/n-type semiconductor contact (a) two materials isolated from each other (b) at thermal equilibrium after the contact is made. 16

2.6 Energy band diagrams for a metal/p-type semiconductor contact (a) two materials isolated from each other (b) at thermal equilibrium after the contact is made. 18

2.7 Energy band diagram of rectifying metal/n-type semiconductor contact at thermal equilibrium. 19

2.8 Energy band diagram of rectifying metal/n-type semiconductor contact (a) after forward bias, (b) after reverse bias and (c) I-V characteristic of the junction. 20

2.9 Band diagram for ohmic metal-semiconductor contact (a) $\phi_M < \phi_S$ for n-type (b) the junction at equilibrium for n-type/metal (c) $\phi_M > \phi_S$ for p-type semiconductors (d) the junction at equilibrium for p-type/metal. 21

2.10 An example of one-dimensional periodic potential with lattice constant *a*. 22

2.11 (a) The free-electron model of electrons being perturbed by a small potential in the extended representation. (b) The reduced representation in the first Brillouin zone achieved by translating band segments in (a) by $\frac{2\pi n}{a}$ to bring them to the basic zone. (c) Separate forbidden and occupied bands. 24

This material is reserved for educational use only, not allowed for commercial use.

Forbidden to modify the content, and cite the document when use.

LIST OF FIGURES (cont.)

FIGURE **PAGE**

2.12 Two-dimensional rectangular lattices in (a) real and (b) reciprocal space. 27

2.13 Generation of a band gap by a reciprocal lattice vector G. The gap appears in the plane where $|\vec{k}| = |\vec{k} - \vec{G}|$. 27

2.14 First four Brillouin zones of the rectangular lattice, displayed as the shaded areas in the reciprocal lattice. These are translated through reciprocal lattice vectors to build successive rectangles, as shown on the right. 28

2.15 (a) Wigner-Seitz cell of a body-centered cubic crystal, (b) The way in which they pack together to fill space. 29

2.16 (a) Brillouin zone for a face-centered cubic crystal, showing the notation for special points and directions. (b) Band structure in the free-electron model showing the effect of folding back the parabola into the reduced zone. 29

2.17 Band structure of four general semiconductor: silicon, germanium, gallium arsenide, and aluminum arsenide. 31

2.18 Schematic sketch of band discontinuity when two semiconductors are brought together. ...33

2.19 (a) chemical structure of C_6H_6 (Benzene), (b) spatial distribution of the σ–bonds, (c) spatial distribution of the π-bonds forming a delocalized π–system. 34

2.20 Energy level of various excitations in organic molecules in (a) neutral manifold, and (b) charged manifold. 37

2.21 Molecular potential energy as a function of the atomic distance (R). The arrows indicate vibronic transitions associated with (a) absorption, (b) emission of photons, and (c) the corresponding absorption and luminescence spectra. 38

2.22 Lattice constant of various semiconductors against their energy gap E_g as a function of wavelength....................41

2.23 Various possible band edge lineups in heterostructure. 42

2.24 The form of the confined energy states in (a) a multiple quantum well and (b) a superlattice. 44

This material is reserved for educational use only, not allowed for commercial use.

Forbidden to modify the content, and cite the document when use.

LIST OF FIGURES (cont.)

FIGURE **PAGE**

2.25 (a) δ-doped layer at $z=z_0$. (a) distribution of charge: $\rho(z)$,
(b) electric field: F(z), and (d) potential: $\phi(z)$ of a δ-doped layer. 46

2.26 Band diagram of δ-doped structure. 47

2.27 Conduction band around a heterojunction between n-AlGaAs and undoped GaAs, showing how electrons are separated from their donors to form a two-dimensional electron gas. 48

2.28 Infinite potential well. 50

2.29 (a) First four allowed energy levels in infinite well, (b) wave functions and (c) the probability density. 51

2.30 Finite square well. 52

2.31 The energy levels and wave functions in parabolic quantum well. 56

2.32 The triangular well. 58

3.1 Schematic diagram of Photoluminescence spectroscopy experiment set up. 64

3.2 Schematic diagram of Photocurrent spectroscopy experiment set up. 65

3.3 Electron beam evaporator system. 67

3.4 DC sputtering system. 68

3.5 Vacuum pump system. 69

3.6 Cryogenic systems; (a) Cold-finger chamber (b) Helium compressor (c) Temperature controller. 70

3.7 Air-cooled Argon ion laser. 71

3.8 Focusing lenses. 72

3.9 514-nm high pass filter (left) and 488-nm band pass filter (right). 72

3.10 Optical chopper. 73

3.11 Optical detector. 73

3.12 Monochromator. 74

3.13 Lock-in Amplifier. 75

4.1 Temperature-dependent photoluminescence of bulk GaAsP 76

4.2 Temperature-dependent photoluminescence of GaAsP with curve fitting. 77

This material is reserved for educational use only, not allowed for commercial use
Forbidden to modify the content, and cite the document when use.

FIGURE **PAGE**

4.3 The experimental temperature dependence of the energy gap of GaAsP........................79

4.4 Variation of energy gap of GaAsP with temperature. The solid line and the dash line represent the best fit to the Vashni and Viña model, respectively. 80

4.5 Full width of half maximum (FWHM) of PL peak of GaAsP as a function of temperature...81

4.6 FWHM of PL spectra of 3-ML sample as a function of temperature............................82

4.7 Variation of homogeneous broadening with temperature. 83

4.8 PL intensity of GaAsP as a function of temperature. The solid line represents the best fit by equation 4.5. 84

4.9 Schematic draw of contact pattern of GaAsP for photocurrent measurement. 85

4.10 Current-Voltage characteristic of GaAsP with ITO and gold contact as Schottky contact...86

4.11 Photocurrent of ITO/GaAsP with different chopper frequency....................................87

4.12 Frequency response of Photocurrent of ITO/GaAsP at vicinity of energy gap..............88

4.13 Photocurrent of ITO/GaAsP at different bias voltage 89

5.1 Flow sequence of gas sources for $In_{0.53}Ga_{0.47}$ As /InP single quantum well. 92

5.2 Sample structure of $In_{0.53}Ga_{0.47}$ As/InP single quantum well. 93

5.3 PL spectra of $In_{0.53}Ga_{0.47}$ As/InP single quantum well with different well width at 15 K......94

5.4 Schematic band diagram of $In_{0.53}Ga_{0.47}$ As/InP single quantum well............................95

5.5 The values of ground state energy level of heavy hole(E_{hh1}), electron (E_{e1}) and e(1)-hh(1) transition energy in $In_{0.53}Ga_{0.47}$ As/InP single quantum well as a function of the well width...95

5.6 Transition energy of e(1)-hh(1) in InP/InGaAs/InP SQWs as functions of well width. Closed squares present calculated values while the closed lozenges denote the transition energies obtained from the PL measurement. 96

5.7 PL spectra of 3-ML sample at different temperature. 97

5.8 PL peak position of 3-ML sample as a function of temperature. 98

5.9 Integrated PL Intensity and FWHM of PL peak of 3-ML sample. 98

5.10 Variation of Integrated PL intensity with temperature of 3-ML sample. 99

5.11 FWHM of PL spectra of 3-ML sample as a function of temperature. 101

Forbidden to modify the content, and cite the document when use.

LIST OF FIGURES (cont.)

FIGURE **PAGE**

5.12 The homogeneous broadening of $In_{0.53}Ga_{0.47}As/InP$ SQW as a function of temperature....102

5.13 Band diagram of InP/InGaAs/In(Ga)AsP/InP stepped quantum well.

1 ML is approximately equal to 0.3 nm. 105

5.14 The e(1)-hh(1) transition energies with different well widths.

Closed squares and closed triangles show the calculated values without SSI effect

and with SSI effect respectively. Closed lozenges denote the PL results. 106

6.1 Sample structure of Er δ- doped InP. 111

6.2 The time sequence of source gases to grow a Er δ-doped InP. 112

6.3 Room temperature photocurrent of (a) undoped InP and

(b) Er δ-doped InP at 80 minutes erbium exposure duration. 113

6.4 Room temperature photocurrent spectra of Er δ-doped InP of

(a) 10 min Er exposure time and (b) 80 min Er exposure time. 114

6.5 The comparison of transition energies obtained by using RQW model,

PQW model and PC measurement. 117

6.6 Room temperature PC of Er δ-doped InP at 80 min exposure duration under bias voltages.

The solid lines represent the best fitting curve of each spectrum................................118

6.7 The ground state transition energies indicated by solid circles and the peak shift

indicated by solid squares as a function of applied electric field. 119

6.8 Ground-state transition energies of Er δ-doped InP at 80 min exposure duration

as a function of electric-field. The solid line is a theoretical fit to the experimental data....120

7.1 The sample structure of NC-ZnSe/p-Si..127

7.2 Chemical Structure of (a) TPD, (b) Alq_3..128

7.3 SEM image of 500nm- thick NC-ZnSe film..129

7.4 Current-voltage characteristics of NC-ZnSe/p-Si heterostructure with different

ZnSe layer thickness. 130

7.5 PC spectra of NC-ZnSe/p-Si heterostructure with different ZnSe layer thickness..............131

7.6 PC spectra of the sample with Alq_3 thickness of 50 nm..132

7.7 Photocurrent of ZnSe/Alq3/TPD/P-Si with different bias voltage. 133

This document is for educational use only, not allowed for commercial use.
Forbidden to modify the content, and cite the document when use.

LIST OF FIGURES (cont.)

FIGURE **PAGE**

7.8 PC of ZnSe/Alq3/TPD(5nm)/N-Si under forward bias....134

7.9 PC of ZnSe/Alq3/TPD(5nm)/N-Si under reverse bias....135

7.10 Room-temperature ER and PC spectra of sample with 50 nm-thick Alq_3....136

7.11 Room-temperature ER spectra as a function of the well thickness.
Arrows indicate the transition energies determined by the fittings....136

7.12 Energy band diagrams of ZnSe/Alq_3 SQW structure. The numbers are not in scale....138

7.13 ER spectra of 50-nm SQW sample measured in applied voltage +6.0 ~ -2.0V....139

8.1 Schematic draw of 15 periods of $In_{0.1}Ga_{0.9}As$/GaAs quantum wells....146

8.2 Photoluminescence spectrum of $In_{0.1}Ga_{0.9}As$/GaAs multiple quantum wells at 12 K....146

8.3 Temperature-dependent photoluminescence of $In_{0.1}Ga_{0.9}As$/GaAs multiple quantum wells..147

8.4 The experimental temperature dependence of the PL emission peak or e1-hh1
transition energy of $In_{0.1}Ga_{0.9}As$/GaAs multiple quantum wells.
The solid line is the best fit of the Vina model....148

8.5 Schematic band diagram of $In_{0.1}Ga_{0.9}As$/GaAs multiple quantum wells used in
calculation of e(1)-hh(1) excitonic transition at 300 K....150

8.6 Integrated PL intensity of $In_{0.1}Ga_{0.9}As$/GaAs multiple quantum wells
as a function of temperature. The solid line represents the best fit to
experimental data using equation 5.1....151

8.7 Temperature dependence of the full width at half maximum (FWHM) of the PL spectra
of $In_{0.1}Ga_{0.9}As$/GaAs multiple quantum wells....151

8.8 Photoluminescence spectra of $In_{0.1}Ga_{0.9}As$/GaAs MQWs as a function of
excitation energy. The measured temperature is kept at 12 K....153

8.9 Dependence of PL intensity from $In_{0.1}Ga_{0.9}As$/GaAs MQWs on laser excitation intensity..153

8.10 Schematic diagram of energy states in quantum wells and their corresponding
density of states....154

This material is reserved for educational use only, not allowed for commercial use.
Forbidden to modify the content, and cite the document when use.

CHAPTER 1

INTRODUCTION

1.1 Motivation

In the last few decades, the semiconductor growth technology had been rapidly developed. Epitaxy growth is one of the most widely useful techniques to grow the high quality heterostructures. In order to investigate the quality of the grown films, many techniques are employed. Optical technique such as photoluminescence and photocurrent spectroscopy are very efficient tools to characterize many physical properties of the film because of their distinguished advantages; i.e., they are easy to probe, can be impinged in a tiny area, and easy to modulate.

This research is focused on the development of optical spectroscopies. Photocurrent spectroscopy and photoluminescence spectroscopy are proposed to characterize the optical and electronic states of the heterostructure semiconductors such as delta-doped III-V compound, III-V quantum well, and organic molecule-inorganic quantum structure. Both optical spectroscopies can reflect the formation, the quality of the growth, the electronic structures, and physical properties of the film. The features are very useful information to optimize in the growth process, and the fabrication of such devices.

1.2 Objective

This research is conducted in order to

1.2.1 study process of photoluminescence spectroscopy and photocurrent spectroscopy

1.2.2 study the physical properties of various kinds of heterostructure semiconductors such as delta-doped structure, single quantum well structure, and organic molecule-inorganic quantum well structure.

1.2.3 utilize photoluminescence and photocurrent spectroscopy to study the optical properties and electronic states of heterostructure semiconductors.

This material is reserved for educational use only, not allowed for commercial use.
Forbidden to modify the content, and cite the document when use.

1.3 Scope of Study

The scope of this study is as follows,

1.3.1 study the theory of heterostructure semiconductors.

1.3.2 study the theory of photoluminescence and photocurrent of semiconductors.

1.3.3 set up the photoluminescence spectroscopy and photocurrent spectroscopy experiment.

1.3.4 utilize the potential the photoluminescence spectroscopy and photocurrent spectroscopy to study the electronic states of heterostructure semiconductors.

1.3.5 study the effect of temperature, and external applied field on electronic states of heterostructure semiconductors.

1.4 Expected Results

1.4.1 Important physical meaning; i.e., electronic states of heterostructure semiconductors and novel devices of this structure will be clearly understood.

1.4.2 Effects of temperature, and external applied field on electronic states of heterostructure semiconductors will be acknowledged.

1.4.3 Potential advantages of photoluminescence and photocurrent spectroscopy are utilized.

King Mongkut's Institute of Technology Ladkrabang

This material is reserved for educational use only, not allowed for commercial use.
Forbidden to modify the content, and cite the document when use.

CHAPTER 2

THEORETICAL BACKGROUND

The major objective of this study is to understand the physical phenomena of the optical properties of bulk semiconductor and heterostructure semiconductors. The photocurrent spectroscopy and photoluminescence spectroscopy have been chosen to investigate their optical properties. In this chapter, the important theories are presented.

2.1 Photoluminescence Spectroscopy

Photoluminescence spectroscopy (PL) is the spontaneous emission of light from material under optical excitation. PL analysis is nondestructive technique which requires very little sample manipulation or environmental control. Because the sample is excited optically, electrical contacts and junctions are unnecessary. PL can be used to investigate and characterize a variety of material parameters. Features of the emission spectrum can be used to identify surface, interface, and impurity levels and to gauge alloy disorder and interface roughness. The intensity of the PL signal provides information on the quality of surfaces and interfaces. In semiconductor researches, PL spectroscopy is chosen as a very sensitive probe for investigating the electronic transition of both bulk and low-dimensional system semiconductor such as quantum wells (QWs), quantum wires (QWRs) and quantum dots (QDs). In general, impurity and defect related luminescence is dominant, particularly at low temperature, except in the very pure material or in thin layer structures which exhibit quantum confinement.

2.1.1 Photoluminescence Process in Semiconductor

A typical photoluminescence process in semiconductors can be divided into three processes as indicated in Fig. 2.1. First, the sample is excited by intense light. In typical PL experiment, the laser light is used for excitation source. Laser light will be absorbed and create a non-thermal distribution of electrons and holes. Electron-hole pairs are created due to transfer of electrons from the valence into the conduction band (Fig. 2.1a). Second, the non-equilibrium electron and hole distributions tend to relax back to the ground state. Non-radiative processes will rapidly move the carriers to a quasi equilibrium explained by the quasi-Fermi levels. This process is called **"Thermalisation"**. The initial intraband relaxation is caused by energy transfer to the crystal lattice, i.e., a step-by-step excitation of lattice vibration or phonons. After that, the

This material is reserved for educational use only, not allowed for commercial use.
Forbidden to modify the content, and cite the document when use.

electron-hole pairs recombine under emission of light which is the luminescence process. The recombination time can be determined by the transition probability. Due to the attractive Coulomb interaction between the charge carriers, the emission spectrum does not contain contributions from states at or above the fundamental energy gap but also sharp discrete lines just below energy gap which originate from bound excitonic states. In high-impurity material or low-dimensional structure, the spontaneous emission from the sample is typically at the lowest excitonic resonance(E_{exc}) as shown in Fig 2.1c.

There are various types of photoluminescence spectroscopy employed to characterize the material parameters. The photoluminescence of intensity variation of light emitted at a specific energy with changing the excitation energy is called **"Photoluminescence Excitation(PLE)"**. This technique is used to probe the absorption of excitation light. It is crucial that the PLE also depends strongly on the different carrier transfer and relaxation processes. Because the absorption of the most materials depends on energy, the penetration depth of the incident light will depend on the excitation wavelength. Hence, different excitation energies probe different regions of the sample. This is possible to distinguish the absorption in a quantum well from that of the substrate if they have different emission energies. The time evolution spectroscopy of the PL is one of crucial techniques that can provide information of both the transfer and the recombination processes. This technique is called **"Time-resolved Photoluminescence"**.

In a certain respect one might consider the photoluminescence (PL) as the inverse process of the absorption, i.e., the rate of optical generation of electron-hole pairs is equal to their rate of radiative recombination. This is called the principle of detailed balancing (van Roosbroeck-Shockley relation). The van Roosbroeck-Shockley relation is mainly subject to Planck's radiation law and the emitted intensity is given by

$$I_{PL}(\lambda,T,T_c) \propto \frac{\alpha(\lambda,T)}{\lambda^2\left[exp\left(\frac{E(\lambda)}{kT_c}\right)-1\right]}. \qquad (2.1)$$

Where k is the Boltzmann constant, T the lattice temperature and T_c the actual carrier temperature. One should stress that the carrier temperature exceeds considerably the lattice temperature ($T_c >> T$). The carrier temperature depends on many body effects and carrier-phonon interactions.

This material is reserved for educational use only, not allowed for commercial use.
Forbidden to modify the content, and cite the document when use.

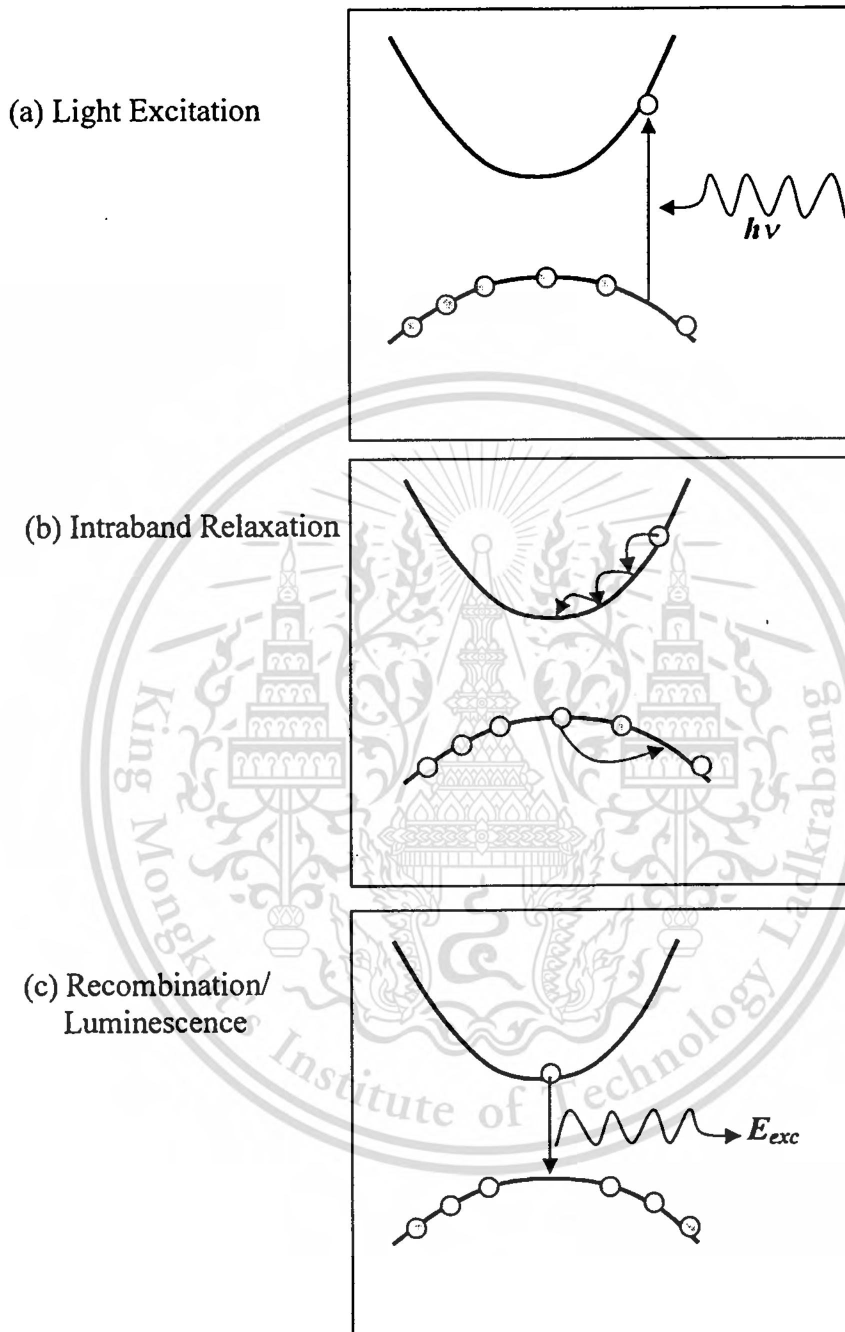

Fig. 2.1 Schematic representation of the basic processes involved in a typical photoluminescence process in semiconductors.

This material is reserved for educational use only, not allowed for commercial use.
Forbidden to modify the content, and cite the document when use.

The more a semiconductor is excited, the higher is the carrier temperature. The absorption coefficient α in equation (2.1) is given by,

$$\alpha_{\hbar\omega} = A\left(\hbar\omega - E_g\right)^{\frac{1}{2}} \quad if \quad \hbar\omega \geq E_g, \text{ and} \tag{2.2}$$

$$\alpha_{\hbar\omega} = A\sqrt{\frac{kT}{2\sigma}}\left(\frac{\sigma}{kT}\left(\hbar\omega - E_g\right)\right) \quad if \quad \hbar\omega < E_g. \tag{2.3}$$

PL measurements can be used to explore the temperature dependence of the band gap. To fit the data the following equation proposed by Vashni has been proven to be useful,

$$E_g(T) = E_g(0K) - \alpha\frac{T^2}{\beta + T}, \tag{2.4}$$

where $E_g(T)$ is the energy gap at temperature T and α and β are parameters to fit the experimental data (referred to as Vashni thermal coefficients).

2.1.2 Photoluminescence Spectrum

Typically, optical transitions provide direct information to the energy level structure of a sample. Photons of a specific energy that are absorbed or emitted by a sample reveal evidence of electronic states differing by that energy within the material. In PL process, PL emission normally tend to separate the lowest-lying states because photoexcited carriers rapidly thermalize through bands and closely spaced states to within kT of the lowest available levels. This unique feature of PL makes it particularly effective in the analysis of the interfaces where discrete defect and impurity states are bounded. If the state is radiative, it will generate particular peaks in the PL spectrum. Thus, the PL measurement is a very sensitive probe of such states.

In the bulk of a crystalline semiconductor, translational symmetry leads to the formation of electronic energy bands. Defects and impurities perturb the band locally. This perturbation can usually be characterized by a discrete energy level lying within the bandgap. The corresponded states act as donor or acceptor of excess electrons in the crystal. Electrons and holes are attracted to the excess of local charge and Coulomb binding occurs. Because electrons and holes have

This material is reserved for educational use only, not allowed for commercial use.
Forbidden to modify the content, and cite the document when use.

different effective masses, donors and acceptors consequently have different binding energies. When the temperature is sufficiently low, carriers will be trapped at these states. If these carriers combine radiatively, the energy of the emitted light can determine the energy of the defect or impurity level. Shallow levels lying near the conduction or valence band edge are more likely to participate in radiative recombination. However, the sample temperature must be small enough to ignore thermal activation of carriers out of the traps. For deep levels, they tend to facilitate non-radiative recombination by providing a stop-over for electrons making their way between the conduction and valence bands by emitting phonons. Fig. 2.2 illustrates several intrinsic and impurity transitions.

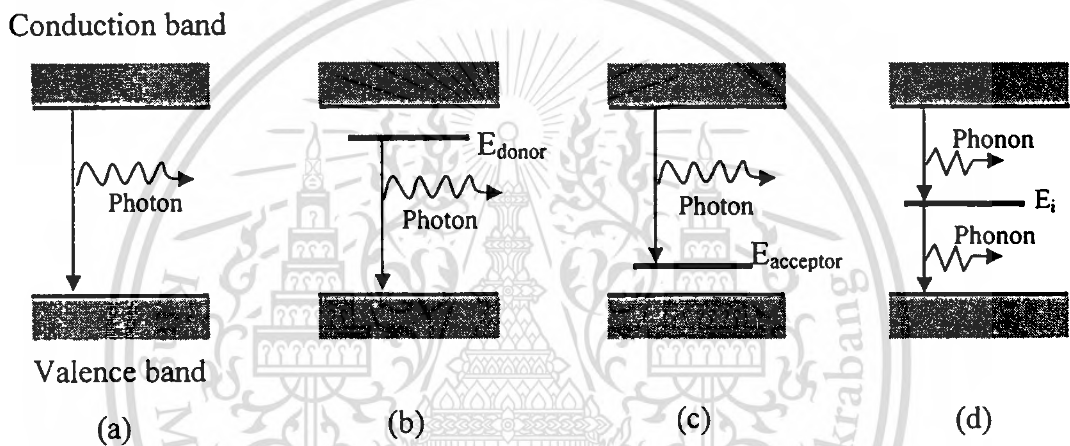

Fig 2.2 (a-c) Radiative recombination paths: (a) band-to-band; (b) donor to valence band; (c) conduction band to acceptor. (d) Nonradiative recombination via an intermediate state (E_i).

2.1.3 Photoluminescence Intensity

The photoluminescence intensity of the PL signal has received attention in the analysis of interfaces. This interest arises due to the fact that large PL signals correlate with good interface properties. PL measurements have been used to evaluate a wide variety of surface processes, including etching, oxidation, adsorption of gas, deposition of coatings and heteroepitaxy. Because a strong PL response is typically regarded as an indicator of a high-quality surface, and PL measurement is nondestructive and environment insensitive, PL intensity measurement is an important in-situ evaluation tool, i.e., PL signal is monitored in real time while the surfaces are modified.

This material is reserved for educational use only, not allowed for commercial use.
Forbidden to modify the content, and cite the document when use.

2.1.4 Luminescence from Quantum Well Structures

Since 1975, a very large literature has pioneered on the spectroscopic assessment of quantum well structures, primarily GaAs/AlGaAs, InP/InGaAs and others. Luminescence spectroscopy is particularly important characterization tools. In semiconductor, quantum size effects begin to appear when the well width becomes less than ~ 50 nm. An electron or hole in the well layer is confined in a potential well. If the well width is of the order of the de Broglie wavelength, the particle motion and their energy levels are quantized. Low temperature photoluminescence measurements primarily detect n=1 exciton recombination because photoexcited carriers rapidly thermalize through bands and closely spaced states to within kT of the lowest available levels. The width of the luminescence peak provides a good measurement of the quality of the interface since fluctuations in well width produce considerable broadening, particularly in narrow wells. Additional, bound exciton luminescence can also occur from donor and acceptors in the wells. The binding energy depends both on the well width and the position of the impurity within the well. It indicates that impurities within wells are mainly segregated at the interface.

King Mongkut's Institute of Technology Ladkrabang

This material is reserved for educational use only, not allowed for commercial use.
Forbidden to modify the content, and cite the document when use.

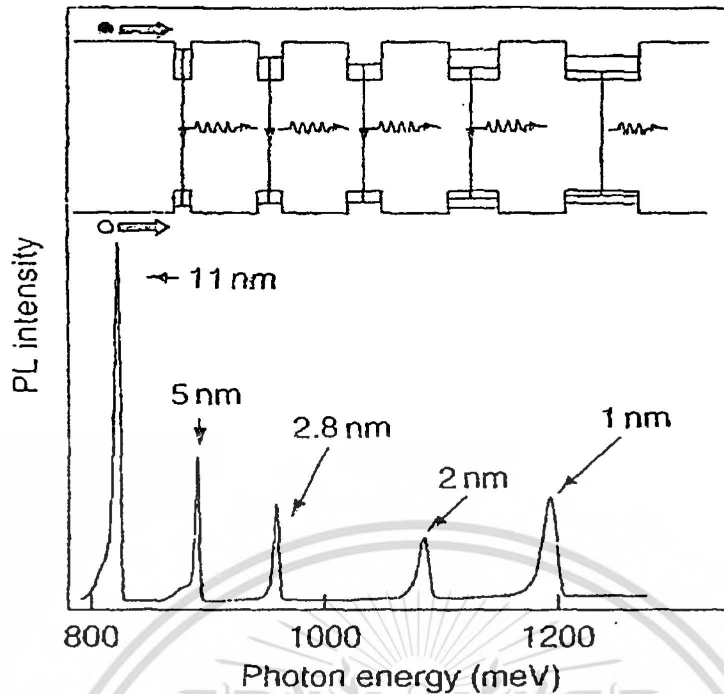

Fig. 2.3 Photoluminescence for a InGaAs/InP quantum well sample with five quantum wells with different thickness, the inset shows the electronic structure and the nature of the optical transitions.

In practice, light with the photon energy greater than the energy gap of barrier is shone on the sample, which excites many electrons from the valence band to the conduction band everywhere. Some of these electrons become trapped in the quantum well, and the same manner happens to the holes in the valence band. It is then possible for an electron to fall from a quantized energy level in conduction band into a hole in valence band and release the difference in energy as light. Only the lowest levels are usually seen. An example of a photoluminescence spectrum in shown in Fig. 2.3. The sample has five wells of different widths, each of which contributes a peak to the PL.

This material is reserved for educational use only, not allowed for commercial use.
Forbidden to modify the content, and cite the document when use.

2.2 Photocurrent Spectroscopy

Photocurrent spectroscopy is an alternative way to measuring the optical properties and electronic properties of semiconductors. The current can be induced by absorption in the structure by the photon. The photocurrent generation is also influenced by carrier transport. The photocurrent technique has the advantage of being a direct measurement in the meaning that the current is proportional to the absorption, avoiding the huge background of the transmission measurements.

2.2.1 Photocurrent Process

Fig. 2.4 shows schematic diagram of photocurrent process in semiconductor. When light illuminates on the semiconductor, electron-hole pairs are generated which change its conductivity. The applied electric field causes the electrons and holes to move in opposite directions, leading to current. The analysis of the photocurrent starts by defining the recombination rate R,

$$R = \frac{\Delta n}{\tau}, \tag{2.5}$$

where Δn is the concentration of generated electrons and τ is the lifetime for the excess carriers. In the dark, the conductivity is

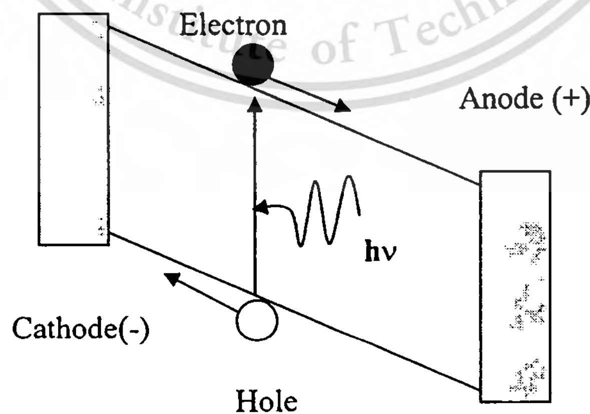

Fig. 2.4 Photocurrent in semiconductor.

This material is reserved for educational use only, not allowed for commercial use.
Forbidden to modify the content, and cite the document when use.

$$\sigma_0 = q(\mu_n n_0 + \mu_p p_0), \tag{2.6}$$

where n_0 and p_0 are the electron and hole densities in the dark, and μ_n and μ_p are the electron and hole mobilities respectively. If the optical signal generates an excess carrier density of $\Delta n = \Delta p$, the conductivity becomes

$$\sigma = q[\mu_n(n_0 + \Delta n) + \mu_p(p_0 + \Delta p)]. \tag{2.7}$$

The excess carrier density is $\Delta p = \Delta n = G\tau$, where G is the generation rate. The change in the conductivity of the material due to the optical signal is called the *photoconductivity* and is given by

$$\Delta\sigma = q\Delta p(\mu_n + \mu_p). \tag{2.8}$$

The current density is then given by

$$J = J_d + J_L = (\sigma_0 + \Delta\sigma)F_{el} \quad . \tag{2.9}$$

Where J_d is the dark current density, J_L is the current density due to the illumination and F_{el} is the electric field. The photocurrent is thus

$$I_{ph} = J_L A = q\Delta p(\mu_n + \mu_p)AF_{el} = qG_L\tau(\mu_n + \mu_p)AF_{el}, \tag{2.10}$$

$\mu_n F_{el}$ and $\mu_p F_{el}$ represent the electron and hole velocities. Let us define the transit time of the electrons in the semiconductor by

$$t_{tr} = \frac{L}{\mu_n F_{el}}, \tag{2.11}$$

where L is the distance of the contacts. Substituting equation (2.11) in (2.10), the photocurrent becomes

This material is reserved for educational use only, not allowed for commercial use.
Forbidden to modify the content, and cite the document when use.

$$I_{ph} = qG\left(\frac{\tau}{t_{tr}}\right)\left(1+\frac{\mu_p}{\mu_n}\right)AL \ . \tag{2.12}$$

This is the photocurrent generate in the circuit. Primarily, We define photocurrent as

$$I_{ph.p}=qGAL. \tag{2.13}$$

This would be the photocurrent if each electron-hole pair simply contributed one charge at the contact, i.e., if there was no gain in the device. Comparing (2.12) to (2.13)The gain in the circuit is now

$$g_{ph} = \frac{I_{ph}}{I_{ph.p}} = \left(\frac{\tau}{t_{tr}}\right)\left(1+\frac{\mu_p}{\mu_n}\right). \tag{2.14}$$

In addition, the total lifetime (τ) of carrier charge involved in the photocurrent is expressed as,

$$\tau = \tau_{surf} + \tau_{Bulk}\left[1 - exp\left(-\frac{x}{l}\right)\right], \tag{2.15}$$

where, τ_{surf} is the life time of the carrier charge at the surface,

τ_{bulk} is the life time of the carrier of bulk semiconductor,

and l is the penetration depth of light into the sample.

In general, the photocurrent depends on the total lifetime(τ) and the carrier generation (G) by the following expression,

$$G(x) = \frac{\alpha_{\hbar\omega}}{\hbar\omega} I_0 \, exp(-\alpha_{\hbar\omega} x), \tag{2.16}$$

and

This material is reserved for educational use only, not allowed for commercial use.
Forbidden to modify the content, and cite the document when use.

$$I_{ph} \propto \frac{I_0}{\hbar\omega}\int_0^t \tau(x)\alpha_{\hbar\omega}\, exp(-\alpha x)dx \, . \tag{2.17}$$

Where t is the thickness of the sample,

I_0 is the intensity of light,

$\hbar\omega$ = Photon energy,

and, $\alpha_{\hbar\omega}$ = Absorption coefficient of photon energy.

After integrating, I_{ph} is obtained,

$$I_{ph} = \frac{I_0}{\hbar\omega}\left[1 - exp(\alpha t) - \left(1 - \frac{\tau_{sur}}{\tau_{blk}}\right)^{-1} \frac{\alpha\ell}{\alpha\ell + 1}\left(1 - exp\left(-\left(\frac{\alpha + 1}{\ell}\right)t\right)\right)\right]. \tag{2.18}$$

Where,

$$\alpha_{\hbar\omega} = A(\hbar\omega - E_g)^{\frac{1}{2}} \quad if \quad \hbar\omega \geq E_g \text{, and}$$

$$\alpha_{\hbar\omega} = A\sqrt{\frac{kT}{2\sigma}}\left(\frac{\sigma}{kT}(\hbar\omega - E_g)\right) \quad if \quad \hbar\omega < E_g \, .$$

A= fitting constant.

σ = phenomenological parameter sealing the steepness of absorption edge.

The intensity of photocurrent also depends on the chopper frequency. This is important parameter for photodetector employing the photo-generated current. During photocurrent measurement, the chopper frequency is changed. It can be assumed that the transient behavior of sample is exponential with time [B. Shen et.al],

$$I_{ph} = I_0\, exp(t/\tau) \, . \tag{2.19}$$

When the light is off, the intensity of photocurrent I decrease as $I_{(t)}$ but stops at t=T_o, at which time the light is turned on again, and then the intensity increases. So the AC signal detected by the lock-in amplifier is,

$$\Delta I_{ph} = I_0\, tanh\left[\frac{1}{4\tau f}\right], \tag{2.20}$$

This material is reserved for educational use only, not allowed for commercial use.
Forbidden to modify the content, and cite the document when use.

where f is the frequency of the chopper.

2.2.2 Photocurrent in Quantum Wells

In quantum well structure, the photocurrent is generally the same expression used for photoconductor,

$$I_{ph} = q\phi_{ph}\eta G , \tag{2.21}$$

where ϕ_{ph} is the total photon arrival rate. The quantum efficiency η is however different from bulk semiconductor since light absorption in this structure occur only in quantum wells but not homogeneously throughout the structure. It is given by,

$$\eta = (1-R)\left[1-exp(-N_p \alpha N_i L_w)\right]E_P P \ . \tag{2.22}$$

Where R is the reflection, N_p is the number of optical passes, and N_i is the number of quantum wells, each of length L_w. The escape probability E_p is a function of bias which extracts the excited carrier out of the quantum wells. P is the polarization correction factor. The photoconductive gain G has been derived to be

$$G = \frac{1}{N_i C_p} , \tag{2.23}$$

where C_p is the capture probability in the well, given by

$$C_p = \frac{t_p}{\tau} = \frac{t_t}{N_i \tau} , \tag{2.24}$$

t_p is the transit time across a single period of the structure and t_t is the transit time across the entire structure.

This material is reserved for educational use only, not allowed for commercial use.
Forbidden to modify the content, and cite the document when use.

2.2.3 Metal-Semiconductor Junctions

In order to extract the photocurrent from the semiconductor, an appropriate metal contact is required. In this session, important theory of metal-semiconductor junctions is described. Many transport properties in semiconductors can be achieved by depositing a metal on a semiconductor, and forming a metal-semiconductor junction. There are typical two types of these junctions: (1) Schottky junction and (2) Ohmic junction.

2.2.3.1 Schottky Junctions or Rectifying Junction

The Schottky junction can be formed between metal and either n-type or p-type semiconductor. Firstly, let us form a junction between a metal and an n-type semiconductor whose band diagrams are illustrated in Fig. 2.5. In the figure, $q\phi_M$ and $q\phi_S$ are the work functions of the metal and the semiconductor, respectively. The work function represents the energy required to move electrons from the corresponded Fermi levels to the vacuum level. The metal is chosen so that ϕ_M is greater than ϕ_S. The Fermi level in the metal is therefore at a lower position than that in the semiconductor. Furthermore, $q\chi$ is the electron affinity of the semiconductor which is the energy difference between the conduction-band edge and the vacuum level. When the junction is aligned, electrons from the conduction band in the semiconductor flow into the metal due to their higher energy. The electrons flow stops when the Fermi levels of both species are at the same height. After electrons flow from semiconductor to metal, the positive donor ions are leaved in the thickness W in the semiconductor; that is, a depletion region with the thickness W. At the interface, the Fermi level must move deeper in to the semiconductor, leading to upward bending of the energy bands. In addition, the presence of these two types of charges on either side of the junction establishes an electric field directing from the semiconductor to the metal. At the interface, a potential V_0 is created and prevents further flow of electrons from the semiconductor into the metal.

This material is reserved for educational use only, not allowed for commercial use.
Forbidden to modify the content, and cite the document when use.

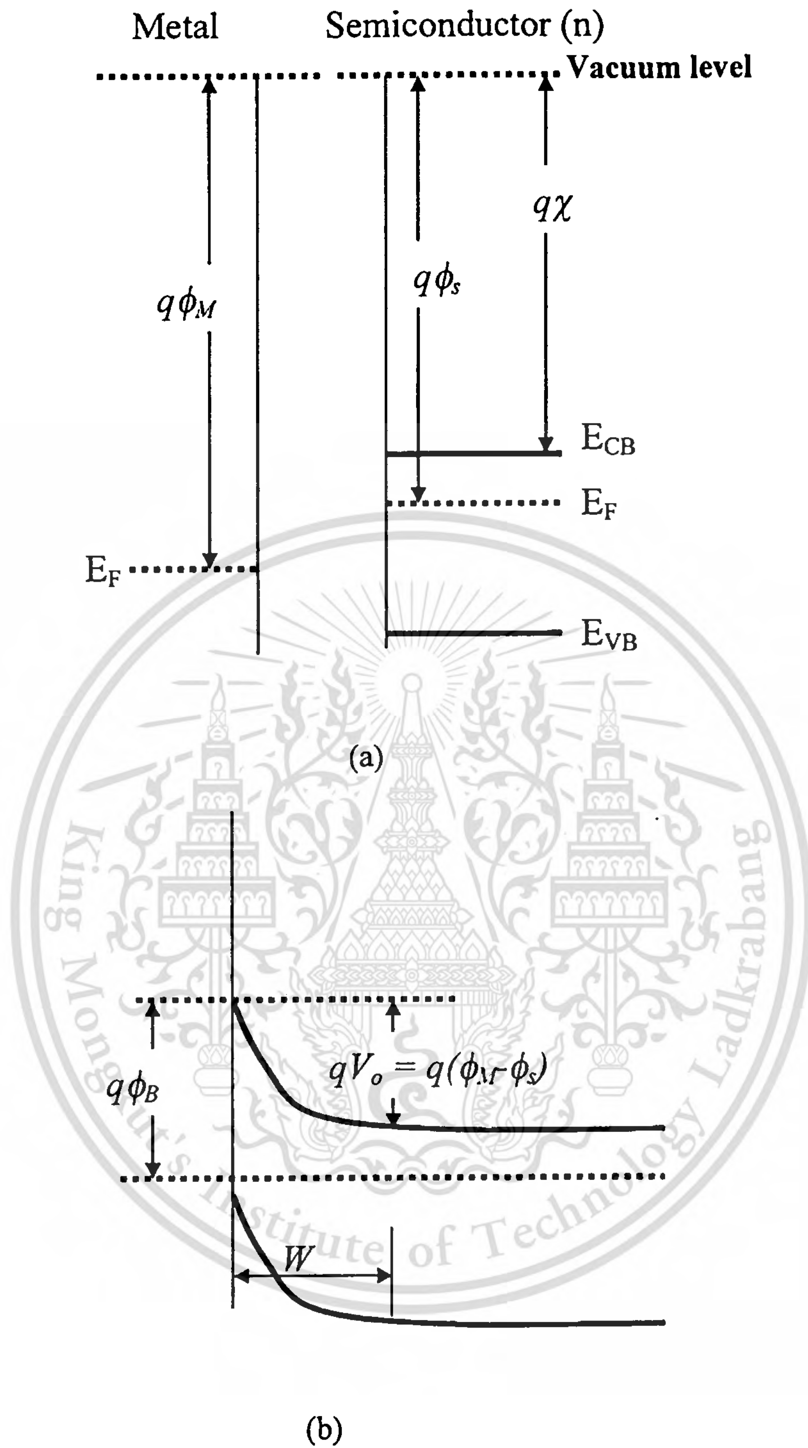

Fig. 2.5 Energy band diagrams for a metal/n-type semiconductor contact (a) two materials isolated from each other (b) at thermal equilibrium after the contact is made.

This material is reserved for educational use only, not allowed for commercial use.
Forbidden to modify the content, and cite the document when use.

สำนักหอสมุดกลาง พระจอมเกล้าลาดกระบัง

It represents the difference between the work function potentials ϕ_M and ϕ_S. The barrier height $q\phi_B$ for the injection of electrons from the metal into the semiconductor is given by

$$q\phi_B = q\phi_M - q\chi \cdot \tag{2.25}$$

This type of metal semiconductor junction is called a **Schottky barrier.**

A Schottky barrier is also formed when a metal is deposited on a p-type semiconductor such that $\phi_M < \phi_S$. This condition is schematically depicted in Fig. 2.6. At the interface, electrons must flow from the metal to the semiconductor, resulting in a positive surface charges in the metal and negative charges on the semiconductor. These exceed charges exist within a depletion region W in which acceptor ions are left uncompensated by the holes. The potential barrier V_0 which equals to ϕ_S - ϕ_M, retards the diffusion of holes from the semiconductor to the metal. From equation (2.25), the Schottky barrier heights $q\phi_B$ for different metals should be different because of the difference of the metal work functions $q\phi_M$. This deduction is not always realized. It is often found that the Schottky barrier heights for various metals on a particular semiconductor are equaled. This behavior is attributed to the presence of a large number of interface states in the band gap of the surface region of the semiconductor. These states arise from the surface dangling bonds and impurities. The addition or removal of electrons from the semiconductor does not change the position of the Fermi level at the surface and the Fermi level is said to be pinned. Its ramification is that the position of E_{CB} at the surface does not alter with the metal, resulting in the constant barrier height.

This material is reserved for educational use only, not allowed for commercial use.
50171
Forbidden to modify the content, and cite the document when use.

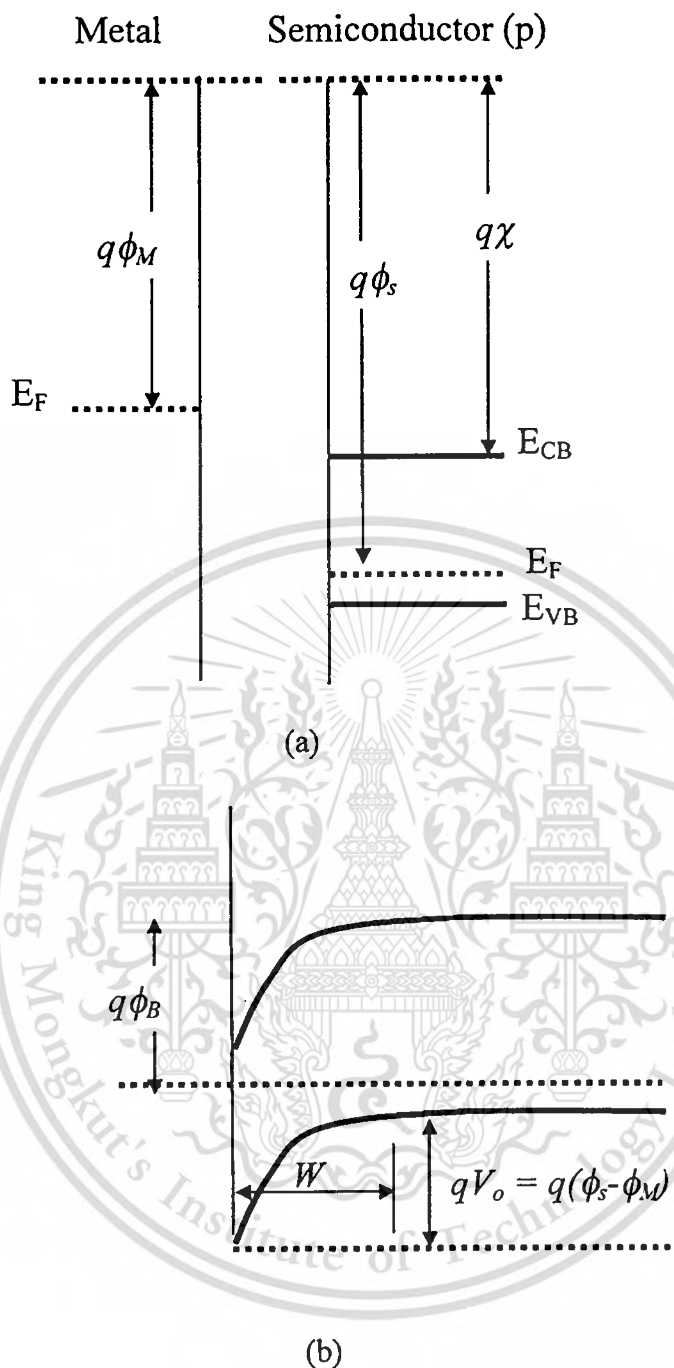

Fig. 2.6 Energy band diagrams for a metal/p-type semiconductor contact (a) two materials isolated from each other (b) at thermal equilibrium after the contact is made.

This type of contact that is said to be rectified in nature, can be illustrated by Fig. 2.7. For n-type, at equilibrium, electrons that have greater energy than qV_0 are thermoionically emitted over the barrier into the metal. Alternatively, if the semiconductor is heavily doped so that the depletion layer becomes very thin, electrons can tunnel into the metal through the barrier. These

This material is reserved for educational use only, not allowed for commercial use.
Forbidden to modify the content, and cite the document when use.

electrons consequently produce a current I_{MS} that flows from the metal to the semiconductor. However, at equilibrium, this current is exactly balanced by a equal but opposite current I_{SM} in order to keep the net current to be zero. When the semiconductor is negative biased with respect to the metal by voltage V_f, that is, forward bias, the barrier to the flow of electron from the semiconductor to the metal decreases from qV_0 to $q(V_0-V_f)$ as shown in Fig. 2.8a. Therefore, more electrons flow from the semiconductor to the metal and also I_{MS} increases above the equilibrium value. However, I_{SM} does not change because $q\phi_B$ remains constant on biasing. Therefore, a net flow of current from the metal to the semiconductor occurs. When reverse-biased V_r is applied (Fig. 2.8b), the electron flow from the semiconductor to the metal reduces because the barrier increases to $q(V_0+V_r)$. I_{MS} is consequently reduced below its equilibrium value, whereas I_{SM} remains almost unchanged. Thus, the net small current flows from the semiconductor to the metal.

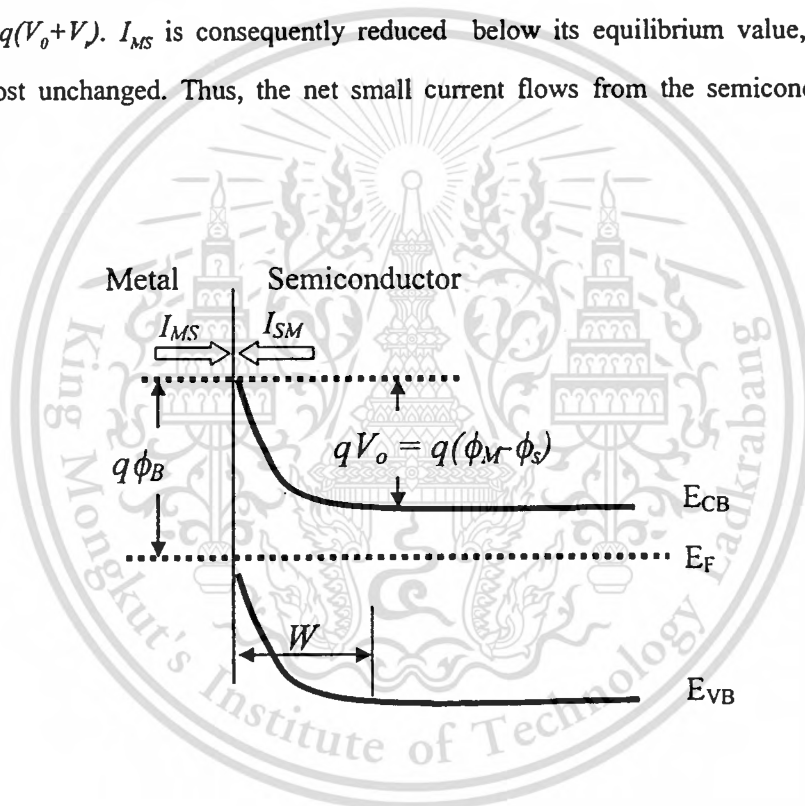

Fig. 2.7 Energy band diagram of rectifying metal/n-type semiconductor contact at thermal equilibrium.

This material is reserved for educational use only, not allowed for commercial use.
Forbidden to modify the content, and cite the document when use.

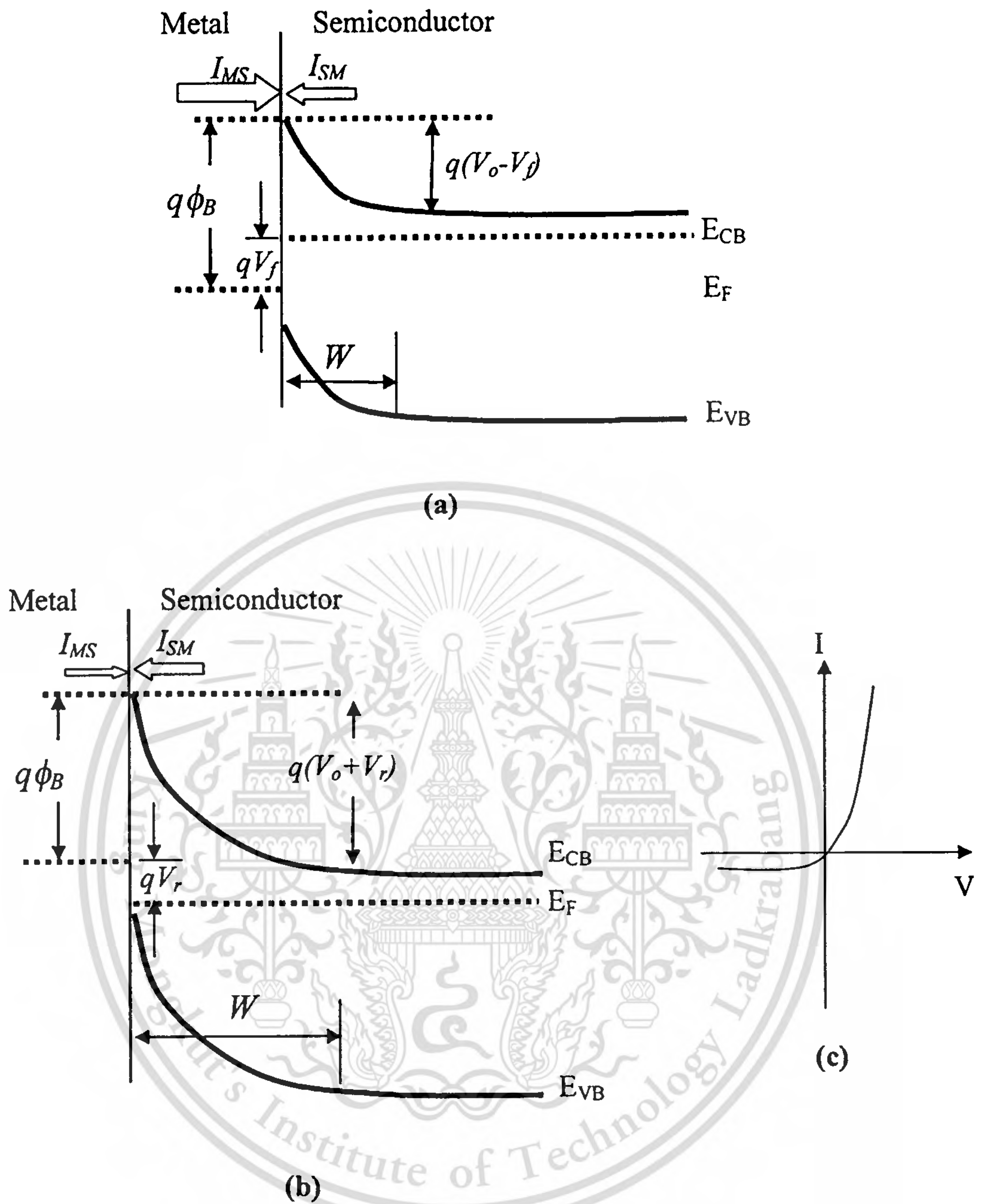

Fig. 2.8 Energy band diagram of rectifying metal/n-type semiconductor contact (a) after forward bias, (b) after reverse bias and (c) I-V characteristic of the junction.

The composite I-V Characteristics of a Schottky barrier diode are shown in Fig. 2.8c. The behaviors and the current-voltage characteristics of Schottky barrier diodes are similar to these behavior of p-n junction diodes.

This material is reserved for educational use only, not allowed for commercial use.
Forbidden to modify the content, and cite the document when use.

2.2.3.2 Ohmic Contacts or Nonrectifying Junctions

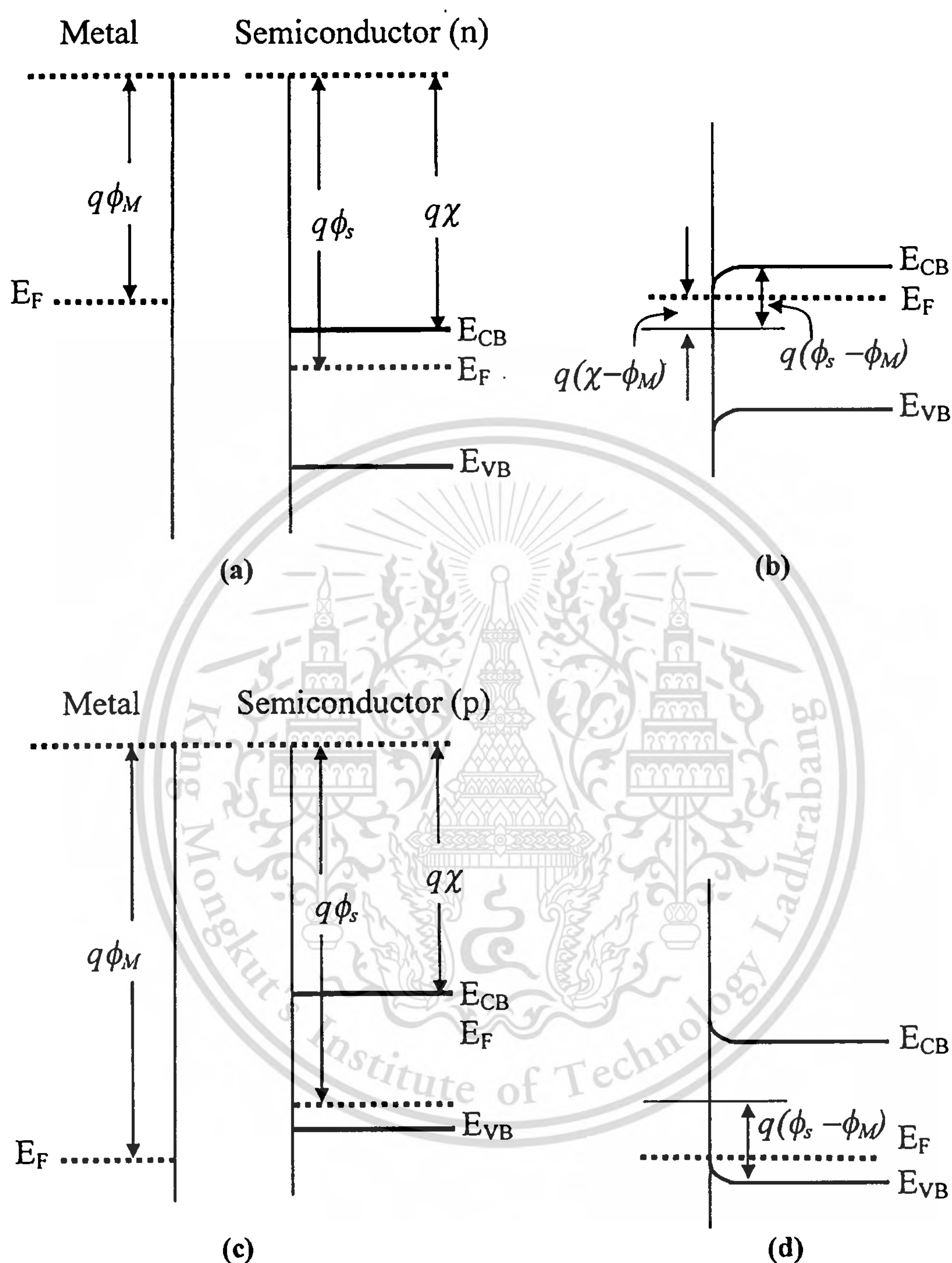

Fig. 2.9 Band diagram for ohmic metal-semiconductor contact (a) $\phi_M < \phi_S$ for n-type (b) the junction at equilibrium for n-type/metal (c) $\phi_M > \phi_S$ for p-type semiconductors (d) the junction at equilibrium for p-type/metal.

This material is reserved for educational use only, not allowed for commercial use.
Forbidden to modify the content, and cite the document when use.

An ohmic contact is a metal-semiconductor contact that has negligible contact resistance relative to the bulk or series resistance of the semiconductor. The ohmic contact can be achieved when metal-semiconductor junctions satisfy the following requirements : $\phi_M < \phi_S$ for n-type and $\phi_M > \phi_S$ for p-type semiconductors. For n-type semiconductor (Fig. 2.9a-b), when $\phi_M < \phi_S$, the Fermi levels are aligned by the transfer of electrons from the metal to the semiconductor. This alignment lifts the electron energies of the semiconductor relative to that in the metal at equilibrium. The barrier to the flow of electrons from the metal to the semiconductor is small and can be easily overcome by a small applied voltage. In similar, when $\phi_M > \phi_S$ and the semiconductor is p-type (Fig. 2.9c-d), the hole flow across the junction can take place readily. Moreover, unlike the case of rectifying contacts discussed in the last section, the depletion regions do not form in the two cases, because the alignment of the Fermi levels requires the accumulation of majority carriers in the semiconductor.

2.3 Band Theory of Semiconductor

2.3.1 Band Structure in One Dimension

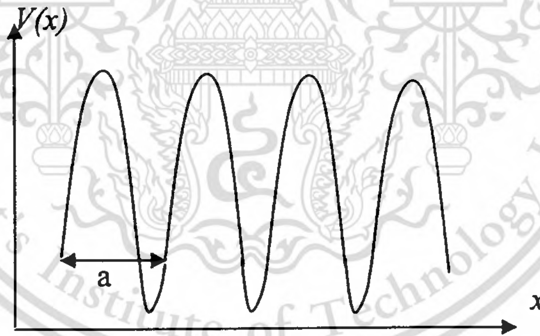

Fig. 2.10 An example of one-dimensional periodic potential with lattice constant *a*.

The potential energy in real crystal is typically periodic. In one dimension, this means that $V(x+a)=V(x)$, where a is the lattice constant, the size of each unit cell of the crystal. A fictitious example of a periodic potential is schematically sketched in Fig. 2.10. Therefore, this potential can be expanded in a Fourier series,

$$V(x)=\sum_{n=-\infty}^{\infty} V_n \exp\left(\frac{2\pi inx}{a}\right)=\sum_{n=-\infty}^{\infty} V_n \exp(iG_n x). \tag{2.26}$$

This material is reserved for educational use only, not allowed for commercial use.

Forbidden to modify the content, and cite the document when use.

Where $G_n = \dfrac{2\pi n}{a}$, called the reciprocal lattice vectors. The corresponding wave function of this potential is expected as translation invariant function. Their probability density is also expected to be a periodic function like the potential, that is, $|\psi(x+a)|^2 = |\psi(x)|^2$. The corresponding wave function called a Bloch's function;

$$\psi_k(x) = u_k(x)exp(ikx), \qquad u_k(x=a) = u_k(x). \tag{2.27}$$

Equation (2.27) is the statement of Bloch's theorem for the wave in a crystal. The equivalent wave function can be written as,

$$\psi_k(x+a) = \psi_k(x)exp(ika). \tag{2.28}$$

Where k is called the Bloch wave number. The value of k is somewhat ambiguous since periodical behavior of the wave function. Hence, it can be written as

$$k = \left(\frac{2\pi}{a}\right) + k' . \tag{2.29}$$

Then, the wave function becomes,

$$\begin{aligned}\psi_k(x) = u_k(x)exp(ikx) &= \left[u_k(x)exp\left(\frac{2\pi ix}{a}\right)\right]exp(ik'x) \\ &= u'_k(x)exp(ik'x)\end{aligned} \tag{2.30}$$

The Bloch wave number is now reduced to the range $-\frac{\pi}{a} < k' < \frac{\pi}{a}$, which is called the **first Brillouin zone.** The same interpretation can be also done for any value of $k = nk'$, where n is an appropriate integer number. The wave function then becomes,

$$\psi_{nk'}(x) = u_{nk'}(x)exp(ik'x). \tag{2.31}$$

This material is reserved for educational use only, not allowed for commercial use.
Forbidden to modify the content, and cite the document when use.

The value k could be any value called the **extended zone scheme.**

The corresponding energy is usually labeled with the wave number in the first Brillouin zone and the band index n, as $\varepsilon_n(k)$. For values of k other than $n\pi/a$, electrons can be treated as free electrons therefore the energy $\varepsilon_n(k) \approx \varepsilon_0(k)$. The exceptions are near the zone boundaries, where $k = \frac{1}{2}G_n = \frac{n\pi}{a}$. Here $\varepsilon_n(k)$ turns away from the free-electron parabola to become flat where it meets the zone boundary, leaving a gap between where the crystal has no propagating states. The modified energy $\varepsilon_n(k)$ is illustrated in Fig. 2.11a. This representation is referred to as an **extended representation** because $\varepsilon_n(k)$ is plotted explicitly for all values of k. Since the crystalline structure and the solution for electron waves are periodic, the solution is not altered. It is therefore possible to display the same information using a **reduced representation** as shown in Fig 2.11b. In this case ε_n are plotted for $-\frac{\pi}{a} < k < \frac{\pi}{a}$. This representation is achieved by translating the individual segments by multiples of $2\pi/a$ to bring them into $-\frac{\pi}{a} < k < \frac{\pi}{a}$ range. Fig 2.11c shows the corresponding occupied and forbidden energy bands.

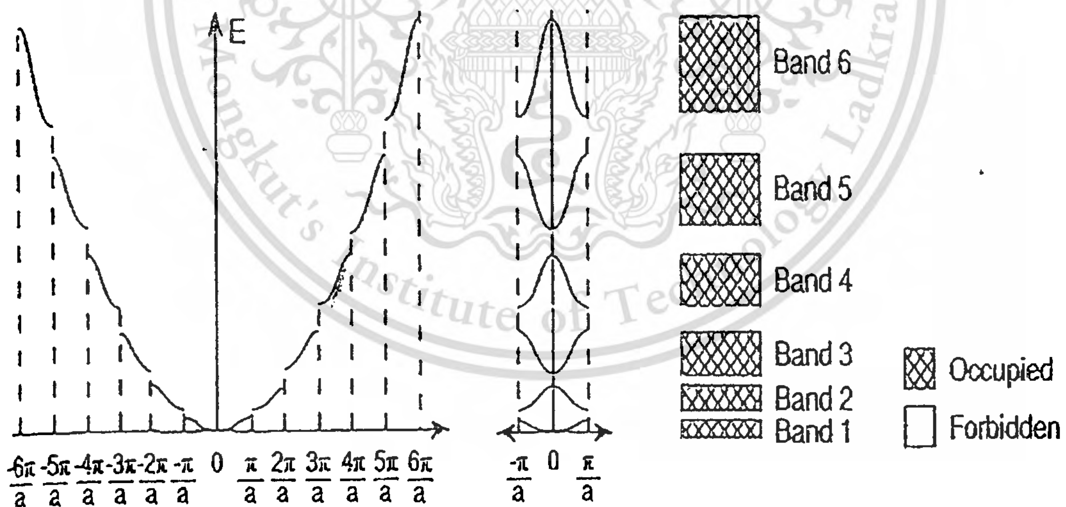

Fig. 2.11 (a) The free-electron model of electrons being perturbed by a small potential in the extended representation. (b) The reduced representation in the first Brillouin zone achieved by translating band segments in (a) by $\frac{2\pi n}{a}$ to bring them to the basic zone. (c) Separate forbidden and occupied bands.

This material is reserved for educational use only, not allowed for commercial use.
Forbidden to modify the content, and cite the document when use.

2.3.2 Motion of Electrons in Bands

Free electrons have group velocity v_g, that is, velocity with which the boundaries of the wave propagate, and are given by

$$v_g = \frac{d(2\pi\upsilon)}{dk}, \tag{2.32}$$

where ν is the frequency of the wave. Equation (2.32) can be rewritten as,

$$v_g = \frac{d}{dk}(\frac{2\pi h\upsilon}{h}) = \frac{1}{\hbar}\frac{d\varepsilon_k}{dk}. \tag{2.33}$$

At the edges of the energy band, the ε_k-k curves are flat; that is , $d\varepsilon_k/dk$ is equal to zero. This means that, at the edge of a Brillouin zone, the electron velocity v_g is also zero and it can not escape into the forbidden energy gap.

When electron moves in solid, its mass is different from the mass of a free electron. This behavior is attributed to interactions between the drifting electrons and the atoms in a crystal. The corresponding electron mass in the solid is referred to as the effective mass (m^*). The acceleration of an electron moving in solid can be obtained by taking the derivative of v_g, i.e.,

$$a = \frac{dv_g}{dt} = \frac{1}{\hbar}\frac{d^2\varepsilon_k}{dk^2}\frac{dk}{dt}. \tag{2.34}$$

Substituting for $k = \frac{p}{\hbar}$ into equation(2.34),

$$a = \frac{1}{\hbar^2}\frac{d^2\varepsilon_k}{dk^2}\frac{dp}{dt} = \frac{1}{\hbar^2}\frac{d^2\varepsilon_k}{dk^2}F. \tag{2.35}$$

Comparing the force F in classical mechanics, the effective mass m^* can be written as,

This material is reserved for educational use only, not allowed for commercial use.
Forbidden to modify the content, and cite the document when use.

$$m^* = \hbar^2 \left(\frac{d^2 E}{dk^2} \right)^{-1} \tag{2.36}$$

From equation (2.36), the effective mass is inversely proportional to the curvature of an E versus k curve that is electron band. The higher the magnitude of the curvature, the smaller the effective mass.

2.3.3 Band Structure in Two and Three Dimension

The principle of band structure in two and three dimensions is the same as in one dimension. However, the result is more complicated because the reciprocal lattice is now two-or three-dimensional. Again k can be reduced to the first Brillouin zone by adding reciprocal lattice vectors. In two dimension, the reciprocal lattice is a rectangular with spacing a along x and b along y. The periodic potential $V(x,y)$ can be expanded as a Fourier series,

$$V(x,y) = \sum_{m,n=-\infty}^{\infty} V_{m,n} \exp\left(\frac{2\pi imx}{a} + \frac{2\pi iny}{b} \right)$$

$$= \sum_{m,n} V_{m,n} \exp\left(i\vec{G}_{m,n} \cdot \vec{r} \right), \tag{2.37}$$

Where $\vec{G}_{m,n} = (2\pi m/a, 2\pi n/b)$ are the reciprocal lattice vectors. This lattice may be also plotted out to form a reciprocal lattice in k-space as shown in Fig. 2.12. The periodic potential introduces band gaps and breaks k-space into Brillouin zones. The simplest argument for the formation of gaps is that based on the mixing of wave functions. A wave function with wave vector k gains components ***k-G*** from each Fourier coefficient-G of the potential. Strong mixing, leading to band gaps, occurs when the energies are equal, which requires $|\vec{k}| = |\vec{k} - \vec{G}|$. This relation defines a plane bisecting the line from the origin to G, as shown in Fig.2.13.

This material is reserved for educational use only, not allowed for commercial use.
Forbidden to modify the content, and cite the document when use.

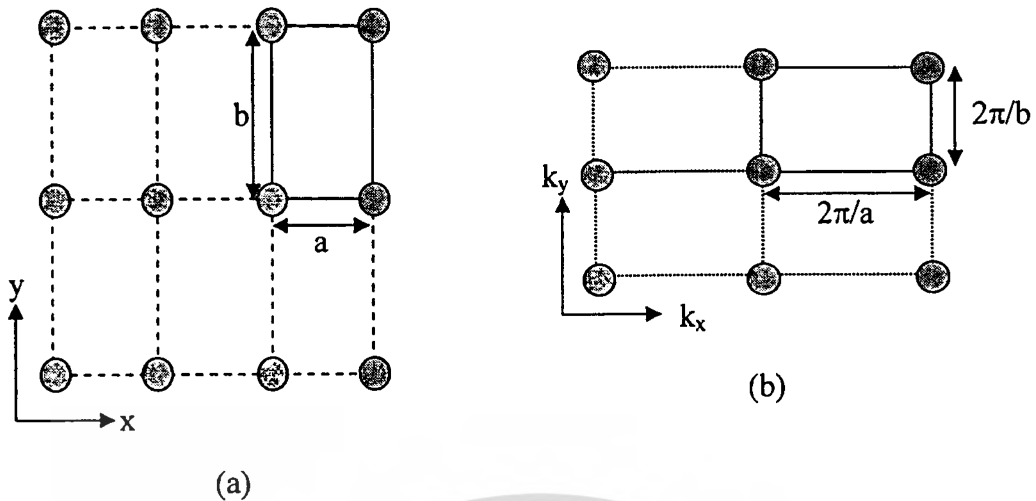

Fig. 2.12 Two-dimensional rectangular lattices in (a) real and (b) reciprocal space.

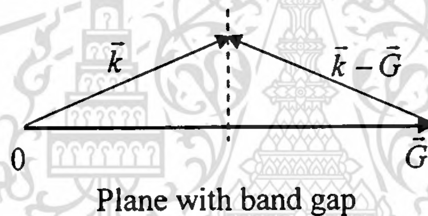

Fig. 2.13 Generation of a band gap by a reciprocal lattice vector **G**. The gap appears in the plane where $|\vec{k}| = |\vec{k} - \vec{G}|$.

The periodic potential gives a band gap on each of these planes, which divide *k*-space into Brillouin zones. Each point in the reciprocal lattice generates a plane and the result for the rectangular lattice. The first zone is a simple rectangle. Beyond this zone, *k*-space is divided into fragments of increasing complexity. In the reduced zone scheme, the fragments must be translated into the first zone by adding an appropriate reciprocal lattice vector. The result for the first four zones is shown in the Fig 2.14.

This material is reserved for educational use only, not allowed for commercial use.
Forbidden to modify the content, and cite the document when use.

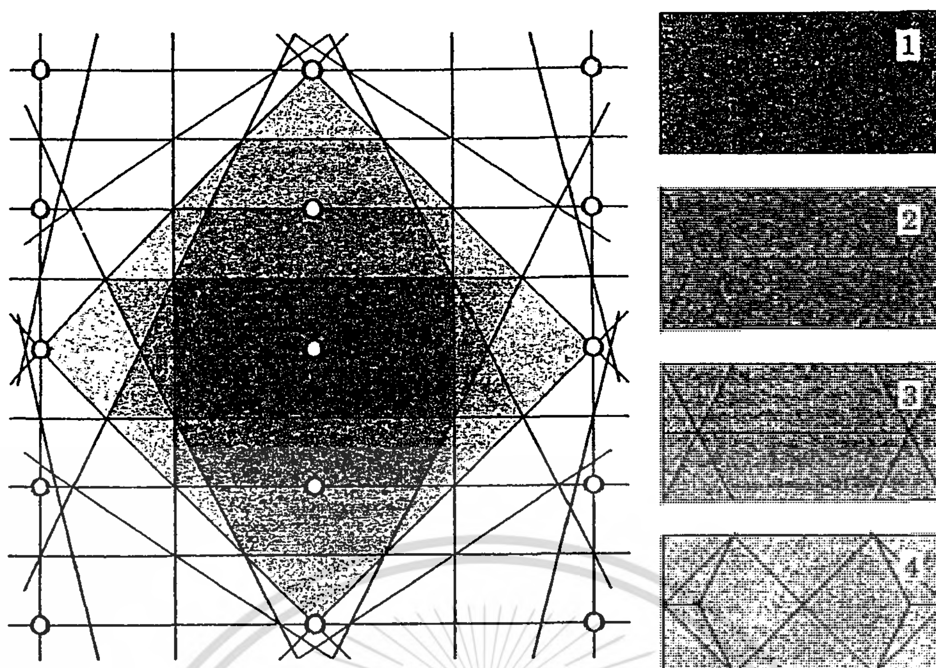

Fig. 2.14 First four Brillouin zones of the rectangular lattice, displayed as the shaded areas in the reciprocal lattice. These are translated through reciprocal lattice vectors to build successive rectangles, as shown on the right.

In a simple cubic lattice with the atoms separated by *a*, it has a simple cubic reciprocal lattice of separation $2\pi/a$. The first Brillouin zone is given by the Wigner-Seitz cell of this lattice, which contains all points that are closer to the atom at the origin than to any other atom. The result for the body-centered lattice is shown in Fig 2.15a, where the cell surrounds the atom in the middle of the cell. The shape is a truncated octahedron. It is bounded by the planes halfway between the origin and the near points of the lattice; the eight hexagonal faces arise from the planes halfway to the atoms at the corners, while the six smaller square faces are halfway to the atoms in the middle of the next cells. The way in which the unlikely unit cells fit together to fill space is shown in Fig. 2.15b.

This material is reserved for educational use only, not allowed for commercial use.
Forbidden to modify the content, and cite the document when use.

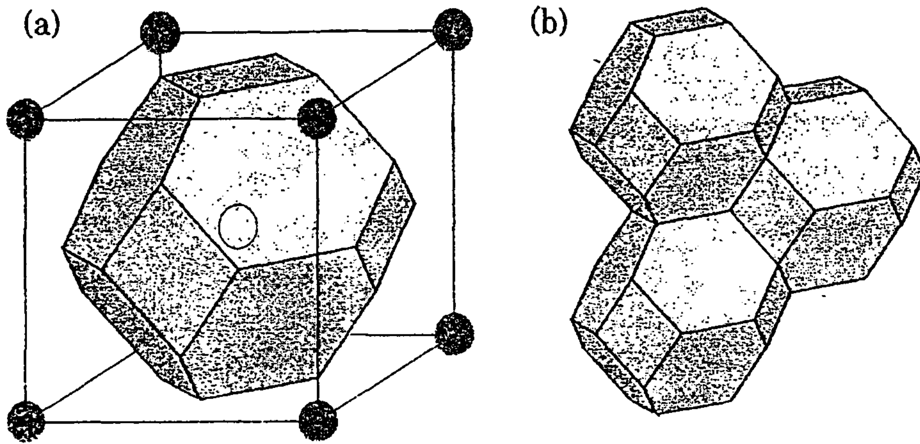

Fig. 2.15 (a) Wigner-Seitz cell of a body-centered cubic crystal, (b) The way in which they pack together to fill space.

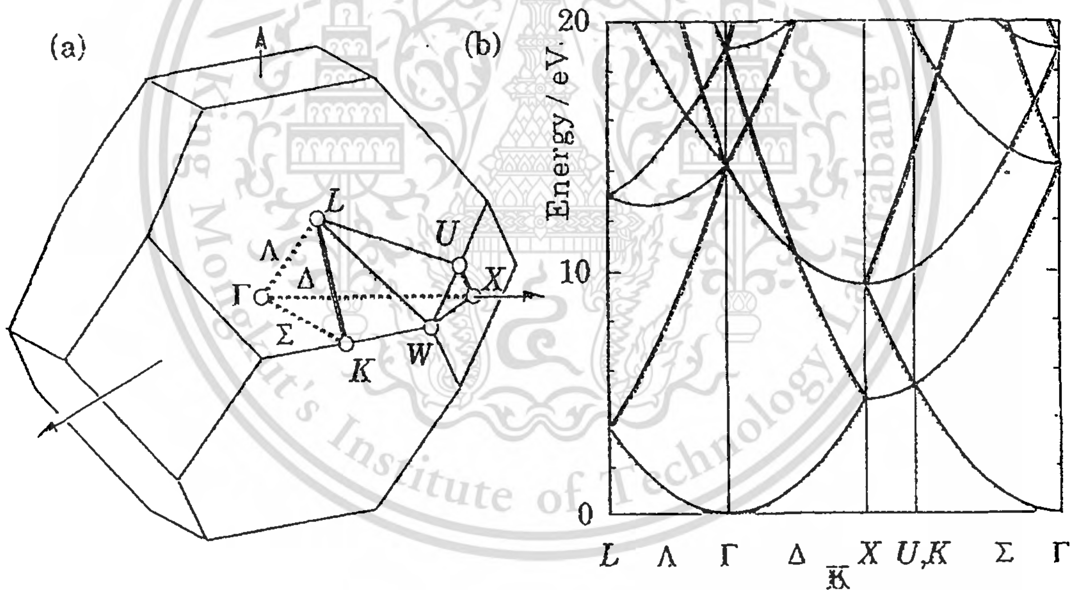

Fig. 2.16 (a) Brillouin zone for a face-centered cubic crystal, showing the notation for special points and directions. (b) Band structure in the free-electron model showing the effect of folding back the parabola into the reduced zone.

Fig. 2.16a shows the standard notation for the points of high symmetry. In general, Greek letters are used to represent points inside the zone, with Roman letters for the surface. The most important points are as follows: Γ is the origin of *K*-space. Δ is a direction to meet the zone boundary at X, in the middle of a square face. Λ is a direction normal to the close-packed planes

This material is reserved for educational use only, not allowed for commercial use.
Forbidden to modify the content, and cite the document when use.

of the face-centered structure. Σ is a direction meets the boundary at K, in the middle of an edge shared by two adjacent hexagons. U lies in the middle of edges shared by a hexagon and a square. W lies at the vertices, each shared by two hexagons and a square. These labels are important in order to interpret the standard plots of band structure. The usual way of displaying band structure is to plot $\varepsilon_n(k)$ along selected directions in the reduced Brillouin zone as shown in Fig. 2.16b for GaAs lattice. The left-hand segment shows the bands between L and Γ, the Λ-direction. The plot then sets off in the Δ-direction to the zone boundary at X. It then turns along the surface of the zone towards U. This point is equivalent to K, from where the plot returns back along the Σ-direction to Γ. Band structures for Si, Ge, GaAs and AlAs are shown in Fig. 2.17. These are calculated using a relatively simple method and do not include the spin-orbit coupling. Qualitatively, the bands of all four materials are similar in shape, as expected from their common structure. However, small differences in energy change, particularly the low-lying conduction bands. This has profound consequences for their electronic properties.

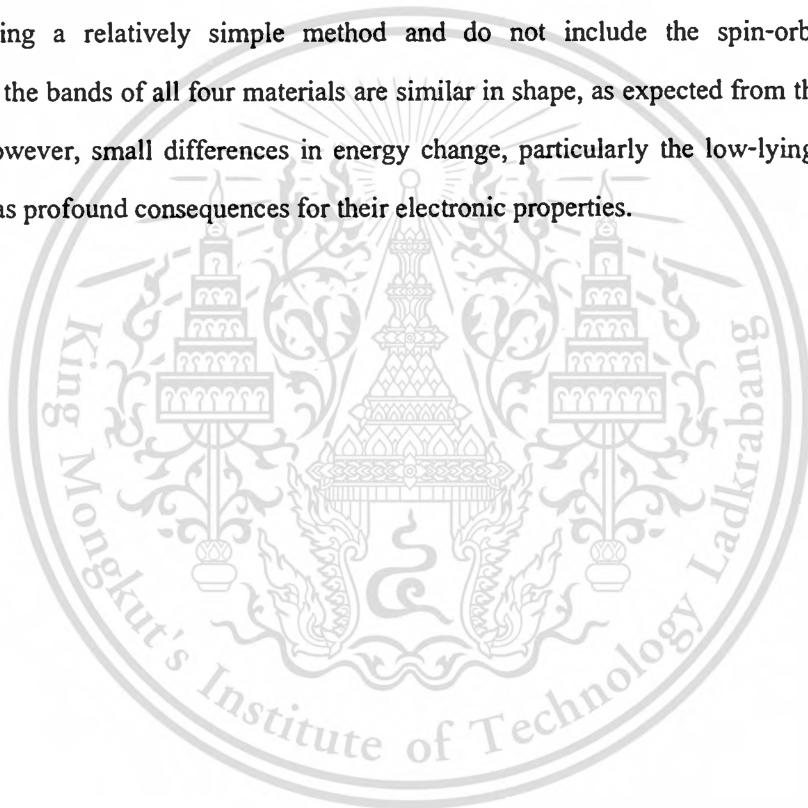

This material is reserved for educational use only, not allowed for commercial use.
Forbidden to modify the content, and cite the document when use.

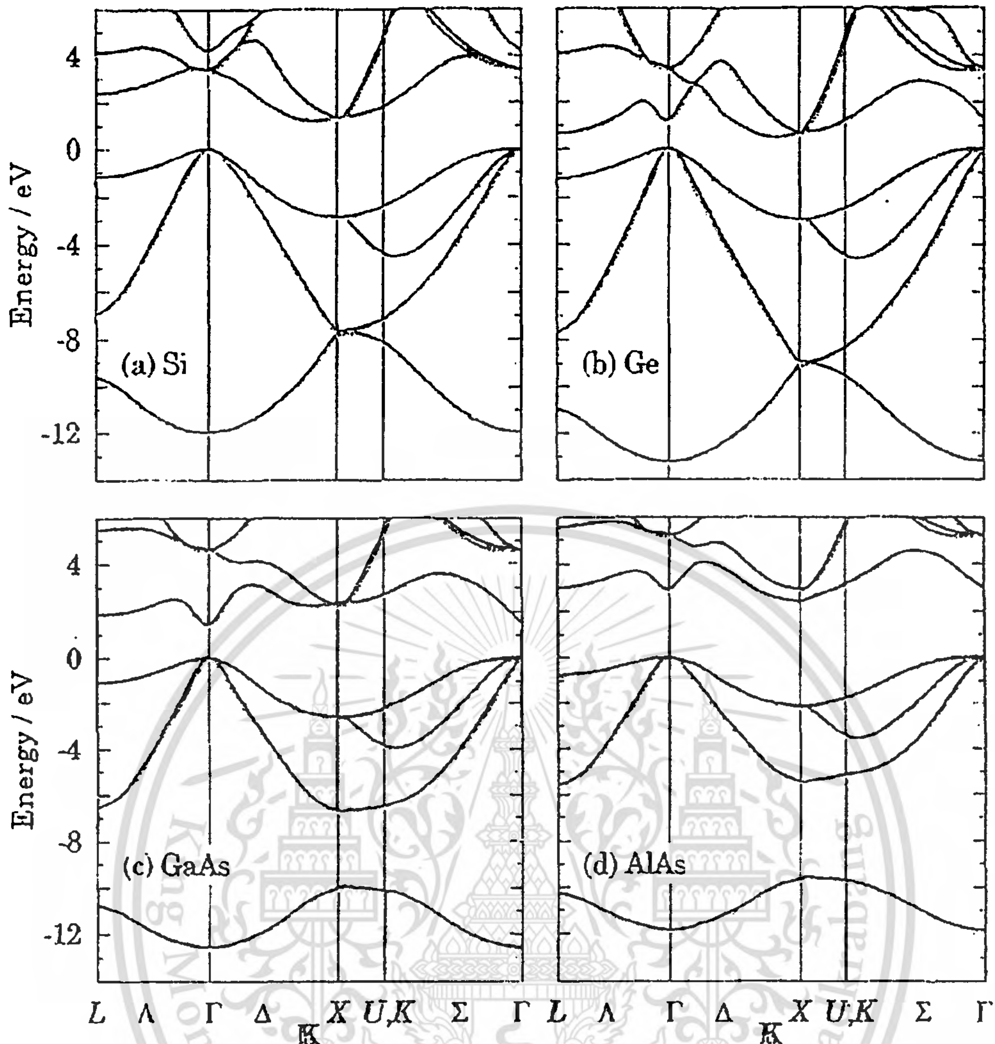

Fig. 2.17 Band structure of four general semiconductor: silicon, germanium, gallium arsenide, and aluminum arsenide.

2.3.4 Modification of Band Structure

The electronic and optical properties of semiconductors devices are strongly dependent upon the bandstructure. Therefore many efforts have been paid to modify the bandstructure of semiconductor materials. In principle, ,many physical phenomena can modify the electronic bandstructures. However, only two important methods are mentioned, since these are widely used for band modification. These two phenomena involve: i) alloying of two or more semiconductor; ii) use of heterostructures to cause quantum confinement.

This material is reserved for educational use only, not allowed for commercial use.
Forbidden to modify the content, and cite the document when use.

2.3.4.1 Modification of Band Structure by Alloying

When two semiconductors A and B are mixed using a suitable growth technique, they have the following properties of the alloy.

1. The crystalline structure of the lattice: In most semiconductors, the two or more components of the alloy have the same structure so that the final alloy also has the same crystal structure. The lattice constant of the alloy generally obeys the **Vegard's law** for the alloy A_xB_{1-x} as following equation,

$$a_{alloy} = xa_A + (1-x)a_B \tag{2.38}$$

2. Band structures of alloys: The band structure of alloys is somewhat difficult to calculate because alloys are not perfect crystals due to random atom placement. A simple approach used for solving the problem is based on the fact that the band structure of the alloy A_xB_{1-x} is simply the weighted band structure of the individual band structures of A and B. Therefore the bandgap is given by

$$E_g^{alloy} = xE_g^A + (1-x)E_g^B\ . \tag{2.39}$$

However, in most alloys, there is a bowing effect arising from the increasing disorder due to the alloying. Hence the bandgap is described by the relation

$$E_g^{alloy} = a + bx + cx^2\ , \tag{2.40}$$

where c is the bowing parameter. Most properties of alloys can be approximately obtained by a linear averaging of the individual properties of the components of the alloy. The relations given above for the lattice constant and bandgap are strictly valid if there is a good mixing in the alloy formation process.

This material is reserved for educational use only, not allowed for commercial use.
Forbidden to modify the content, and cite the document when use.

2.3.4.2 Modification of Band Structure by Heterostructures

Some important growth techniques such as MBE and MOCVD can be used for grow a sequence of different bandgap semiconductor layers forming heterostructure. An extremely important parameter in the heterostructure problem is the band edge discontinuity produced when two semiconductors are brought together. As shown in Fig. 2.18, a part of the bandgap discontinuity, E_g^A-E_g^B, of two semiconductors A and B would appear in the conduction band and a part would appear in the valence band. Based on electron affinity rule by taking the vacuum energy level as reference, the conduction band discontinuity is given by

$$\Delta E_c = e\left(\chi^B - \chi^A\right). \tag{2.41}$$

However, the problem is not so simple because of charge transfer that occurs when the two semiconductors are brought together. At the interface, there is a charge sharing across these bonds which can be considered to produce an interface dipole. This effect produces a correction to the simple electron affinity model. Many theoretical models have been proposed to calculate the band edge discontinuities. Experimental evaluations of the discontinuities are still being carried out. It is useful to point out that the band discontinuities obey the transitivity relation. If the discontinuity between A and B is ΔE_c^{AB} and that between B and C is ΔE_c^{BC}, then the discontinuity between A and C is ΔE_c^{AB} - ΔE_c^{BC}.

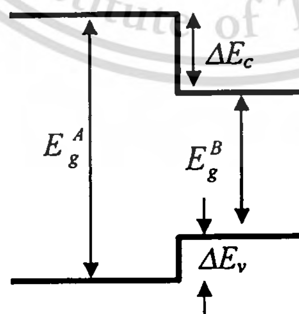

Fig. 2.18 Schematic sketch of band discontinuity when two semiconductor are brought together.

This material is reserved for educational use only, not allowed for commercial use.
Forbidden to modify the content, and cite the document when use.

2.4 Molecular Orbital Theory

In this section, the fundamental electronic, and optical properties of organic semiconductors are described.

2.4.1 σ-Bond and π-Bonds

In an organic materials, atoms within the molecules have covalent bonding with the others, and the intermolecular interaction is caused by relatively weak van der Waals forces and hydrogen bonds. Therefore, the overlap of the molecular orbital is comparatively small and the physical properties of an organic semiconductor thin film are strongly influenced by the structure and concentration of functional groups within the contained molecules. The occurrence of conductivity in organic material implies that the organic molecules have sub-units that provide conductivity. The molecular conductivity of typical organic materials is based on the presence of delocalized π-electrons formed in unsaturated hydrocarbons with alternating single and double bonds.

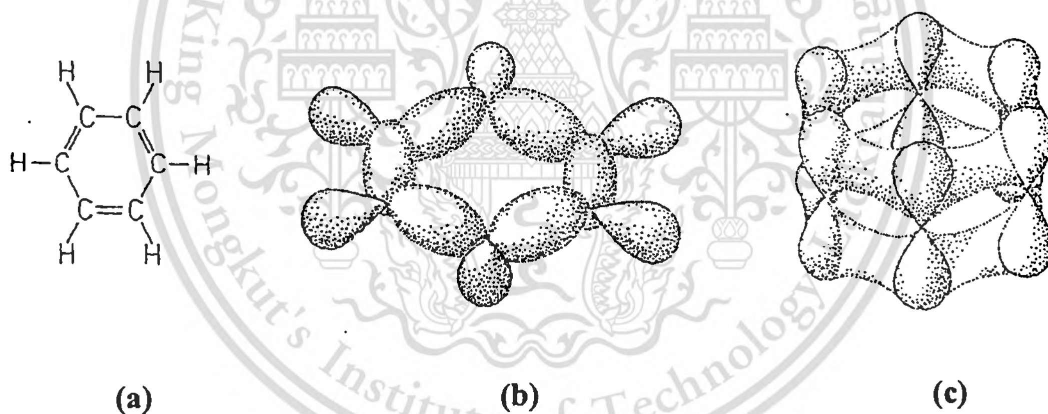

Fig. 2.19 (a) chemical structure of C_6H_6 (Benzene), (b) spatial distribution of the σ–bonds, (c) spatial distribution of the π–bonds forming a delocalized π-system.

In benzene ring depicted in Fig. 2.19a, each carbon atom provides four valence electrons. Three of them form so-called σ–bonds(Fig 2.19b), atomic bonding that overlap along the direction of the bond axis, with neighboring carbon or hydrogen atoms. These are localized bonds giving the skeletal framework for the molecules. The remaining valence electrons of six carbon atoms occupying p_z orbitals. These orbitals that overlap along a direction perpendicular to the

This material is reserved for educational use only, not allowed for commercial use.

Forbidden to modify the content, and cite the document when use.

bond axis form π-bonds(Fig. 2.19c). These π-bonds also contribute to the bonding of the molecule but are much weaker than those in σ–bonds. In addition, when several carbon atoms are bonded together, the π-electrons delocalize to produce a conjugated system. These delocalized π-electrons which are relatively weakly bound are responsible for the important semiconducting properties such as electronic and optical properties. In benzene, the σ-bonds result from the overlap of sp^2 orbitals formed from the hybridization of one $2s$ orbital with two $2p$ (p_x *and* p_y) orbitals. Meanwhile, π–bonds result from the overlap of the p_z orbitals as shown in Fig. 2.19c. The conjugated π–system of electrons extends across any molecule with a series of alternating single and double carbon bonds. Because these single and double bonds are resonant, these delocalize the π-electrons.

2.4.2 Electronic States and Transitions of Organic Semiconductor

In organic semiconductor, the electronic and optical properties are strongly determined by its π-electron system. The ground state of organic semiconductor is formed by a series of energetic levels of the π-electrons or π-band. The highest π-electron level is referred to the **highest occupied molecular orbital (HOMO).** In the excited state, the π-electrons from the π^*-band. The lowest π-electron level is referred to the **lowest unoccupied molecular orbital (LUMO).** The HOMO and LUMO are found experimentally that both levels have continuous distribution. The top edge of the HOMO distribution which is the closest level to vacuum corresponds to the ionization potential (IP) of the molecule. Meanwhile, the bottom edge of the LUMO distribution, the furthest level from vacuum, corresponds to the electron affinity (EA).

In the lowest electronic excitation, electrons can be excited and lifted from the HOMO to the LUMO. This $\pi \rightarrow \pi^*$ transition has the same manner as a transition from the valence to the conduction band in inorganic semiconductors. The Coulomb interaction between an electron in the LUMO and a hole in the HOMO leads to the formation of strongly bound excitons, either singlets or triplets depending on the relative spin of electron and hole. The relevant many-particle states are usually represented in term of molecular term symbol which is a shorthand expression of the group representation and angular momenta. It has general form as follows,

$$n^{2s+1}\Lambda^{(+/-)}_{(g/u)}$$

This material is reserved for educational use only, not allowed for commercial use.
Forbidden to modify the content, and cite the document when use.

where, S is the total spin quantum number,

Λ is the orbital angular momentum along the internuclear axis,

g/u is the parity,

+/- is the reflection symmetry along an arbitrary plane, and

n is a counter for respective state.

Fig 2.20a shows the sketch the energy levels of neutral excitations. In general case, the ground state is a singlet with even parity, labeled as 1^1A_g. In addition, the binding energy (E_b) of the triplet excitons is higher than E_b in the singlet excitons, so that the triplet 1^3B_u is the lowest neutral excited state. Here, A_g and B_u denote the symmetry class and parity of the wave function; gerade and ungerade. The optical properties of the molecule depend strongly on the relative energetic position of the lowest two excited singlet states. Because the photon emission requires a change of parity, possible luminescence is only observed if the state 1^1B_u is aligned below 2^1A_g. In the simplified notation the wave function symmetry is neglected and only singlet, S_n, and triplet states, T_n, are distinguished. Other type of excitation of organic semiconductor is charged excitation. Both negatively and positively charged excitations affect the optical properties of organic semiconductors. Excess electrons on a molecule lead to a localized structural relaxation. An radical anion is consequently formed having two energy levels within the HOMO-LUMO gap of neutral molecule, the lower level contains two electrons brought up from the HOMO as shown in Fig. 2.20b. Meanwhile, the upper level contains an excess electron. A similar manner also holds for a radical cation. The radicals on organic semiconductor are typically referred to polarons, P^- and P^+. A polaron can move freely on its own chain even though its energy levels are in the gap. If a negative and positive polaron meet each other, they can recombine to a Coulombically bound exciton.

This material is reserved for educational use only, not allowed for commercial use.
Forbidden to modify the content, and cite the document when use.

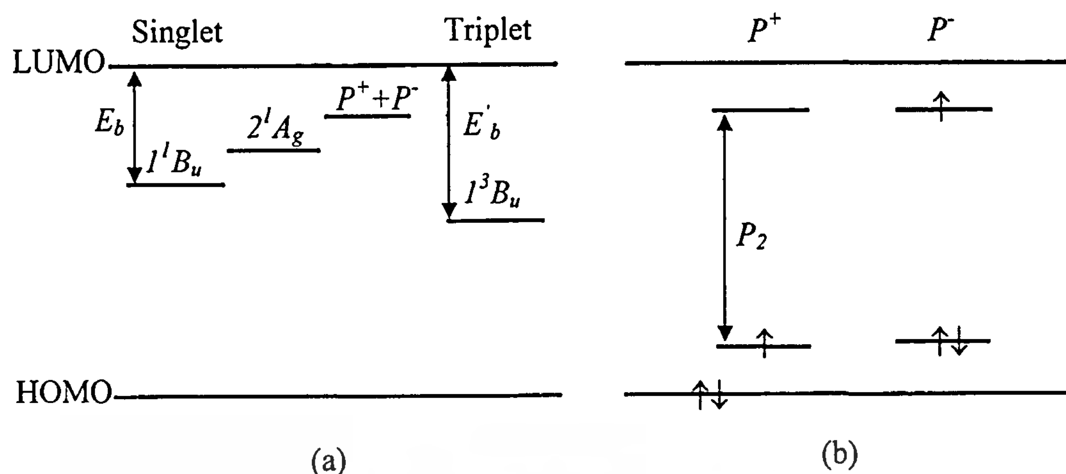

Fig. 2.20 Energy level of various excitations in organic molecules in (a) neutral manifold, and (b) charged manifold.

In conjugated segment of organic molecule, several processes might occur following photoexcitation process into the vibronic manifold 1^1B_u as follows:

1. Fast (~ 100 fs) thermalization of the excited state to the lowest 1^1B_u vibronic state, followed by radiative decay to the ground state.

2. Charge transfer from the 1^1B_u to the neighboring molecule. This process may also extremely rapid.

3. Intersystem crossing (ISC) from the 1^1B_u to the lowest state in the triplet manifold, i.e. 1^3B_u.

This material is reserved for educational use only, not allowed for commercial use.
Forbidden to modify the content, and cite the document when use.

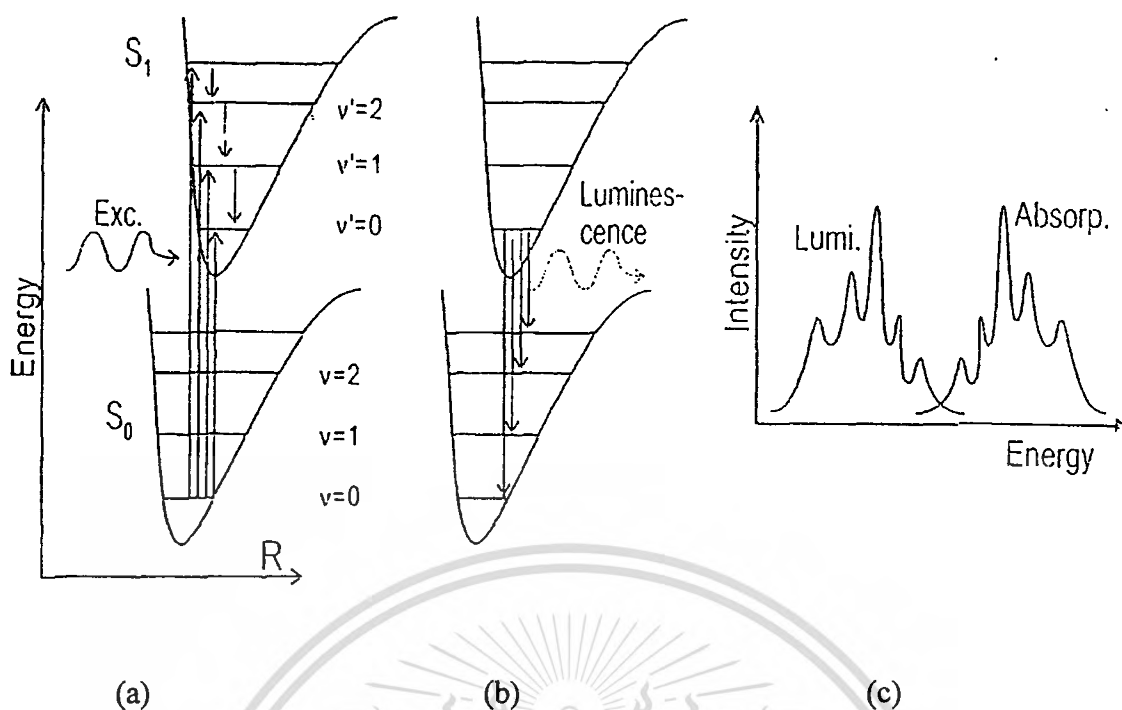

Fig. 2.21 Molecular potential energy as a function of the atomic distance (R). The arrows indicate vibronic transitions associated with (a) absorption, (b) emission of photons, and (c) the corresponding absorption and luminescence spectra.

Electronic transitions in organic molecules are strongly coupled to the vibrational modes of the molecule. In absorption and fluorescence spectrum these vibronic transitions cause characteristic side-bands above and below the purely electronic transition. Fig. 2.21 depicts the molecular potential energy as a function of the generalized nuclear coordinate *R*. The ground state and electronically excited state are denoted as S_0 and S_1, respectively. The horizontal lines represent the vibrational states of the bonds. The vibronic states are denoted as v and v' respectively. Because the associated energy of vibronic excitation is typically much higher than the thermal energy, a organic molecule in thermal equilibrium fills the state S_0 and $v = 0$. With suitable photons, the molecule will absorb the energy from photon and make the transition to higher level ($S_0, v \longrightarrow S_1, v'$). This process is governed by the **Franck-Condon principle**, which states that electronic transitions are much faster than nuclear rearrangement. Hence transitions occur vertically from ground state equilibrium position to the most probable interatomic spacing of a vibrational mode of the excited state that is close to the ground state equilibrium distance. The relative intensity of these is controlled by the overlap integral between the electronic ground

This material is reserved for educational use only, not allowed for commercial use.
Forbidden to modify the content, and cite the document when use.

state and the vibronic ground state($v = 0$) and excited state and vibronic state 0, 1, 2,... (Franck-Condon factors). After that, the molecule will give a rapid radiationless relaxation, typically of order of 10^{-12} s, of the excited state into its lowest vibronic level by internal conversion process. After typically between 1 and 10 ns, the molecule emits the photon when it make the transition, accompanied by spontaneous or stimulated emission, to the lowest vibronic level of the ground state(0-0 transition), the first vibrational state (0-1 transition), second vibrational state (0-2 transition), and so on. This gives rise to the occurrence of several peaks in the absorption and fluorescence spectra. This spectra shape is called *vibronic satellites* (Fig. 2.21c). Vibronic spacing is similar in the ground and excited states. However, in solid-state samples, the vibronic structure can often not be resolved due to homogeneous and inhomogeneous broadening of transitions. The apparent Stokes-shift between the absorption and emission maxima of the purely electronic transition is caused by intramolecular structural relaxation and intermolecular energetic dissipation. The luminescence mechanisms of the organic molecules are based on the recombination of a polaron pair in the antisymmetric singlet configuration to a singlet excitons, i.e.,

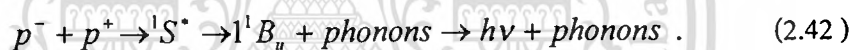

$$p^- + p^+ \rightarrow {}^1S^* \rightarrow 1^1B_u + phonons \rightarrow h\nu + phonons \; . \qquad (2.42)$$

Meanwhile, a polaron pair in the symmetric singlet configuration or the triplet configuration may recombine to a triplet excitons,

$$p^- + p^+ \rightarrow {}^3T^* \rightarrow 1^1B_u + phonons. \qquad (2.43)$$

In luminescent π-conjugated polymers the rate of reaction (2.42) is typically higher than that of (2.42), so the yield of singlet excitons is higher than that of triplet excitation. In addition, the recent study shows that some of emission is due to triplet-triplet annihilation to singlet excitons,

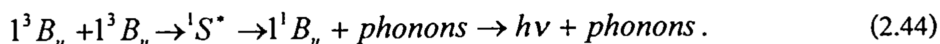

$$1^3B_u + 1^3B_u \rightarrow {}^1S^* \rightarrow 1^1B_u + phonons \rightarrow h\nu + phonons. \qquad (2.44)$$

This material is reserved for educational use only, not allowed for commercial use.
Forbidden to modify the content, and cite the document when use.

2.5 Heterostructure Semiconductors

This section provides a overview of the general properties of **heterostructure,** meaning that semiconductors composed of more than one compound. Variations in composition are used to control the motion of carriers by **band engineering**. Alignment of bands at a heterojunction, where two materials meets is important.

A large variety of devices has been fabricated from heterostructures, for both optical and electronic applications. A wide range of III-V compounds has been widely investigated for their semiconductor properties, but only a few of them are usually used in heterostructures. In order to increase the range of properties, alloys between the various compounds are also widely used such as $Al_xGa_{1-x}As$, and $In_xGa_{1-x}As$. Two of the important properties of different materials, the minimum bandgap and the lattice constant of III-V compounds are plotted in Fig. 2.22. The bandgap expressed as a function of wavelength is significant since many of the applications of the III-V compound are used in optoelectronic, where particular wavelength is designated to make the optimized usages. The active regions of heterostructures are typically at or close to the interfaces. This statement is true not only for III-V materials but also in metal-semiconductor junction and the most economically important semiconducting devices, moving along an interface between Si and SiO_2. Heterostructures must have nearly perfect interfaces if they are to perform the best properties. The demands on growth such as molecular-beam epitaxy(MBE) and metal-organic chemical vapor deposition(MOVCD) are therefore required.

This material is reserved for educational use only, not allowed for commercial use.
Forbidden to modify the content, and cite the document when use.

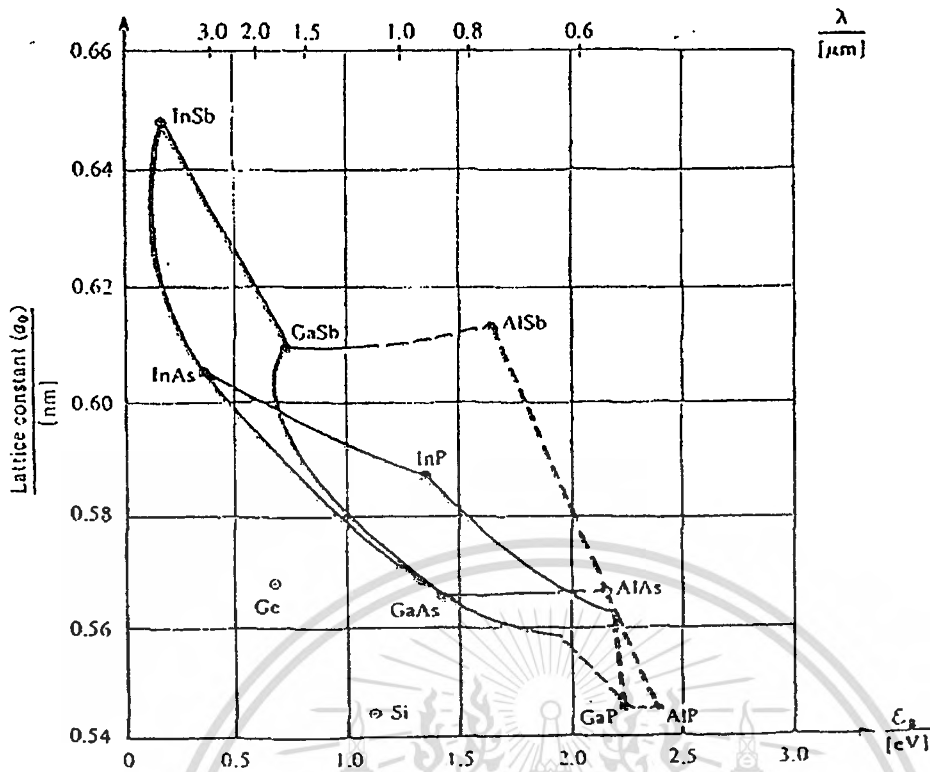

Fig. 2.22 Lattice constant of various semiconductors against their energy gap E_g as a function of wavelength.

In principle of heterostructure, two materials must be joined perfectly. This requires firstly that they should have the same crystal structure, or at least symmetry to each other. This is satisfied for the general III-V compounds. A second requirement, if there is to be no strain in the structure, is that the two lattice constants must be nearly identical. The lattice constant of an alloy is typically given by linear interpolation between its constituents. This is known as **Vegard's law.** For example, the lattice constant of $Al_xGa_{1-x}As$ is expressed as $xa_{AlAs}+(1-x)a_{GaAs}$. From this formula, its lattice constant of this alloy noticeably changes by less than 0.15% as a function of x. Thus it is possible to grow layers of GaAs and AlAs or any of the intermediate alloys AlGaAs on top of one another without significant stress.

Recently, much wider choices of materials are available for heterostructures. In this section, practical heterostructures such as delta-doped structure, quantum well structure are presented.

This material is reserved for educational use only, not allowed for commercial use.
Forbidden to modify the content, and cite the document when use.

2.5.1 Quantum Wells and Low-Dimensional Structure

Typically, real electrons are free to move in three dimensions. However, they can be confined and allowed to move only in fewer dimensions. This can be achieved by trapping them in a narrow potential well that restricts their motion and make their energies to be discrete levels. If the separation between these energy levels is large enough, the electrons prefer to be in the ground state and no motion is possible in this dimension. This result is a two-dimensional electron gas (2DEG). The same effect can be achieved with a two-dimensional and three-dimensional potential well, which leaves the electrons free to move in only one dimension and zero dimension , respectively.

In semiconductor technology, quantum well structure can be obtained by letting a thin layer of one compound being sandwiched by other compound that has different bandgap. Typical quantum wells can be categorized depending on their band alignment as shown in Fig. 2.23. Three types of structures are possible. Type I quantum well has the entire gap of small bandgap semiconductor resides within the conduction and valence bands of the large gap material. For type II, one of the band offsets may be larger than the difference between the semiconductor band gaps, but smaller than the magnitude of the larger semiconductor band gap. If one of the offsets is larger than the gap of the largest bandgap semiconductor, this alignment is type III. In type I quantum well, there is a well in both conduction and valence bands. GaAs/AlGaAs, InGaAs/InP are the examples of type I quantum well. In this case the well traps both electrons and holes and the energy levels can be measured by optical experiment; i.e., photocurrent spectroscopy. This process originates the basis of most optoelectronic devices.

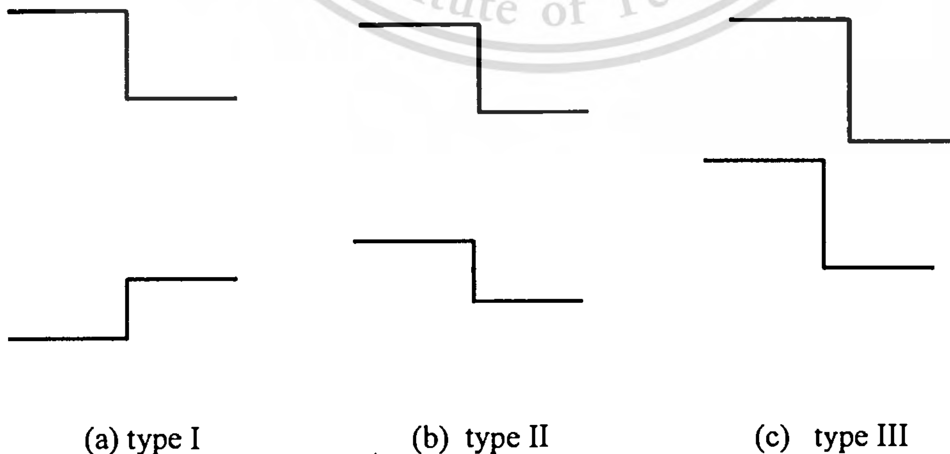

(a) type I (b) type II (c) type III

Fig. 2.23 Various possible band edge lineups in heterostructure.

This material is reserved for educational use only, not allowed for commercial use.
Forbidden to modify the content, and cite the document when use.

2.5.2 Superlattice

It is possible to fabricate a structure consisting of many quantum wells, with each well separated from neighboring wells by a barrier. If the barriers are sufficiently thick, carriers located in different wells are essentially isolated and the structure behaves identically to a single well, although some properties will increase linearly with the total number of wells. In this case the structure is known as a multiple quantum well as shown in Fig. 2.24a. However, if the thickness of the barriers is reduced, carriers can tunnel from one well to its neighbors. Significant interaction will occur if the wavefunctions overlap strongly, requiring relatively thin barriers. This effect destroys the sharp bound level associated with the well, but in this case the result is a *miniband* as shown in Fig. 2.24b. This system is known as a **superlattice**. The superlattice gives a periodic potential, so the general theory of one-dimensional crystals holds. Therefore, motion along the direction of growth is governed by Bloch's theorem and band structure. Superlattice is a second level of periodicity imposed on the first level that is the crystalline nature of the semiconductors. A major difference is that it affects motion in only one direction. The period is surely longer than that of the crystal and the periodic potential is weaker. This results that the bands and gaps appear on a much smaller of scale of energies, hence the name of minibands. The band structure can be turned by varying the composition and thickness of the layers. Superlattice is used to filter the energy of electrons, allowing only those within the minibands to pass or reflecting those in the minigap.

This material is reserved for educational use only, not allowed for commercial use.
Forbidden to modify the content, and cite the document when use.

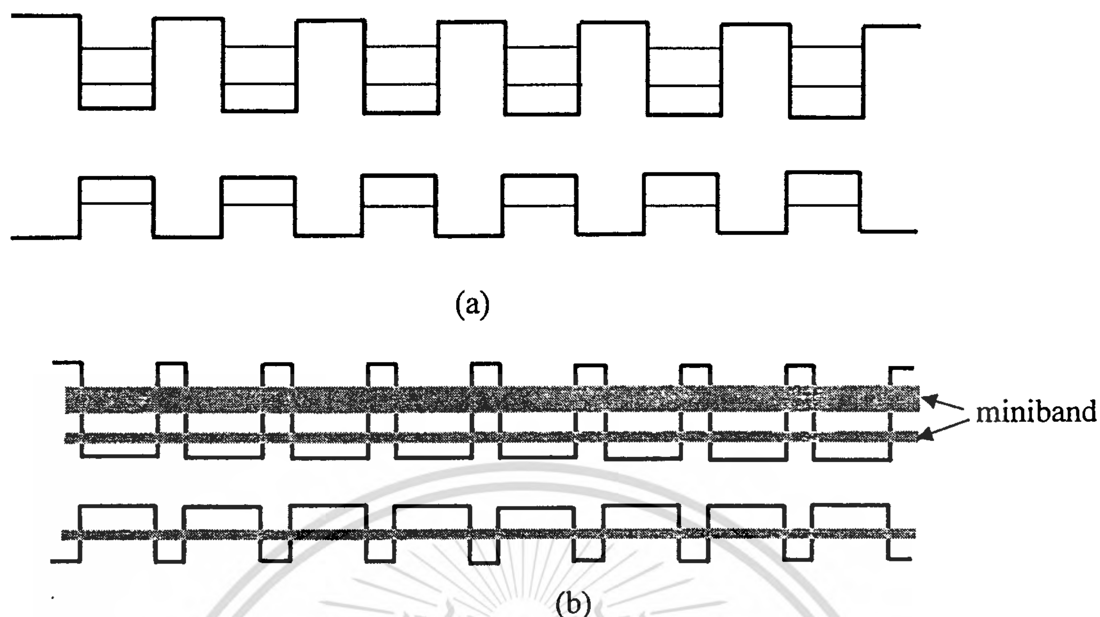

Fig. 2.24 The form of the confined energy states in (a) a multiple quantum well and (b) a superlattice.

2.5.3 Doped Heterostructure

Devices in the forms of heterostructures such as resonant-tunneling diode rely on electrons and holes for conduction and these must be introduced by doping. In this section, the effect of doping on band diagrams is considered.

2.5.3.1 Delta-Doped Structure

The capability of confining dopants and their related carriers in a very narrow region is in considerable interest for many device applications. With the advances in epitaxy growth, controlling the growth in such a way that the dopants localized in a single atomic layer becomes possible. The proposed structure is called **"delta-doped structure"**. The delta-doped semiconductors can be defined as "semiconductors that contain a doping profile much narrower (at least a factor of 2) than the corresponding ground-state wave function". The delta-function-like doping profile was obtained by interrupting the growth of the semiconductor host crystal and immediately inserting the doped layer. In general, the flux of dopant is chosen to be less than $1 \times 10^{12} cm^{-2} s^{-1}$. Thus, delta-doping is a two-dimensional doping technique the puts impurities upon a single atom layer of the nongrowing surface. To obtain a narrow doping profile, sources with small diffusion coefficient must be employed as dopant. Si source and Be source has been widely

This material is reserved for educational use only, not allowed for commercial use.

Forbidden to modify the content, and cite the document when use.

used as the n-type and p-type in samples grown by any III-V compound. The ideal doping profile of a delta-doped layer can be expressed by Dirac's delta function (δ-function). In Fig. 2.25a, dopant atoms substituted a few percent of host material sites, and the ionized donors form a continuous sheet of charge at $z = z_o$. The doping profile can be explained by the Dirac delta function,

$$N_D(z) = N_D^{2D}\delta(z - z_o), \tag{2.45}$$

where N_D^{2D} is the two-dimensional dopant concentration. However, in reality, the doping profile can only be estimated to be a Gaussian profile due to thermal diffusion. The full width of half maximum (FWHM) of a delta-doped layer increases with the increase of growth temperature and doping concentration. Therefore, the profile of the dopants in the z-direction, in reality, can be described by the Gaussian function,

$$N_D(z) = N_D^{2D}\frac{1}{\sigma\sqrt{2\pi}}exp\left[-\frac{1}{2}\left(\frac{z - z_o}{\sigma}\right)^2\right], \tag{2.46}$$

where σ is the standard deviation of the Gaussian function. The doped layer thickness in the z-direction is approximately two standard deviations (2σ). If the standard deviation σ is much smaller than the spatial extent of the ground-state wave function of electrons or holes in the δ-doped layer, the subband structure or electronic structure will not be influenced by the magnitude of the standard deviation. Therefore, if the thickness of the doped layer is less than or equal 2.5 nm, the doping profile can be described by δ-function. On the other hand if the thickness of the doped layer is 10 nm or greater, the doping profile cannot be considered as δ-function-like.

This material is reserved for educational use only, not allowed for commercial use.
Forbidden to modify the content, and cite the document when use.

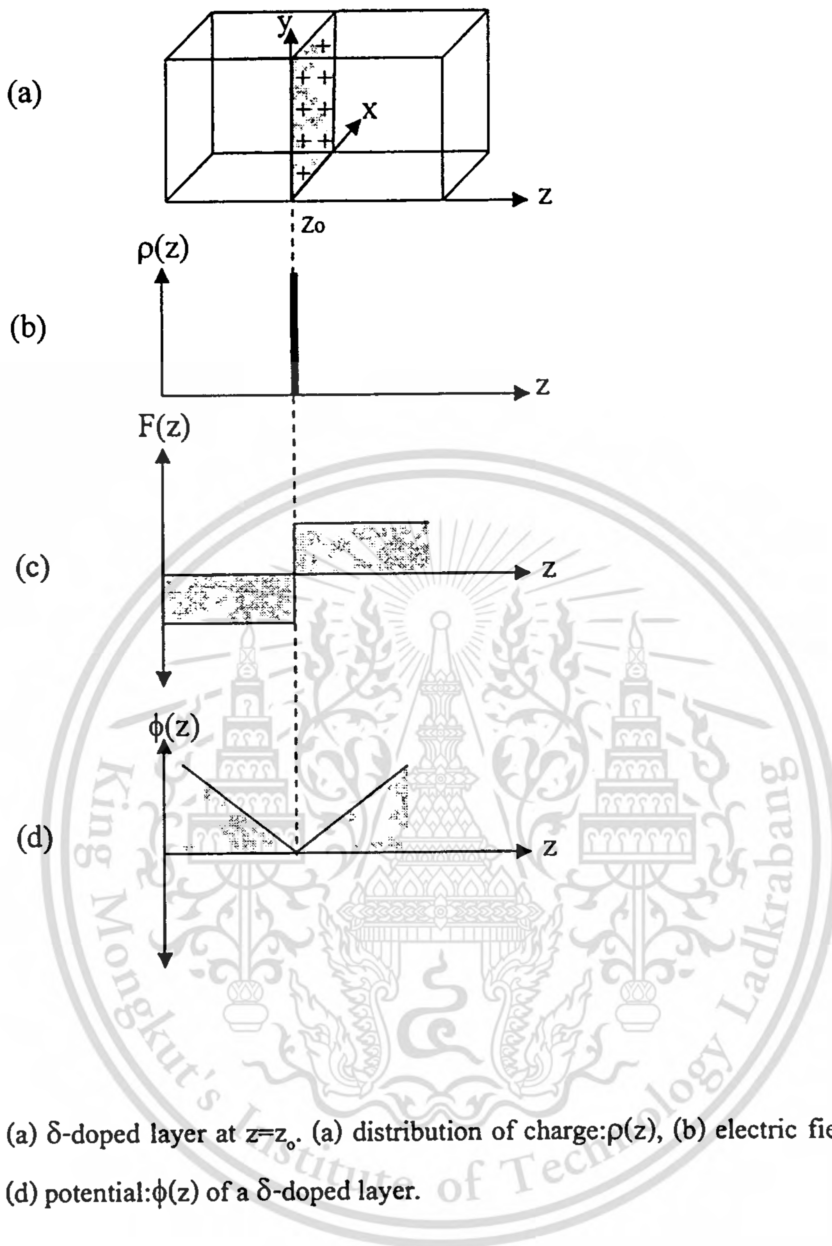

Fig. 2.25 (a) δ-doped layer at $z=z_o$. (a) distribution of charge:ρ(z), (b) electric field: F(z), and (d) potential:φ(z) of a δ-doped layer.

The electric field (F) and the potential (φ) of a δ-function-like charge distribution is obtained by integration of Poisson's equation. The expression for the corresponding electric field is

$$F(z) = -\frac{1}{2}\frac{eN_D^{2D}}{\varepsilon} + \frac{eN_D^{2D}}{\varepsilon}\sigma(z - z_o), \tag{2.47}$$

This material is reserved for educational use only, not allowed for commercial use.
Forbidden to modify the content, and cite the document when use.

where e is the elementary charge, ε is the permittivity of the semiconductor, and $\sigma(z-z_o)$ is the step function. The potential is obtained by the second integration of Poisson's equation which is expressed as,

$$\phi(z) = -\frac{eN_D^{2D}}{2\varepsilon}(z-z_o) + \frac{eN_D^{2D}}{\varepsilon}(z-z_o)\sigma(z-z_o). \tag{2.48}$$

The profiles of electric field and potential distribution are depicted in Fig. 2.25c and Fig. 2.25d, respectively. Fig. 2.26 shows the band diagram for a δ-doped structure.

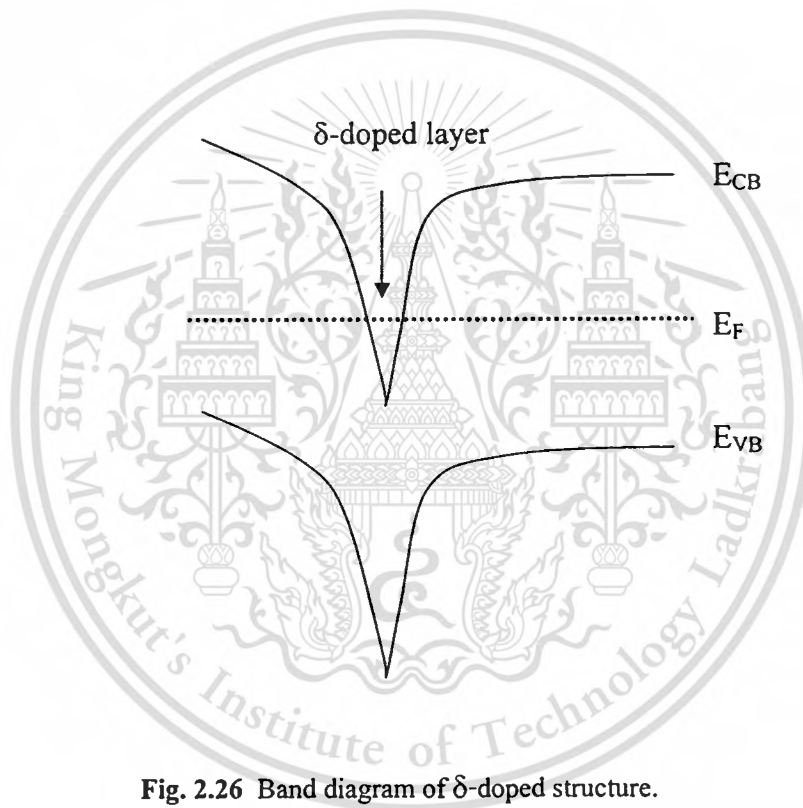

Fig. 2.26 Band diagram of δ-doped structure.

The differences between δ-doping system and the other two-dimensional (2D) carrier systems are as follows:

(i) The electrons in δ -doping can occupy several excited subbands even at a moderate doping concentration.

(ii) Due to the proximity of the bare ionized impurities, the ground-state subband electrons exhibit the lowest mobility In comparison to electrons in the excited subbands. This is contradictory to the two-dimensional electron gas (2DEG) of selectively doped heterostructures.

This material is reserved for educational use only, not allowed for commercial use.
Forbidden to modify the content, and cite the document when use.

(iii) The carriers in the dopant plane are considerable delocalized so that the electronic states are spread out over the ionized donors that form the V-shaped potential well, For δ -doping concentrations from 1×10^{12} to 1×10^{13} cm^{-2}, the lowest subband can extend from 10 to 5 nm that is still significantly less than the 20 nm diameter of the hydrogen-like *1s* orbit.

Up to now, the delta-doping technique has been applied extensively to the design of device structure, such as planar doped field effect transistor, delta high electron mobility transistor(HEMT), sawtooth superlattice laser, resonant tunneling devices delta, and delta-doping induced negative differential resistance devices.

2.5.3.2 Modulated Doped Structure

Fig. 2.27 Conduction band around a heterojunction between n-AlGaAs and undoped GaAs, showing how electrons are separated from their donors to form a two-dimensional electron gas.

Modulation doping is the doping is grown in one region that but the carriers subsequently migrates to another. Fig. 2.27(a) illustrates a heterojunction between n-AlGaAs and undoped GaAs. The material is neutral everywhere and the band are flat if the electrons sit on their donors in the n-AlGaAs. The electrons travel around after being released and some cross into GaAs. There they lose energy and become trapped because they cannot climb the barrier presented by ΔE_C. This motion separates the negatively charged electrons from their positively charged donors, which sets up an electrostatic potential ϕ that tends to drive electrons back into the AlGaAs. The discontinuity ΔE_C, and the electrostatic potential $-e\phi$ will affect the total energy of the electrons to be at the bottom of the conduction band E_C, as shown in Fig. 2.28(b). The discontinuity ΔE_C has a major effect because it prevents the electric field from returning the electrons to their donors. The field can only squeeze the electrons against the interface, where they are trapped in a roughly

This material is reserved for educational use only, not allowed for commercial use.
Forbidden to modify the content, and cite the document when use.

triangular potential well. This well is typically about 10 nm wide at the energy of the electrons, and the energy levels for motion are quantized. Often only the lowest level is occupied. All electrons remain free in the other two dimensions. This is the two-dimensional electron gas (2DEG). It is the basis for the majority of electronic devices in heterostructures. The modulation doping has achieved two benefits: it has separated electrons form their donors to reduce scattering by ionized impurities, and confined the electrons to two dimensions.

2.6 Quantum Theory for Semiconductor

In this part, theory of quantum mechanics relevated to heterostructures is briefly described. Some simple one-dimensional potential wells used to trap electrons are firstly discussed. The infinitely deep square well cannot be made in practice, but its simplicity makes it a frequently used model. A well of finite depth provides a much better description of a real quantum well. Another applicable models are parabolic and triangular wells.

2.6.1 Infinite Square Well

Infinite square well, by far, is the simplest example of a quantum well. Fig. 2.28 schematically shows the infinite well. The carrier has zero potential energy in the region $0 < z < a$, and infinitely high potential barriers. The Schrödinger equation describing this situation can be written as

$$\frac{d^2\psi}{dz^2} + \frac{2m}{\hbar^2} E\psi = 0 . \tag{2.49}$$

The general solution of this equation is

$$\psi(x) = A\sin(kz) + B\cos(kz) , \tag{2.50}$$

where $$k = \sqrt{\frac{2mE}{\hbar^2}} . \tag{2.51}$$

Apply boundary conditions that $\psi = 0$ for $z \le a$ and $z \ge a$, we obtain

This material is reserved for educational use only, not allowed for commercial use.
Forbidden to modify the content, and cite the document when use.

$$\psi(0) = B = 0\text{, and } \psi(a) = 0 = A\sin(ka)\text{.} \tag{2.52}$$

Except for the trivial result $\psi = 0$ obtained by setting $A = 0$, the solution is satisfied only when (ka) is an integer multiple of π. Therefore, k is restricted to the values.

$$k = \pm\frac{n\pi}{a}, \qquad n = 1,2,3..... \tag{2.53}$$

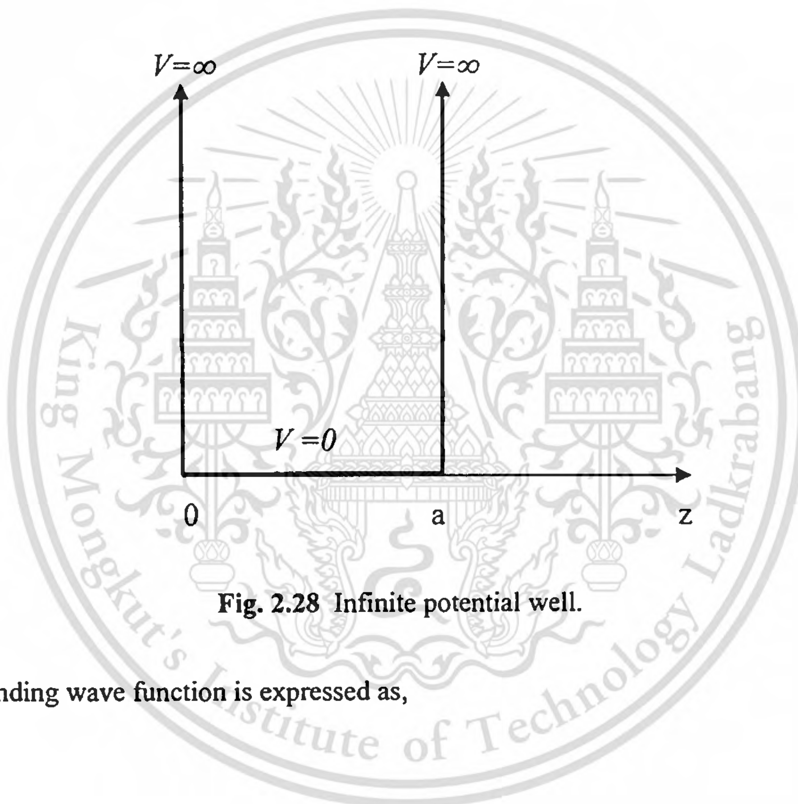

Fig. 2.28 Infinite potential well.

The corresponding wave function is expressed as,

$$\psi_n(z) = A_n \sin\left(\frac{n\pi z}{a}\right) \text{ for } 0 \le z \le a\text{.} \tag{2.54}$$

Likewise, by substituting for k into Equation (2.51) ,E_n can be written as

$$E_n = \frac{\pi^2\hbar^2}{2ma^2}n^2\text{.} \tag{2.55}$$

The integer n is called a ***quantum number***.

This material is reserved for educational use only, not allowed for commercial use.
Forbidden to modify the content, and cite the document when use.

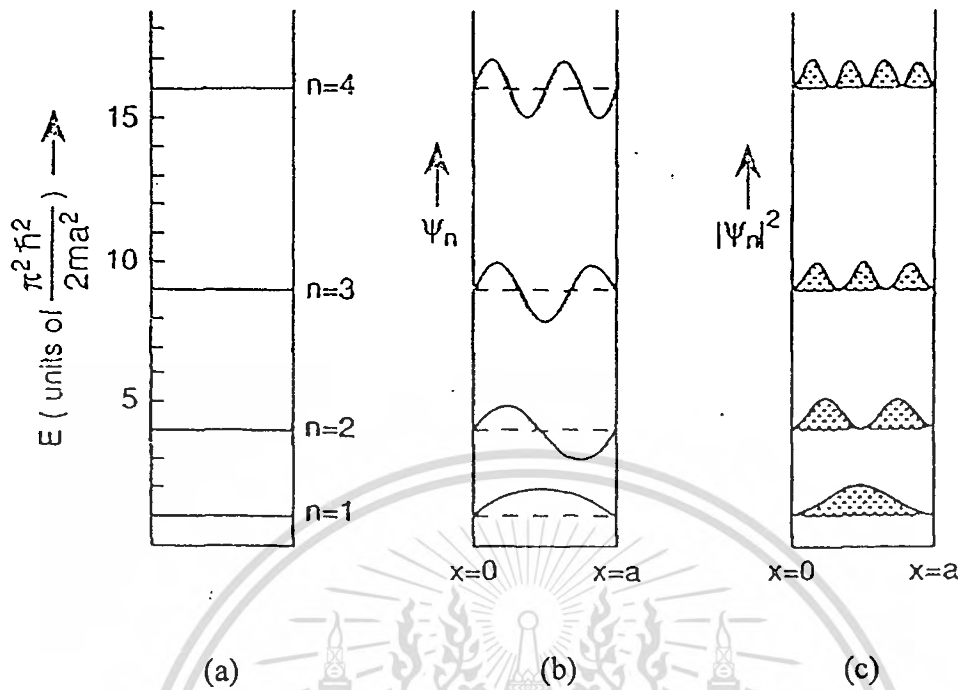

Fig. 2.29 (a) First four allowed energy levels in infinite well, (b) wave functions and (c) the probability density.

It is clearly seen that the energy levels in the well are discrete. Fig. 2.29 shows the first four energy levels, their corresponding wave functions, and probability densities $|\psi|^2 = \psi\psi^*$. It is obvious that the wave functions are standing waves, and are consistent with the idea that an electron is reflected from the walls.

This material is reserved for educational use only, not allowed for commercial use.
Forbidden to modify the content, and cite the document when use.

2.6.2 Finite Square Well

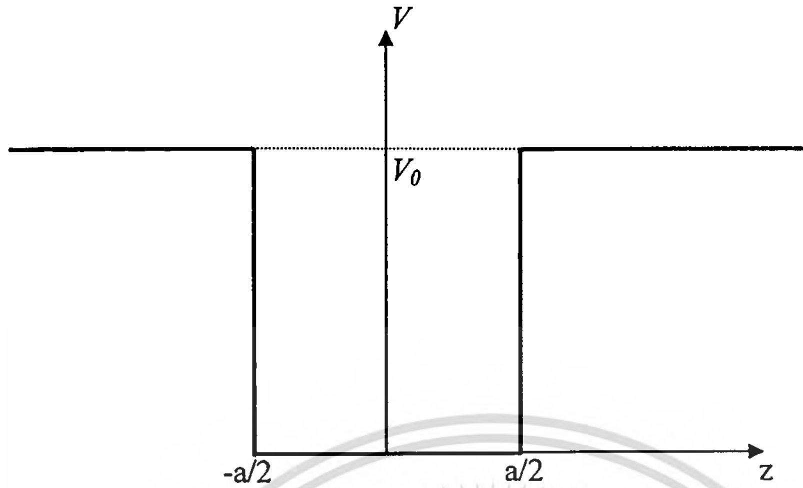

Fig. 2.30 Finite square well.

The finite square well is generally the most practical model for quantum well. The square well with the depth V_0 and the width of a is depicted in Fig. 2.30. Inside the well, the SchrÖdinger equation is,

$$-\frac{\hbar^2}{2m}\frac{d^2\psi}{dz^2} = E\psi . \tag{2.56}$$

The general solution for wave function with possible symmetry can be written as,

$$\begin{aligned} \psi(z) &= C\cos(kz) \quad \textit{for even symmetry,} \\ \psi(z) &= C\sin(kz) \quad \textit{for odd symmetry.} \end{aligned} \tag{2.57}$$

For $-\frac{a}{2} < z < \frac{a}{2}$, with $E = \frac{\hbar^2 k^2}{2m}$.

Outside the well, the SchrÖdinger equation becomes,

This material is reserved for educational use only, not allowed for commercial use.
Forbidden to modify the content, and cite the document when use.

$$-\frac{\hbar^2}{2m}\frac{d^2\psi}{dz^2}+V_0\psi = E\psi \,. \tag{2.58}$$

The solutions are,

$$\psi(z) = D\,exp(\pm\kappa z)\,,$$

with
$$\frac{\hbar^2\kappa^2}{2m} = V_0 - E\,. \tag{2.59}$$

The wave functions (2.57) and (2.58) must be matched at $z = \frac{a}{2}$. Continuity of the wave function requires

$$\psi(a/2) = C\begin{Bmatrix} cos \\ sin \end{Bmatrix}\left(\frac{ka}{2}\right) = D\,exp\left(-\frac{1}{2}\kappa a\right). \tag{2.60}$$

Similarly, matching the derivative at $z = \frac{a}{2}$ gives

$$\left.\frac{d\psi}{dz}\right|_{z=a/2} = Ck\begin{Bmatrix} -sin \\ cos \end{Bmatrix}\left(\frac{ka}{2}\right) = D\kappa\,exp\left(-\frac{1}{2}\kappa a\right). \tag{2.61}$$

There are three unknown in (2.60) and (2.61): the normalization factors C and D, and the energy E, which is in term of k and κ. dividing equation (2.61) by (2.60) gives

$$k\begin{Bmatrix} -tan \\ cot \end{Bmatrix}\left(\frac{ka}{2}\right) = -\kappa\,. \tag{2.62}$$

Equation (2.61) is transcendental equation which can lead to the energy level E by finding out the interception between $tan\left(\frac{ka}{2}\right)$ or $-cot\left(\frac{ka}{2}\right)$ and $\frac{\kappa}{k}$. Several important results follow this graph.

This material is reserved for educational use only, not allowed for commercial use.
Forbidden to modify the content, and cite the document when use.

(i) Equation (2.62) shows that there is always at least one solution : a one- dimensional square well always has at least one bound state, however shallow or narrow the well. This result holds for any one-dimensional well, not just a square well. It also holds for any two dimensions, although shallow wells have a weakly bound state. It is not true for three-dimensional wells (quantum dot), which must exceed a critical radius or depth for a bound state to exist.

(ii) If the well is very shallow, with only one bound state, we can use the approximation $\tan\theta \approx \theta$. Equation (2.62) is simplified, and the energy is therefore

$$E_1 = V_0 - \frac{ma^2V_0^2}{2\hbar^2}. \qquad (2.63)$$

(iii) If the well is very deep, V_0 tends to be infinity, the solutions lie on the steep parts of the tangent curves, and the intersections approach $\frac{ka}{2} = \frac{1}{2}n\pi$, where n = 1,2,3....... . Then $k = \frac{n\pi}{a}$ and the energy are the same as those for an infinite well.

2.6.3 Parabolic Well

A simple realization of the parabolic potential is the harmonic oscillator, such as vibration of the crystal lattice or phonons. The corresponding potential is in the form

$$V(z) = \frac{1}{2}m\omega_0^2 z^2. \qquad (2.64)$$

In semiconductors, It is also possible to grow parabolic wells by continuously varying the composition of an alloy. The magnetic field also gives rise to a parabolic potential. In quantum mechanics we must begin with the time-independent SchrÖdinger equation,

$$\left(-\frac{\hbar^2}{2m}\frac{d^2}{dz^2} + \frac{1}{2}m\omega_0^2 z^2\right)\psi(z) = E\psi(z). \qquad (2.65)$$

This material is reserved for educational use only, not allowed for commercial use.
Forbidden to modify the content, and cite the document when use.

Rearranges equation (2.61), giving

$$\left(-\frac{d^2}{dz^2}+\left(\frac{m\omega_0}{\hbar}\right)^2 z^2\right)\psi(z)=\frac{2mE}{\hbar^2}\psi(z), \tag{2.66}$$

or,

$$\left(-\frac{d^2}{d\bar{z}^2}+\bar{z}^2\right)\psi(\bar{z})=\frac{2E}{\hbar\omega_0}\psi(\bar{z}). \tag{2.67}$$

Equation (2.67) is obtained by letting

$$\bar{z}=\frac{z}{z_0}, \qquad z_0=\sqrt{\frac{\hbar}{m\omega_0}}. \tag{2.68}$$

z_0 is called the *length scale*. It is easy to simplify equation (2.68) by defining the energy scale E_0,

$$\bar{E}=\frac{E}{E_0}, \qquad E_0=\hbar\omega_0. \tag{2.69}$$

The result is the dimensionless Schrödinger equation,

$$-\frac{d^2}{d\bar{z}^2}\psi(\bar{z})+(2\bar{E}-\bar{z}^2)\psi(\bar{z})=0. \tag{2.70}$$

A wave function that satisfies equation (2.70), including normalization, is in the form of Hermite polynomials,

$$\psi_{n+1}(z)=\left(\frac{1}{2^n n!\sqrt{\pi}}\right)^{1/2}\left(\frac{m\omega_0}{\hbar}\right)^{1/4} exp\left(-\frac{m\omega_0 z^2}{2\hbar}\right)H_n\left[\left(\frac{m\omega_0}{\hbar}\right)^{1/2} z\right]. \tag{2.71}$$

This material is reserved for educational use only, not allowed for commercial use.
Forbidden to modify the content, and cite the document when use.

The Eigen energy E_n can also be obtained,

$$E_n = \left(n - \frac{1}{2}\right)\hbar\omega_0 . \tag{2.71}$$

The lowest few wave functions are plotted in Fig. 2.31. They show the even-odd alternation seen in symmetric square wells.

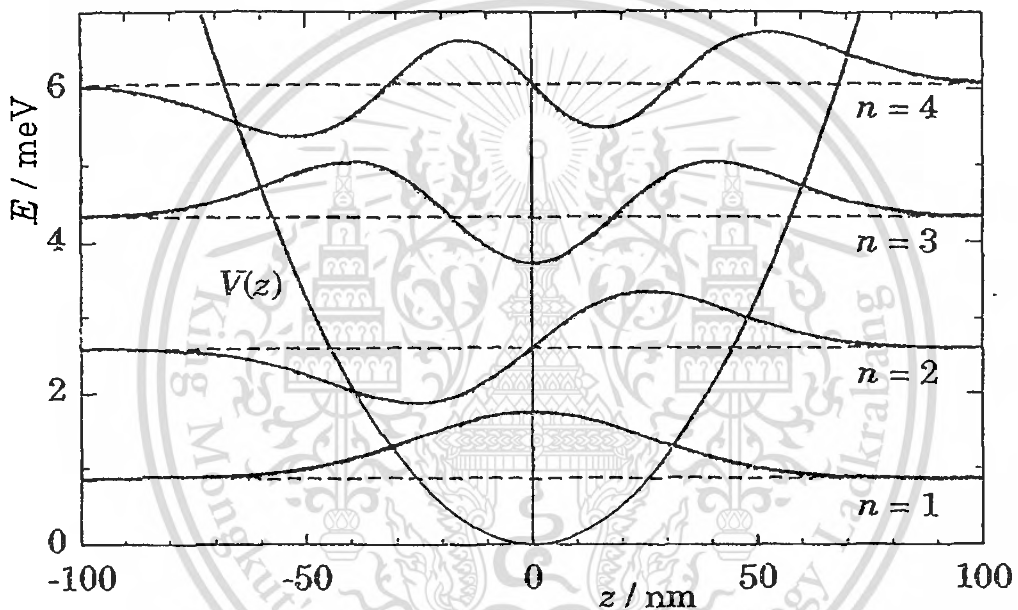

Fig. 2.31 The energy levels and wave functions in parabolic quantum well.

2.6.4 Triangular Well

The triangular well is useful because it is a simple description of the potential well at a doped heterojunction, and for a well in the applied electric field. There is an infinitely high barrier for $z < 0$ with the linear potential $V(z)=eFz$ for $z > 0$. It is convenient to write $V(z)$ in this way so that it describes a charge e in an electric field F. Note that F is used for the electric field rather than E to avoid confusion with the energy. In this case, the Schrödinger equation becomes,

This material is reserved for educational use only, not allowed for commercial use.
Forbidden to modify the content, and cite the document when use.

$$\left(-\frac{\hbar^2}{2m}\frac{d^2}{dz^2}+eFz\right)\psi(z)=E\psi(z)\,. \tag{2.73}$$

The boundary condition is that $\psi(z=0) = 0$ and is imposed by the infinite barrier. We again introduce dimensionless variables. Similar manipulation as for the harmonic oscillator shows that scales of distance and energy are

$$z_0=\left(\frac{\hbar^2}{2meF}\right)^{1/3},\quad E_0=\left[\frac{(eF\hbar)^2}{2m}\right]^{1/3}=eFz_0\,. \tag{2.74}$$

The Schrödinger equation becomes

$$\frac{d^2\psi}{d\bar{z}^2}=\left(\bar{z}-\bar{E}\right)\psi(\bar{z})=s\psi\,, \tag{2.75}$$

where $s=\bar{z}-\bar{E}$. Equation (2.71) is called the Stokes or Airy equation. Its two independent solutions, the Airy functions *Ai(s)* and *Bi(s)*, are depicted in Fig. 2.32. We also require a wave function that is well behaved as $z \to +\infty$, which is the same as $s \to +\infty$. This means that we can ignore *Bi(s)*. The boundary at $z=0$ is applied, giving the allowed energies to be

$$E_n=c_n\left[\frac{(eF\hbar)^2}{2m}\right]^{1/3},n=1,2,3...... \tag{2.76}$$

This material is reserved for educational use only, not allowed for commercial use.
Forbidden to modify the content, and cite the document when use.

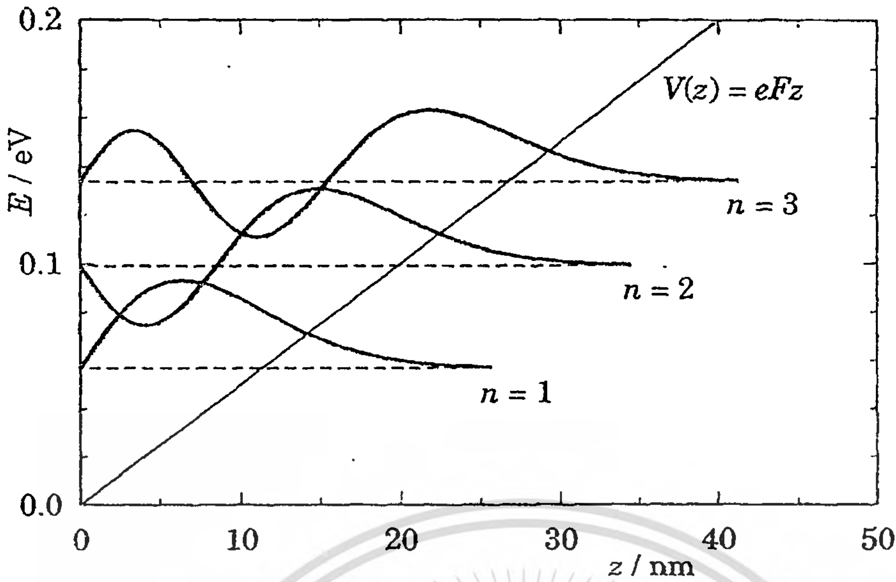

Fig. 2.32 The triangular well.

Using WKB theory to approximate the parameter c_n will give

$$c_n = \left[\frac{3}{2}\pi\left(n-\frac{1}{4}\right)\right]^{3/2}. \tag{2.77}$$

As n increases, the energy levels get closer together since the well broadens as the energy is raised. The corresponding wave function is expressed as

$$\psi_n(z) = CAi(s) = CAi\left(\frac{eFz-E}{E_0}\right), \tag{2.78}$$

where C is normalized constant that can be determine from given boundary condition.

This material is reserved for educational use only, not allowed for commercial use.
Forbidden to modify the content, and cite the document when use.

2.6.5 Perturbation Theory

Generally, perturbation theory provides a framework for calculating the slight change in the Hamiltonian. This approach works well if the potential can be divided into a large part that can be solved exactly and a small perturbation. There are several methods of perturbation such as Variational method, the Wentzel, Kramers, and Brillouin (WKB) method, the $k \cdot p$ theory. However, in this part, the general theory of time-independent perturbation theory is only mentioned.

The general idea is to split the Hamiltonian $\hat{H}$ of the system that we wish to solve into two parts, $\hat{H} = \hat{H}_0 + \hat{V}$. Note that $\hat{H}_0$ and $\hat{V}$ are the unperturbed and small perturbed Hamiltonian. Thus, the SchrÖdinger equation is expressed as

$$\hat{H}\psi_n = (\hat{H}_0 + \hat{V})\psi_n = E_n\psi_n . \tag{2.79}$$

The idea of perturbation theory is to expand the energy and wave function in powers of the small potential $\hat{V}$. Let $\hat{H} = \hat{H}_0 + \lambda\hat{V}$ so that powers of λ identify degrees of smallness. Finally, we will set $\lambda = 1$. The energy and wave functions have the expansions

$$E_n = E_n^{(0)} + \lambda E_n^{(1)} + \lambda^2 E_n^{(2)} + \ldots\ldots\ldots\ldots \tag{2.80}$$

$$\psi_n = \psi_n^{(0)} + \lambda\psi_n^{(1)} + \lambda^2\psi_n^{(2)} + \ldots\ldots\ldots\ldots \tag{2.81}$$

Note that the subscript labels the state and the superscript labels the power of λ, which is the degree of smallness. Substitutes these expansions into the SchrÖdinger equation in equation (2.81) and compares the coefficient of each term of powers of λ. For powers 0,1,2 this gives

$$\hat{H}_0\psi_n^{(0)} = E_n^{(0)}\psi_n^{(0)}, \tag{2.82}$$

$$\hat{V}\psi_n^{(0)} + \hat{H}_0\psi_n^{(1)} = E_n^{(1)}\psi_n^{(0)} + E_n^{(0)}\psi_n^{(1)}, \tag{2.83}$$

This material is reserved for educational use only, not allowed for commercial use.
Forbidden to modify the content, and cite the document when use.

$$\hat{V}\psi_n^{(1)} + \hat{H}_0\psi_n^{(2)} = E_n^{(2)}\psi_n^{(0)} + E_n^{(1)}\psi_n^{(1)} + E_n^{(0)}\psi_n^{(2)}. \tag{2.84}$$

The first term of these, equation (2.83), is just the unperturbed Schrödinger equation. This term implies that the zeroth-order estimates of the wave function are just the unperturbed ones. For simplicity, let $\psi_n^{(0)} = \phi_n$, $E_n^{(0)} = \varepsilon_n$. Inserting these results into the first –order equation (2.84) and gathering terms gives

$$\left(\hat{H}_0 - \varepsilon_n\right)\psi_n^{(1)} = \left(E_n^{(1)} - \hat{V}\right)\phi_n. \tag{2.85}$$

To make further progress we need to use the results of the previous section. Expand $\psi_n^{(1)}$ in terms of the complete set ϕ_n, which are the eigenfunctions of $\hat{H}_0$.

$$\psi_n^{(1)} = \sum_k a_{nk}^{(1)}\phi_k. \tag{2.86}$$

With this expansion, the first-order equation (2.85) becomes

$$\sum_k \left(\hat{H}_0 - \varepsilon_n\right)a_{nk}^{(1)}\phi_k = \left(E_n^{(1)} - \hat{V}\right)\phi_n. \tag{2.87}$$

Using the identity of equation (2.82) results the expansion to be

$$\sum_k a_{nk}^{(1)}\left(\varepsilon_k - \varepsilon_n\right)\phi_k = E_n^{(1)}\phi_n - \hat{V}\phi_n. \tag{2.88}$$

The next step is to use the orthogonality of the states ϕ_n and reduce $\hat{V}$ to a matrix element. Multiply equation (2.88) on the left by ϕ_n^* and integrate. There is only one term that $k = n$ left because the other terms all vanish by orthogonality. However, the difference $(\varepsilon_k - \varepsilon_n)$ causes this

This material is reserved for educational use only, not allowed for commercial use.
Forbidden to modify the content, and cite the document when use.

remaining term to vanish too. On the right hand side, the first term integrates to unity, and the other term with the potential becomes a matrix element V_{nn} to give

$$E_n^{(1)} = \int \phi_n^* \hat{V} \phi_n \equiv V_{nn}. \tag{2.89}$$

Equation(2.85) shows that the first-order change to the energy is simply the expectation value of the perturbing potential $\hat{V}$ in the unperturbed state ϕ_n. The coefficient of the wave function can also be obtained by using orthogonality. This gives

$$a_{nm}^{(1)} = \frac{V_{mn}}{\varepsilon_n - \varepsilon_m}. \tag{2.90}$$

The corresponding perturbed wave function is written as

$$\psi_n^{(1)} = a_{nn}^{(1)} \phi_n + \sum_{k,n \neq k} \frac{V_{kn}}{\varepsilon_n - \varepsilon_k} \phi_k. \tag{2.91}$$

The second-order perturbation can be achieved by following the same manner. First, using the result of the zeroth and the first order for equation (2.83) and expanding the wave function $\psi_n^{(2)} = \sum_k a_{nk}^{(2)} \phi_k$ gives

$$(\hat{H}_0 - \varepsilon_n) \sum_k a_{nk}^{(2)} \phi_k = (\hat{V}_{nn} - \hat{V}) \sum_k a_{nk}^{(1)} \phi_k + E_n^{(2)} \phi_n. \tag{2.92}$$

Secondly, use the orthogonality identity to get the second-order perturbed energy which is

$$E_n^{(2)} = \sum_{k,n \neq k} \frac{|V_{kn}|^2}{\varepsilon_n - \varepsilon_k}. \tag{2.93}$$

King Mongkut's Institute of Technology Ladkrabang

This material is reserved for educational use only, not allowed for commercial use.
Forbidden to modify the content, and cite the document when use.

The process can be carried out both the perturbed Eigen value and Eigen wave function to higher order. However, it is rarely necessary because the much higher order gives the much smaller value than the first two orders.

This material is reserved for educational use only, not allowed for commercial use.
Forbidden to modify the content, and cite the document when use.

References

[1] J.H. Davies, **The Physics of Low-dimensional Semiconductors**, Cambridge: Cambridge University Press, 2000.

[2] S. Mahajan, K.S. Sree Harsha, **Principles of Growth and Processing of Semiconductors,** New Delhi: WCB McGraw-Hill, Inc., 1998.

[3] E. Rosencher and B. Vinter, **Optoelectronics**, Cambridge: Cambridge University Press, 2002.

[4] G. Bastard, **Wave Mechanics applied to Semiconductor Heterostructures,** New York: Halsted Press, 1988.

[5] D. Dragoman and M. Dragoman, **Optical Characterization of Solids,** Berlin: Springer, 2002.

[6] R.W. Kelsall, I.W. Hamley, M. Geoghegan, **Nanoscale Science and Technology,** Chichester: John Wiley & Sons, Inc., 2005.

[7] M. Fukuda, **Optical Semiconductor Devices,** New York: John Wiley & Sons, Inc., 1998.

[8] J. Singh, **Physics of Semiconductors and Their Heterostructures,** Singapore: McGraw-Hill, Inc., 1993.

[9] J. Shinar, **Organic Light-Emitting Devices,** New York: Springer, 2004.

[10] K.K. Ng, **Complete Guide to Semiconductor Devices**, New York: McGraw-Hill, Inc., 1995.

King Mongkut's Institute of Technology Ladkrabang

This material is reserved for educational use only, not allowed for commercial use.
Forbidden to modify the content, and cite the document when use.

CHAPTER 3

EXPERIMENTS

In this chapter, the photoluminescence and photocurrent spectroscopy experiment set up are described. The contact growth process for photocurrent measurement is also mentioned.

3.1 Photoluminescence Spectroscopy Set Up

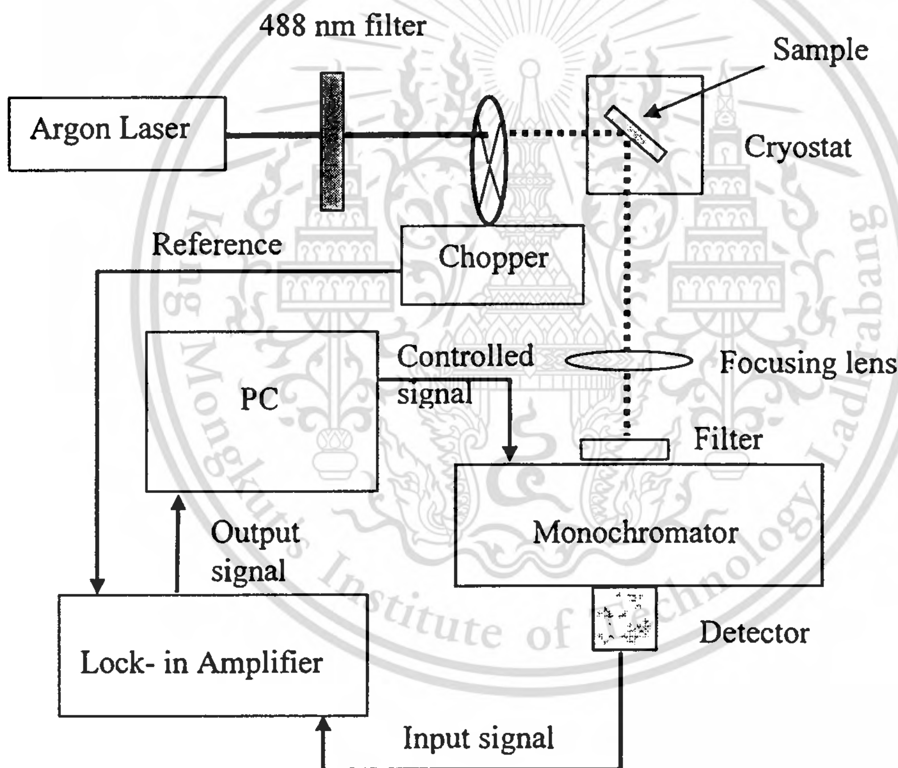

Fig. 3.1 Schematic diagram of Photoluminescence spectroscopy experiment set up.

Fig. 3.1 shows a schematic diagram of basic photoluminescence (PL) experiment set up. Photoluminescence experiment was conducted at department of Physics, Silprakorn University. The air-cooled Argon ion (Ar^+) laser with filtered wavelength of 488 nm was used as optical excitation source. The sample was cooled down to 10 K in a cryostat. The luminescence from the sample was collected by focusing lens with appropriate focal length. At the same time, unwanted

This material is reserved for educational use only, not allowed for commercial use.
Forbidden to modify the content, and cite the document when use.

reflected laser light from the sample was blocked by high-pass filter with cut-off wavelength of about 514 nm. PL signal was then dispersed by the monochromator and was carried out by detector. The signal was amplified by a lock-in amplifier and displayed by a computer. The stepped motor of the monochromator was controlled by a signal from computer via RS-232 port.

3.2 Photocurrent Spectroscopy Set Up

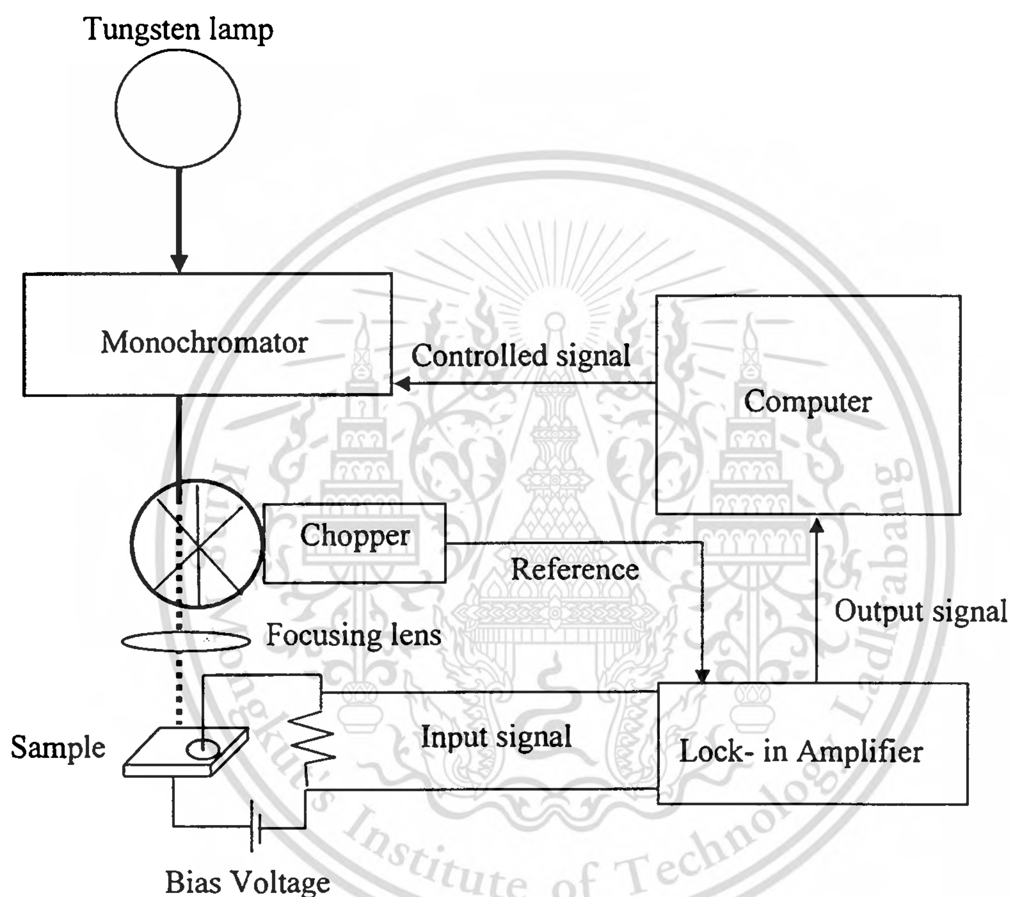

Fig. 3.2 Schematic diagram of Photocurrent spectroscopy experiment set up.

Fig. 3.2 illustrates a schematic diagram of photocurrent experiment set up. Photocurrent experiment was conducted at Quantum and Optical Semiconductor Laboratory, department of Applied Physics, King Mongkut's Institute of Technology Ladkrabang. The light from a tungsten lamp impinges on the sample through a monochromator. The wavelength of light is selected by the monochromator that is controlled by computer. Before illuminating on the sample, light is chopped by a chopper. Photocurrent from the sample is carried out and amplified by the lock-in amplifier. A computer is used to control the monochromator, collect data from the lock-in

This material is reserved for educational use only, not allowed for commercial use.
Forbidden to modify the content, and cite the document when use.

amplifier, and produces plots and data files. All PC measurement was conducted at room temperature.

3.3 Contact Growth Processes

Before the photocurrent spectroscopy is measured, the conducting contact on semiconductor is required. The contact growth processes are needed. The processes are described.

3.3.1 Surface Cleaning Process

The surface cleaning process is needed before the contact is grown on the sample. Different sample uses different process. For GaAsP, the cleaning processes are as follows,

1. Wash the contamination on the surface with Trichloethylene for 5 minutes, and then with Acetone for 5 minutes, followed by Methylalcholhol for 5 minutes. All steps are done in ultrasonic cleaner.
2. Clean the surface with de-ionized (DI) water and then dry in Nitrogen ambient.
3. Etch the oxide layer with H_2SO_4 (96%) : H_2O_2 (31%) : DI Water with 5:1:1 by volume for 20 seconds, HCl Solution for 5 minutes, and wash out with DI water.
4. Dry out the surface with Nitrogen gas.
5. Bake the sample at $150^{\circ}C$ for 1 hour.

3.3.2 Growth of Indium Tin Oxide Contact

The Indium Tin Oxide (ITO) is the transparent conducting contact that is suitably used as optical window in optical semiconductor device. In order to gather the photocurrent, ITO is chosen as the Schottky contact. The ITO thin film was grown by electron beam evaporator at Quantum and Semiconductor Laboratory, as shown in Fig. 3.3. The processes include,

1. The high vacuum is operated until the pressure of 5.0×10^{-6} mbar is obtained.
2. Oxygen is fed to the chamber trough a needle valve.
3. The substrate is heated to reach $200^{\circ}C$.
4. Operate the electron gun and rotate the substrate holder.
5. Observe the growth rate at the crystal monitor. The rate should be in the range of 1-3 Å/s. Then open the shutter to grow the ITO thin film on the substrate.
6. Keep the operation until the required thickness is obtained, then close the shutter and turn off the gun.

This material is reserved for educational use only, not allowed for commercial use.
Forbidden to modify the content, and cite the document when use.

7. Let the substrate cool down to room temperature. Open the chamber and bring the sample out.

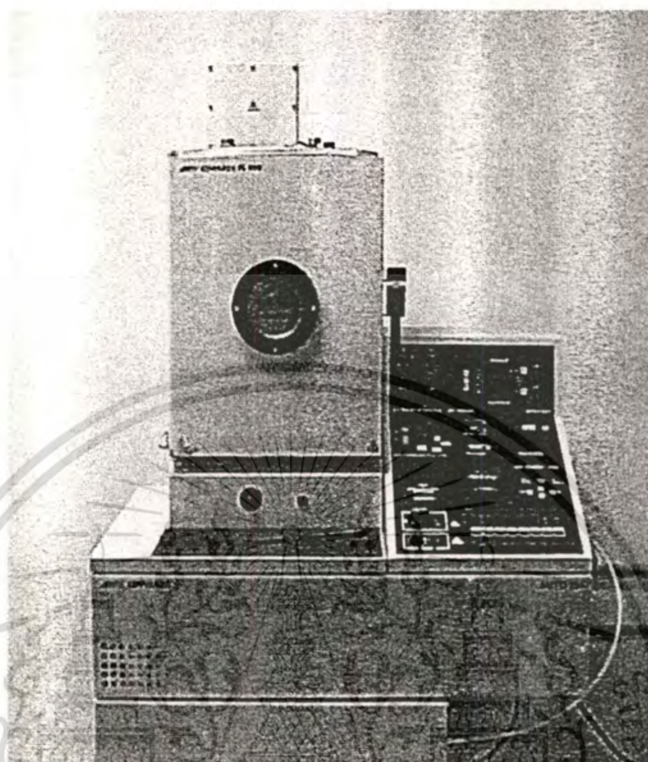

Fig. 3.3 Electron beam evaporator system.

3.3.3 Growth of Gold Contact

Gold contact can be used as both Schottky and Ohmic contacts depending on its thickness. Conventional DC sputtering technique was used to grow the gold thin film with 500 nm thick as Schottky contact and 200 nm thick as Ohmic contact. DC sputtering system is shown in Fig. 3.4. The Gold thin film thickness can be calculated by this following equation,

$$D = 0.17It, \quad (3.1)$$

where I is supplied current, and t is the sputtered time.

This material is reserved for educational use only, not allowed for commercial use.
Forbidden to modify the content, and cite the document when use.

King Mongkut's Institute of Technology Ladkrabang

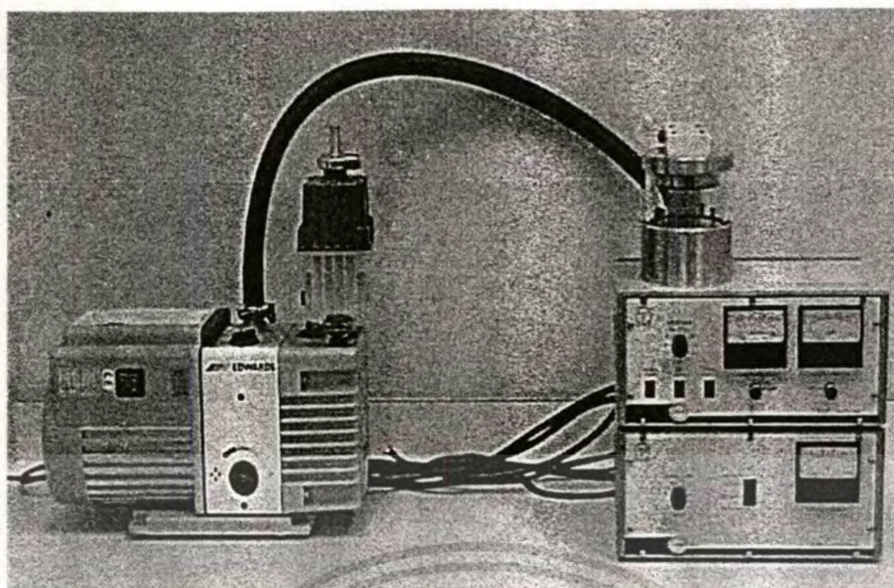

Fig. 3.4 DC sputtering system.

3.4 Equipment for Photoluminescence and Photocurrent Spectroscopy

The details of equipment involved in photoluminescence and photocurrent spectroscopy are described.

3.4.1 Temperature Controller and Vacuum Unit

For low temperature measurements, two important instruments are needed; the vacuum pump and cryostat system.

(i) Vacuum pump shown in Fig. 3.5 is used to evacuate air from the cryostat chamber. The operated pressure is about 10^{-6} mbar. The vacuum pump system includes two vacuum pumps; diffusion pump which can make vacuum environment of 10^{-3}-10^{-7} mbar, and backing rotary pump which evacuate the chamber from atmosphere to about 10^{-3} mbar. The vacuum pressure is monitor with either an Active Pirani Gauge (atmosphere to 10^{-4} mbar) and Penning Guage (10^{-3} to 10^{-7} mbar).

This material is reserved for educational use only, not allowed for commercial use.
Forbidden to modify the content, and cite the document when use.

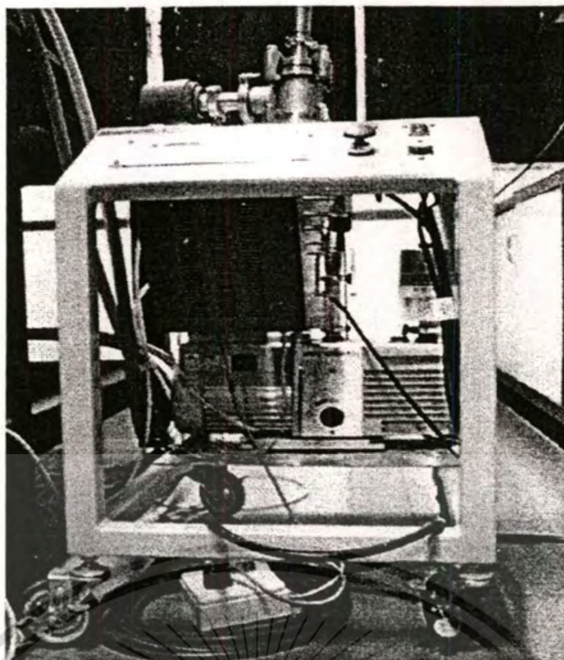

Fig. 3.5 Vacuum pump system.

(ii) Cryogenic system is used to make the low temperature environment. the sample mounts in the cryostat on the copper cold-finger in the chamber (Fig. 3.6a). The cryostat is cooled with pressurized helium from the helium compressor (Fig. 3.6b). The chamber is enclosed in the vacuum environment with windows transparent to both the laser and PL emission. The temperature, monitored with a silicon-diode sensor mounted on the cold-finger, is controlled via temperature controller (Fig. 3.6c) which supply current to a heater assembly that is also mounted on the cold-finger. The temperature can cool down to 10 K.

This material is reserved for educational use only, not allowed for commercial use.
Forbidden to modify the content, and cite the document when use.

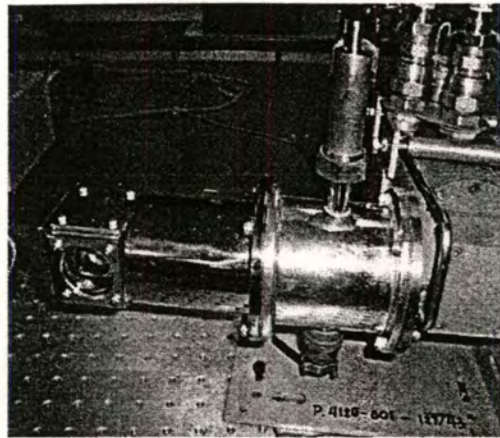

(a)

(b)

(c)

Fig. 3.6 Cryogenic systems; (a) Cold-finger chamber (b) Helium compressor (c) Temperature controller.

This material is reserved for educational use only, not allowed for commercial use.
Forbidden to modify the content, and cite the document when use.

3.4.2 Light Sources

(i) Argon laser is chosen as intense excitation source for photoluminescence measurement because its power is adjustable and its photon energy is suitable. Typically, Argon laser emits three powerful lines, 488 nm, 497 nm and 515 nm. In this PL measurement, 488-nm line is selected using a 488-nm band pass filter.

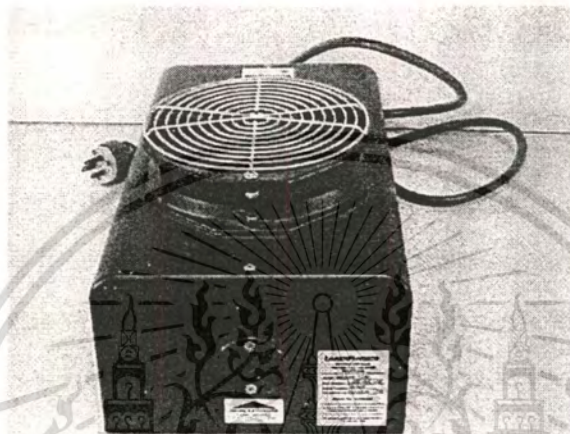

Fig. 3.7 Air-cooled Argon ion laser.

(ii) Tungsten lamp is used as wide wavelength range light source in photocurrent spectroscopy. Its wavelength can be chosen using typical monochromator.

3.4.3 Optical Equipment

(i) In PL measurement, The convexes lenses with appropriate focal length are designated to focus the luminescence light from the sample on the entrance slit of the monochromator. In PC measurement, the convex lens is used to focus light from tungsten lamp on the sample being measured.

King Mongkut's Institute of Technology Ladkrabang

This material is reserved for educational use only, not allowed for commercial use.
Forbidden to modify the content, and cite the document when use.

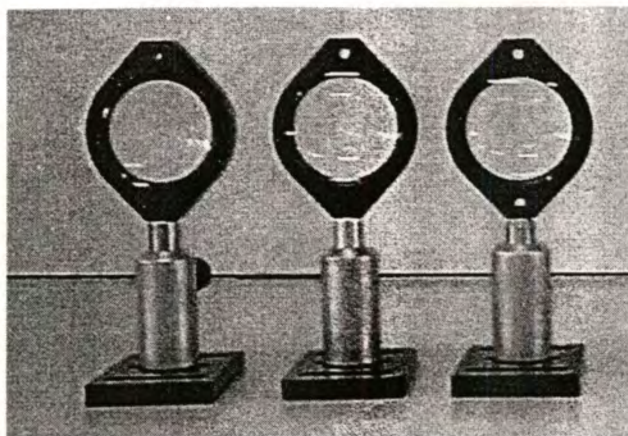

Fig. 3.8 Focusing lenses.

(ii) Band-pass optical filter at 488 nm is used to allow only 488 nm line from Argon ion laser to excite the sample. High-pass filter with cut-off wavelength of about 514 nm was used to block unwanted reflected laser light from the sample into monochromator.

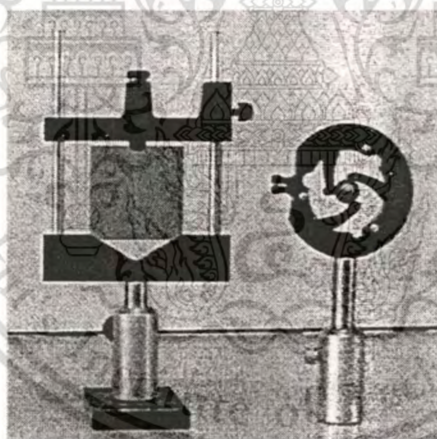

Fig. 3.9 514-nm high pass filter (left) and 488-nm band pass filter (right).

(iii) Chopper is used to modulate laser light. The chopped frequency is selectable up to 4000 Hz. The frequency of the chopper is used as the reference for a lock-in amplifier.

This material is reserved for educational use only, not allowed for commercial use.
Forbidden to modify the content, and cite the document when use.

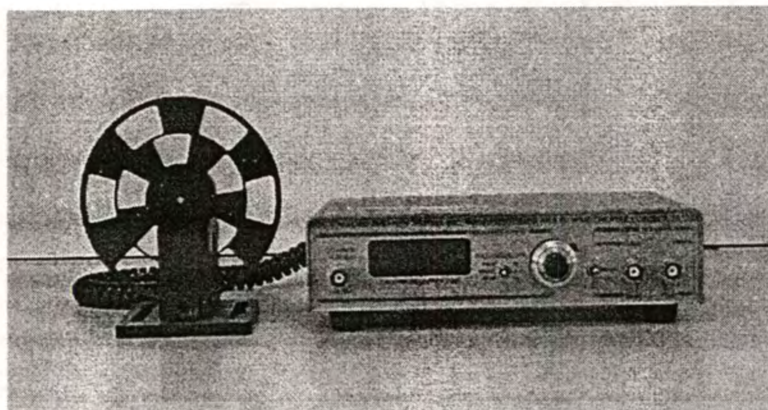

Fig. 3.10 Optical chopper.

3.4.4 Signal Acquisition Equipment

(i) Optical detectors are used to detect optical signals from the sample. Silicon detector is required to detect low-intensity visible wavelength signal. Its response wavelength ranges from about 300 nm to 1100 nm. However, for many important semiconductor materials and structures, their optical signals are in the infrared (IR) region, Ge detector is suitable since it is sensitive to infrared signals from 800 nm to 1700 nm. Also, it is conventional to use the lock-in detection technique to deal with weaker signals and to minimize the effects of noise.

Fig. 3.11 Optical detector.

This material is reserved for educational use only, not allowed for commercial use.
Forbidden to modify the content, and cite the document when use.

(ii) Monochromator is important equipment to disperse light to the desired wavelength by reflection grating. Intensity of focused light entering the monochromator can be adjusted through entrance slit. The optical signal fills the first mirror which collimates the light beam fall upon the grating. The grating can be rotated so that a particular wavelength is selected and illuminates the second mirror. The second mirror then focuses this dispersed light from the grating onto the exit slit. The monochromator can be controlled either manually through control module keyboard or automatically by a computer via RS-232 port.

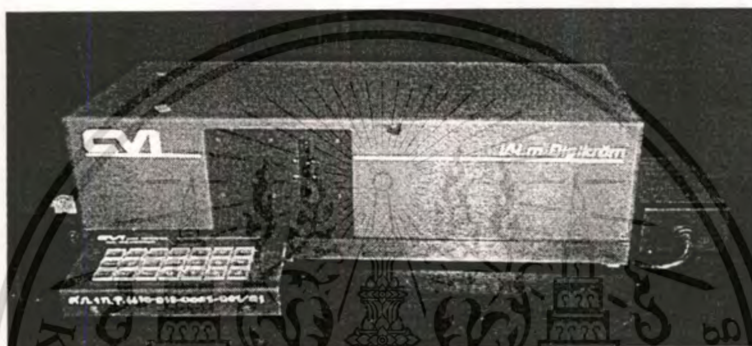

Fig. 3.12 Monochromator.

(iii) Lock-in amplifier is required to measure and amplify the weak luminescence signal from detectors since a lock-in is a filter with an arbitrarily narrow bandwidth which is tuned to the frequency of the signal. Such a filter can reject most unwanted noise to allow the effectiveness of signal measurement. The frequency of the chopper is used as the reference for a lock-in amplifier. The chopper controller sends a reference signal with the same frequency that the beam is being chopped to the lock-in amplifier. This sets the frequency to be detected by the lock-in and fixes the timing of the signal to allow phase sensitive detection to occur. The amplified signal is sent to the computer for evaluation.

This material is reserved for educational use only, not allowed for commercial use.
Forbidden to modify the content, and cite the document when use.

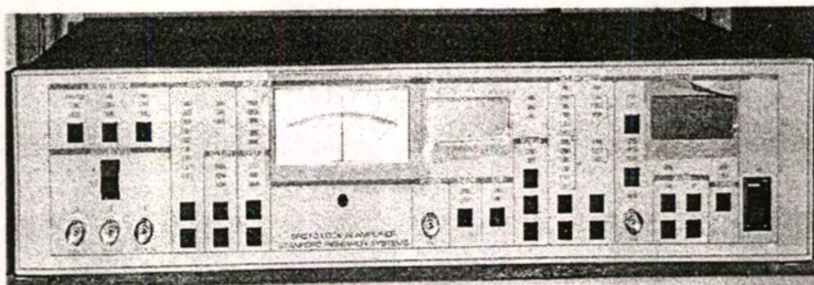

Fig. 3.13 Lock-in Amplifier.

This material is reserved for educational use only, not allowed for commercial use.
Forbidden to modify the content, and cite the document when use.

CHAPTER 4

PHOTOLUMINESCENCE AND PHOTOCURRENT OF BULK SEMICONDUCTOR

4.1 Photoluminescence of Bulk Semiconductor

First experiment, the physical properties, especially the optical and electronic states of bulk semiconductor have been investigated. GaAsP is chosen because its bandgap is in the visible range that is applicable for useful optoelectronic devices such as photodetector. Photoluminescence spectroscopy of GaAsP was conducted. Important parameters which should be involved the photoluminescence phenomena such as temperature is investigated. Fig. 4.1 shows photoluminescence of bulk GaAsP measured as a function of photon energy at different temperature. The measured temperature ranges from 20 K to 80 K. The PL signals show its peak in the vicinity of 2.0-2.1 eV.

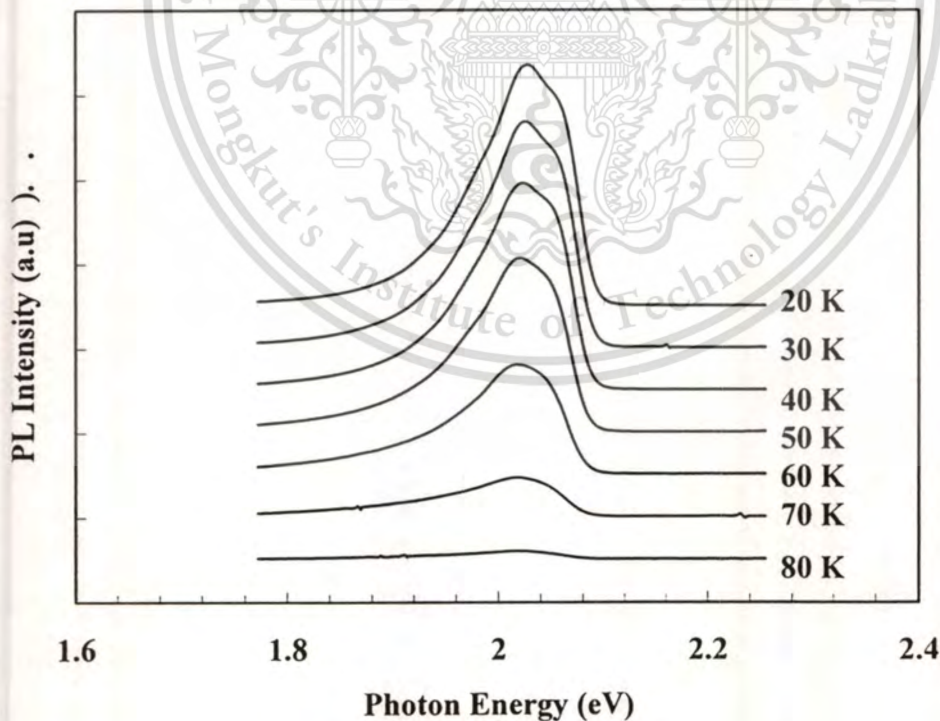

Fig. 4.1 Temperature-dependent photoluminescence of bulk GaAsP.

This material is reserved for educational use only, not allowed for commercial use.
Forbidden to modify the content, and cite the document when use.

In PL measurement of bulk semiconductor, the important parameters that lead to determination of its properties are the maximum peak, PL peak intensity, and the full width at half maximum (FWHM). These values are achieved by the best fitting. Fig. 4.2 shows the PL signals of GaAsP and the best fitting data and the fitting parameters are listed in Table 4.1.

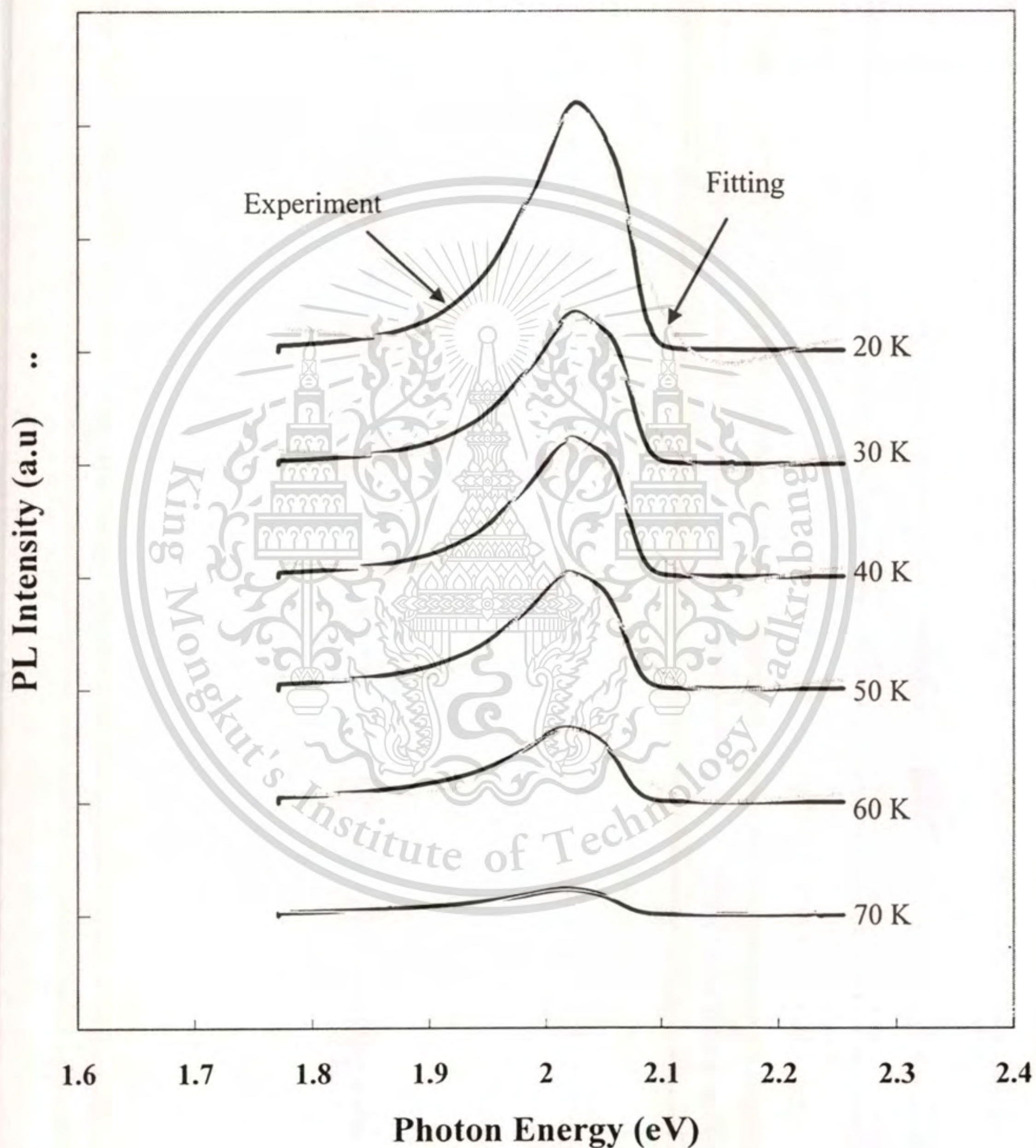

Fig. 4.2 Temperature-dependent photoluminescence of GaAsP with curve fitting .

This material is reserved for educational use only, not allowed for commercial use.
Forbidden to modify the content, and cite the document when use.

Table 4.1 Full width at half maximum of PL spectra, Energy gap and the maximum amplitude of PL peak of GaAsP by the best fitting.

Temperature (K)	FWHM (meV)	Energy gap (eV)	PL intensity x 10^{-7} (a.u)
20	11.31	2.035	1.914
30	11.40	2.036	1.541
40	11.44	2.034	1.480
50	11.51	2.03	1.353
60	11.80	2.028	1.186
70	12.36	2.026	0.659

The change of the fundamental band gap of semiconductor materials with temperature is of considerable importance both in basic science and technological applications. In typical, two mechanisms are responsible for the temperature dependence of the forbidden gap or excitonic transitions of bulk semiconductor materials: the electron-phonon interaction and the thermal expansion of the lattice[1]. Fig. 4.3 shows the temperature dependence of energy gap of GaAsP as function of temperature in the 20 – 70 K range. These values were obtained by the best fitting as shown in Table 4.1. The temperature-dependent energy gap of semiconductor materials is typically expressed empirical relations proposed by many analytical models. The conventional model is the Vashni empirical model[2] explained by the following equation:

$$E_g(T) = E_g(0K) - \alpha \frac{T^2}{\beta + T}. \tag{4.1}$$

where $E_g(T)$ is the energy gap at temperature T and α and β are parameters to fit the experimental data (referred to as Vashni thermal coefficients). Another model which takes the Bose-Einstein occupation factor for photons into account was proposed by Viña *et.al.* [3] and expressed as the following equation:

$$E_g(T) = E_B - a_B\left[1 + \frac{2}{exp(\Theta_B / T) - 1}\right]. \tag{4.2}$$

This material is reserved for educational use only, not allowed for commercial use.
Forbidden to modify the content, and cite the document when use.

where a_B represents the electron-phonon interaction strength, $\Theta_B = \dfrac{\hbar\omega}{k_B}$ is the characteristic temperature parameter representing the effective phonon energy on the temperature scale and $E_B = E_g(0K) + a_B$.

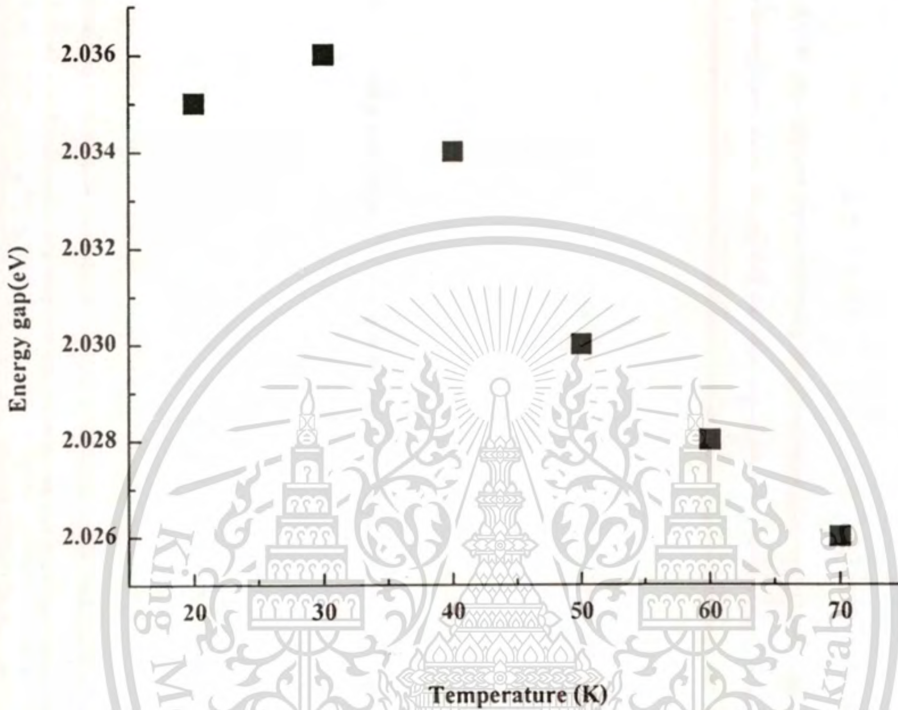

Fig. 4.3 The experimental temperature dependence of the energy gap of GaAsP.

King Mongkut's Institute of Technology Ladkrabang
This material is reserved for educational use only, not allowed for commercial use.
Forbidden to modify the content, and cite the document when use.

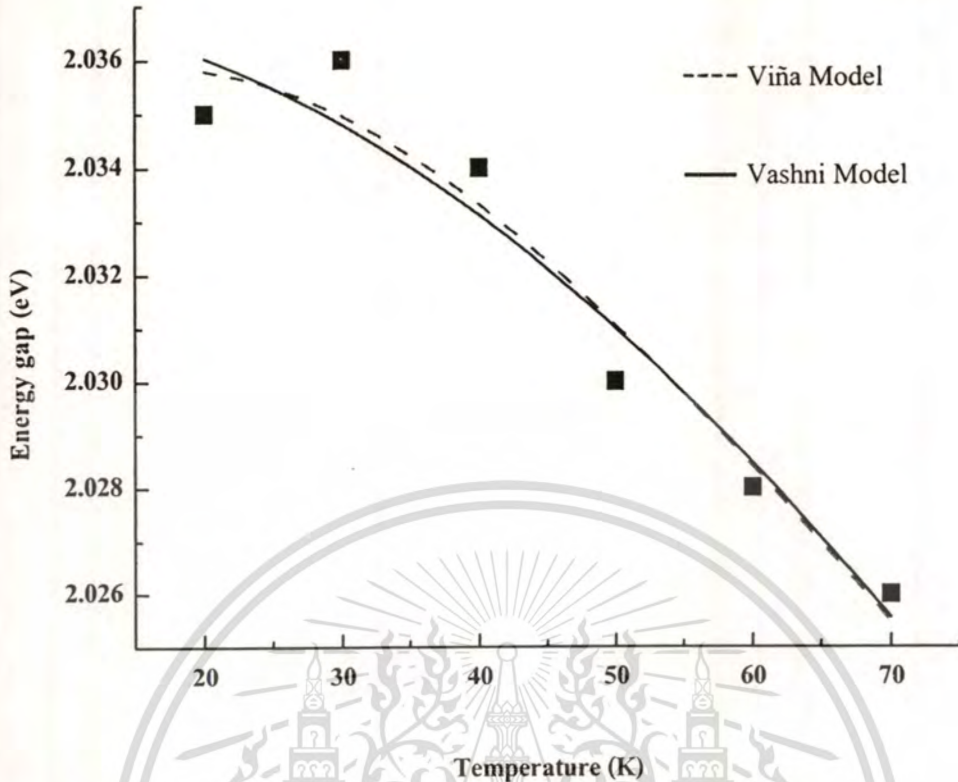

Fig. 4.4 Variation of energy gap of GaAsP with temperature. The solid line and the dash line represent the best fit to the Vashni and Viña model, respectively.

In Fig. 4.4, the temperature dependence of energy gap of GaAsP is shown with the numerical fit based on Vashni and Viña model expressed by equation (4.1) and (4.2), respectively. The solid line represents the best fit of Vashni expression meanwhile the dashline represents the best fit of Viña expression. Both models show almost identical curve lines and good description of the experimental points. Based on Vashni model, the parameters obtained from the fit are $E_g(0K)$ = 2.037 eV, α = 1.51 meV / K, and β = 574 K. Meanwhile, the fitting parameters obtained by Viña model are E_B = 2.057 eV, a_B = 21.5 meV, and the phonon temperature; Θ_B = 114 K. Based on Viña model, the energy gap of GaAsP at 0 K can be obtained by the relationship $E_g(0K) = E_B - a_B$ = 2.036 eV. The energy gap of GaAsP at zero Kelvin obtained by both models is in good agreement. In addition, the value of electron-phonon interaction strength in GaAsP is about 21.5 meV. This includes contribution both from the acoustical and optical phonons.

This material is reserved for educational use only, not allowed for commercial use.
Forbidden to modify the content, and cite the document when use.

The full width of half maximum (FWHM) of PL spectra from fitting is plotted as function of temperature and shown in Fig. 4.5. The FWHM of emission peaks gradually increase from 11.31 meV to 11.51 meV as temperature increases from 20 K to 50 K and then abruptly increase to 12.36 meV with when the temperature increases to 70 K.

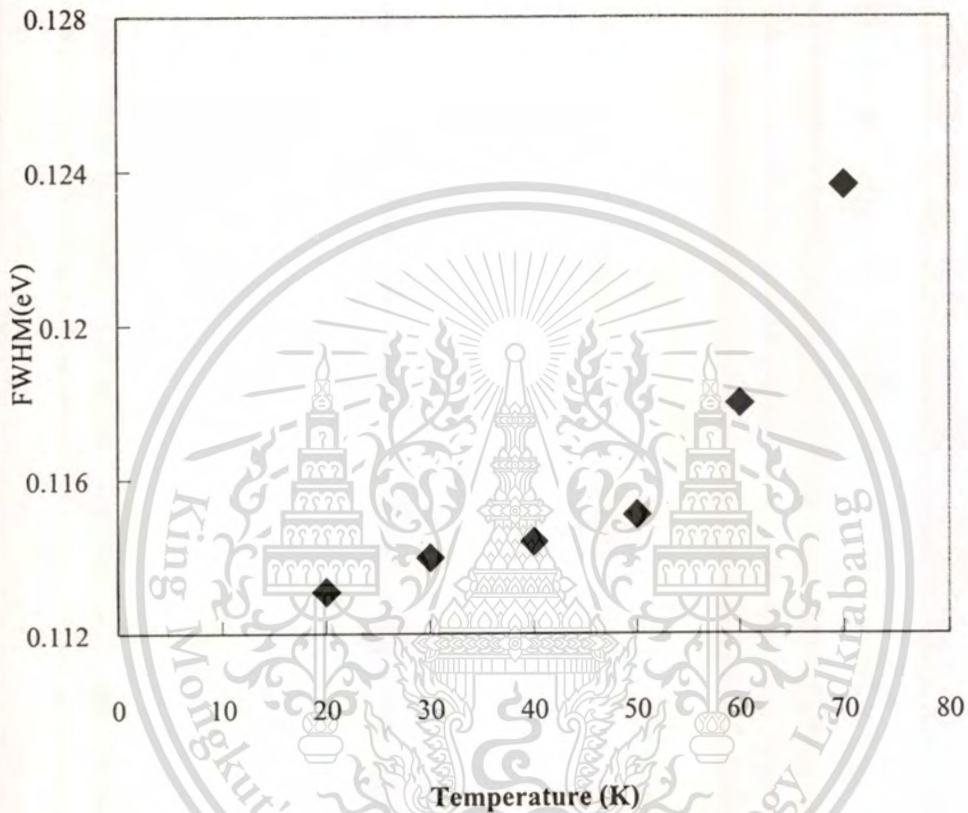

Fig. 4.5 Full width of half maximum (FWHM) of PL peak of GaAsP as a function of temperature.

In general, the broadening of the PL spectra in bulk semiconductor or quantum well heterostructure can be summarized as the sum of two components [4]. These two components are temperature-independent inhomogeneous broadening which is due to interface roughness, fluctuations in binding energies alloy fluctuations (Γ_{in}), and the temperature-dependent homogeneous broadening which typically due to electron-optical phonon or exciton-phonon interactions, Γ_{hom}. Therefore the total broadening is expressed as the summation of inhomogeneous broadening and homogeneous broadening due to the electron-phonon interaction,

This material is reserved for educational use only, not allowed for commercial use.
Forbidden to modify the content, and cite the document when use.

$$\Gamma_{total}(T) = \Gamma_{in} + \Gamma_{hom}(T) \ . \tag{4.3}$$

The homogeneous broadening is given by the following expression,

$$\Gamma_{hom} = \frac{\Gamma_{LO}}{exp\left(\dfrac{E_{LO}}{k_B T}\right) - 1}, \tag{4.4}$$

where Γ_{LO} is the electron-phonon or exciton-LO-phonon coupling constant and E_{LO} is the optical phonon energy. Fig 4.6 illustrates the values of linewidth of PL spectra from the GaAsP as a function of temperature. The solid line is the fitting curve to the measured point using equations (4.3) and (4.4). The fitting curve shows good agreement with the experimental data. The corresponded parameters extracted from the curve fitting are obtained as follows, Γ_{LO}=1.25 eV, E_{LO} = 29.2 meV, and Γ_{in} = 113.7 meV.

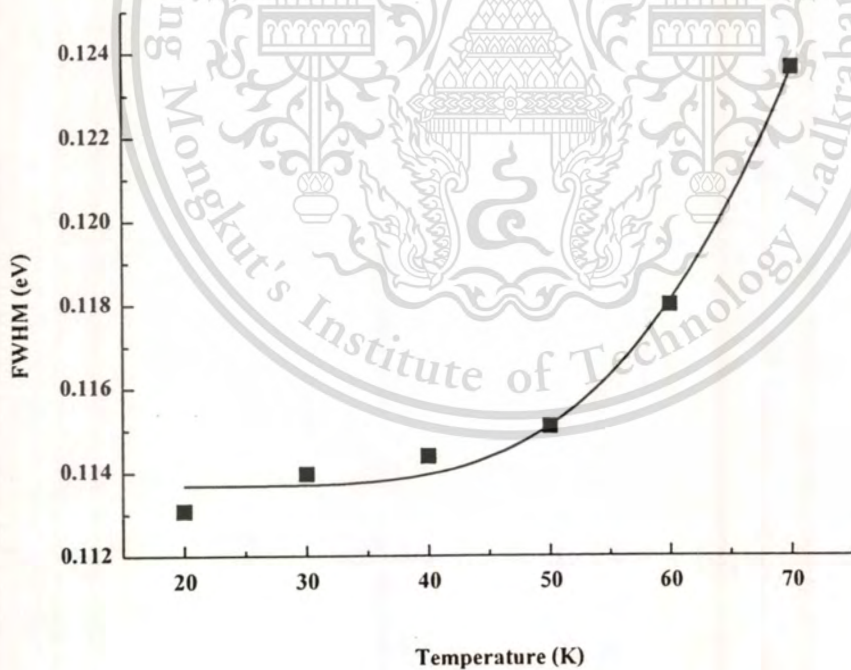

Fig. 4.6 FWHM of PL spectra of 3-ML sample as a function of temperature.

This material is reserved for educational use only, not allowed for commercial use.
Forbidden to modify the content, and cite the document when use.

From the fitting parameters, the homogeneous broadening of PL emission of GaAsP is obtained using equation 4.4. Fig. 4.7 shows the variation of homogeneous broadening (Γ_{hom}) of GaAsP with temperature. At low temperature of 20 – 50 K range, the value of Γ_{hom} is insignificant comparing to inhomogeneous broadening indicating the suppression of electron-phonon interaction. This result suggests that the inhomogeneous broadening is responsible for the broadening mechanism of photoemission of GaAsP at low temperature. As temperature increases from 50 K to 200 K, The value of Γ_{hom} rapidly increase from about 1 meV to 300 meV. Therefore, at this temperature range, both broadening mechanisms play important roles on broadening mechanism of the sample. In addition, at high temperature, the bound excitons are ionized into free excitons and the donors and or acceptors are ionized as well. Therefore, the electron-phonon interaction becomes the dominant broadening mechanism at high temperature.

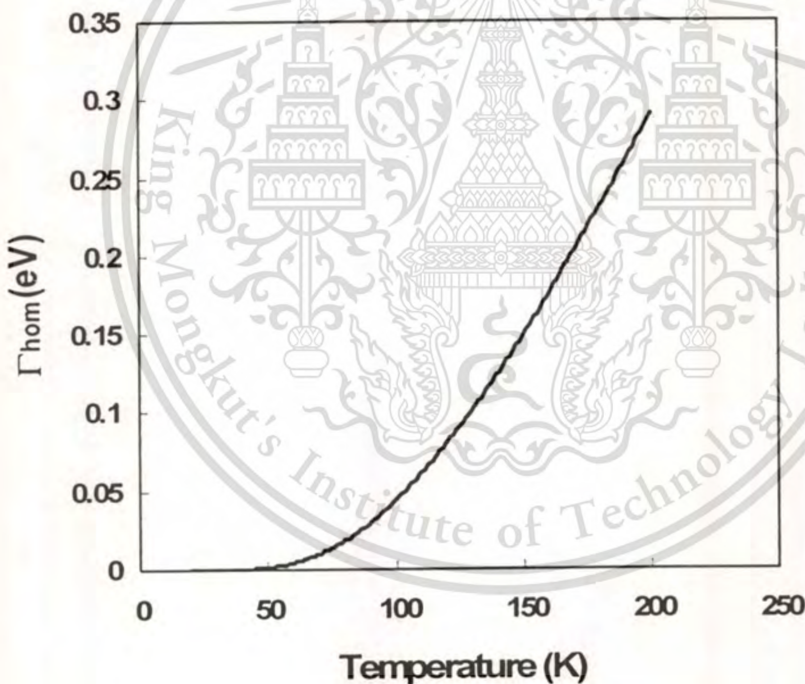

Fig. 4.7 Variation of homogeneous broadening with temperature.

Fig. 4.8 illustrates the plot of the intensity of PL spectra as function of temperature. It is revealed that the PL amplitude decreases with increasing temperature. In general, the temperature dependent PL intensity is associated with the thermal activation energy as the following expression [5],

This material is reserved for educational use only, not allowed for commercial use.
Forbidden to modify the content, and cite the document when use.

$$I_{PL}(T) = \frac{I_0}{1 + A exp(-E_A / k_B T)}, \tag{4.5}$$

where I_0 is the integrated PL intensity near 0 K, A is a constant, and E_A is the thermal activation energy which is responsible for the quenching of PL intensity in the temperature-independent PL spectra. The corresponded parameters extracted from the curve fitting are obtained as follows, I_0 = 1.71×10^{-7} a.u , A= *0.022*, and E_A = 21.5 meV.

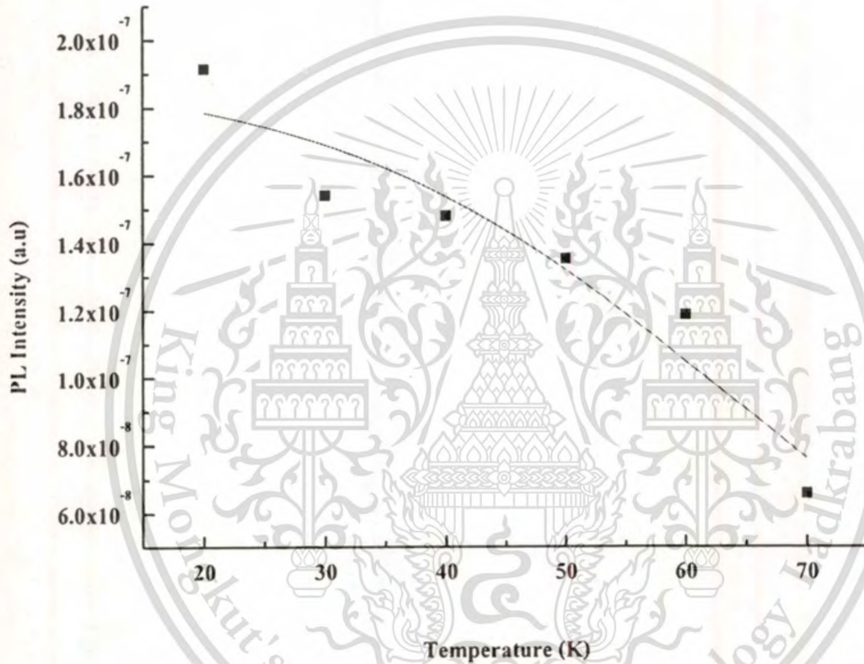

Fig. 4.8 PL intensity of GaAsP as a function of temperature. The solid line represents the best fit by equation 4.5.

This material is reserved for educational use only, not allowed for commercial use.
Forbidden to modify the content, and cite the document when use.

4.2 Current – Voltage Characteristics of Bulk GaAsP

Before the PC is measured, The current-voltage (I-V) characteristics of the sample should be conducted so that the good contacts are confirmed. Fig. 4.9 schematically shows the contact patterns of GaAsP.

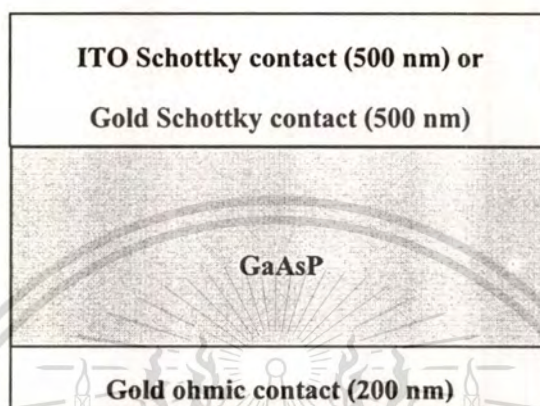

Fig. 4.9 Schematic draw of contact pattern of GaAsP for photocurrent measurement.

In Fig. 4.10, both Indium Tin Oxide (ITO) and Gold (500 nm thick) form such good Schottky contacts with GaAsP. In addition, gold contact with 200 nm thick performs as good Ohmic contact to both samples. When the samples are forward biased, the threshold current initializes at about 500 mV. The current of the sample with ITO contact increases more rapidly than one with gold contact. This feature can be explained by the different of work function of each contact. The work function of ITO of 4.7 eV is approximately 0.5 eV smaller than the work function of gold of 5.2 eV. It can be observed that this difference is corresponded to the difference of the saturated voltage, when forward biased.

This material is reserved for educational use only, not allowed for commercial use.
Forbidden to modify the content, and cite the document when use.

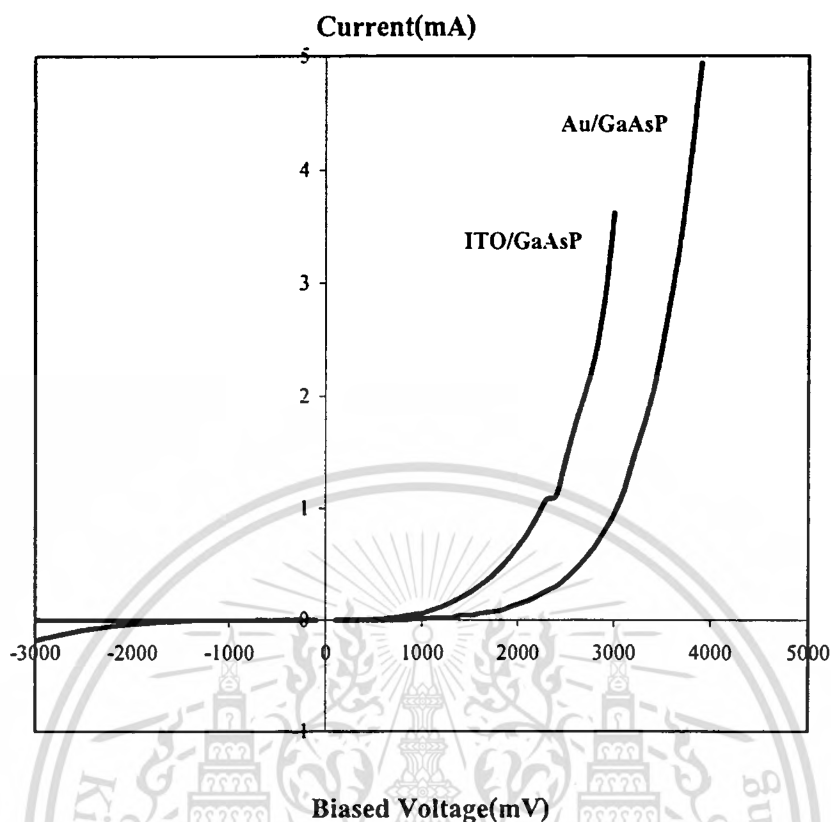

Fig. 4.10 Current-Voltage characteristic of GaAsP with ITO and gold contact as Schottky contact.

4.3 Photocurrent of Bulk Semiconductor

The photocurrent spectroscopy of bulk semiconductor was set up at room temperature. GaAsP is selected as a characterized sample. Its PC signal with different Schottky contacts; Gold and ITO is compared. Fig. 4.11 exhibits the PC spectra of GaAsP at different chopped frequency. For this sample, 500-nm thick ITO and 200-nm thick gold is used as Schottky and Ohmic contacts, respectively. All PC spectra begin to raise at around 2.0 eV, at which corresponded to the absorption energy of GaAsP. At low frequency, PC spectra have greater amplitude than at high frequency. The effect of chopped frequency on PC amplitude is plotted in Fig. 4.12. The solid line presents fitting curve using following equation,

$$I_{PC} = I_1 + \frac{I_0}{\sqrt{1+(2\pi f\tau)^2}} \tag{4.6}$$

This material is reserved for educational use only; not allowed for commercial use.
Forbidden to modify the content, and cite the document when use.

Where I_l, I_0 and τ are the background current, PC at f = 0 Hz, and the PC response time, respectively[6]. The fitted values of these three parameters are listed in table 4.1

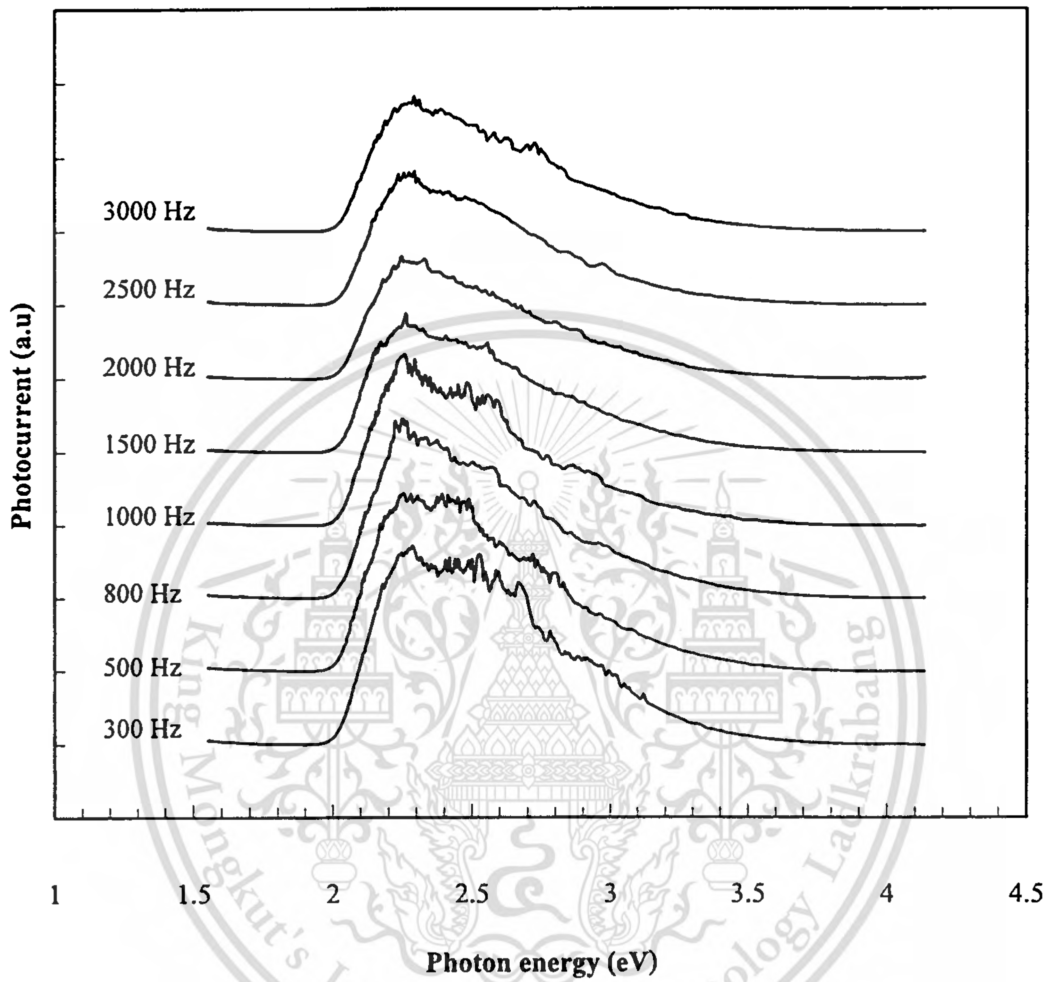

Fig. 4.11 Photocurrent of ITO/GaAsP with different chopper frequency.

This material is reserved for educational use only, not allowed for commercial use.
Forbidden to modify the content, and cite the document when use.

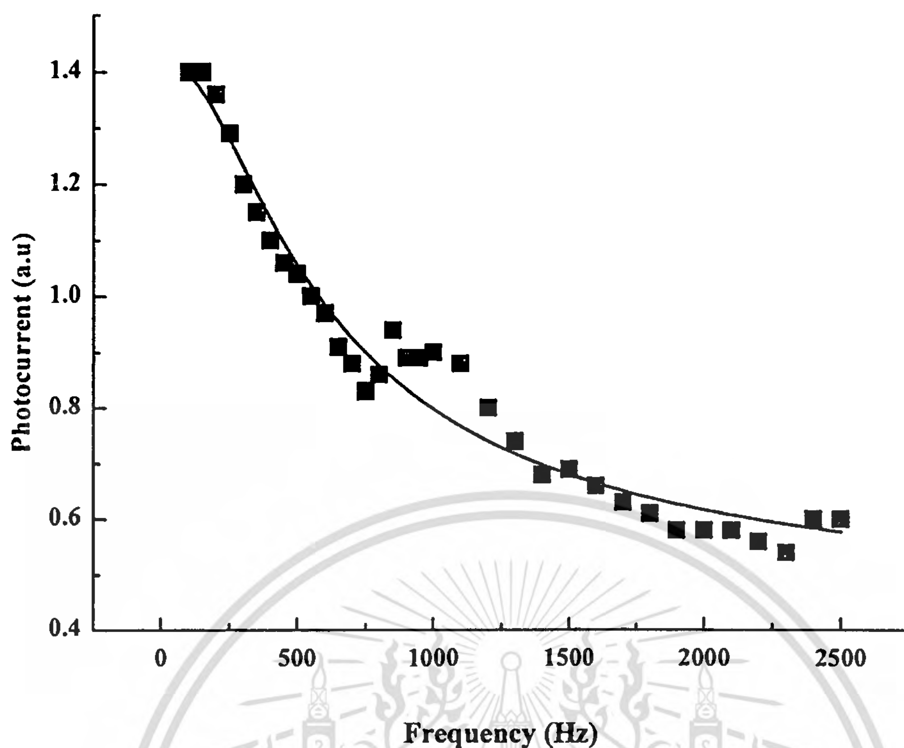

Fig. 4.12 Frequency response of Photocurrent of ITO/GaAsP at vicinity of energy gap. Solid line represents the fitted curve by equation (4.6).

Table 4.2 fitted parameters of GaAsP from frequency sensitive photocurrent measurement.

I_l(a.u)	0.413
I_0(a.u)	1.014
τ (ms)	0.39

The PC of GaAsP under biasing was studied. The biased voltages are varied from 0 Volt to 3 Volt as shown in Fig. 4.13. The PC amplitude increases as the forward biased voltage increases. This feature is explained in section 2.2.3. However, the position of the peak does not change with the increment of biased voltage because the sample is just bulk semiconductor and the quantum effects is not consequently observed.

This material is reserved for educational use only, not allowed for commercial use.
Forbidden to modify the content, and cite the document when use.

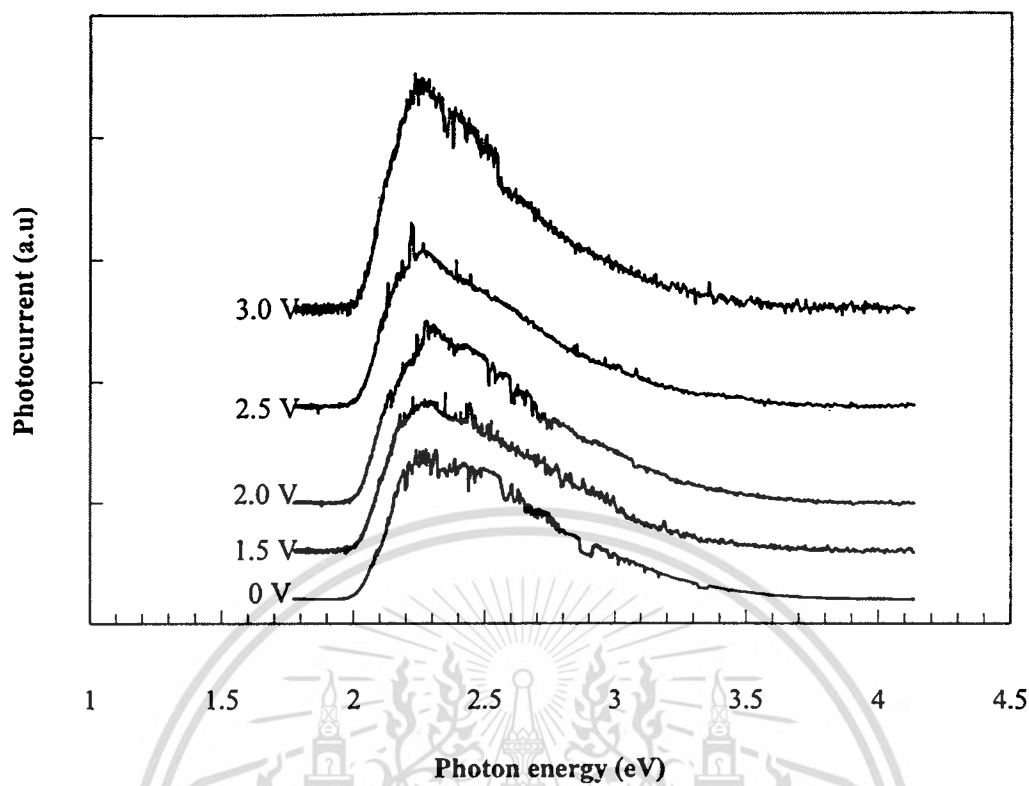

Fig. 4.13 Photocurrent of ITO/GaAsP at different bias voltage.

King Mongkut's Institute of Technology Ladkrabang

This material is reserved for educational use only, not allowed for commercial use.
Forbidden to modify the content, and cite the document when use.

References

[1] S.A. Lourenco, I.F.L. Dias, J.L. Duarte, and E. Laureto, "Temperature dependence of optical transitions in AlGaAs", **Journal of Applied Physics**, Vol. 89, pp. 6159-6164, 2001.

[2] Y.P. Vashni, **"Temperature dependence of the energy gap in semiconductors"**, Physica, Vol. 34, pp. 149-154, 1967.

[4] M. Furis, A.N. Cartwright, H. Wu, and W.J. Schaff, **"Emission mechanisms inUV emitting GaN/AlN multiple quantum well structure"**, Material Research Society Symposium 2004, Vol. 798, 2004.

[5] M. Furis, A. N. Cartwright, J. Hwang, and W.J. Schaff, **"Time resoloved photoluminescence of Si-doped high Al mole fraction AlGaN epilayers grown by plasma-enhanced molecular beam epitaxy"**, Material Research Society Symposium 2004, Vol. 798, 2004.

[6] C.H. Qiu and J.I. Pankove, **"Deep levels and persistent photoconductivity in GaN thin films"**, Applied Physics Letters, Vol. 70, pp. 1983-1985, 1997.

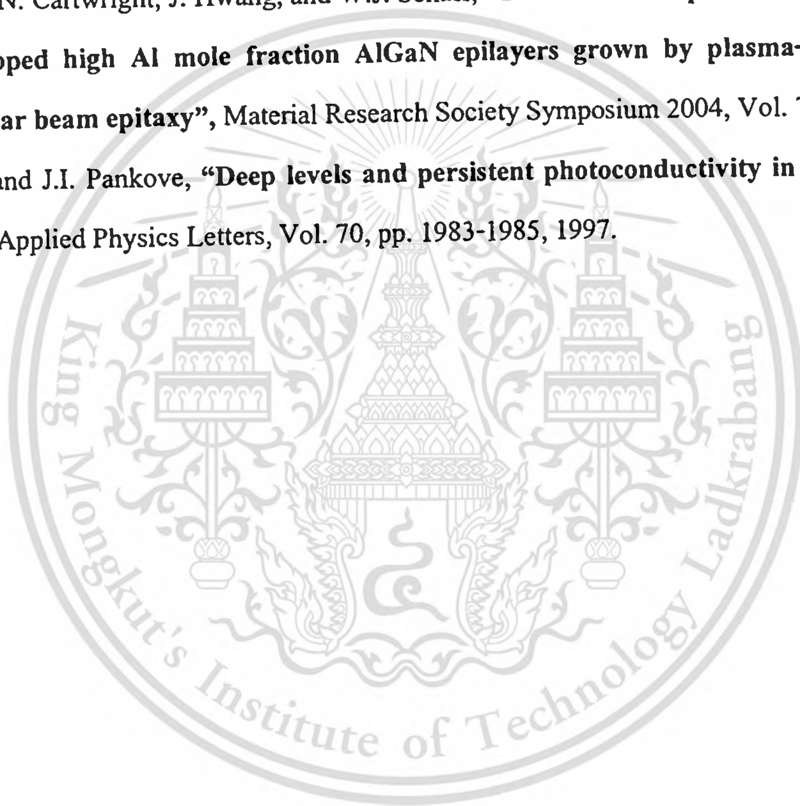

This material is reserved for educational use only, not allowed for commercial use.
Forbidden to modify the content, and cite the document when use.

CHAPTER 5

PHOTOLUMINESCENCE OF NARROW WELL WIDTH InGaAs/InP SINGLE QUANTUM WELL

5.1 Literature Review

Semiconductor compound materials from group III and V in the periodic table have recently attracted considerable interest according to promising properties for novel optoelectronic devices such as lasers and light emitting diodes. Most of devices are fabricated in form of quantum structure. $In_{0.53}Ga_{0.47}As$ lattice-matched to InP has promised for ultrahigh speed devices, utilizing the high electron mobility and high peak velocity. The band gap of 0.75 eV is good for photodetector in optical communication systems. Moreover, semiconductor injection lasers using InGaAs/InP quantum well structures can be shifted into the 1.30-1.55 μm region by changing the well thickness. Room – temperature measurements of the quantum confined Stark effect in single InGaAs/InP quantum wells grown by low-pressure MOVPE were studied[1]. The well thickness ranges from 45 to 110 Å. Photocurrent measurements on p-i-n diodes containing single quantum wells have been used to demonstrate strong excitonic absorption features which exhibit substantial spectral shift in an applied electric field. The optical properties of excitons in InGaAs/ InP quantum wells for the use in tunable resonant cavity enhanced photodetectors were analyzed by photoluminescence and photocurrent spectroscopy[2]. The results implied the formation of InAs or InAsP monolayer at the interface between InGaAs QW and InP barrier. Low – temperature photoluminescence of InGaAs/InP quantum wells with well thickness ranging from 1 to 16 nm was performed in order to investigate the source supply interruption (SSI) at the interface [3]. The observed PL peak energy shifts toward a higher energy as the SSI becomes longer. PL is measured to study the optical features of GaAs/AlGaAs multiple quantum wells. The results suggest that As pressure influence on densities of the defects that can be tailored by As pressure during the MBE growth [4].

In this chapter, the formation of $In_{0.53}Ga_{0.47}As$/InP single quantum well with narrow well width grown by Organometallic Vapor Phase Epitaxy is verified by photoluminescence spectroscopy. PL spectra exhibit the e(1)-hh(1) transition in the well. PL measurement was

This material is reserved for educational use only, not allowed for commercial use.
Forbidden to modify the content, and cite the document when use.

conducted at various temperatures from 15K to 200K in order to investigate the important temperature-dependent parameters of this structure.

5.2 Sample Structure

Few monolayers $In_{0.53}Ga_{0.47}As/InP$ SQWs were grown by Organometallic Vapor Phase Epitaxy (OMVPE) at low pressure. Trimethylgallium (TMGa), Trimethylindium (TMIn), AsH_3, and PH_3 were used as the source gases for Ga, In, As and P respectively. Flow sequence of source gases are shown in Fig. 5.1. A 100-nm thick InP buffer layer was grown on semi-insulating InP substrate. After the gas source for In and P was suspended, InGaAs well layer was grown with varied thickness from 1-5 monolayer before InP cap layer with 2 nm thick was grown. The growth temperature was 600°C. The sample structure is schematically depicted in Fig.5.2.

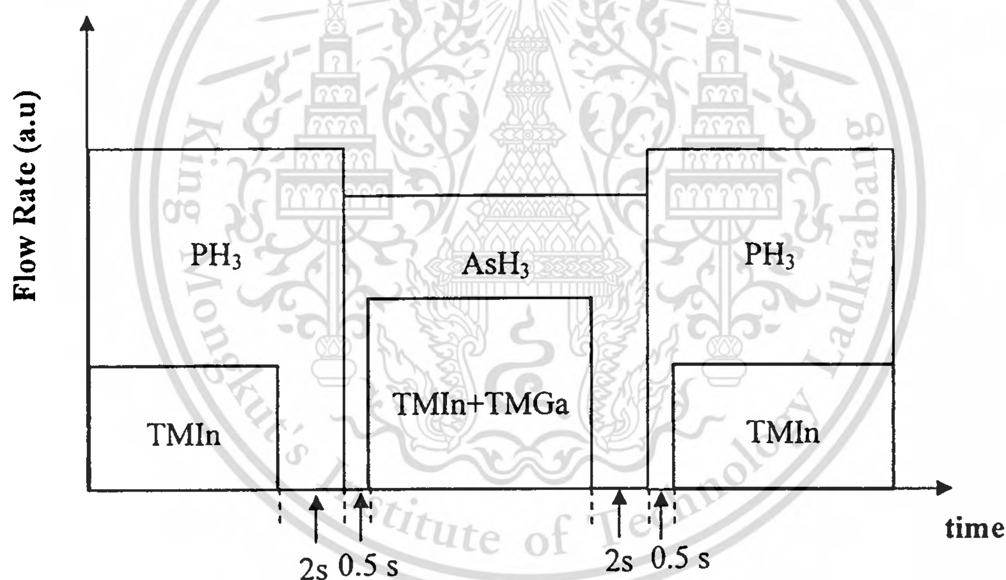

Fig. 5.1 Flow sequence of gas sources for $In_{0.53}Ga_{0.47}$ As /InP single quantum well.

This material is reserved for educational use only, not allowed for commercial use.
Forbidden to modify the content, and cite the document when use.

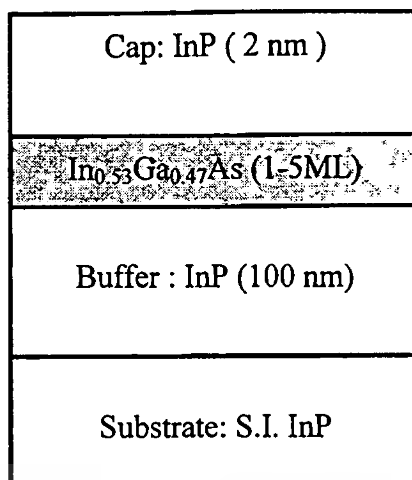

Fig. 5.2 Sample structure of $In_{0.53}Ga_{0.47}$ As/InP single quantum well.

5.3 Results and Discussion

In Fig. 5.3, PL spectra of all samples at 15 K exhibit clear peaks, which are attributed to the luminescence from quantum well. The solid lines represent the fitting curves of each sample. The observed PL peak of the sample with the well width of 4ML, 3ML, and 2 ML is at 1.079 eV, 1.151 eV, and 1.198 eV respectively. The peaks due to the n=1 excitonic transition (e(1)-hh(1)) are clearly identified. PL peak has a dramatic increase (about 40-60meV) when the well width is decreased by only one monolayer. These features reflect the formation of the extremely thin well-width single quantum well between lattice-matched InP and InGaAs. The sample with 3ML-well width shows the strongest intensity, implying the optimization of good formation and uniformity of the sample.

This material is reserved for educational use only, not allowed for commercial use.
Forbidden to modify the content, and cite the document when use.

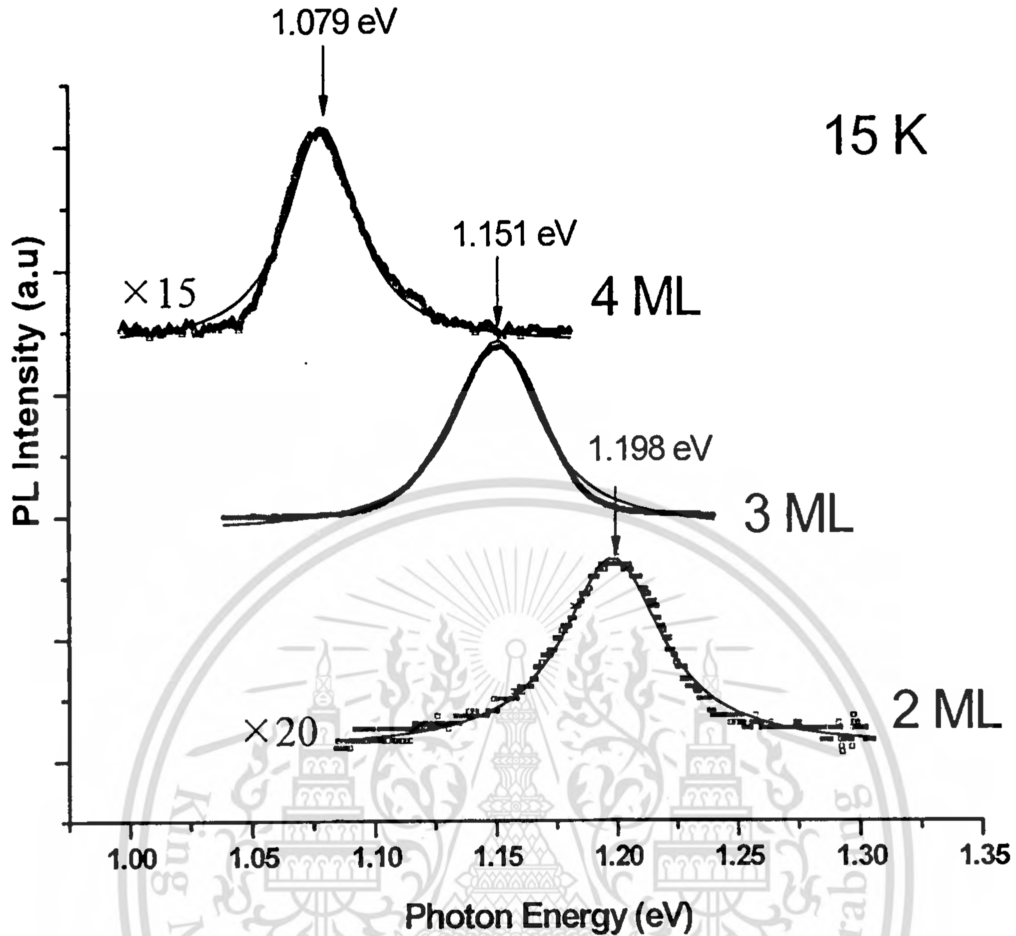

Fig. 5.3 PL spectra of $In_{0.53}Ga_{0.47}$ As/InP single quantum well with different well width at 15 K.

The calculation of the peak observed in the PL spectra of the particular quantum well transition is done by estimating the transition energies expected for a quantum well with a given well width. The ground state energy level in the quantum well is calculated by solving one-dimensional Schrödinger equation of a finite square well. In the calculation, the energy gap of InP and $In_{0.53}Ga_{0.47}As$ are 1.35 eV and 0.73 eV respectively[5]. The effective mass of electron (m_e^*) and hole (m_{hh}^*) for $In_{0.53}Ga_{0.47}As$ are $0.0416m_0$ and $0.46m_0$ respectively. The band discontinuity for conduction band ,ΔE_c, and valence band ,ΔE_v, are 0.217 eV and 0.403 eV respectively [5]. The corresponding schematic band diagram of $In_{0.53}Ga_{0.47}$ As/InP single quantum well is depicted in Fig 5.4.

This material is reserved for educational use only, not allowed for commercial use.
Forbidden to modify the content, and cite the document when use.

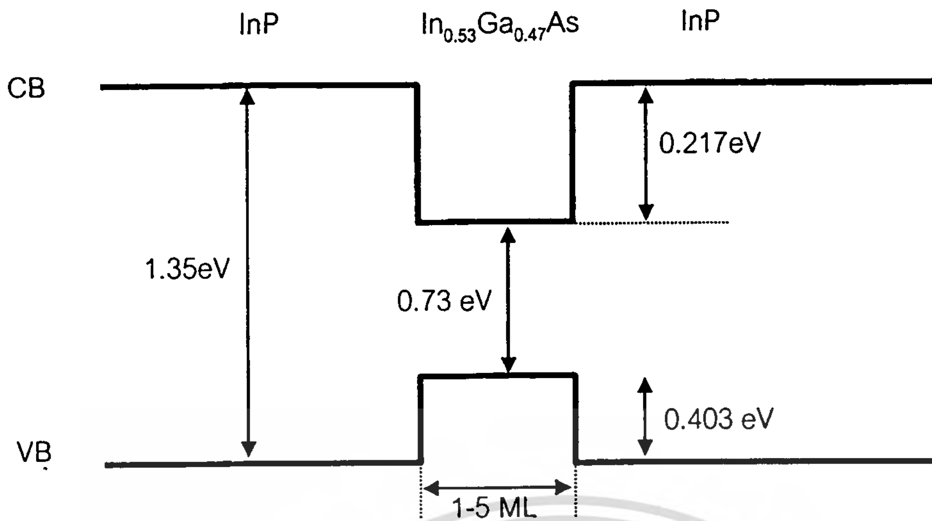

Fig 5.4 Schematic band diagram of $In_{0.53}Ga_{0.47}$ As/InP single quantum well.

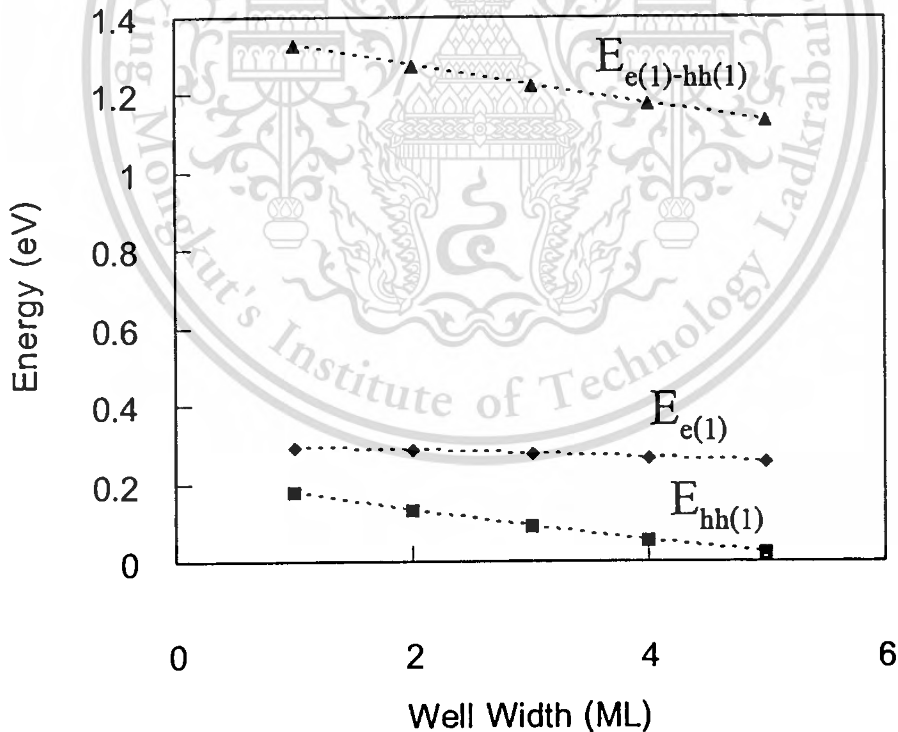

Fig. 5.5 The values of ground state energy level of heavy hole(E_{hh1}), electron (E_{e1}) and e(1)-hh(1) transition energy in $In_{0.53}Ga_{0.47}$ As/InP single quantum well as a function of the well width.

This material is reserved for educational use only, not allowed for commercial use.
Forbidden to modify the content, and cite the document when use.

Fig. 5.5 illustrates the values of ground state energy level of heavy hole(E_{hh1}), electron (E_{e1}) and e(1)-hh(1) transition energy in $In_{0.53}Ga_{0.47}$ As/InP single quantum well as a function of the well width from 1ML to 5 ML. In Fig. 5.6, the calculation results of e(1)-hh(1) transition energy are plotted by closed squares while the closed lozenges denote the transition energies obtained from the PL measurement. The calculation shows the higher values (about 70-90 meV) than the measured values. The origin of the difference may come from the imperfection at the interface between the extremely thin layer of InGaAs and InP barrier [6]. This influence will be discussed in section 5.4.

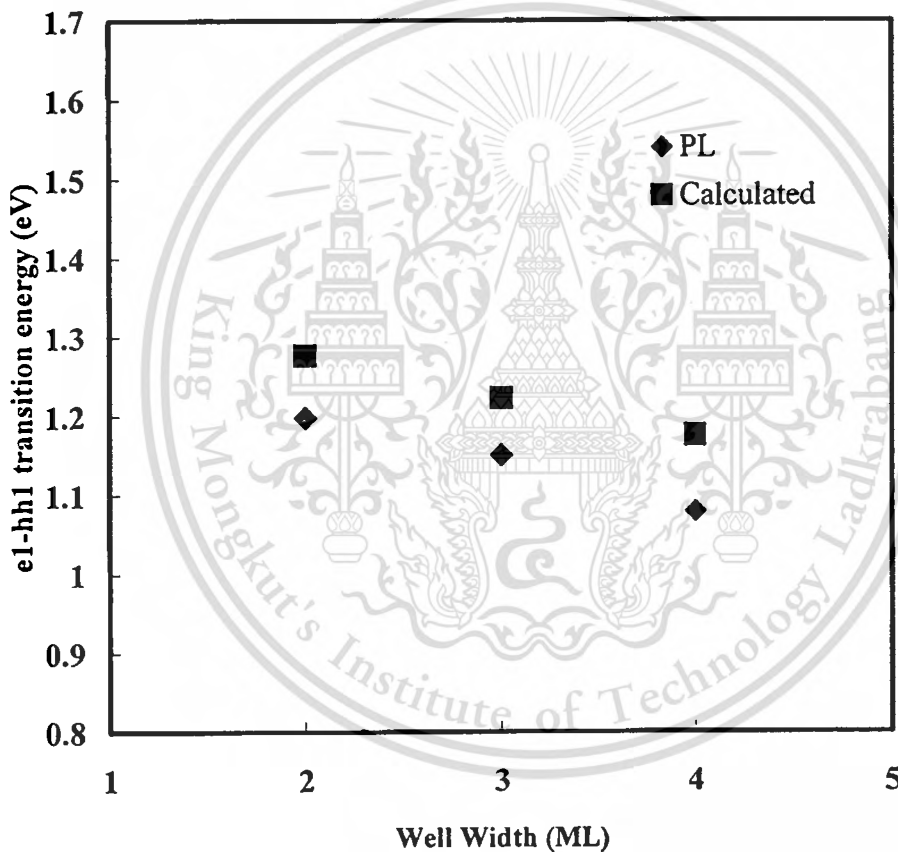

Fig. 5.6 Transition energy of e(1)-hh(1) in InP/InGaAs/InP SQWs as functions of well width. Closed squares present calculated values while the closed lozenges denote the transition energies obtained from the PL measurement.

Fig. 5.7 shows temperature-dependent PL of the sample with 3 ML well width. As temperature increases from 15 K to 200 K, PL spectra are weaker and exhibit the red shift, moving to the lower photon energy. The tendency of the shift is illustrated by a dashed line. The

This material is reserved for educational use only, not allowed for commercial use.
Forbidden to modify the content, and cite the document when use.

PL peak position versus measured temperature is illustrated in Fig. 5.8. The PL peak of about 1.152 eV at 15 K slightly shifts to lower energy of 1.138 eV at 200 K. The red shift of about 14 meV from 15 K to 200 K is probably caused by the decrease in the band-gap energy as the temperature increases[7]. It can be deduced that the luminescence of the extremely thin or small quantum structure is almost independent of the temperature [8].

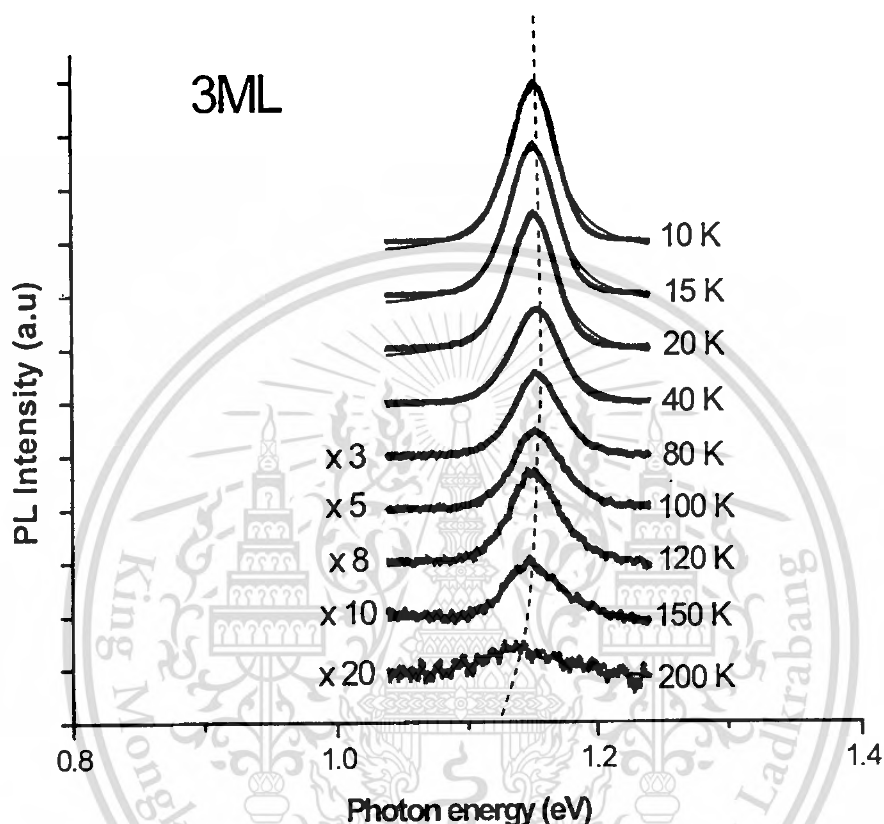

Fig. 5.7 PL spectra of 3-ML sample at different temperature.

Meanwhile, the PL intensity drop as temperature increases is due to the fact that when temperature increases, the photocarriers have more probability meet various types of defects and recombine non-radiatively on them[8] and the small binding energy of the exciton. At higher temperature, the thermal energy is significant comparing to the binding energy of the exciton, and the exciton-phonon interaction is considerable, reflecting in weaker and broader PL spectra[7].

This material is reserved for educational use only, not allowed for commercial use.
Forbidden to modify the content, and cite the document when use.

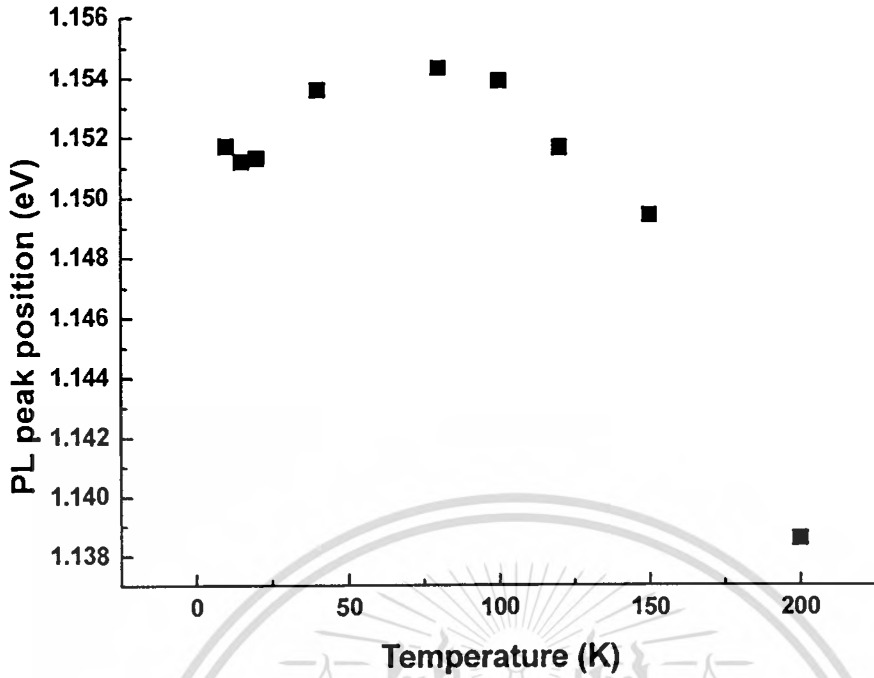

Fig. 5.8 PL peak position of 3-ML sample as a function of temperature.

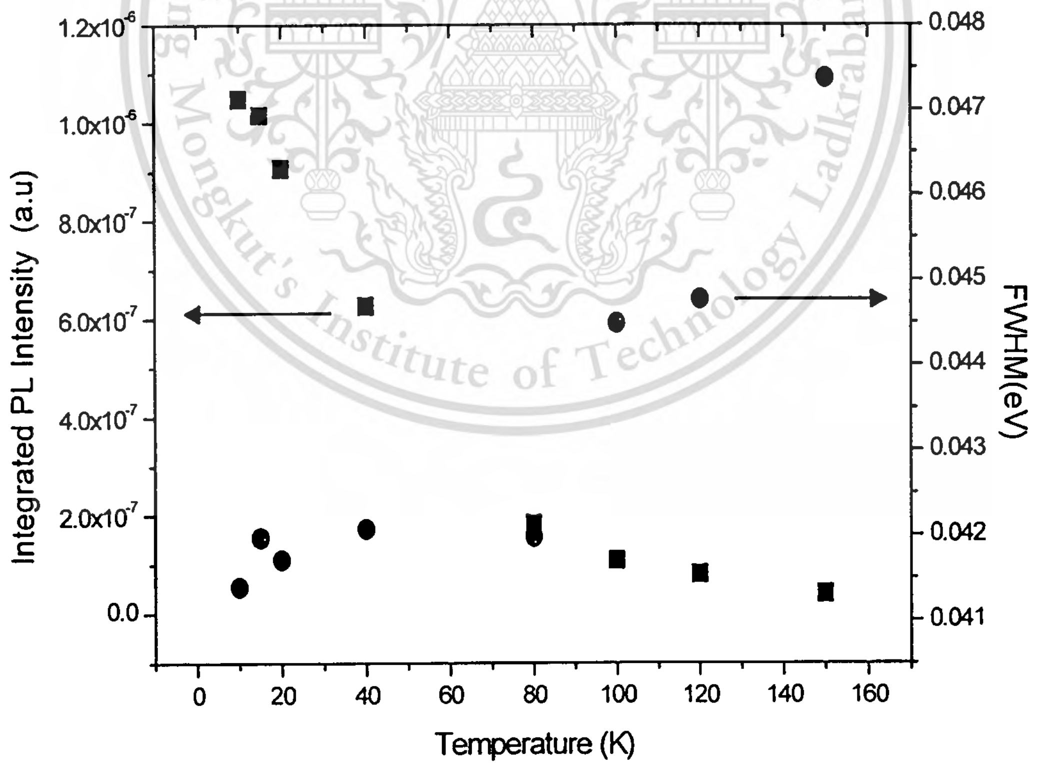

Fig. 5.9 Integrated PL Intensity and FWHM of PL peak of 3-ML sample.

This material is reserved for educational use only, not allowed for commercial use.
Forbidden to modify the content, and cite the document when use.

The effect of temperature on PL characteristics of 3-ML sample is thoroughly investigated. The integrated PL intensity shown by closed square and full width at half maximum (FWHM) of the PL peak shown by closed circle of 3-ML sample as a function of temperature is plotted in Fig. 5.9. As the temperature increases from 15 K to 80 K, The PL intensity rapidly decreases. Further increase in temperature from 80 K to 150 K causes insignificant decrease of PL intensity. Meanwhile, The FWHM of PL peak increases with increasing temperature, especially after 80 K. The temperature dependence of the integrated PL intensity of an exciton emission peak is expressed as following equation [9-10]

$$I_{PL}(T) = \frac{I_0}{1 + A\,exp(-E_A / k_B T)}. \tag{5.1}$$

Where I_0 is the integrated PL intensity near 0 K, A is a constant, E_A is the thermal activation energy which is responsible for the quenching of PL intensity in the temperature-independent PL spectra, T is the temperature, and k_B is Boltzmann constant.

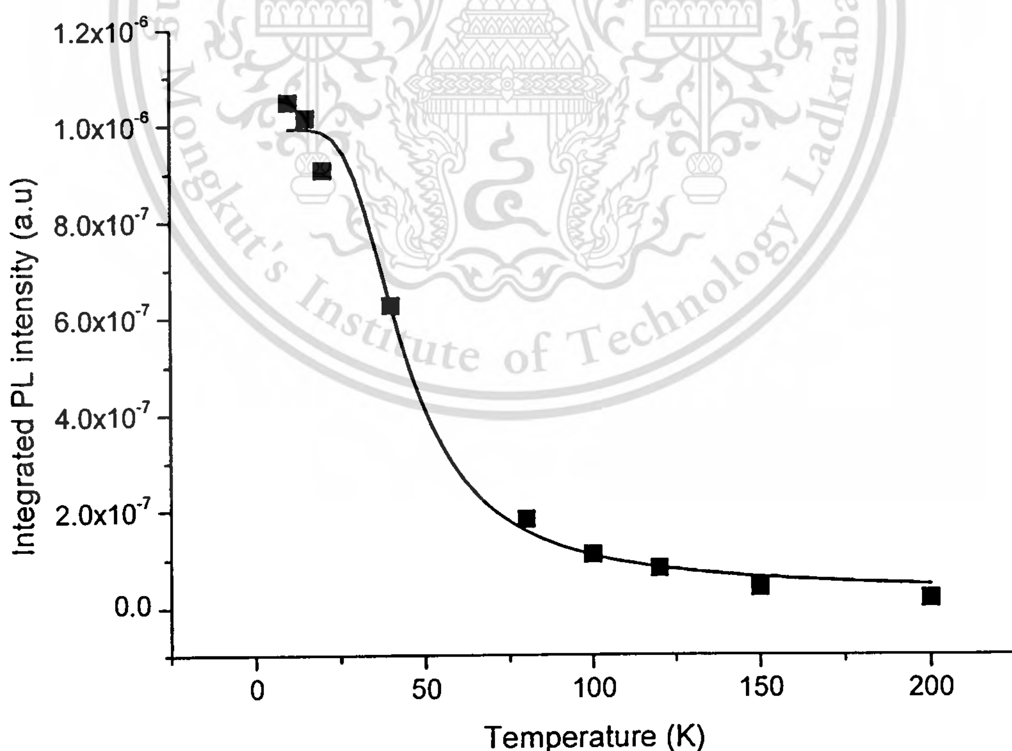

Fig. 5.10 Variation of Integrated PL intensity with temperature of 3-ML sample.

This material is reserved for educational use only, not allowed for commercial use.

Forbidden to modify the content, and cite the document when use.

Fig. 5.10 presents the integrated PL intensity of 3-ML sample. These measured values were fitted using equation (5.1) and shown by the solid line. The fitting curve obviously exhibits satisfactory consistence with the experimental data. From fitting curve, the thermal activation energy (E_A) of this structure of 15.1 meV is obtained. Normally, the temperature-induced quenching of luminescence in quantum well structure is caused by two mechanisms: thermal emission of charge carriers out of confined states in the well into barrier states [11] and thermal dissociation of excitons into free-electron-hole pairs [7]. Because of very narrow well width, the subband energy of electron in conduction band and hole in valence band are closed to the top of the well. The confined carriers can easily escape from the quantum wells. Therefore the first quenching mechanism dominates and the small thermal activation energy can be regarded as the delocalization energy of carriers in the well[7].

The temperature-dependent broadening of PL spectra of this structure is also investigated. Typically, the broadening of the PL spectra in quantum well structure can be summarized as the sum of two components: a temperature-independent inhomogeneous broadening due to interface roughness, fluctuations in binding energies alloy fluctuations (Γ_{in}), and the temperature-dependent homogeneous broadening which typically due to electron-optical phonon or exciton-phonon interactions, Γ_{hom}, which is given by the following expression[12],

$$\Gamma_{hom} = \frac{\Gamma_{LO}}{exp\left(\frac{E_{LO}}{k_B T}\right) + 1} . \qquad (5.2)$$

Note that, Γ_{LO} is the electron-phonon or exciton-LO-phonon coupling constant and E_{LO} is the optical phonon energy. Therefore the total broadening is the summation of inhomogeneous broadening and homogeneous broadening due to the electron-phonon interaction,

$$\Gamma_{total}(T) = \Gamma_{in} + \Gamma_{hom}(T) . \qquad (5.3)$$

This material is reserved for educational use only, not allowed for commercial use.
Forbidden to modify the content, and cite the document when use.

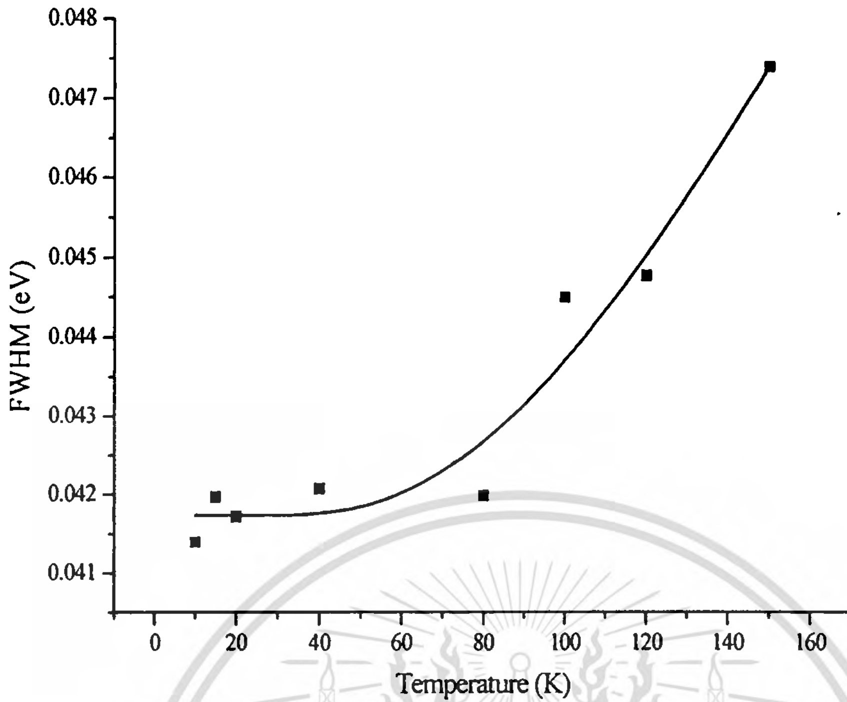

Fig. 5.11 FWHM of PL spectra of 3-ML sample as a function of temperature.

Fig 5.11 shows the FWHM of PL spectra from the sample with 3-ML well width as a function of temperature. The solid line is the fitting curve to the measured point using equations (5.2) and (5.3). It agrees well with the experimental data. The corresponded parameters extracted from the curve fitting are obtained as follows, Γ_{LO} =32.0 meV, E_{LO} = 24.5 meV, and Γ_{in} = 42.7 meV. Fitting data reveals that inhomogeneous broadening mechanism is the dominant mechanism responsible to the broadening of PL spectrum of this structure. The inhomogeneous broadening which is independent to temperature depends on several mechanisms such as well width fluctuation, donor-to-acceptor recombination and local fluctuation in the strain[12].

This material is reserved for educational use only, not allowed for commercial use.
Forbidden to modify the content, and cite the document when use.

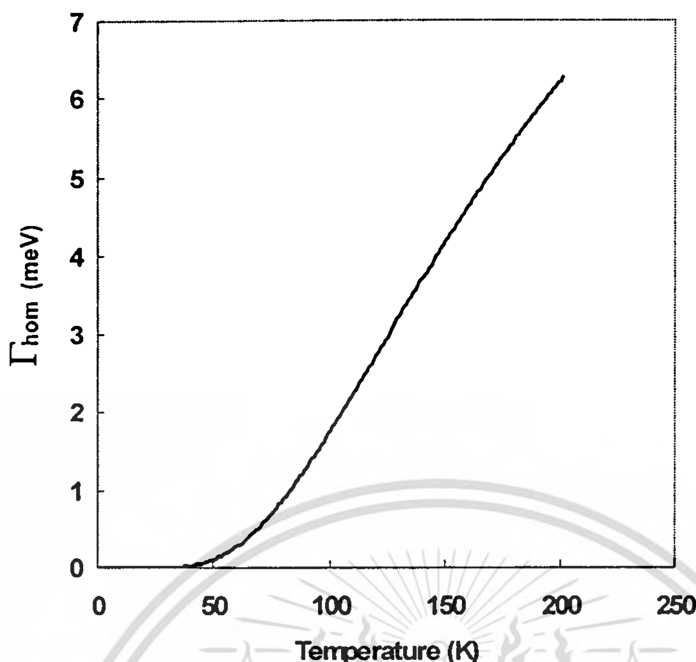

Fig. 5.12 The homogeneous broadening of $In_{0.53}Ga_{0.47}As/InP$ SQW as a function of temperature.

For this quantum structure of very narrow well, the well width fluctuation should dominates and the local fluctuation in the strain is neglected due to lattice matching between InP and $In_{0.53}Ga_{0.47}As$. The second part of broadening of PL spectrum is homogeneous broadening which is temperature-dependent mechanism. Fig 5.12 shows the homogeneous broadening of $In_{0.53}Ga_{0.47}As/InP$ SQW as a function of temperature. The homogeneous broadening is negligible at low temperature (<40 K). At higher temperature, its value increase drastically from 0 meV to 4 meV with increasing temperature from 40 K to 150 K. At low temperature, the carriers are trapped in the well resulting in minimum variations of the binding energies of the carriers and the inhomogeneous broadening mechanism dominates. At elevated temperatures, the electron-phonon interaction becomes the dominant broadening mechanism and the FWHM consequently increases with increasing temperature.

This material is reserved for educational use only, not allowed for commercial use.
Forbidden to modify the content, and cite the document when use.

5.4 Gas Source Supply Interruption Effect During Growth on Quantum Well Structure of Narrow-Well Width $In_{0.53}Ga_{0.47}As$/Inp SQWs

From the previous part, the PL characteristic of this structure reveals the influence of well width fluctuation on the broadening of PL emission peak. This fluctuation may occur during growth process. Fig. 5.1 shows the flow sequence of gas source supply into the reactor to grow the samples. Considering the gas source interruption process at the interface, the gas source TMIn and TMGa was stopped for 2 seconds, and PH_3 was subsequently allowed to flow into the reactor for 0.5 second before TMIn flow. K. Hosomi *et.al* [3] studied effect of source supply interruption (SSI) time at the InGaAs to InP interface by photoluminescence spectroscopy. They found that the SSI effect was noticeable if the interruption time ranged from 0 to 12 seconds. Based on this fact, the compound of extremely thin (1monolayer) In(Ga)AsP transition layer at the InGaAs-to-InP interface can be formed. The change in the As compostion depends on the SSI time. This formation consequently affects shape of the well as asymmetric stepped finite rectangular well. The well width of this stepped well is therefore widened to 2-6 ML, including 1 ML of InGaAsP.

Fig. 5.13 shows the SSI dependent–band diagram profile of InP/InGaAs/InGaAsP/InP stepped quantum well. The energy of InP and $In_{0.53}Ga_{0.47}As$ are 1.35 eV and 0.73 eV respectively [5]. The effective mass of electron (m_e^*) and hole (m_{hh}^*) for InGaAs are $0.0416m_0$ and $0.46m_0$ respectively. The energy gap of InGaAsP is 0.83 eV [13]. The band discontinuity for conduction band ,ΔE_c, and valence band ,ΔE_v, are 0.217 eV and 0.403 eV respectively [5]. In order to calculate the e(1) and hh(1) energy level of this quantum well, we assume that the well shape is firstly a finite rectangular well with well width of 2-6 ML, i.e., 0.6-1.8 nm. Solving Schrödinger equations numerically yields the non-perturbed e(1) and hh(1) energy levels in the well and also the intersubband transition energy. After that we employed perturbation theory as mention in section 2.6.5, taking the stepped potential of In(Ga)AsP into account. The perturbed potential (V_p) is expressed in equation (5.4),

$$V_p = E_a \qquad a-d < x < a\,, \tag{5.4}$$

where a is half of well width, d is the length of 1 ML (3 nm) and E_a is the height of the stepped potential. The first order perturbed energy (ΔE) of the stepped well can be obtained from equation (5.5),

This material is reserved for educational use only, not allowed for commercial use.
Forbidden to modify the content, and cite the document when use.

$$\Delta E = \left\langle \psi_1^0 \middle| V_P \middle| \psi_1^0 \right\rangle , \tag{5.5}$$

where ψ_1^0 is either non-perturbed e(1) or hh(1) wave function. Solving equation (5.5) and applying all boundary conditions yields the solution for ΔE,

$$\Delta E = E_a A^2 \left[\frac{1}{4q} \left(\sin 2qa - \sin 2q(a-d) \right) \right] + \frac{E_a A^2 d}{2} . \tag{5.6}$$

A is the amplitude of the ground state wave function which is expressed as,

$$A = \left[\frac{2kq}{q \cos 2qa + k \sin 2qa + q + 2kqa} \right]^{\frac{1}{2}} . \tag{5.7}$$

q and k are the wave number in the well and out of the well respectively,

$$q = \sqrt{\frac{2m^* E_1^0}{\hbar^2}} \text{, and } k = \sqrt{\frac{2m^* \left(V - E_1^0\right)}{\hbar^2}} , \tag{5.8}$$

where m^* is the effective mass, E_1^0 is either non-perturbed e(1) or hh(1) energy value, and V is the potential difference between well and barrier.

King Mongkut's Institute of Technology Ladkrabang

This material is reserved for educational use only, not allowed for commercial use.
Forbidden to modify the content, and cite the document when use.

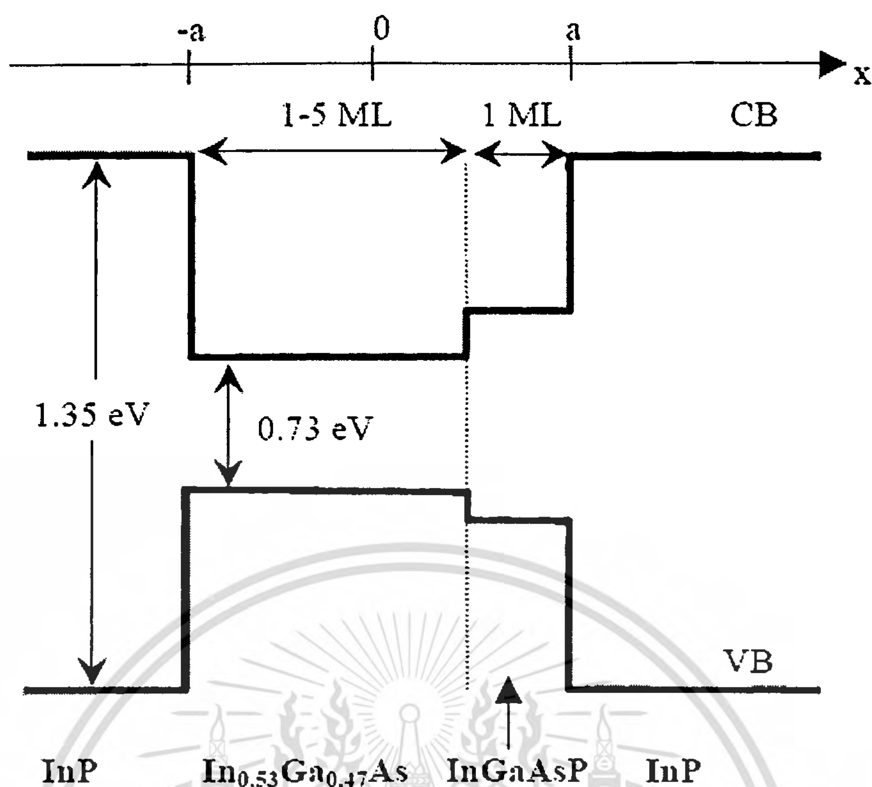

Fig. 5.13 Band diagram of InP/InGaAs/In(Ga)AsP/InP stepped quantum well. 1 ML is approximately equal to 0.3 nm.

The experimental data of e(1)-hh(1) transition energy as a function of well width is already shown in Fig. 5.6. In order to verify the formation of 1ML In(Ga)AsP at the InGaAs-to-InP interface, we have also made a simple calculation for quantum level in the finite rectangular well of InP/InGaAs/InP by solving one-dimensional Schrödinger equation. The resultant energies of finite rectangular well are compared to these energies of stepped quantum well affected by SSI. These comparison is plotted together with experimental data and shown in Fig. 5.14. In Fig. 5.14, the calculation results without SSI effect and with SSI effect are plotted by closed squares and opened triangles respectively, while the closed lozenges denote the transition energies determined from the PL measurement. The calculated values without SSI effects show significant difference about 70-90 meV above the measured values. When the calculation is involved by SSI effect, the calculated values are in good agreement with the experiment values. However, there are approximately 30-meV discrepancy between calculated values with SSI effect and measured values for 2 ML and 3 ML samples. The origin of the differences may come from the

This material is reserved for educational use only, not allowed for commercial use.
Forbidden to modify the content, and cite the document when use.

imperfection of the interface between each species. Another possible candidate for the discrepancy are the uncertainty of the roughness of the potential barrier height of InGaAsP [6].

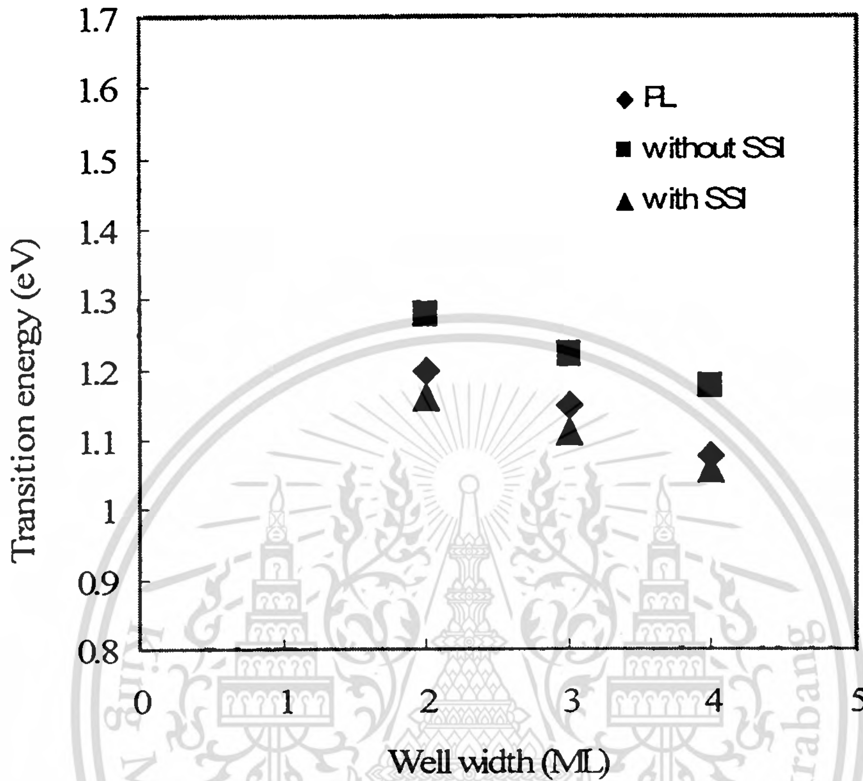

Fig. 5.14 The e(1)-hh(1) transition energies with different well widths. Closed squares and closed triangles show the calculated values without SSI effect and with SSI effect respectively. Closed lozenges denote the PL results.

This material is reserved for educational use only, not allowed for commercial use.
Forbidden to modify the content, and cite the document when use.

5.5 Summary

In summary, the photoluminescence of very thin $In_{0.53}Ga_{0.47}As/InP$ SQWs grown by OMVPE was conducted. The PL peaks reveal the luminescence from the recombination between e(1)-hh(1) in quantum wells. The photon energy of PL peak increases dramatically as the well width decreases by only few monolayers and has such good agreement to calculated results. The temperature-dependence of The PL spectra was investigated. As temperature increase, PL emission peaks become broader, weaker, and exhibit significant redshift. The thermal activation energy that affects PL intensity quenching of this structure is obtained from the plot of integrated PL intensity versus temperature. Due to small thermal activation energy in the narrow well, carriers can easily escape from the well to the barrier states resulting in the PL intensity quenching at low temperature. The broadening of PL emission peak is analyzed in terms of homogeneous and inhomogeneous broadening mechanisms. It is revealed that Inhomogeneous mechanism is the dominant mechanism for the broadening of PL peak and homogeneous mechanism has significant role at high temperature due to electron-phonon interaction. The mathematical model of few monolayer $InP/In_{0.53}Ga_{0.47}As/InP$ SQWs grown by OMVPE taking the influence of source supply interruption into account is proposed. In the model, The 1-ML potential barrier of InGaAsP is formed at the InGaAs-to- InP interface, widening the well and causing asymmetric stepped well. The theoretical prediction with SSI shows better agreement with experimental data than the prediction without SSI.

This material is reserved for educational use only, not allowed for commercial use.
Forbidden to modify the content, and cite the document when use.

References

[1] A.J. Moseley, D.J. Robbins, A.C. Marshall, M.Q. Kearney, J.I. Davies, **"Quantum confined Stark effect in InGaAs/InP single quantum wells investigated by photocurrent spectroscopy"**, Semiconductor Science and Technology,Vol. 4, No. 3, pp 184-190, 1989.

[2] J. Borgulova, B. Rheinglander, J. Kovae, F. Uherek, V. Gottschalch, G. Wagner, S. Nassauer, G. Benndorf, M. Gerhardt, J. Skriniarova, J. Jakabovie, **"Optics of excitons in InGaAs/InP quantum wells"**, Proceeding of IEEE International Conference on Indium Phosphide and Related Materials, pp. 515 –518,1999.

[3] K. Hosomi, T. Mozume, H. Kashima, K. Oushi, **"Photoluminescence investigation of InGaAs/InP quantum wells grown by gas-source molecular-beam epitaxy with source-supply interruption"** , Proceedings of IEEE International Conference on Indium Phosphide and Related Materials, pp. 109-112, 1995.

[4] Y.J. Han, L.W. Guo, C.L. Bao, Q. Huang, J.M. Zhou, **"Effects of As pressure on optical features of low-temperature grown GaAs/AlGaAs multiple quantum wells"**, Journal of Crystal Growth, Vol. 236, pp. 90-94, 2002.

[5] J. Nukeaw, R. Asaoka, Y. Fujiwara, Y. Takeda, **"Photoreflectance study of InP/InGaAs (1-5 ML)/InP single quantum well"**, Thin Solid Films, Vol. 334, pp. 44-48, 1998.

[6] J. Boherer, A. Krost, D. Bimberg, **"InAsP islands at the low interface of InGaAs/InP quantum wells grown by metalorganic chemical vapor deposition"**, Applied Physics Letters, Vol. 60, pp. 2258-2260, 1992.

[7] Y.T. Shih, Y.L. Tsai, C.T. Yuan, C.Y. Chen, C.S. Yang, W.C. Chou, **"Photoluminescence of $ZnSe_xTe_{1-x}/ZnSe$ multiple-quantum-well structures grown by molecular-beam epitaxy"**, Journal of Applied Physics, Vol. 96, No. 12, pp. 7267-7271, 2004.

[8] B. lambert, A. Le Corre. V. Drouot, H.L. Haridon, S. Loualiche, **"High photoluminescence efficiency of InAs/InP self-assembled quantum dots emitting at 1.5-1.6 μm"**, Semiconductor Science and Technology,Vol. 13, No 1, pp. 143-145, 1998.

[9] M. Furis, A. N. Cartwright, J. Hwang, and W.J. Schaff, **"Time resoloved photoluminescence of Si-doped high Al mole fraction AlGaN epilayers grown by plasma-enhanced molecular beam epitaxy"**, Material Research Society Symposium 2004, Vol. 798, 2004.

This material is reserved for educational use only, not allowed for commercial use.
Forbidden to modify the content, and cite the document when use.

[10] Y.A. Chang, J.R. Chen, H.C. Kuo, Y.K. Kuo, and S.C. Wang, **"Theoretical and experimental analysis on InAlGaAs/AlGaAs active region of 850-nm vertical-cavity surface-emitting lasers"**, Journal of Light Wave Technology, Vol. 24, No. 1, pp. 536-543, Jan. 2006.

[11] S. Weber, W. Limmer, K. Thonke, R. Sauer, K. Panzlaff, G. Bacher, H.P. Meier, and P. Roentgen, **"Thermal carrier emission from a semiconductor quantum well"**, Physical Review B, Vol. 52, pp. 14739-14747, 1995.

[12] M. Furis, A.N. Cartwright, H. Wu, and W.J. Schaff, **"Emission mechanisms inUV emitting GaN/AlN multiple quantum well structure"**, Material Research Society Symposium 2004, Vol. 798, 2004.

[13] S. Adachi, **Physical properties of III-V semiconductor compounds**, New York: John Wiley & Sons, Inc.,1992.

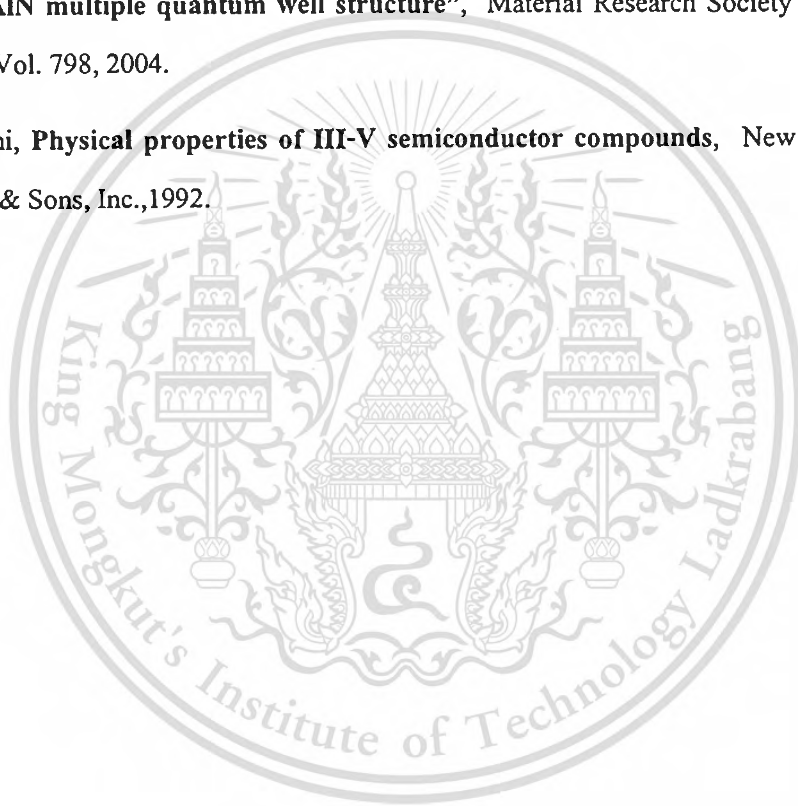
King Mongkut's Institute of Technology Ladkrabang

This material is reserved for educational use only, not allowed for commercial use.
Forbidden to modify the content, and cite the document when use.

CHAPTER 6

PHOTOCURRENT OF ERBIUM DELTA-DOPED InP STRUCTURE

6.1 Literature Review

Over the past few years, interest in Erbium (Er) doped III-V compound semiconductors have been considerably increased after good quality samples between rare-earth (RE) element and group V element on group III-V semiconductor by epitaxy growth were achieved. III-V compounds themselves have broad applicability to various optoelectronic devices. By doping rare earth element such as Erbium, new function of RE-V on III-V compounds can be obtained. This new structure has a great potential not only for novel electronic devices such as resonant tunneling devices[1] but also in optical communication systems operating in the vicinity of 1.5 μm wavelength. When Er^{3+} was delta-doped (δ-doped) on InP, Er atom formed rocksalt ErP with a lattice constant of 0.5595 nm[2]. The distribution of Er atoms at the δ-doped layers and structure of ErP were monitored by X-ray crystal truncation rod (CTR) scattering[3]. The trap states in Er-doped InP were also observed by the technique of photoreflectance[4]. The transition of bandgap of InP from 1.35 to 1.31 eV is involved by an Er trap. However, in our knowledge, few researches on fundamental physical properties using optical characterization of Er doped III-V compounds were reported.

Photocurrent spectroscopy (PC) has been applied extensively in order to study transition phenomena in quantum structure semiconductor. Photocurrent is a fast and comparatively simple technique without any modulations. Photocurrent spectra can also observe the photoabsorption lineshape when carrier escape from the quantum well[5]. This technique was employed to investigate the excitonic transitions in $In_xGa_{1-x}As/In_yAl_{1-y}As$ multiple quantum wells with and without applied electric field [5]. The results for the PC data at 300 K for several applied electric fields displayed that many excitonic transitions shifted to longer wavelengths as the applied electric increased. The PC spectra at room temperature of InGaAlAs/InP type-II superlattice were carried out [6]. These spectra exhibited the quantum confined Stark effect (QCSE) of interband transition energies under various voltages. This technique was employed to observe the transition energies in a GaAs/AlAs coupled quantum well structure under applied electric field at room

This material is reserved for educational use only, not allowed for commercial use.
Forbidden to modify the content, and cite the document when use.

temperature. The results of field induced decoupling effect showed a large change in the absorption coefficient and refractive index[7]. PC study of InAs/GaAs self-assembled quantum dots was carried out [8]. Under an applied electric field an asymmetry of the quantum confined Stark effect is observed, implying that the dots possess a permanent dipole moment.

In this chapter, the room-temperature PC spectroscopy was conducted in order to investigate the formation of ErP quantum structure by Er δ-doping on InP. We also observed QCSE when samples were biased.

6.2 Sample Structure

The structure of Er δ-doped InP is schematically illustrated in Fig. 6.1. All samples were grown by Organometallic Vapor Phase Epitaxy (OMVPE) with a vertical quartz reactor at 0.1 atm. TMIn (trimethylindium), TBP (tertiarybutylphosphine) and $Er(MeCp)_3$ (tri(methylcyclopentadienyl)erbium) were used as source materials. All samples were grown at Department of Material Science and Engineering, Nagoya University, Japan.

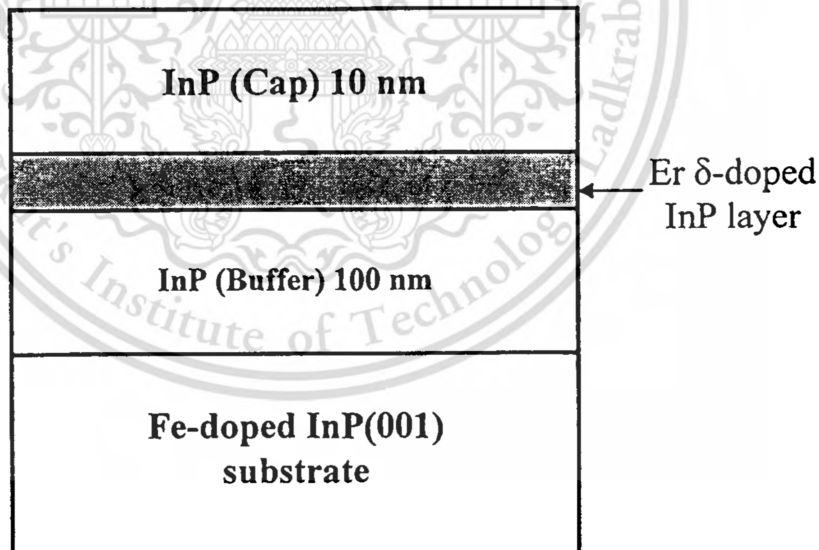

Fig 6.1 Sample structure of Er δ- doped InP.

This material is reserved for educational use only, not allowed for commercial use.
Forbidden to modify the content, and cite the document when use.

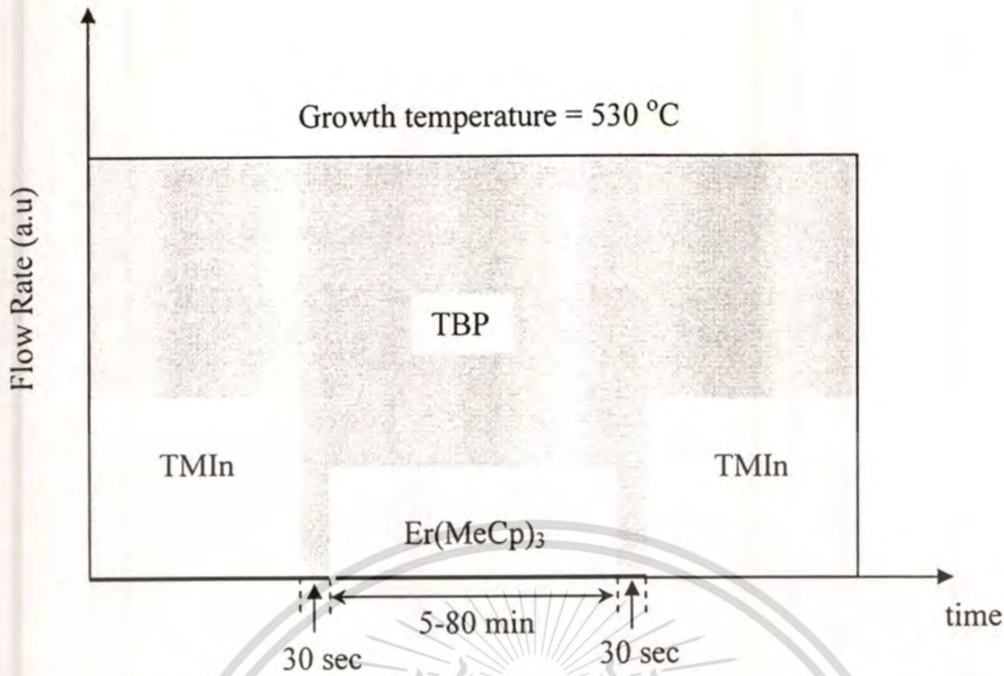

Fig. 6.2 The time sequence of source gases to grow a Er δ-doped InP.

The time sequence of source gases to grow the Er δ-doped InP is shown in Fig. 6.2. A 100 nm undoped InP buffer layer was grown on a Fe-doped InP (001) substrate at substrate temperature of 530 °C. TMIn was then stopped to suspend the growth of the InP. Er^{3+} from $Er(MeCp)_3$ was subsequently supplied to form an atomic plane of Er on the substrate. Its coverage was controlled by varying Er-exposure durations from 5 to 80 minutes. After the Er source was stopped, a 10 nm undoped InP cap layer was grown.

A conventional photocurrent spectroscopy was conducted in a standard scheme using tungsten lamp chopped at 400 Hz for excitation source. The PC signal was detected using typical lock-in amplifier. All photocurrents were measured at room temperature.

6.3 Results and Discussion

Room-temperature PC of Er δ-doped InP with 10 min and 80 min Er exposure duration were measured and compared to undoped InP. Photon energies varied by monochromator ranged from 0.8 to 1.1 eV. Fig. 6.3 shows the PC signal of undoped InP and Er δ-doped InP with 80 min Er exposure duration. Three obvious peaks with corresponding photon energies of 0.868, 0.927, and 1.033 eV labeled as (1), (2) and (3), respectively, are only observed in the doped

This material is reserved for educational use only, not allowed for commercial use.
Forbidden to modify the content, and cite the document when use.

sample. These features should be related to Er-doping because it is not been observed so far in the undoped InP specimen.

6.3.1 Quantum Island Model

In the previous work, the formation of flat ErP islands with size of 200-500 nm and height of 1-4 nm had been reported[9]. The well defined PC spectra of the doped sample therefore ensure a high-quality formation of ErP layer on InP by using this growth technique. L. Bolotov *et al.*[1] reported a semimetal behavior for ErP islands with thickness larger than 3.4 nm while a semiconducting gap varying up to 1 eV was revealed for the islands thinner than 3.4 nm. Because the energy gap of ErP islands depend on the their thickness, the PC spectra of doped sample, in the range of 0.8-1.1 eV, should arise from interband transitions between the confined electron and hole states [8,10].

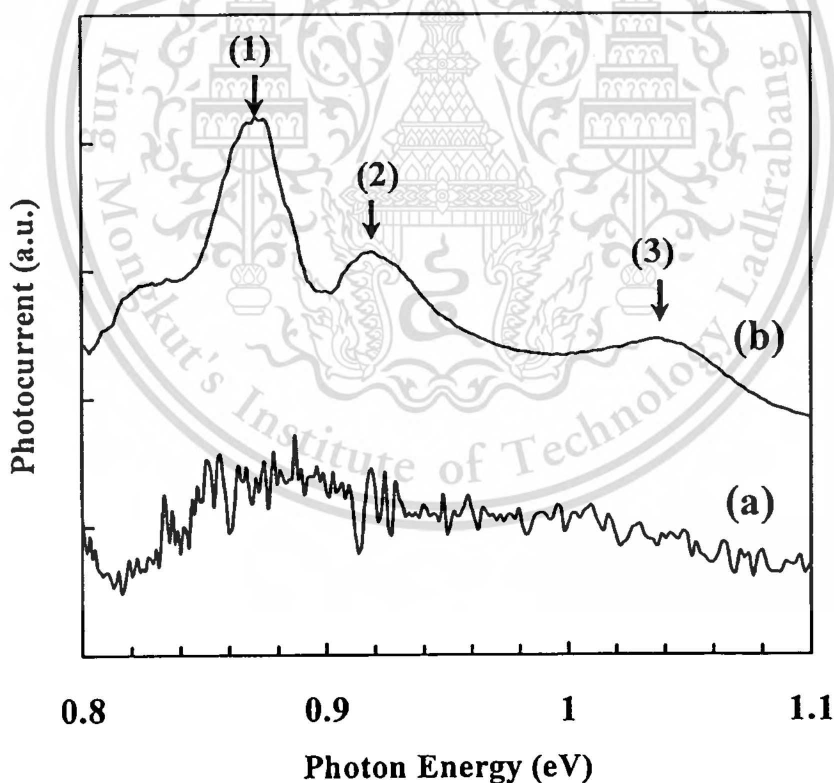

Fig. 6.3 Room temperature photocurrent of (a) undoped InP and (b) Er δ-doped InP at 80 minutes erbium exposure duration.

This material is reserved for educational use only, not allowed for commercial use.
Forbidden to modify the content, and cite the document when use.

A comparison of PC spectra of Er δ-doped InP with 10 min and 80 min Er exposure duration is illustrated in Fig. 6.4. Both signal are smooth and in the same trend. These manners imply that the thickness of ErP islands does not change considerably with increasing Er exposure time. In addition, the spectra of the 80 min Er-exposure time sample are comparably sharper than the spectra of the 10 min Er-exposure time specimen. The influence of Er-exposure time on ErP occupation sites on InP were studied[3]. It was found that, when the specimens were exposed to Er source for more than 10 min, the ErP layer was formed and the total number of incorporated Er atoms increased exponentially with increasing exposure time. The total amounts of ErP islands therefore increase with increasing Er exposure time, reflected in the sharper of the PC spectra.

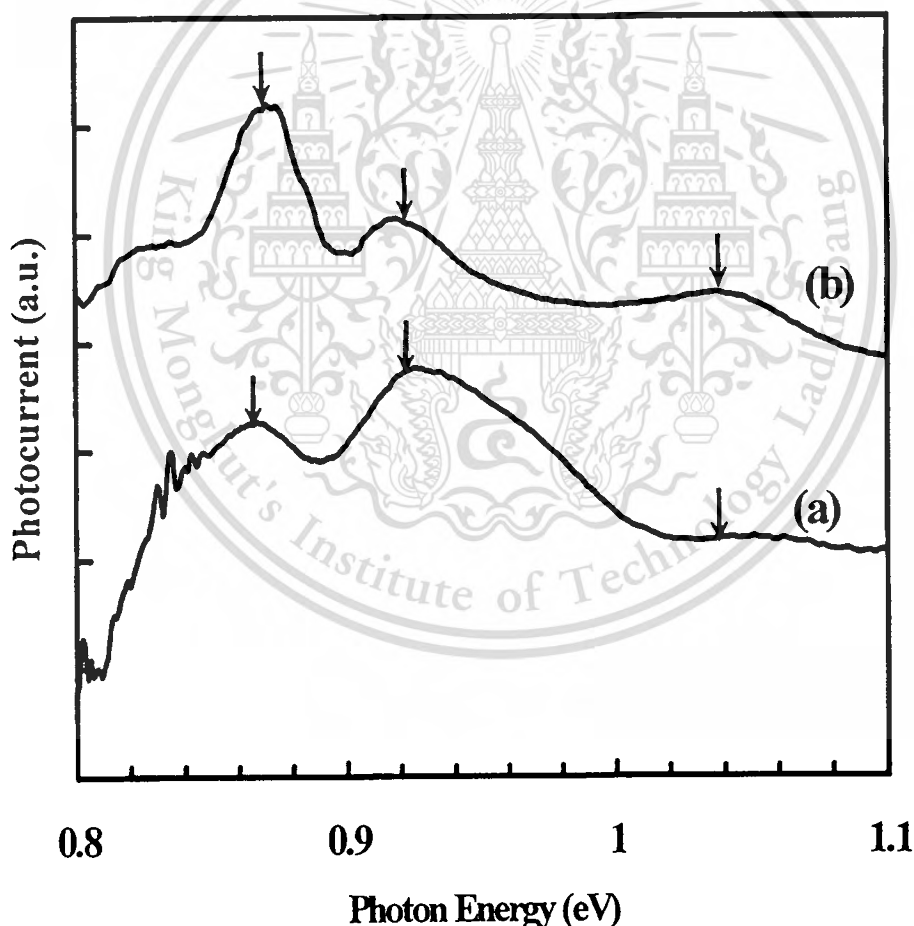

Fig. 6.4 Room temperature photocurrent spectra of Er δ-doped InP of (a) 10 min Er exposure time and (b) 80 min Er exposure time.

This material is reserved for educational use only, not allowed for commercial use.
Forbidden to modify the content, and cite the document when use.

6.3.2 Quantum Well Model

From Fig. 6.3, comparing to undoped sample, PC spectra of doped samples exhibit three extinct peaks with photon energy of 0.86, 0.92 and 1.04 eV respectively. At this point, It can be deduced that these manners should be affected by Er doping. It was reported that the Er atoms in the InP were considered to form the rocksalt structure ErP when InP were exposed to Er atmosphere for more than 10 minutes [1]. The other model is proposed. Because of the formation of ErP between InP buffer and cap, single quantum well (SQW) of ErP/InP could be aligned if the number of ErP islands are large enough to form ErP layer. These three PC peaks extracting from PC measurement should correspond to the transition energies in the well. The sharpest peak with photon energy of 0.86 eV should relate to the transition of the ground state and the other peaks should be the transition energies of the higher subbands. In order to obtain the values of transition energies, mathematical models is developed using with both finite rectangular quantum well (RQW) and parabolic quantum well (PQW) based on reasonable assumptions. Important parameters for the calculation were discussed. Because these three interband energies are smaller than both bandgap of InP (1.35 eV) and bandgap of ErP (1.24eV) [11], the ErP/InP should be type-II quantum well. This assumption also coincides to band diagram of delta-doped semiconductor whose alignment at doped layer is a type –II like quantum well.

For RQW, the well width, which is the thickness of ErP layer, is considered. It was reported that the ErP layer thickness at full width of half maximum of X-ray CTR result was approximately 8 monolayers (ML). This averaged value is used as well width for RQW. First three subband energy levels in a ErP/InP SQW and the interband transition energies are achieved by solving Schrodinger equation explicitly. The equation of SQW of conduction band is written as

$$\frac{\hbar^2}{2m_e^*}\frac{d^2\psi}{dz^2}+V\psi=E\psi \tag{6.1}$$

where m_e^* is an effective mass of electron in conduction band. Potential V due to the bandedge discontinuity equals to $-\Delta E_c$ in the region $-a//2 < z < a/2$ and equals to zero elsewhere. By matching the wave function and its derivative at the boundaries of the well, it can be shown that the subband energy levels are given by the solution to the transcendental equations

This material is reserved for educational use only, not allowed for commercial use.
Forbidden to modify the content, and cite the document when use.

$$\frac{k}{q} = \tan qa \quad \text{for even parity}, \quad \text{and} -\frac{k}{q} = \cot qa \quad \text{for odd parity} \qquad (6.2)$$

where $k^2 = -\frac{2m_e^* E}{\hbar^2}$ and $q^2 = \frac{2m_e^*(E+V)}{\hbar^2}$. These equations can be solved numerically to obtain the Eigenvalues E. For valence band the equations are also solved and the corresponding levels are continuum since holes are in a finite potential barrier caused by bandedge discontinuity. The energy gap of InP and ErP are 1.35 eV and 1.24 eV[1,11] respectively. The well width which is designated by the distribution of $ErP^{2.3}$ is taken to be 2.4 nm (8 ML) for both samples. The effective mass of electron and hole are $1.71m_0$ and $0.14m_0$ respectively[1,11]. The band discontinuity and band offset have to be determined. There is unfortunately no report of the band offset of ErP/InP structure. However, this information can be obtained from fitting optical data and the acceptable band offset is revised to be around 60:40[12]. In this calculation, the band offset at the best fit is 56:44 which is closed to conventional value.

Solving Schrödinger equation of RQW of conduction band gave three valid subbands of 0.47 eV, 0.40 eV and 0.27 eV below the welledge. The energy level of valence band were found continuously because holes were in the finite barrier caused by type-II quantum well. The interband transition energies which are the difference between valence bandedge of InP and each subband levels in the well are therefore 0.86 eV, 0.95 eV and 1.08 eV respectively. This simple model shows the well-agreed results to the PC peaks in Fig. 6.3. However small shift from the calculated values and the broadening of all spectra may be caused by temperature induced effect. and phonon scattering[13].

For PQW, we take the local distribution ErP layers and the quantum sized effects into account. The width (W_p) at the top of PQW was considered by the profile of CTR results. This value is in the vicinity of 22 ML (6.6 nm). The other parameters used in calculation were the same values as used in RQW. The calculation method is similar to E.P. Sinyavskii et al [14]. The subband in the well of conduction band are determined by the expression.

This material is reserved for educational use only, not allowed for commercial use.
Forbidden to modify the content, and cite the document when use.

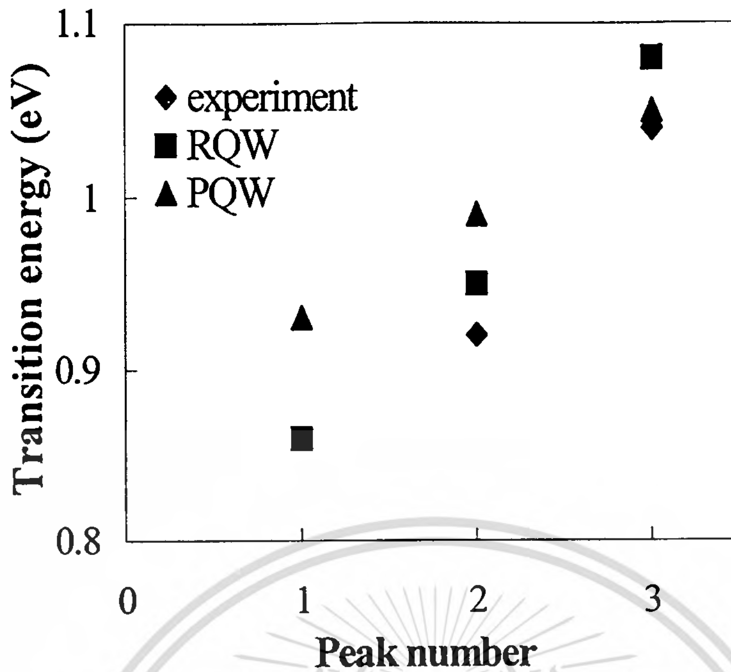

Fig. 6.5 The comparison of transition energies obtained by using RQW model, PQW model and PC measurement.

$$E_n = \frac{\hbar}{w_p}\left(\frac{8\Delta E_C}{m_e^*}\right)^{\frac{1}{2}}\left(n+\frac{1}{2}\right), \tag{6.3}$$

where ΔE_c is the conduction band discontinuity and m_e^* is the electron effective mass. The first three subbands in the PQW have their transition energies of 0.93 eV, 0.99 eV and 1.05 eV respectively. First two calculated values are 70 meV and 50 meV higher than the experimental data but the third value is well-agreed to the experiment. The transition energies using RQW model and PQW model are compared to experimental data and shown in Fig. 6.5.

This material is reserved for educational use only, not allowed for commercial use.
Forbidden to modify the content, and cite the document when use.

6.3.3 Quantum Confined Stark Effects

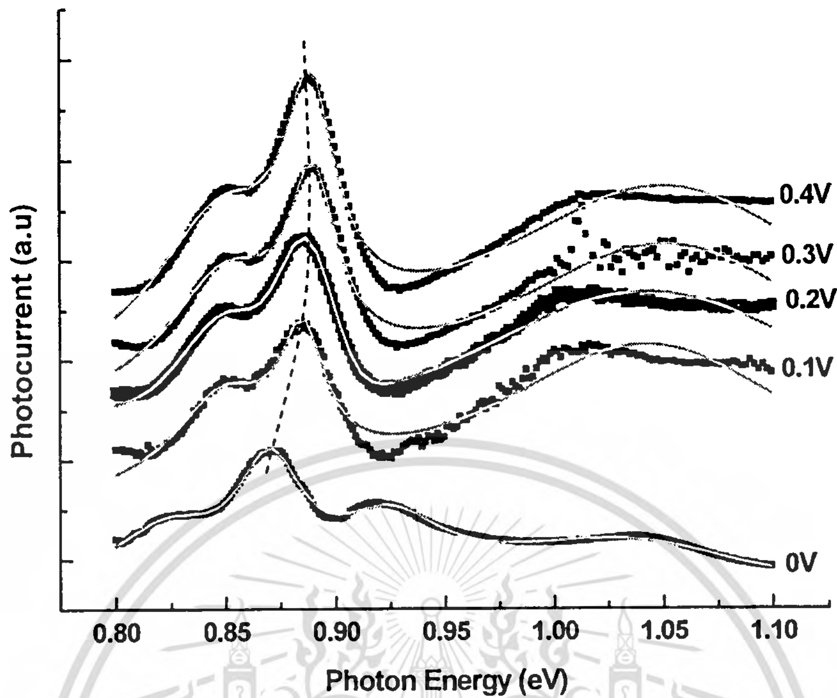

Fig. 6.6 Room temperature PC of Er δ-doped InP at 80 min exposure duration under bias voltages. The solid lines represent the best fitting curve of each spectrum.

Fig. 6.6 exhibits the PC spectra of the Er δ-doped InP with 80 minutes exposure duration time under several bias voltages. The PC signal at various bias voltage was fitted so that the peak position and the peak shift due to external electric field were obtained. The best fitted curves are shown by the solid lines. Comparing to the signal of the sample without bias voltage, the dominant peaks clearly show a significant shift because of applied electric field which is called Quantum Confined Stark Effect (QCSE). The shift is consequently called Stark shift. The tendency of the shift is shown by a dash line. The ground state transition energies indicated by solid circles and the peak shift indicated by solid squares are plotted as a function of applied electric field in Fig. 6.7. In the calculation of electric field, the associated thickness is about 112 nm.

This material is reserved for educational use only, not allowed for commercial use.
Forbidden to modify the content, and cite the document when use.

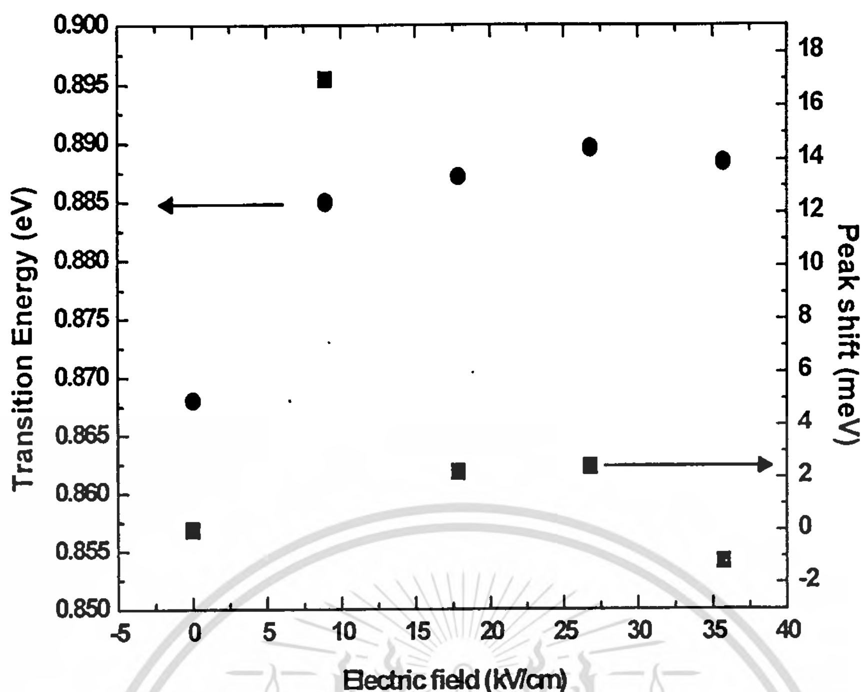

Fig. 6.7 The ground state transition energies indicated by solid circles and the peak shift indicated by solid squares as a function of applied electric field.

The dominant peak with photon energy of 0.868 eV shifts to the higher photon energy with increasing forward bias voltage from 0V to 0.1V. The Stark shift is approximately 17 meV. When the doped samples are biased, the applied electric field that is normal to ErP islands plane suppresses the bandgap of ErP[15]. The electrons and holes are thus no longer bound. The carriers are able to escape from the islands by tunneling effect[16] and three well-defined features in the range 0.8-1.1 eV are observed. In addition, the excitons acquire a finite lifetime, reflected in broader PC spectra and the blur out. The lifetime decreases as the electric field are stronger[17]. After bias voltage of 0.1 V, the increment of the shift is approximately 23 meV/V when the voltage varies from 0.1 to 0.3 V. When the bias voltage increases from 0.3 V to 0.4 V, the transition energy shows a redshift of about 2 meV. Further increasing in bias voltage, the shift is not observed because this voltage can cause too high electric field for very thin quantum island. In addition, a new peak with lower photon energy is observed when the sample is biased. This appearance can be explained theoretically. When the external electric field is applied to a quantum structure, the increasing electric field causes the conduction and valence band to tilt along the direction of the electric field[18] and a new ground state will align at lower level than

This material is reserved for educational use only, not allowed for commercial use.
Forbidden to modify the content, and cite the document when use.

the exist one. This new peak therefore corresponds to the transition energy of the new ground state. Moreover, because the well is inclined when biasing, the higher energy levels will increase. At this point, the subband level will be absent. The absence of the higher subband level is also observed when the biased voltage is increased.

The electric-field dependence of the ground-state transition of the quantum dot-like structure due to QCSE is typically described by the following equation[19-20]

$$E(F) = E(F_0) + pF + \beta F^2, \tag{6.4}$$

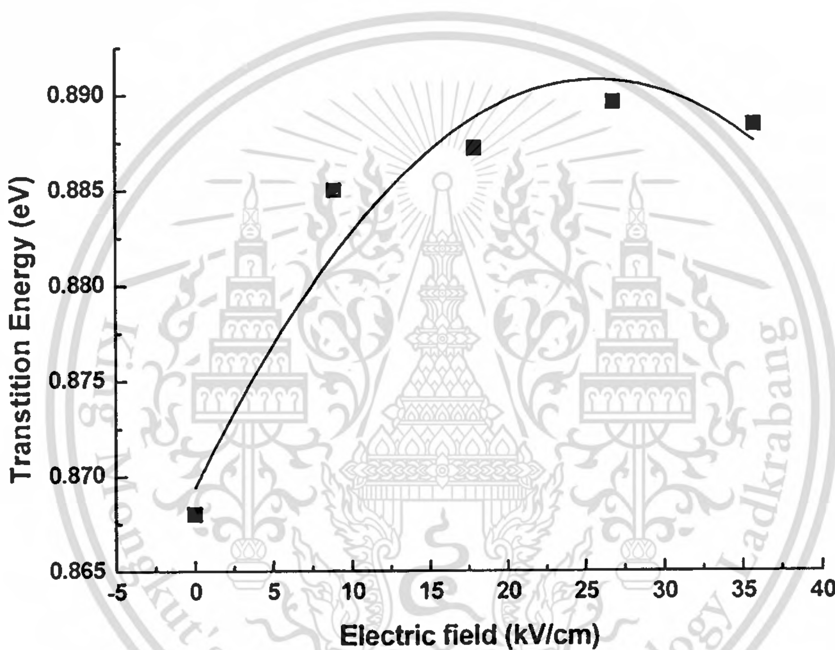

Fig. 6.8 Ground-state transition energies of Er δ-doped InP at 80 min exposure duration as a function of electric-field. The solid line is a theoretical fit to the experimental data.

where $E(F_0)$ is the transition energy at zero field, p describes the non-zero dipole moment and β is the polarizability of the electron-hole system in the quantum dot-like structure due to QCSE. Curve fitting of the above equation to the experimental data, as shown in Fig. 6.8, results in values of E_0 =0.869 eV, p = 2.672 x10^{-27} C·m, and β = -4.8 x 10^{-34} J·m^2V^{-2}. The transition energy exhibits a significant asymmetry about F = 0, with the maximum point for a non-zero field of about 25 kV/cm. This asymmetry attributes to the considerable permanent dipole moment of this structure[16]. The dipole moment may originate from their non-uniform shape along the electric field direction[21].

This material is reserved for educational use only, not allowed for commercial use.
Forbidden to modify the content, and cite the document when use.

6.4 Summary

In summary, photocurrent spectroscopy was used to characterize the Er δ–doped InP grown by OMVPE. The clear PC spectra of the doped samples reflect the high quality formation of ErP layer in InP. The PC spectra of doped samples with different Er exposure duration show that the total number of ErP islands increase with increasing exposure time, reflected in the sharper PC spectra. When the voltage is applied, it suppresses the energy gap of ErP causing unbound excitons and the blur out of the PC spectra. All features revealed by photocurrent spectroscopy demonstrate the formation of ErP islands layer in InP. In addition, the photocurrent spectra of doped sample exhibited distinguished peaks, which may correspond to the interband transitions of a ErP/InP single quantum well formed during growth. The theoretical model based on both rectangular well and parabolic well were studied. The results from the rectangular model have a better agreement to the experiment than the parabolic model. The photocurrent of the doped specimen also showed the quantum confined Stark effect at low voltages. The peak position is shifted to higher energy when the biased voltage is increased from 0.1 – 0.3 V. The new peak of lower energy is also observed. The field dependence of ground state transition energy leads to the existence of permanent dipole moment due to non-uniform ErP islands.

King Mongkut's Institute of Technology Ladkrabang

This material is reserved for educational use only, not allowed for commercial use.
Forbidden to modify the content, and cite the document when use.

References

[1] L. Bolotov, T. Tsuchiya, A. Nakamura, T. Ito, T. Fujiwara, Y. Takada, **"Semimetal to semiconductor transition in ErP islands grown on InP(001) due to quantum-size effects"**, Physical Review B, Vol. 59, pp. 12236-12239 ,1999.

[2] Y. Takada, K. Fujita, M. Matsubara, N. Yamada, S. Ichiki, M. Tabuchi and Y. Fujiwara, **"Layer structure analysis of Er δ-doped InP by x-ray crystal truncation rod scattering"**, Journal of Applied Physics, Vol. 82, pp. 635-638, 1997.

[3] K. Fujita, J. Tsuchiya, S. Ichiki, H. Hamamatsu, N. matsumoto, M. Tabushi, Y. Fujiwara, and Y. Takeda, **"Occupation site and distribution of δ-doped Er in InP measured by X-ray CTR scattering"**, Applied Surface Science, Vol. 117/118, pp. 785-789, 1997.

[4] J. Nukeaw, J. Yanagisawa, N. Matsubara, Y. Fujiwara, and Y. Takeda, **"Observation of trap states in Er-doped InP by photoreflectance"**, Applied Physics Letters, Vol. 70, pp. 84-86, 1997.

[5] T.W. Kim, D.U. Lee, D.C. Choo, J.H. Kim, M.D. Kim, H.D. Jeong, K.H. Yoo, J.Y. Kim, and H.J. Lim, **"1.55 μm wavelength strain-compensated $In_xGa_{1-x}As$ /$In_yAl_{1-y}As$ electroabsorption modulators with high extinction ratio and low polarization-dependent loss"**, Japanese Journal of Applied Physics, Vol. 40, pp. 3120-3123, 2001.

[6] H. Kobayashi, Y. Kawamura, and H. idetoshi, **"Optical properties of an InGaAlAs/InP type-II superlattice"**, Japanese Journal of Applied Physics, Vol. 33, pp. 887-889, 1994.

[7] Y.C. Chan and K. Tada, **"Field induced optical effects in coupled quantum wells"**, IEEE Journal of Quantum Electronics, Vol. 27, pp. 702-707, 1991.

[8] P.W. Fry, D.J. Mowbray, I.E. Itskevich, M.S. Skolnick, J.A. Barker, E.P. O'Reilly, M. Hopkinson, M. Al-khafaji, J.P.R. David, A.G. Cullis, and G. Hill, **"Photocurrent spectroscopy of InAs/GaAs self-assembled quantum dots"**, Physica Status. Solidi(b), Vol. 224, pp. 497-502, 2001.

[9] L. Bolotov, J. Tsuchiya, Y. Fujiwara, Y.Takeda, and A. Nakamura, **"Formation of ErP islands on InP(001) surface by organometallic vapor phase epitaxy"**, Japanese Journal of Applied Physics, Vol. 36, pp. L1534-L1537, 1997.

This material is reserved for educational use only, not allowed for commercial use.
Forbidden to modify the content, and cite the document when use.

[10] P.W. Fry, I.E. Itskevich, D.J. Mowbray, M.S. Skolnick, J.J. Finley, J.A. Barker, E.P. O'Reily, L.R. Wilson, I.A. Larkin, P.A. Maksym, M. Hopkinson, M. Al-Khafaji, J.P.R. David, A.G. Cullis, and J.C. Clark, **"Inverted electron-hole alignment in InAs-GaAs self-assembled quantum dots"**, Physical Review Letters, Vol. 84, pp. 733-736, 2000.

[11] A.G. Petukhov, W. R. L. Lambrecht, and B. Segall, **"Electronic structure of rare-earth pnictides"**, Physical Review B, Vol. 53, pp. 4324-4339, 1996.

[12] J. Singh, **Physics of Semiconductors and Their Heterostructures**, Singapore: McGraw-Hill, Inc., 1993.

[13] X.L. Huang, Y.G. shin, E.K. Suh, H.J. Lee, Y.G. Hwang, and Q. Huang, **"Temperature induced blue shift and broadening of intersubband absorption and photocurrent spectra in GaAs/$Al_{0.3}Ga_{0.7}As$ multiple quantum wells"**, Journal of Applied Physics, Vol. 82, pp. 4394-4399, 1997.

[14] E.P. Sinyavskii, S.M. Sokovnich, and F.I. Pasechnik, **"Energy of the bound state in a parabolic quantum well in magnetic and electric fields"**, Physical Status Solidi(b), Vol. 209, pp. 55-62, 1998.

[15] G. Bastard, **Wave Mechanics applied to Semiconductor Heterostructures** New York: Halsted Press, 1988.

[16] P.W. Fry, I.E. Itskevich, D.J. Mowbray, M.S. Skolnick, J.A. Barker, E.P. O'Reilly, L.R. Wilson, P.A. Maksym, M. Hopkinson, M. Al-Khafaji, J.P.R. David, A.G. Cullis, G. Hill, and J.C. Clark, **"Photocurrent spectroscopy of InAs/GaAs self-assembled quantum dots:observation of a permanent dipole moment"**, Physica E, Vol. 7, pp. 408-412, 2000.

[17] J.H. Davies, **The Physics of Low-Dimensional Semiconductors**, Cambridge: Cambridge University Press, 2000.

[18] K.H. Lee, J.W. Robinson, J.H. Rice, J.H. Na, and R.A. Taylor, **"Simulation of the quantum-confined Stark effect in a single InGaN quantum dot"**, The fifth international conference on numerical simulation of optoelectronic devices(NUSOD'05), 19-22 September, 2005, Berlin, Germany.

[19] P. Leoni, B. Partoens, F.M. Peeters, **"Influence of strain on the Stark effect in InP/GaInP quantum discs"**, Physica E, Vol. 26, pp. 312-316, 2005.

This material is reserved for educational use only, not allowed for commercial use.
Forbidden to modify the content, and cite the document when use.

[20] G. Fasching, F.F. Schrey, T. Roch, A.M. Andrews, W. Brezna, J. Smoliner, G. Strasser, and K. Unterrainer, **"Single InAs/GaAs quantum dots: Photocurrent and cross-sectional AFM analysis"**, Physica E, Vol. 32, pp. 183-186, 2006.

[21] M. Grundmann, O. Steir, and D. Bimberg, **"InAs/GaAs pyramidal quantum dots: Strain distribution, optical phonons, and electronic structure"**, Physical Review B, Vol. 52, pp. 11969-11981, 1995.

This material is reserved for educational use only, not allowed for commercial use.
Forbidden to modify the content, and cite the document when use.

CHAPTER 7

PHOTOCURRENT OF NANOCRYSTAL ZnSe and $ZnSe/Alq_3$/TPD HETEROSTRUCTURE ON SILICON SUBSTRATE

7.1 Literature Review

II-VI Semiconductor compound materials have attracted considerable interest owing to suitable properties for optoelectronic devices. Due to its successful application in blue -green wavelength, Zinc Selenide (ZnSe) is widely used in many applications such as optical windows, light emitting diode, dielectric mirror and filter. Recently, advanced deposition techniques were developed so that the high quality atomic structures can be achieved. ZnSe nanoparticles and nanocrystalline (NC) were successfully grown by various methods such as pulsed laser deposition [1], and metal organic vapor phase epitaxy (MOVPE) [2]. For intentional n-type doping, the group III elements serve as donor dopants at Zn sites as do the group VII impurities on Se sites [3]. ZnSe can also be grown in form of heterostructure. Fabrication of the first ZnSe/GaAs heterostructure bipolar transistors grown by molecular beam epitaxy (MBE) was done by *A.S Glaeser et.al* [4]. ZnS/ZnSe multiple quantum well (MQW) for laser diode operating in the 400 nm spectral range was successfully grown by MOVPE [5]. Another heterostructures based on ZnSe such as $ZnSe/Alq_3$ quantum wells [6], ZnCdSe quantum dots on ZnSe were also reported [7]. Up to now, many researches on semiconductor heterostructures have led to discoveries of many novel devices such as quantum well semiconductor laser and photodetector. In the last few years, new class of optoelectronic devices consisting of contacts between organic and inorganic semiconductors has been reported. The most promising applications of organic-inorganic heterostructure include electroluminescent devices[8], photovoltaic cells[9] and diode for microwave applications[10]. The major advantages of organic materials include color tunability, low power consumption, ease of fabrication and its high absorption constant [11]. However, in contrast to inorganic semiconductors, organic materials have the slow mobility of carriers and strong chemical interaction between two compounds, which prevents the injection of charges into

This material is reserved for educational use only, not allowed for commercial use.
Forbidden to modify the content, and cite the document when use.

organic [12]. The use of hybrid organic-inorganic structures to combine the comparatively good transport properties of semiconductors is one of potential candidates to improve efficiency of the device [13]. It is also believed that, because of large enhancement of the interaction between the organic and inorganic layers, novel functionality combined with properties of the organic and inorganic layers, especially in form of low-dimensional systems, are expected to appear [14]. For example, thermal evaporation of amorphous multiplayer of copper phthalocyanine (CuPc) and TiO_2, with a periodicity of 5 nm, forms a composite material with a modulated electronic structure analogous to that of type - II quantum well structures [15,16]. The physical properties of the organic and inorganic quantum well structure are two-dimensional quantum confinement effect due to the large difference in the band gaps and the dielectric constants between layers. The multiple-quantum-well (MQW) structures of TPD/GaN as organic/inorganic semiconductors have been investigated to ultraviolet-emitting devices [17]. A peak emission wavelength of 400 nm was measured. The external quantum efficiency was about 0.35%. Modulation spectroscopy is an important technique to study and characterize the energy-band structures of semiconductors. Modulation techniques such as electroreflectance (ER) and photoreflectance (PR) are particularly useful since they yield spectra with sharp features at the critical-point energies. The features in the spectra appear at energies corresponding to the band gap characteristic points or other peculiarities in the dielectric function. ER is of considerable interest because it is sensitive to surface and interface electric fields [18,19]. The ER technique was used to study the creation of space charge distributions in a polymer light emitting diode, by monitoring the real third order nonlinear optical response of the electroluminescent layer [20]. The diode is based on an aluminum/polymer/indium tin oxide (ITO) stack, where the polymer is a derivative of poly (p-phenylene-vinylene) in which oxidiazole groups were grafted as side chains. The measured signal is strongly influenced by a space charge distribution and by screening in the organic layer. The space charge distribution is the superposition of a long-lived contribution, close to indium tin oxide, due to charges trapped in deep levels, and of that of relatively mobile charges injected in the polymer film.

In this chapter, The fabrication and characterization of Si-based inorganic and organic/inorganic heterojunction device are reported. The heterostructures consist of ZnSe, Tris(8-hydroxyquinoline) aluminum(III), Alq_3, as an electron transport layer(ETL), N, N'–bis(3-methylphenyl)-N,N'- diphenyl - benzidine (TPD), as hole transport layer(HTL). Optical and

This material is reserved for educational use only, not allowed for commercial use.
Forbidden to modify the content, and cite the document when use.

electrical properties of these structures were extensively investigated by mean of photocurrent and electroreflectance measurement.

7.2 Sample Structure

7.2.1 Sample Structure of Nanocrystal ZnSe/p-Si

The samples were prepared at Quantum and Optical Semiconductor Laboratory(QOS), Department of Applied Physics, King Mongkut's Institute of Technology Ladkrabang. The schematic diagram of sample structure is depicted in Fig. 7.1. Prior to loading into the evaporation chamber, the Si substrate was cleaned by Piranha process. ZnSe layer was grown on p-Silicon substrate by high vacuum multi-pocket electron-beam evaporator (Edward Auto306). The ZnSe film thickness was measured by a crystal monitor (Edwards FTM7). There are three samples with different ZnSe layer thickness, 3 μm, 1 μm, and 500 nm. The gold contact was grown on the sample using DC sputtering.

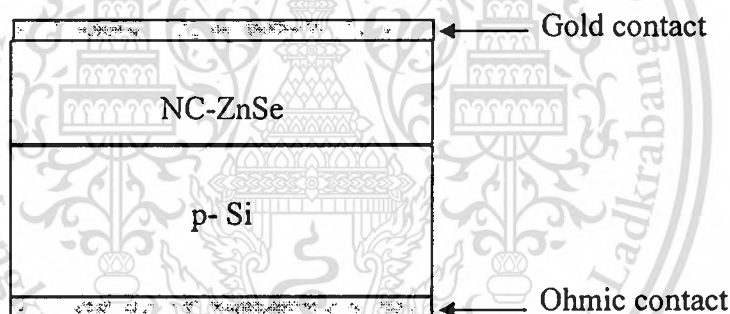

Fig. 7.1 The sample structure of NC-ZnSe/p-Si.

7.2.2 Sample Structure of ZnSe/Alq_3/TPD/Si

Organic/inorganic heterostructures of ZnSe/Alq_3/TPD on Si substrate was grown by high vacuum multi-pocket electron-beam evaporator (Edwards AUTO306). The chemical structure of Alq_3 and TPD are shown in Fig. 7.2. Prior to loading into the evaporation chamber, the Si substrate was cleaned by Piranha process. The base pressure in the evaporator was $\sim 5\times10^{-6}$ mbar. The substrate temperature was kept at room temperature. The layer structure was grown starting with a 50-nm TPD buffer layer on Si substrate, followed by Alq_3 layers with varied thickness from 10 nm to 50 nm, a 200-nm ZnSe cap layer, and a 200-nm ITO as a transparent front

This material is reserved for educational use only, not allowed for commercial use.
Forbidden to modify the content, and cite the document when use.

electrode, respectively. The film thickness and growth rate of all layers were measured by a quartz crystal thickness monitor (Edwards FTM7). The deposition rate of each layer was kept at rate of 0.1nm/s.

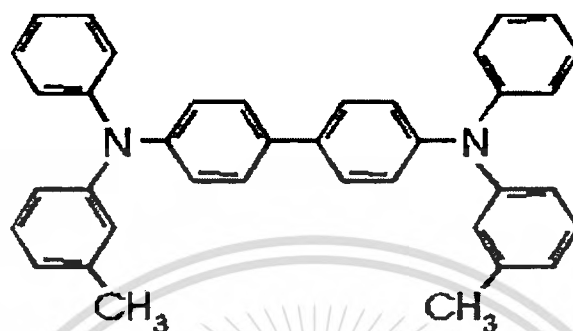

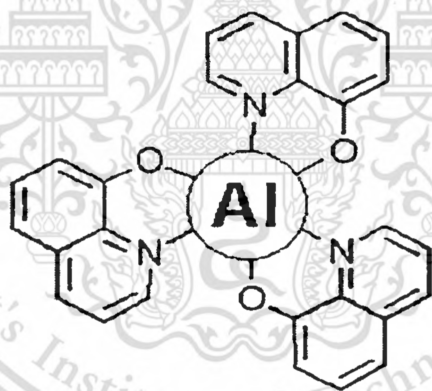

Fig. 7.2 Chemical structure of (a) TPD, (b) Alq_3.

This material is reserved for educational use only, not allowed for commercial use.
Forbidden to modify the content, and cite the document when use.

7.3 Results and Discussion

7.3.1 Nanocrystal ZnSe/p-Si

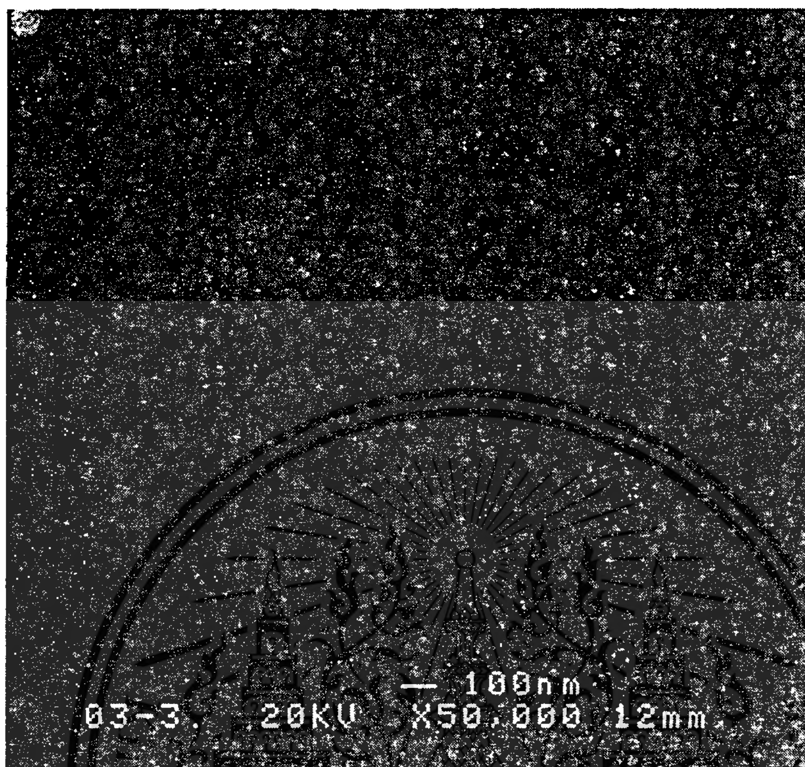

Fig. 7.3 SEM image of 500nm- thick NC-ZnSe film.

The surface morphology of ZnSe nanocrystal film was investigated by field emission scanning electron Microscope (FE-SEM), as seen in Fig. 7.3. The image shows good uniformity of the ZnSe film as nanocrystal.

This material is reserved for educational use only, not allowed for commercial use.
Forbidden to modify the content, and cite the document when use.

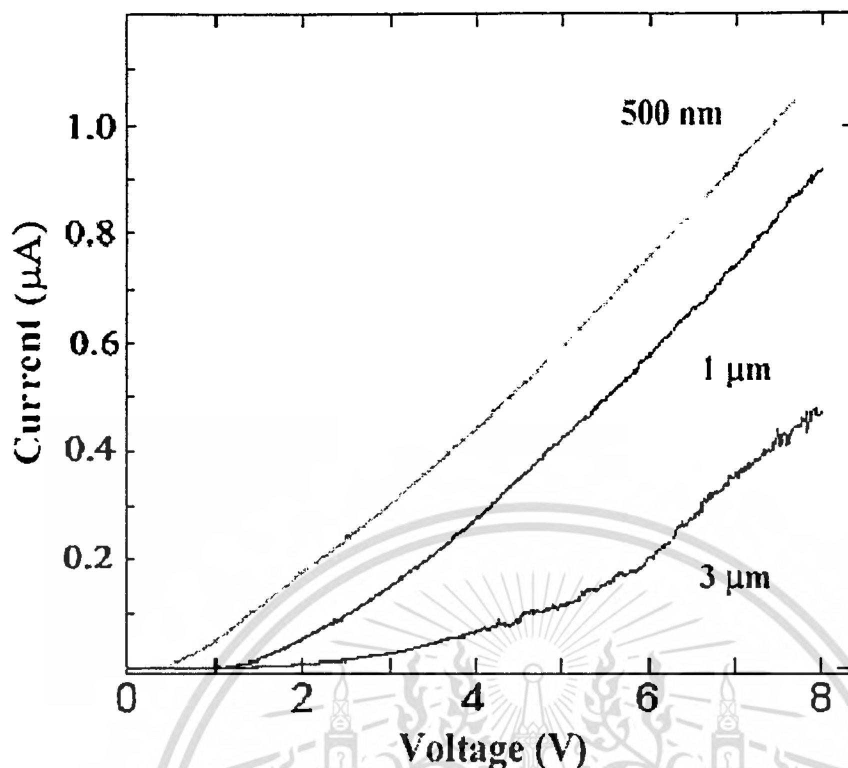

Fig. 7.4 Current-voltage characteristics of NC-ZnSe/p-Si heterostructure with different ZnSe layer thickness.

Fig. 7.4 shows the current-voltage characteristics of NC-ZnSe/p-Si heterostructure with different ZnSe layer thickness. Samples A, B, and C are designated for the samples with NC-ZnSe layer thickness of 500nm, 1 μm, and 3 μm, respectively. It is observable that the threshold voltage for current injection of sample A is less than of sample B and C. This can be concluded that the threshold voltage increases with increasing in ZnSe layer thickness. As the ZnSe layer thickness increases, its potential barrier consequently increases, causing the difficulty of current injection through the barrier. Therefore, it requires more bias voltage to overcome higher barrier.

This material is reserved for educational use only, not allowed for commercial use.
Forbidden to modify the content, and cite the document when use.

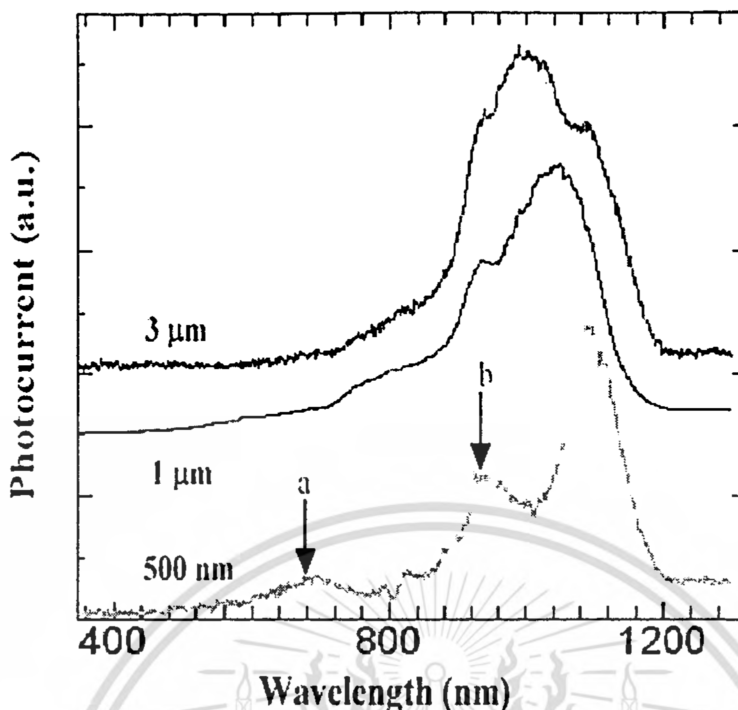

Fig. 7.5 PC spectra of NC-ZnSe/p-Si heterostructure with different ZnSe layer thickness.

Fig. 7.5 is the PC spectra of NC-ZnSe/p-Si heterostructure with different ZnSe layer thickness. The PC spectra of all samples are in 800-1200 nm spectral range, that is corresponded to the response wavelength of absorption edge of p-Si. However, different PC signal was observed for different ZnSe layer thickness. The full width at half maximum (FWHM) of PC spectra increases when the ZnSe layer thickness increases. Moreover, the response range is shifted to the lower wavelength or higher photon energy as the thickness increases. This behavior can be qualitatively explained. Since the absorption of photon in photocurrent process occurs in the depletion region at the heterojunction. The increment of ZnSe layer thickness widens depletion layer and shifts this region into ZnSe layer. More photons with higher energies close to ZnSe band gap (2.82 eV) can consequently be absorbed.

It is clearly observed that there are two additional PC peaks at approximately 750 nm labeled as peak 'a' and 900 nm labeled as peak 'b'. Peak 'b' is much sharper than peak 'a'. The origin of these two peaks is discussed. It is noticeable that the photon energy of these two peaks is between the band gap of Si and ZnSe. When ZnSe layer decrease to 500 nm, more photons can penetrate to the depletion region, at which the optical transition of the carriers at the interface can play the dominant role. PC spectroscopy was employed to investigate the defects and optical

This material is reserved for educational use only, not allowed for commercial use.
Forbidden to modify the content, and cite the document when use.

transition at the interface of heterostructure. It was found that, at the interface of doped heterojunction of thin layer, the energy band diagram can cause the confinement of electrons[21-22]. Such electrons are call two-dimensional electron gas (2DEG). Based on this fact, these two peaks should arise from the transition of 2DEG at the interface. The sharpness difference of these two peaks reflects the probability density of electrons in quantized states.

7.3.2 ZnSe/Alq_3/TPD/Si

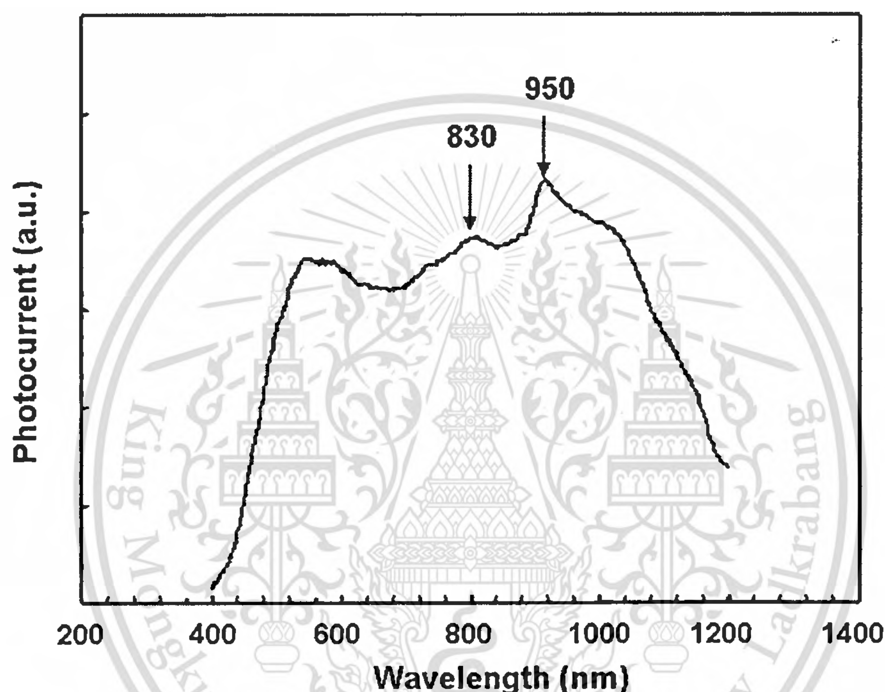

Fig. 7.6 PC spectra of the sample with Alq_3 thickness of 50 nm.

PC of the sample shown in Fig. 7.6 indicates wide response wavelength ranging from 450 nm to 1100 nm. The PC signal decreases significantly as photon energy is above 2.7 eV. This feature is due to photons with photon energy greater than the energy gap of ZnSe of 2.7 eV [23] are absorbed by ZnSe layer and then recombined nonradiatively. This PC spectra also suggests an application of this structure for wide range photodetector. It can be also observed that the response of the device is faster than the organic thin films itself. This behavior attributed to high carrier mobility of inorganic semiconductor[23] indicates that inorganic semiconductor in contact with organic material can improve the response speed of device. PC signal also shows two pronounced maxima at wavelength of 830 nm and 950 nm as indicated by arrows. When sample

This material is reserved for educational use only, not allowed for commercial use.
Forbidden to modify the content, and cite the document when use.

is illuminated, photons with energy lower than energy gap of Alq_3 and TPD, they can penetrate to silicon substrate at which they can be absorbed. These two peaks are, therefore, attributed to fundamental absorption of the silicon layer [24]. As TPD thickness varies, PC of the sample increases dramatically with increasing in TPD thickness. Light with photon energy in visible range can be absorbed by TPD layer and generate corresponded photocurrent signal. This feature suggests that TPD layer plays an important role in photo-generated current process, especially in visible range. As TPD thickness increases, more photo-excited carriers are generated, reflecting in the increment of PC signal.

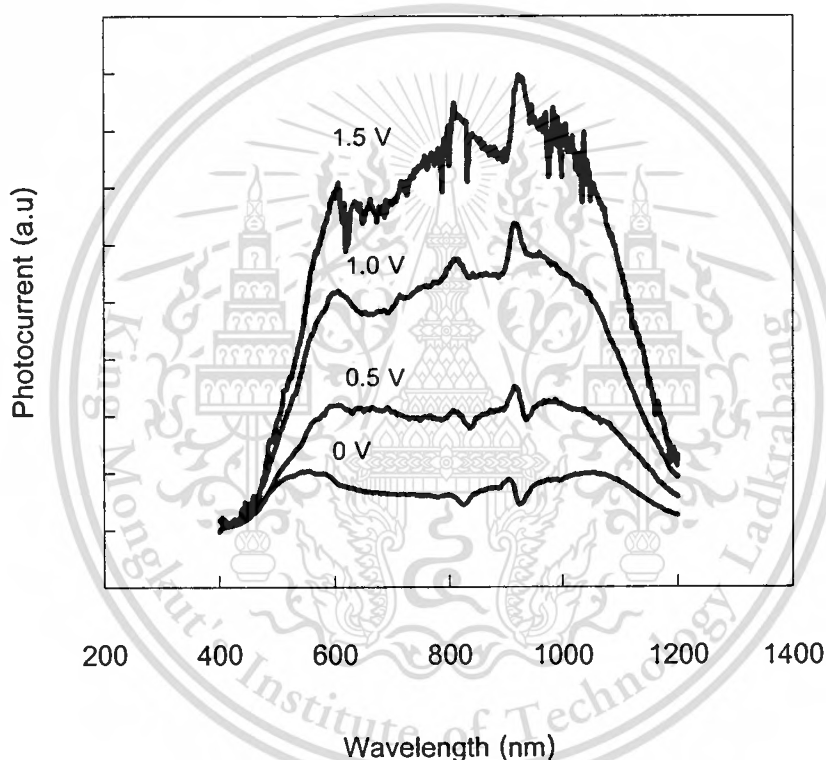

Fig. 7.7 Photocurrent of ZnSe/Alq3/TPD/P-Si with different bias voltage.

Fig. 7.7 shows PC of ZnSe/Alq3/TPD/P-Si with different bias voltage. As the forward bias voltage increase from 0-1.5 V, The PC intensity dramatically increase. The increased voltage helps the photo-generated carriers to transport to the contacts and overcome the barrier at each interface. In addition, PC clearly shows three clear peaks, indicating by arrows, whose shapes become sharper, intensity become stronger, and their positions shift to higher wavelength when the bias voltage increases. This behavior implies the confinement of the carriers at the interfaces. Fig. 7.8 and 7.9 show PC signal of ZnSe/Alq3/TPD(5nm)/N-Si under forward bias and reverse

Forbidden to modify the content, and cite the document when use.

bias respectively. Under forward bias from 0-0.2 V, the pronounced peaks intensity obviously increase. Further forward bias causes the decrement in intensity and then blur out after forward bias over 1.0 Volt. In Fig. 7.9, PC signal increase with increasing reverse bias voltage up to -0.7 Volt and show significant shift to higher photon energy. These phenomenon may connect to the external electric field caused-carrier confinement at ZnSe/Alq3 interface.

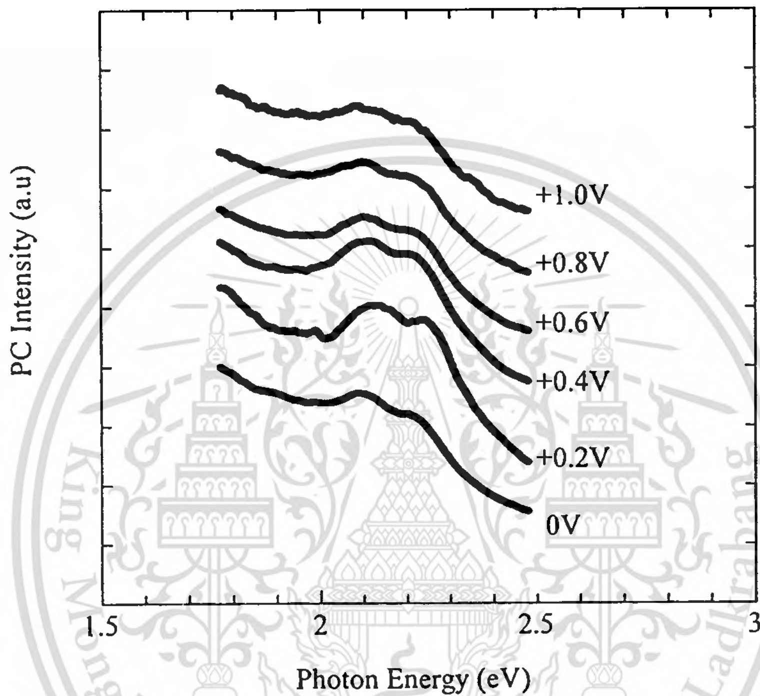

Fig. 7.8. PC of ZnSe/Alq3/TPD(5nm)/N-Si under forward bias.

This material is reserved for educational use only, not allowed for commercial use.
Forbidden to modify the content, and cite the document when use.

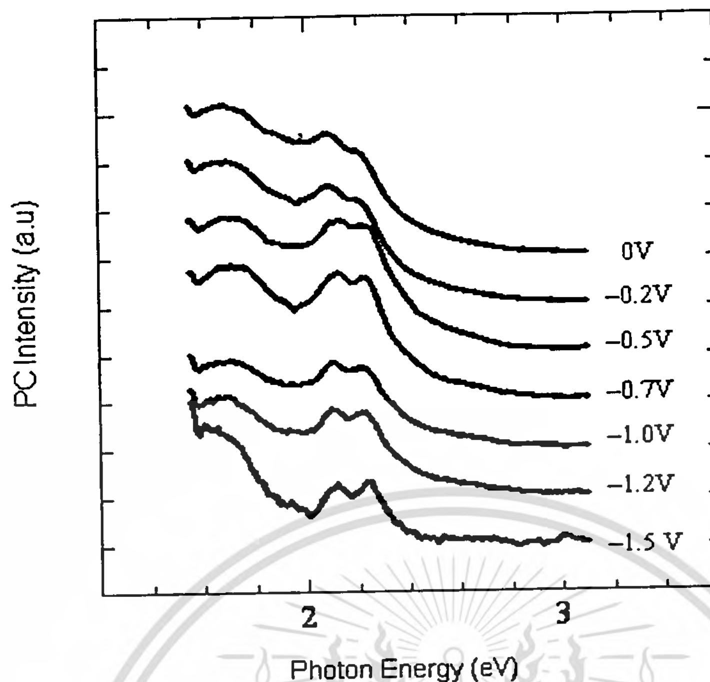

Fig. 7.9 PC of ZnSe/Alq3/TPD(5nm)/N-Si under reverse bias.

The ER spectrum of the structure with 50-nm thick Alq_3 layer compared with photocurrents (PC) is shown in Fig. 7.10. In ER measurement, DC voltage and AC voltage with frequency of 300 Hz and amplitude of 0.05 V were applied to modulate surface potential. A 100 W tungsten lamp was dispersed by a 25-cm monochromator and used as an excitation source. VIS-Si detector detected the modulation reflectance signal, and the signal from the detector was fed to a lock-in amplifier. The subband energy of the sample at 2.24 eV was clearly observed in both PC and ER spectra.

This material is reserved for educational use only, not allowed for commercial use.
Forbidden to modify the content, and cite the document when use.

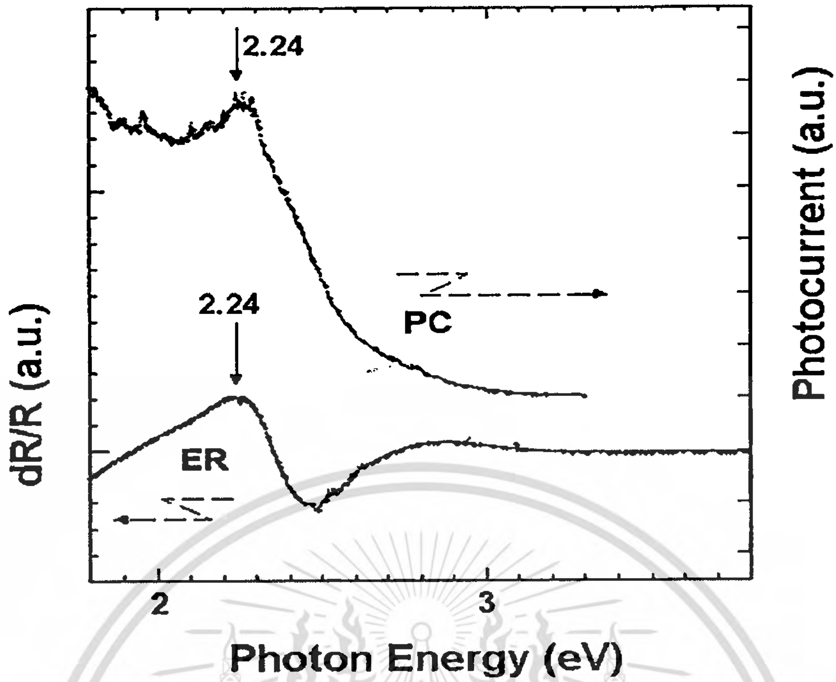

Fig. 7.10. Room-temperature ER and PC spectra of sample with 50 nm-thick Alq_3.

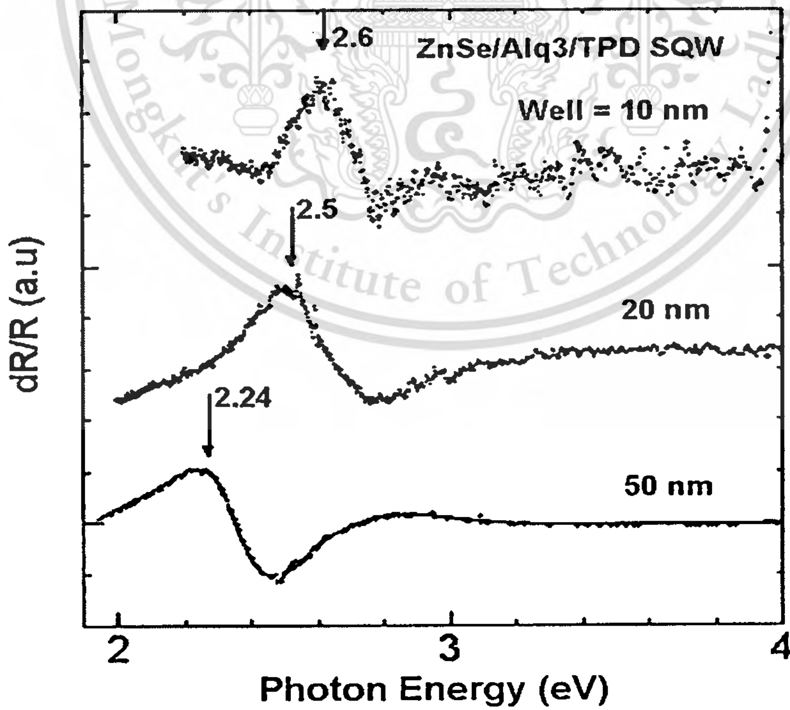

Fig.7.11 Room-temperature ER spectra as a function of the well thickness. Arrows indicate the transition energies determined by the fittings.

This material is reserved for educational use only, not allowed for commercial use.
Forbidden to modify the content, and cite the document when use.

The ER spectra of all the samples are shown in Fig. 7.11. The transition energies increase from 2.24 eV to 2.6 eV with decreasing Alq_3 thickness from 50 nm to 10 nm, respectively. The results have the same feature observed in a new class of superlattice materials consisting of alternating layers of Alq_3 and MgF_2 by vacuum deposition [25]. The changes of the exciton energy could be interpreted as the confinement effects of exciton in the Alq_3 thin layers. Therefore, this structure forms a single quantum well (SQW). In order to analyze such complicated behavior of ER spectra, we carried out a line shape analysis by using the low-field electroreflectance spectrum proposed by Aspnes [26]. We have fitted the measured spectra, modulated reflectance *dR/R*. The ER spectra as a function of photon energy can be analyzed using Aspnes third-derivative function in the low electric field limit [26], i.e.

$$\frac{dR}{R} = Re\sum_{j=1}^{p} C_j e^{i\theta_j}(E - E_{gi} + i\Gamma_j)^{-n}. \tag{7.1}$$

Where R is the reflectance, dR is the induced change in the reflectance by modulation light, E is the photon energy, p is the total number of spectral structures to be fitted E_{gi}, Γ_j, C_j and θ_j are transition energy, broadening parameter, amplitude and phase, respectively, of the feature corresponding to the jth critical point. The parameter n is a factor used to specify the critical point dimension. The energy level associated with transition energy was determined by least-square fitting of Eq. (7.1) to ER spectra obtained experimentally. In this calculation, the n value is 3 for the quantum well transition feature [27]. The transition energies determined by the fittings are indicated by arrows, as also shown in Fig. 7.11. The transition energy decreased with increasing well thickness. In Fig. 7.12, taking the vacuum energy level as a reference, the electronic structure of the conduction band and valence bands of ZnSe are at –4.1 and –6.8 eV below the vacuum level [8,23]. The lowest unoccupied molecular orbital (LUMO) and highest occupied molecular orbital (HOMO) levels of TPD are at –2.3 and –5.4 eV [28,29], However, the LUMO and HOMO levels of Alq_3 should be discussed. Mason et.al [30] had founded that an original HOMO level of Alq_3 with could shifted to be at –6.4 due to the Alq_3^- radical anion and the gap state is formed in the forbidden gap at an energy of about 1.6 eV. The corresponded LUMO of Alq_3 of this structure should be at about -4.8 eV. The shifts of electronic structures of Alq_3 should be attributed to charge transfer and the formation of an interface dipole at the organic/inorganic

This material is reserved for educational use only, not allowed for commercial use.
Forbidden to modify the content, and cite the document when use.

interface of Alq_3/ZnSe[31]. From the configuration and the energy band diagrams, the structure was like inorganic quantum well structure, so conveniently, it was called organic-inorganic quantum well structure, where ZnSe and TPD act as barrier potential and Alq_3 as potential well.

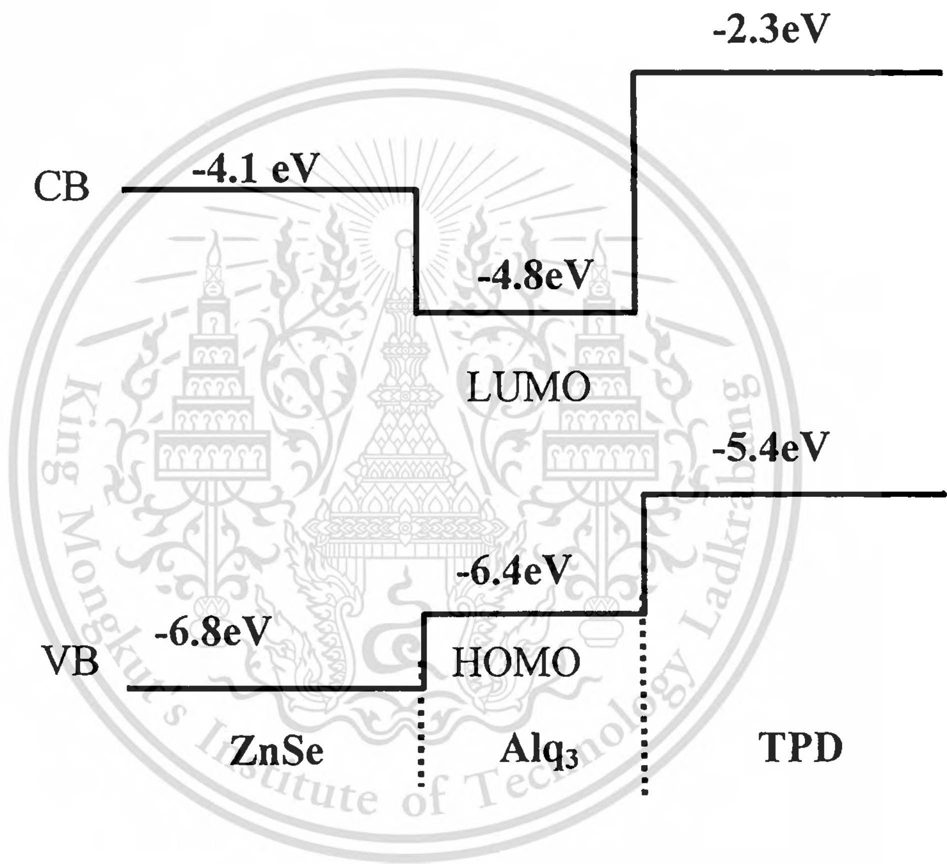

Fig. 7.12 Energy band diagrams of ZnSe/Alq_3 SQW structure. The numbers are not in scale.

The transition energy decreases with increasing Alq_3 thickness might be due to the increase of well results in the reduction of quantum confinement energies. Decrease in the size should affect properties of film. The properties of larger size film should be similar to that of bulk where the effect of quantum confinement is small.

This material is reserved for educational use only, not allowed for commercial use.
Forbidden to modify the content, and cite the document when use.

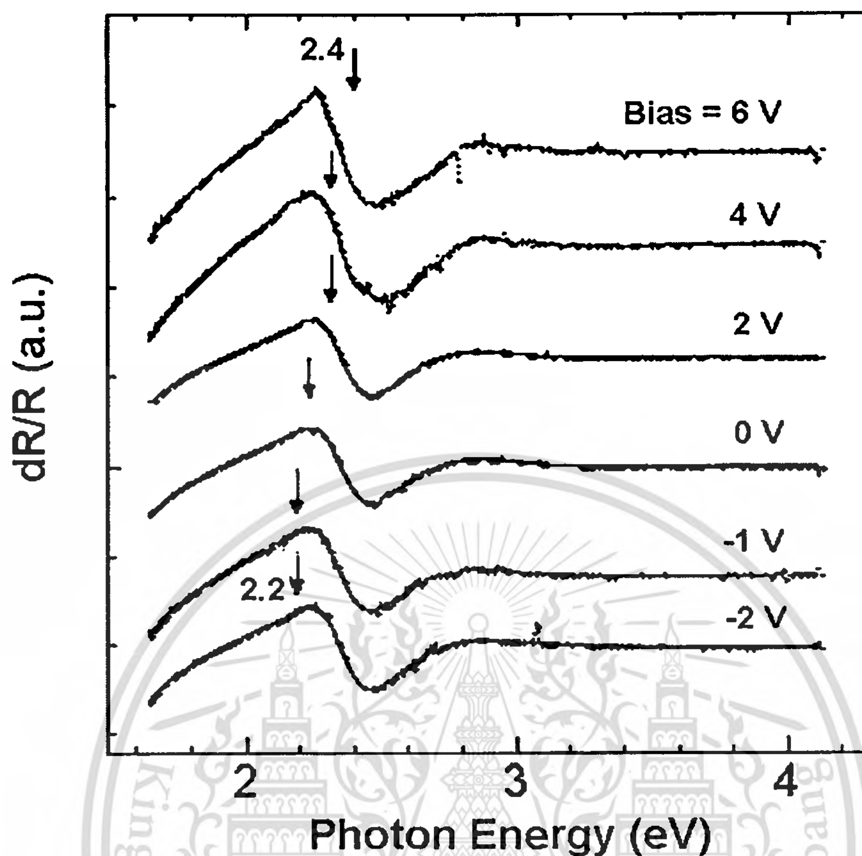

Fig.7.13 ER spectra of 50-nm SQW sample measured in applied voltage +6.0 ~ -2.0V.

Fig. 7.13 shows the electroreflectance spectra of 50-nm SQW measured in applied DC voltages from +6 V to -2 V. The transition energies obtained from these fittings are indicated by arrows. The peaks show significant red- shift from 2.24 eV to about 2.2 eV with increasing applied negative voltage from 0V to -2 V. With forward bias from 0V to +6 V, the ER peak exhibited blue-shift from 2.24 eV to 2.4 eV. Such red-shift and blue-shift are clearly due to the quantum confined Stark shift.

This material is reserved for educational use only, not allowed for commercial use.
Forbidden to modify the content, and cite the document when use.

7.4 Summary

Photocurrent spectroscopy on NC-ZnSe/p-Si heterostructure with different ZnSe layer thickness was conducted. PC signal shows that the FWHM of PC spectra is widened and the response wavelength has significant blue shift to lower wavelength as the ZnSe layer thickness increases. The sample with 500nm-ZnSe layer additionally exhibits two more peaks that should arise from the quantum confinement at the heterojunction between NC-ZnSe and p-Si. Organic/inorganic heterostructures based on ZnSe/Alq_3/TPD were successfully grown by electron beam evaporator. The wavelength response of the structure covers visible to near infrared spectrum. From experiment, it could be concluded that TPD plays a crucial role in photocurrent process of the device, especially in visible range. In addition, PC and ER measurements were used to investigate optical and electrical properties of the samples. The ER spectra showed the optical transition energies in SQWs as Alq_3 well thickness varied from 10 to 50 nm. The transition energy was determined by fitting the ER spectra to the theoretical line-shape expression. The optical transition energy decreased with increasing in well thickness is due to the increase of well size in addition to reduction of quantum confinement energy. The ER signals also showed the significant Stark shift when the device was under external electric field.

This material is reserved for educational use only, not allowed for commercial use.
Forbidden to modify the content, and cite the document when use.

References

[1] N. Xu, and B.H Boo, **Pulsed laser deposition of nanocrystalline ZnSe:N thin films,** Semiconductor Science and Technology, Vol. 18, pp. 300-302, 2003.

[2] D. Sarigiannis, J.D. Peck, G. Kioseoglou, A. Petrou, and T.J. Mountziaris, **"Characterization of vapor-phase-grown ZnSe nanoparticles"**, Applied Physics Letters, Vol. 80, pp. 4024-4026, 2003.

[3] S. Bhaskar, P.S. Dobal, B.K. Rai, R.S. Katiyar, H.D. Bist, J.O. Ndap, and A. Burger, **"Photoluminescence study of deep levels in Cr-doped ZnSe"**, Journal of Applied Physics, Vol. 85, pp. 439-443, 1999.

[4] A.S. Glaeser, J.L. Merz, R.E. Nahory, and M.C. Tamargo, **"Fabrication and characterization of ZnSe/GaAs heterostructure bipolar transistors grown by molecular beam epitaxy"**, Applied Physics Letters, Vol. 60, pp.1345-1347, 1992.

[5] N. Lovergine, P. Prete, G. Leo, L. Calcagnile, N. Cingolani, A.M. Mancini, F. Romanato, and A.V. Drigo, **"MOVPE growth of wide band-gap II-VI compounds for near-UV and deep-blue light emitting devices"**, Crystal Research Technology, Vol. 33, pp. 183-196, 1998.

[6] J. Nukeaw, K. Upprakhot, S. Rahong, B Tunhoo, and W. Yindeesuk, **Observation of optical transition energy in ZnSe/tris(8-hydroxyquinoline) aluminum (Alq3)/ZnSe single quantum wells by photoreflectance spectroscopy** , Physica E, Vol. 21, pp. 1070-1073, 2004.

[7] B.P. Zhang, T. Yasuda. W.X. Wang, Y. Segawa, K. Edamatsu, T. Itoh, H. Yaguchi, and K. Onabe, **"A new approach to ZnCdSe quantum dots"**, Materials Science and Engineering B, Vol. 51, pp. 127-131, 1998.

[8] W. Yu, Z. Xu, F. Teng, S. Yang, Y. Hou, L. Qian, C. Qu, S. Quan, X. Xu, **"Blue electroluminescence of ZnSe thin film in an organic-inorganic heterostructures device"**, Physics Letters A, Vol. 338, pp. 402-406, 2005.

[9] M.Y. Song, K.J. Kim, D.Y. Kim, **"Enhancement of photovotaic characteristics using a PEDOT interlayer in TiO_2/MEHPPV heterojunction devices"**, Solar Energy Materials & Solar Cells, Vol. 85, pp. 31-39, 2005.

This material is reserved for educational use only, not allowed for commercial use.
Forbidden to modify the content, and cite the document when use.

[10] G. Ginev, T. Riedl, R. Parashkov, H-H. Johannes, W. Kowalsky, **"Organic-GaAs heterostructure diodes for microwave applications"**, Applied Surface Science, Vol. 234, pp. 22-27, 2004.

[11] G. Meinhardt, D. Gruber, G. Jakopic, Y. Greets, W. Papousek, G.Leising, **"Photocurrent action spectroscopy in organic photovoltaic cells"**, Synthetic Metals, Vol. 121, pp. 1593-1594, 2001.

[12] V.M. Agranovich, D.M. Basko, G.C. La Rocca, F.Bassani, **"New concept for organic LEDs: non-radiative electronic energy transfer from semiconductor quantum well to organic overlayer"**, Synthetic Metals, Vol. 116, pp. 349-351, 2001.

[13] V.M. Agranovich, G.C. La Rocca, F. Bassani, **"Efficient electronic energy transfer from a semiconductor quantum well to an organic material"**, Journal of Experimental and Theoretical Physics Letters, Vol. 66, pp. 748-751, 1997.

[14] M. Era, K. Maeda, T. Tsutsui, **"Self-organization approach to organic/inorganic quantum-well based on metal halide-based layer perovskite"**, Thin Solid Films, Vol. 331, pp. 285-290, 1998.

[15] J. Takada, H. Awaji, M. Koshioka, A. Nakajima, and W.A. Nevin, **"Organic–inorganic multilayers: A new concept of optoelectronic material"**, Applied Physics Letters, Vol. 61, pp. 2184-2186, 1992.

[16] J. Takada, **"Organic-inorganic hetero nanosystems as an approach to molecular optoelectronics"**, Japanese Journal of Applied Physics, Vol. 34, pp.3864-3870, 1995.

[17] C.F. Qiu, L.D. Wang, H.Y. Chen, M. Wang, and H.S. Kwok, **"Room temperature ultraviolet emission from an organic light-emitting diode"**, Applied Physics Letters, Vol. 79, pp. 2276-2278, 2001.

[18] J. Nukeaw, Y. Fujiwara, and Y. Takeda, **"Observation of electric fields at surface and interface of doped GaAs/semi-insulating GaAs structures by fast Fourier transformed photoreflectance"**, Japanese Journal of Applied Physics, Vol. 36, pp. 7019-7023, 1997.

[19] J. Nukeaw, Y. Fujiwara, Y. Takeda, M. Funato, S. Aoki, Sz. Fujita, and Sg. Fujita, **"Observation of high electric field at ZnSe/GaAs heterointerfaces by fast Fourier transformed photoreflectance"**, Thin Solid Films, Vol. 334, pp. 11-14, 1998.

This material is reserved for educational use only, not allowed for commercial use.
Forbidden to modify the content, and cite the document when use.

[20] T. M. Hsu, W.-H. Chang, C. C. Huang, N. T. Yeh and J.-I. Chyi, **"Quantum-confined Stark shift in electroreflectance of InAs/$In_xGa_{1-x}As$ self-assembled quantum dots"**, Applied Physics Letters, Vol. 78, pp. 1760-1762, 2001.

[21] J.Z. Li, J.Y. Lin, H.X. Jiang, M. Asif Khan, and Q. Chen, **"Persistent photoconductivity in a two-dimensional electron gas system formed by an AlGaN/GaN heterostructure"**, Journal of Applied Physics, Vol. 82, pp. 1227-1229, 1997.

[22] B. Sciana, D. Radziewicz, B. Paszkiewicz, M. Tlaczala, M. Utko. P. Sitarek, J. Misiewicz, R. Kinder, and J. kovac, **"Epitaxial Growth and Characterisation of Silicon Delta-Doped GaAs, AlAs and $Al_xGa_{1-x}As$"**, Crystal Research Technology, Vol. 36, pp.1145-1154, 2001.

[23] Y. Wenge, X. Zheng, T. Feng, Y. Shengyi, Q. Lei, Q. Chong, Q. Shanyu, and X. Xurong, **"Different emission mechanism of organic-inorganic heterostructure device"**, Displays, Vol. 25, pp. 61-65, 2004.

[24] A. Komolov, K. Schumburg, and V. Monakhov, **"Photovoltage and photoconductivity in Si/organic film/metal structures with films made of poly(3-alkylthiophene) molecules and polycyclic conjugated molecules"**, Synthetic Metals, Vol. 105, pp. 29-33, 1999.

[25] S. Tokito, J. Sakata, and Y. Taga, **"Structures and optical properties of organic/inorganic superlattices"**, Applied Physics Letters, Vol. 64, pp. 1353-1355, 1994.

[26] D. E. Aspnes, **"Third-derivative modulation spectroscopy with low-field electroreflectance"**, Surface Science, Vol. 37, pp. 418-442, 1973.

[27] P. Basmaji, A. M. Ceschin, M. Siu Li, O. Hipolito, A. A. Bernussi, F. Iikawa, and P. Motisuke, **"MBE growth and characterization of δ-doping in GaAs and GaAs/Si"**, Surface Science, Vol. 228, pp. 356-358, 1990.

[28] K. Okumoto and Y. Shirota, **"Development of high-performance blue–violet-emitting organic electroluminescent devices"**, Applied Physics Letters, Vol. 79, pp.1231-1233, 2001.

[29] V.V.N. Ravi Kishore, M.P. Patankar, N. Periasamy, and K.L Narasimhan, **"Transient electroluminesence in alloy-based organic light-emitting diodes"**, Synthetic Metals, Vol. 143, pp. 295-303, 2004.

This material is reserved for educational use only, not allowed for commercial use.
Forbidden to modify the content, and cite the document when use.

[30] M.G. Mason, C.W. Tang, L.S. Hung, P. Raychaudhuri, J. Madathil, D.J. Giesen, L. Yan, Q.T. Le, Y. Gao, S.T. Lee, L.S. Liao, L.F. Cheng, W.R. Salaneck, D.A. dos Santos, and J.L. Bredas, **"Interfacial chemistry of Alq_3 and LiF with reactive metals"**, Journal of Applied Physics, Vol. 89, pp. 2756-2765, 2001.

[31] T. Chasse, C.-I. Wu, I.G. Hill, and A. Kahn, **"Band alignment at organic-inorganic semiconductor interfaces: α-NPD and CuPc on InP(001)"**, Journal of Applied Physics, Vol. 85, pp. 6589-6592, 1999.

This material is reserved for educational use only, not allowed for commercial use.
Forbidden to modify the content, and cite the document when use.

CHAPTER 8

PHOTOLUMINESCENCE OF InGaAs/GaAs MULTIPLE QUANTUM WELL STRUCTURE GROWN BY MOLECULAR BEAM EPITAXY

8.1 Literature Review

InGaAs/GaAs have attracted much attention according to their appropriate properties for microelectronic and optoelectronic applications[1]. This structure has considerable potential for optoelectronic applications within the wavelength region of 1.1-1.3 μm. Growth of strained layers of InGaAs/GaAs quantum wells on (111) GaAs allows the devices to reach wavelength beyond 1.1 μm[2]. InGaAs/GaAs MQWs grown on high index GaAs substrate show a strain-induced piezoelectric field due to lattice-mismatch[3]. This kind of structure has been applied for sophisticated electrooptic devices. An ultra low-voltage InGaAs/GaAs MQWs electro-optic modulators with organic-inorganic distributed Bragg reflector was proposed[4]. With ON-OFF driving reverse voltage of 0.5 and 1.8 V, this device can be suitable for analog electro-optic modulation. According to strong charge accumulation effects in InGaAs/GaAs MQWs PIN diodes grown on (111)B GaAs substrates, this structures can be applied as novel memory devices[5]. The applications of this structure on optical switching, logic devices, laser diodes and non-linear electro optical devices have been reported[6].

Optical characterization techniques have been utilized to investigate important properties of the structure. Nature of light hole in InGaAs/GaAs MQWs was studied by means of photoreflectance spectroscopy[7]. The results showed the type II light hole exciton with indium content of 0.115 and 0.125 and big heavy hole valence band offset of 0.33 and 0.38, respectively.

8.2 Sample Structure

Fig. 8.1 shows a schematic of the sample. The $In_{0.1}Ga_{0.9}As$/GaAs MQW sample was grown on GaAs substrate by molecular beam epitaxy technique. The sample consists of a GaAs buffer layer followed by 15 periods of $In_{0.1}Ga_{0.9}As$/GaAs QWs. The well and barrier width were fixed at 8 nm and 15 nm, respectively. The topmost GaAs layer was deposited as a cap layer.

This material is reserved for educational use only, not allowed for commercial use.
Forbidden to modify the content, and cite the document when use.

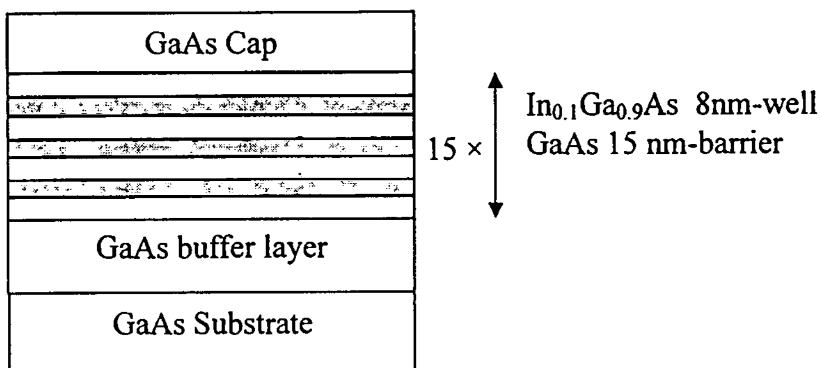

Fig 8.1 Schematic draw of 15 periods of $In_{0.1}Ga_{0.9}As/GaAs$ quantum wells.

8.3 Results and Discussion

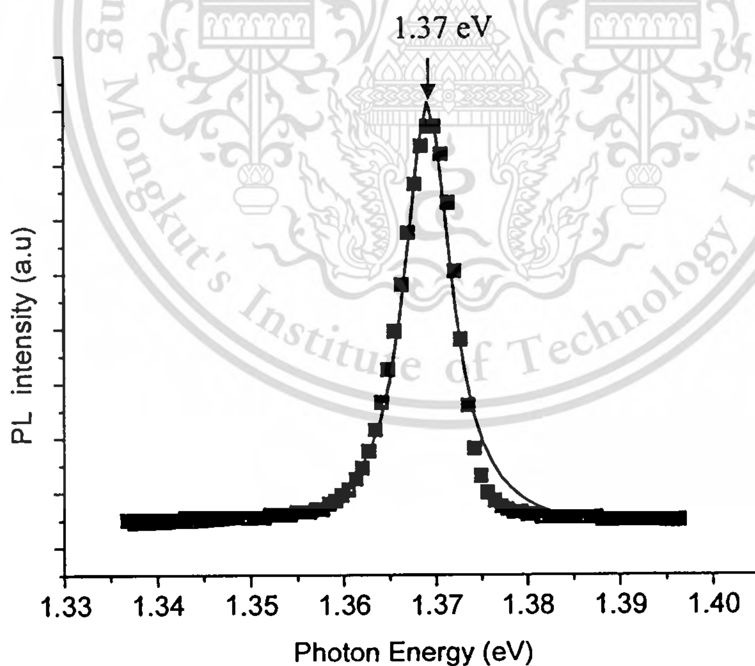

Fig. 8.2 Photoluminescence spectrum of $In_{0.1}Ga_{0.9}As/GaAs$ multiple quantum wells at 12 K.

This material is reserved for educational use only, not allowed for commercial use.
Forbidden to modify the content, and cite the document when use.

Fig. 8.2 shows the PL spectrum taken at 12 K. The PL peak position is at 1.37 eV. This PL spectra is associated wirh the e(1)-hh(1) excitonic transition in the wells. The measured PL spectrum is also in good agreement with other research works[1,3]. It is northworthy that this sample grown by molecular beam epitaxy exhibits a single narrow PL emission peak with FWHM of 6.15 meV at 12 K. Such narrow FWHM of 6.15 meV at low temperature corresponds to less than ±1ML well width fluctuation thoughtout the entire structure[8]. This feature also demonstrates the high interfacial quality and periodic reproducibility of $In_{0.1}Ga_{0.9}As/GaAs$ multiple quantum wells by MBE technique.

Temperature-dependent PL measurement of $In_{0.1}Ga_{0.9}As/GaAs$ multiple quantum wells was conducted in order to investigate the photo-emission mechanisms in the wells. The measured temperature was varied from 12K to 120 K and corresponded PL emission spectra were shown in Fig. 8.3. The solid lines show the best fitting curve to the experimental data. The PL spectra exhibit two main features; PL intensity decrement and red-shift of PL emission peak with increasing temperature. The photon energy of PL emission peak position of $In_{0.1}Ga_{0.9}As/GaAs$ MQWs as function of temperature is illustrated in Fig. 8.4.

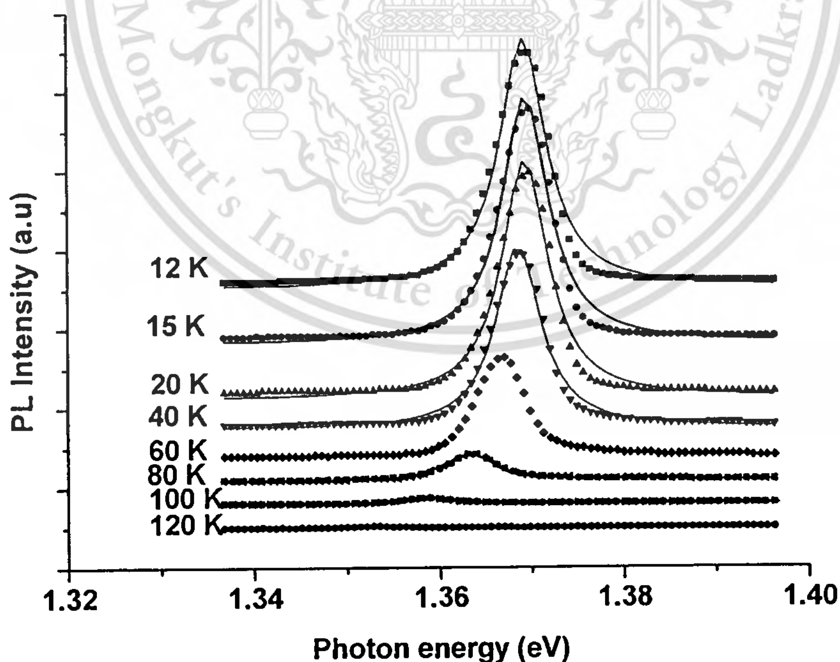

Fig. 8.3 Temperature-dependent photoluminescence of $In_{0.1}Ga_{0.9}As/GaAs$ multiple quantum wells.

This material is reserved for educational use only, not allowed for commercial use.
Forbidden to modify the content, and cite the document when use.

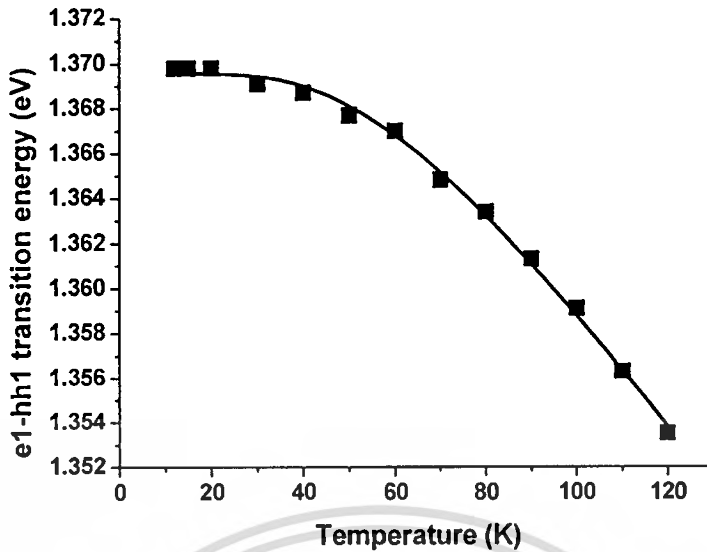

Fig. 8.4 The experimental temperature dependence of the PL emission peak or e1-hh1 transition energy of $In_{0.1}Ga_{0.9}As/GaAs$ multiple quantum wells. The solid line is the best fit of the Vina model.

As temperature increases, the PL intensity drops rapidly, the peak position exhibits redshift, and line shape broadens. The redshift is attributed to the decrease in the band-gap energy as temperature increases due to thermal expansion[9]. At low temperature range, the PL peak position slightly shifts from 1.370 eV at 12 K to 1.368 eV at 60 K. As the temperature increases from 60 K to 120 K, an abrupt shift of about 15 meV in the PL peak position from 1.368 eV at 60 K to the lower energy of 1.353 eV at 120 K is observed. The temperature dependence of the peak energy can be fitted using empirical Viña model[10,11]. The solid line represents the best fit by Viña expression as mentioned by equation (4.2). From the fitting, important parameters are extracted and listed in table 8.1.

Table 8.1 Parameters obtained by fitting equation (4.2) to the peak energy versus temperature data in Fig. 8.4.

Parameters	Value
Electron-phonon interaction strength; a_B	29 meV
Characteristic temperature; θ_B	185 K
Transition energy at 0 K; $E_T(0K)$	1.369 eV
$E_B = E_T(0K) + a_B$	1.398 eV

This material is reserved for educational use only, not allowed for commercial use.
Forbidden to modify the content, and cite the document when use.

In order to understand this PL emission, the theoretical calculation of electronic states in quantum wells was done based on simple finite square wells. In the calculation, the energy gap at room temperature (300K) of GaAs is 1.423 eV[12]. The energy gap of $In_{0.1}Ga_{0.9}As$ can be calculated from the following relationship[12]; $E_g(In_xGa_{1-x}As) = 0.36 + (1-x)1.064$. Therefore, for x =0.1, giving the energy gap of this alloy of 1.318 eV. The effective mass of electron $\left(m_e^*\right)$ and hole $\left(m_{hh}^*\right)$ for $In_{0.1}Ga_{0.9}As$ are dependent on the Indium concentration are as follows[1];

$$m_e^*(x) = 0.066 - 0.054x + 0.012x^2 \text{, and}$$
$$m_{hh}^*(x) = 0.445 - 0.035x.$$

Therefore, the effective mass of electron $\left(m_e^*\right)$ and hole $\left(m_{hh}^*\right)$ of $In_{0.1}Ga_{0.9}As$ alloy(x=0.1) are $0.061m_0$ and $0.441m_0$ respectively. The band discontinuity for conduction band ,ΔE_c, and valence band ,ΔE_v, using band offset ratio $\Delta E_c:\Delta E_v$ =2:1[7], are 70 meV and 35 meV, respectively The band diagram of this structure is schematically drawn in Fig. 8.5. The theoretical calculation shows that the e(1) electronic state is aligned at 0.029 eV above the bottom of the wells, and the hh(1) state is position at 0.007 eV above the bottom of the wells. Based on simple model at room temperature, the corresponding e(1)-hh(1) excitonic transition of 1.354 eV is obtained. This value is in good agreement with experimental data reported in ref. 7. However, comparing this value to the value predicted Viña model, it is found that there is about 40 meV discrepancy between two values. The origin of this difference may be due to the omission of any complicated effects such as piezoelectric effect, coupled effectand exciton binding energy in the calculation[8] and also the mole fraction fluctuation during growth processes.

This material is reserved for educational use only, not allowed for commercial use.
Forbidden to modify the content, and cite the document when use.

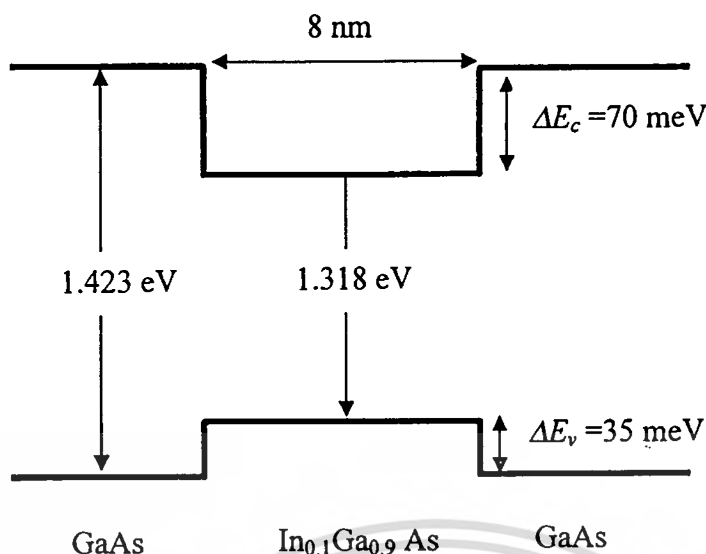

Fig. 8.5 Schematic band diagram of $In_{0.1}Ga_{0.9}As/GaAs$ multiple quantum wells used in calculation of e(1)-hh(1) excitonic transition at 300 K.

By plotting the PL integrated intensity as a function of temperature, the activation energies responsible for PL quenching can be obtained. Fig. 8.6 presents the variation of integrated PL intensity with temperature of $In_{0.1}Ga_{0.9}As/GaAs$ multiple quantum wells. As temperatue increases from 40 K to 80 K, the integrated PL intensity abruptly decreases by over one order of magnitude. At low temperature limit, the temperature dependence of the integrated PL intensity can be fitted using equation (5.1). The best fit is shown by the solid line and the thermal activation energy E_A of 21.5 meV is obtained. As mentioned in chapter 5, two main mechanisms are responsible for the temperature-induced quenching of luminescence in quantum well structures. For this structure, because of low indium mole fraction (x = 0.1), both conduction and valence band offset are small leading to shallow quantum wells. The delocalization energy of such shallow wells is comparably small supporting the escape of the carriers from the wells. Therefore the thermal emission of charge carriers out of confined states in the wells into barrier states is dominated. The obtained activation energy can be consequently regarded as the delocalized energy of the carriers in the confined states[13].

This material is reserved for educational use only, not allowed for commercial use.
Forbidden to modify the content, and cite the document when use.

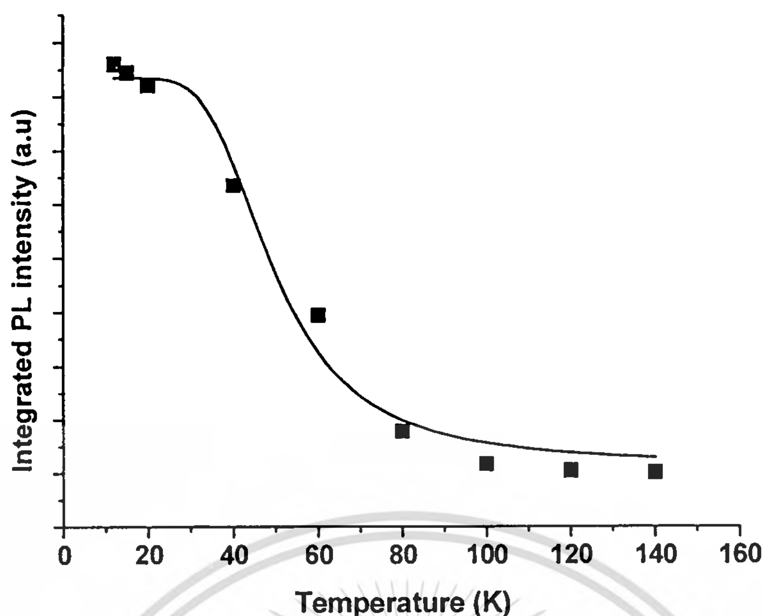

Fig. 8.6 Integrated PL intensity of $In_{0.1}Ga_{0.9}As/GaAs$ multiple quantum wells as a function of temperature. The solid line represents the best fit to experimental data using equation 5.1.

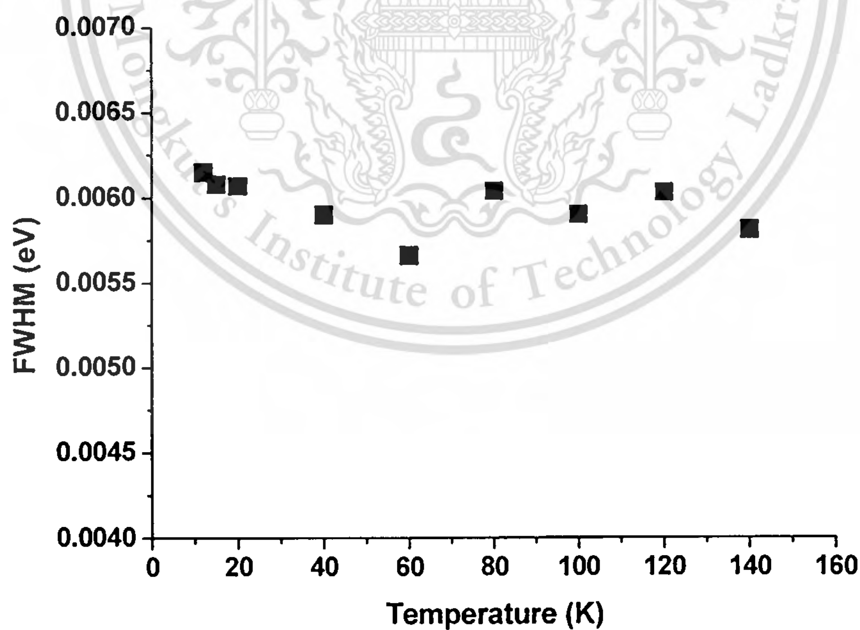

Fig. 8.7 Temperature dependence of the full width at half maximum (FWHM) of the PL spectra of $In_{0.1}Ga_{0.9}As/GaAs$ multiple quantum wells.

This material is reserved for educational use only, not allowed for commercial use.
Forbidden to modify the content, and cite the document when use.

The broadening of PL spectra of $In_{0.1}Ga_{0.9}As/GaAs$ multiple quantum wells is investigated. Fig. 8.7 illustrates the full width at half maximum (FWHM) of PL emission spectra of this structure. In contrast to InGaAs/InP quantum well structure, the FWHMs of PL spectra of $In_{0.1}Ga_{0.9}As/GaAs$ MQWs are almost independent to temperature. This characteristic implies that the temperature-independent inhomogeneous broadening of about 5.8 meV is responsible for the broadening mechanisms of PL emission of this structure. The temperature-independent inhomogeneous broadening is typically caused by interface roughness, alloy fluctuations, fluctuations in the binding energies of growth defects, etc. With very small value of this broadening, it could be deduced that the high interfacial quality between two compounds forming quantum structure by MBE technique is confirmed. In addition, due to comparably thin well width, the electron-phonon interaction is suppressed [14] resulting in an unobvious role of temperature-dependent homogenous broadening on PL emission of this structure.

Further experiment is conducted in order to investigate the influence of the excitation intensity on the PL emission spectra of this structure. To do this, the sample was pumped by an Argon-ion laser at 488 nm and the laser intensity was varied from 3.50 to 27 mW/cm^2. During PL measurement, the temperature was kept at 12 K. The dependence of PL emission spectra of $In_{0.1}Ga_{0.9}As/GaAs$ MQWs on photo-excitation intensity is shown in Fig. 8.8. The peak position remains at 1.370 eV when the sample was excited with various excitation intensities. It is obvious that the PL emission intensity increases linearly with excitation intensity as seen in Fig. 8.9.

This material is reserved for educational use only, not allowed for commercial use.
Forbidden to modify the content, and cite the document when use.

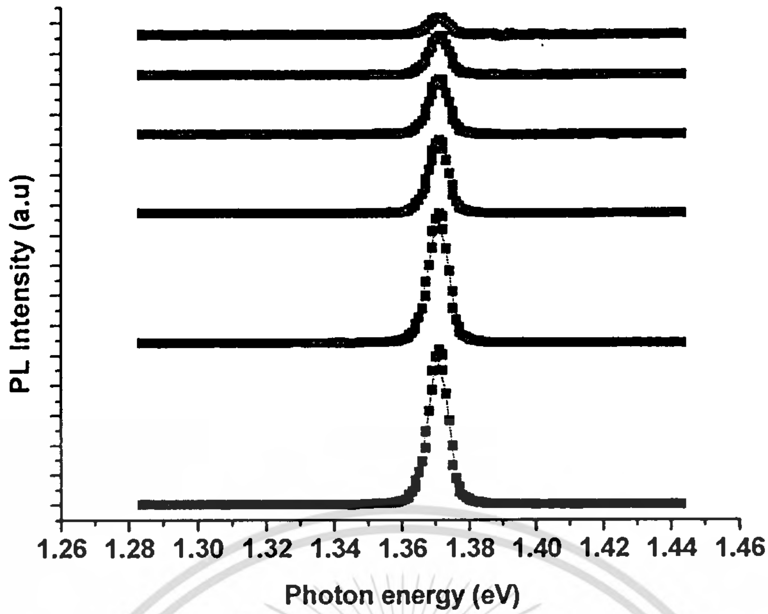

Fig. 8.8 Photoluminescence spectra of $In_{0.1}Ga_{0.9}As/GaAs$ MQWs as a function of excitation energy. The measured temperature is kept at 12 K.

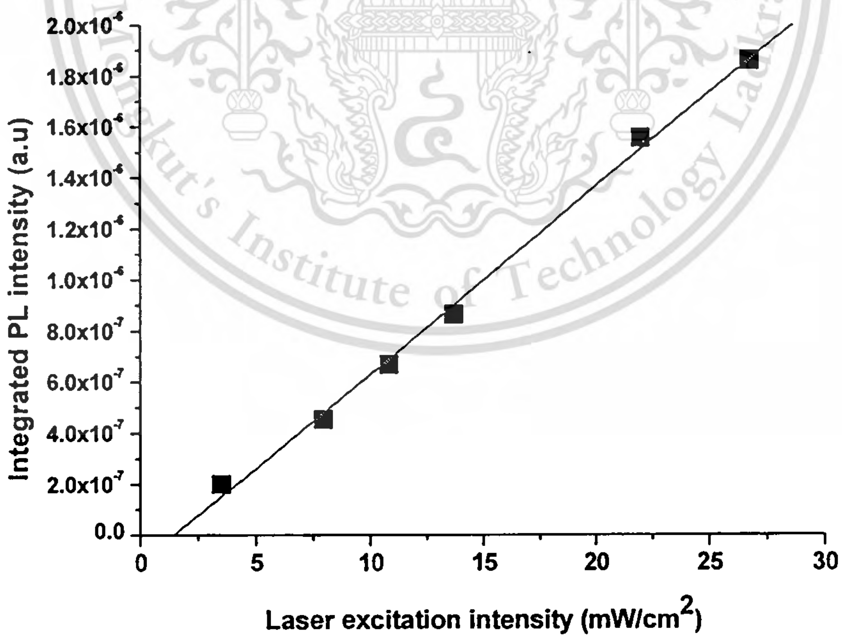

Fig. 8.9 Dependence of PL intensity from $In_{0.1}Ga_{0.9}As/GaAs$ MQWs on laser excitation intensity.

This material is reserved for educational use only, not allowed for commercial use.
Forbidden to modify the content, and cite the document when use.

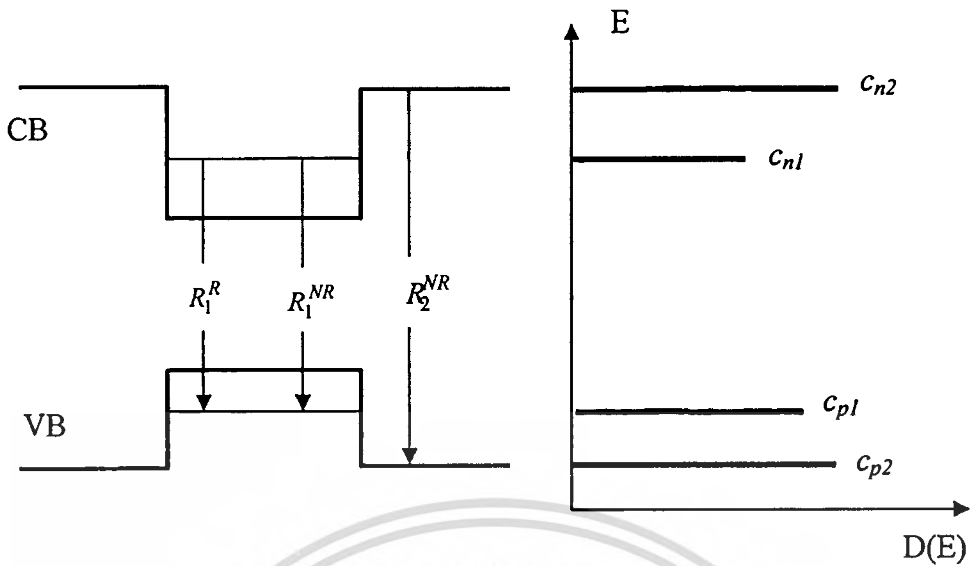

Fig. 8.10 Schematic diagram of energy states in quantum wells and their corresponding density of states.

In order to explain the dependence of PL intensity on excitation intensity, simple model based on the density of states on population of electronic state in quantum wells is proposed. The density of states of carriers in quantum well structures are typically δ-function shape as schematically shown in Fig. 8.10 and expressed as

$$D(E) = c_1\delta(E - E_1) + c_2\delta(E - E_2)\,. \tag{8.1}$$

Where c_1 and c_2 are constants related to degeneracy of two states. The total concentration of charge carriers during excitation are $n = n_0 + \delta n$ for electrons in conduction band, and $p = p_0 + \delta p$ for holes in valence band. Note that n_0 and p_0 are equilibrium carrier densities of electrons and holes, respectively whereas δn and δp are optically generated electron density and hole density, respectively. The excess carrier densities due to photo-excitation are typically equal, $\delta n = \delta p$. For undoped semiconductor, $n_0 = p_0 = N$. The concentration or population of each state should obey the Fermi-Dirac statistics, i.e.,

$$n_j = nF_{nj}\ , \text{ and} \tag{8.2}$$

$$p_j = pF_{pj}\,, \tag{8.3}$$

This material is reserved for educational use only, not allowed for commercial use.
Forbidden to modify the content, and cite the document when use.

where F_j is Fermi-Dirac distribution of energy level j.

After at short time of excitation, electrons and holes can recombine by either radiative (R) or nonradiative (NR) decays. PL emission of quantum well structure is normally due to electrons e(1) state recombine radiatively with heavy holes in hh(1) state. Therefore the PL intensity should read as,

$$I_{PL} \propto r_1^R (n_1 p_1 - n_{01} p_{01}) \approx r_1^R (2N\delta n + \delta n^2) F_{n1} F_{p1} . \tag{8.4}$$

The rate equation of carrier generation by photo-excitation and recombination is expressed as,

$$\frac{d}{dt}\delta n = \frac{d}{dt}\delta p = aI_0 - R_1^R - R_1^{NR} - R_2^{NR} . \tag{8.5}$$

Where R_1^R, R_1^{NR}, R_2^{NR} are rates of the radiative and nonradiative recombination of corresponding states. Typically, the nonradiative recombination is described by the Shockley-Read-Hall mechanism and is usually temperature dependent with an activation energy between two corresponding states, whereas radiative rate is kept constant at constant excitation intensity. The first term on the right-hand side of equation (8.5) denoted as the generation rate of electron-hole pairs should be proportional to the excitation density I_0. The last three terms are expressed as,

$$R_1^R = r_1^R (2N\delta n + \delta n^2) F_{n1} F_{p1} , \tag{8.6}$$

and

$$R_j^{NR} = r_j^{NR} \frac{(N + \delta p)\delta p F_{pj} F_{nj}}{(N + \delta p) F_{pj} + \delta p F_{nj}} \quad (j=1,2) \ [15] \tag{8.7}$$

Under steady-state condition with continuous laser excitation,

$$\frac{d}{dt}\delta n = \frac{d}{dt}\delta p = aI_0 - R_1^R - R_1^{NR} - R_2^{NR} = 0 . \tag{8.8}$$

For low excitation intensity $\delta n = \delta p << N$ and $F_{nj} \approx F_{pj}$, equation (8.6) and (8.7) become

This material is reserved for educational use only, not allowed for commercial use.
Forbidden to modify the content, and cite the document when use.

$$R_1^R = 2r_1^R F_{n1} F_{p1} N\delta p = bN\delta p\ , \tag{8.9}$$

and

$$R_j^{NR} = r_j^{NR} F_{nj}\delta p = b_j \delta p\ , \tag{8.10}$$

where $b = 2r_1^R F_{n1} F_{p1}$ and $b_j = r_j^{NR} F_{nj}$. The rate equation (8.8) is now written as

$$aI_0 - bN\delta p - b_1\delta p - b_2\delta p = 0, \tag{8.11}$$

or

$$\delta p = \frac{aI_0}{bN + b_1 + b_2}. \tag{8.12}$$

Therefore I_{PL} in equation (8.4) reduces to

$$I_{PL} = aI_0 \frac{bN}{bN + b_1 + b_2}. \tag{8.13}$$

From equation (8.13), it is clearly seen that the PL intensity, I_{PL}, is directly proportional to excitation intensity, I_0, especially at low temperatures, where radiative recombination rate in the quantum well dominates. The proposed model can therefore clearly explain the dependence of I_{PL} of this structure on photo-excitation intensity as seen in Fig. 8.7 and 8.8.

8.5 Summary

In summary, the photoluminescence of $In_{0.1}Ga_{0.9}As/GaAs$ MQWs grown by MBE was carried out. The sharp PL spectra due to the excitonic transition associated with the quantum wells are clearly observed. The well-defined PL spectra indicate high interfacial quality heterostructure between these two compounds. Their temperature dependency of this structure is thoroughly investigated and related parameters such as activation energy, electron-phonon interaction strength, and broadening mechanisms are obtained. The dependence of PL intensity on laser excitation intensity is also characterized. The experimental data showed that the PL intensity is linearly proportional to excitation intensity. The feature can be clearly explained by proposed model.

This material is reserved for educational use only, not allowed for commercial use.
Forbidden to modify the content, and cite the document when use.

References

[1] Kh. Moumanis, R.P. Seisyan, S.I. Kokhanovskii and M.E. Sasin, **"Light and heavy hole excitons in absorption and magnetoabsorption spectra of InGaAs/GaAs MQWs"**, Thin Solid Films, Vol. 364, pp. 249-253, 2000.

[2] M. Hopkinson, J.J. Sánchez, M. Gutiérrez, D. González, G. Aragón, I. Izpura and R. Garcia, **"Optical properties of $In_xGa_{1-x}As$/GaAs MQW structures on (111)B GaAs grown by MBE: dependence on sustrate miscut"**, Journal of Crystal Growth, Vol. 201/202, pp. 1085-1088, 1999.

[3] M.J Romero, D. Araújo, J.L. Sánchez-Rojas, E. Callerja, E. Muñoz and R. García, **"Piezoelectric InGaAs/GaAs(111)B multiple quantum well photodiodes: optoelectronic properties by electron beam induced current and cathodoluminescence"**, Microelectronics Journal, Vol. 30, pp. 413-417, 1999.

[4] M.D. Vittorio, M. Lomascolo, A. Passaseo and R. Cingolani **"Electro-optic low-voltage InGaAs/GaAs multiple quantum well modulator with organic-inorganic distributed Bragg reflector"**, Superlattices and Microstructures, Vol. 25, No. 1/2, pp. 313-317, 1999.

[5] J.F. Valtueña, I. Izpura, J.L. Sánchez-Rojas, E. Muñoz, E.A. Khoo, J.P.R. David, J. Woodhead, R. Grey and G.J. Rees, **"Memory effects on piezoelectric InGaAs/GaAs MQW PIN diodes"**, Microelectronics Journal, Vol. 28, pp. 757-765, 1997.

[6] X.R. Huang, A.N. Cartwright, D.R. Harken, D.S. McCallum, A.L. Smiri, J.L. Sánchez-Rojas, A. Sacedón, E. Calleja, and E. Muñoz, **"Per-carrier nonlinear optical response of [111]-oriented piezoelectric InGaAs/GaAs multiple quantum wells"**, Journal of Applied Physics, Vol.79(1), pp. 417-, 1996.

[7] G. Sek, D. Radaiewicz, M. Tlaczala, M. Panek, and R. Korbutowicz, **"Study of the nature of light hole excitonic transitions in InGaAs/GaAs quantum well"**, Vacuum, Vol. 50, pp. 199-201, 1998.

[8] S. Cho, A. Sanz-Hervás, J. Kim, A. Majerfeld, C. Villar, B.W. Kim, **"Metalorganic vapor phase epitaxy growth and properties of GaAs/AlGaAs and InGaAs/GaAs quantum well structures on (111)A GaAs substrates,** Microelectronics Journal, Vol. 30, pp. 455-459, 1998.

This material is reserved for educational use only, not allowed for commercial use.
Forbidden to modify the content, and cite the document when use.

[9] S.A. Lourenco, I.F.L. Dias, J.L. Duarte, E. Laureto, E.A. Moneses, J.R. Leite, I. Mazzaro, **"Temperature dependence of optical transitions in AlGaAs"**, Journal of Applied Physics, Vol. 89, No. 11, pp. 6159-6164, 2001.

[10] M. Furis, A.N. Cartwright, H. Wu, W.J. Schaff, **"Room-temperature ultraviolet emission from GaN/AlN multiple-quantum-well heterostructures"**, Applied Physics Letters, Vol. 83, No. 17, pp. 3486-3488, 2003.

[11] S.B. Bouzid, F. Bousbih, A. Hamdouni, R. Chtourou, J.C. Harmand, P. Voisin, **"Photocurrent and photoluminescence investigations of GaInNAs and GaInNAs(Sb) quantum wells grown by molecular beam epitaxy"**, American Journal of Applied Sciences, Vol. 2(9), pp. 1370-1374, 2005.

[12] J. Singh, **Physics of Semiconductors and Their Heterostructures**, Singapore: McGraw-Hill, Inc., 1993.

[13] Y.T. Shih, Y.L. Tsai, C.T. Yuan, C.Y. Chen, C.S. Yang, W.C. Chou, **"Photoluminescence of $ZnSe_xTe_{1-x}$/ZnSe multiple-quantum-well structures grown by molecular-beam epitaxy"**, Journal of Applied Physics, Vol. 96, No. 12, pp. 7267-7271, 2004.

[14] M. Furis, A.N. Cartwright, H. Wu, and W.J. Schaff, **"Emission mechanisms inUV emitting GaN/AlN multiple quantum well structure"**, Material Research Society Symposium 2004, Vol. 798, 2004.

[15] J. Pannekamp, S. Weber, W. Limmer, R. Sauer, **"Temperature and excitation-density-dependent photoluminescence in GaAs/AlGaAs quantum well"**, Journal of Luminescence, Vol. 85, pp. 37-43, 1999.

This material is reserved for educational use only, not allowed for commercial use.
Forbidden to modify the content, and cite the document when use.

CHAPTER 9

CONCLUSION

In conclusion, the photoluminescence and photocurrent spectroscopies are successfully utilized to characterize the electronic states and relevant properties of essential optoelectronic heterostructure semiconductors. Theoretical background regarding photoluminescence and photocurrent spectroscopies are described in chapter 2. Important theories of semiconductors, heterostructures, and quantum mechanics are also explained in this chapter. Photoluminescence and photocurrent experiment arrangement and relevant equipment is mentioned in chapter 3.

In chapter 4, photoluminescence spectroscopy was employed to investigate the optical bandgap and related parameters such as broadening mechanisms in photoluminescence emission of bulk GaAsP and thermal activation energy. The temperature-dependent bandgap energy is investigated using Vashni and Viña empirical models. Relevant temperature-dependent parameters including empirical equation of bandgap energy as a function of temperature, the phonon temperature, and electron-phonon interaction strength are obtained. In addition, the temperature dependence of PL peak intensity of GaAsP results in the thermal activation energy of about 21.5 meV. The inhomogeneous broadening mechanism is found to be the dominant mechanism for the broadening of GaAsP. The photocurrent spectroscopy of GaAsP was carried out at room temperature. The current-voltage characteristic curves show good both Schottky and Ohmic contacts. The effect of chopped frequency on photocurrent signal is examined and results in the response of the sample of 0.39 millisecond. When the sample was biased, the photocurrent intensity increased with increasing bias voltage, showing diode behavior.

In chapter 5, $In_{0.53}Ga_{0.47}As/InP$ SQWs grown by OMVPE were characterized by mean of photoluminescence spectroscopy. The photoluminescence peaks show the luminescence from the recombination between e(1)-hh(1) in quantum wells. The photon energy of photoluminescence peak increases with decreasing well width and agrees well to calculated results. The temperature-dependence of photoluminescence spectra is investigated. The weaker and broader photoluminescence emission peak is obtained when the measured temperature is elevated. The small value of thermal activation energy that affects photoluminescence intensity quenching of this structure is obtained from the temperature-dependent behavior of integrated photoluminescence intensity. The small thermal activation energy in the narrow well suggests that

This material is reserved for educational use only, not allowed for commercial use.
Forbidden to modify the content, and cite the document when use.

carriers can easily escape from the well to the barrier states. The broadening of photoluminescence emission peak is discussed in term of homogeneous and inhomogeneous broadening mechanisms. It is revealed that inhomogeneous mechanism is the dominant mechanism for the broadening of photoluminescence peak and homogeneous mechanism has significant role at high temperature due to electron-phonon interaction. Due to very thin quantum well layer, the effect of source supply interruption(SSI) during growth on the well shape is taken into account. The mathematical model of few monolayer $InP/In_{0.53}Ga_{0.47}As/InP$ SQWs grown by OMVPE taking the influence of source supply interruption into account is proposed. In the model, the 1-ML potential barrier of InGaAsP is formed at the InGaAs-to- InP interface, causing asymmetric stepped well. The theoretical calculation with SSI showed better agreement with experimental data than the prediction without SSI.

In chapter 6, photocurrent spectroscopy was employed to characterize the Er δ-doped InP grown by OMVPE. Three extinct photocurrent peaks of the doped samples exhibit the high quality formation of ErP layer between InP layers. The photocurrent spectra of doped samples with different Er exposure duration show that the total number of uniform ErP islands increase with increasing exposure time, reflected in the sharper photocurrent spectra. When the voltage is applied, it suppresses the energy gap of ErP causing unbound excitons and the blur out of the photocurrent spectra. All features revealed by photocurrent spectroscopy demonstrate the formation of ErP islands layer in InP. In addition, the photocurrent spectra of doped sample exhibit distinguished peaks, which may correspond to the interband transitions of a ErP/InP single quantum well formed during growth. The theoretical model based on both rectangular well and parabolic well are proposed. The results from the rectangular model have a better agreement to the experiment than the parabolic model. The photocurrent of the doped specimen also shows the quantum confined Stark effect at low voltages. The peak position is shifted to higher energy when the biased voltage is increased from 0.1 – 0.3 V. The new peak of lower energy is also observed. The field dependence of ground state transition energy leads to the existence of permanent dipole moment due to non-uniform ErP islands.

In chapter 7, organic/inorganic heterostructure of $ZnSe/Alq_3/TPD$ grown on silicon(Si) by electron beam evaporator was characterized by photocurrent spectroscopy. The effect of thickness of TPD layer, Alq_3 layer, and type of Si substrate are analyzed. The wavelength response of the structure covers visible to near infrared spectrum. It is concluded that TPD layer plays a crucial role in photocurrent process of the device, especially in visible range. The effect of

Forbidden to modify the content, and cite the document when use.

type of Si substrate indicates that p-Si shows improvement in the photocurrent intensity. In addition, photocurrent and electroreflectance were used to investigate optical and electrical properties of the samples. Both photocurrent and electroreflectance spectra exhibit clear optical transition energies in SQWs as Alq_3 well thickness varied from 10 to 50 nm. The optical transition energy decreases with increasing in well thickness due to the increase of well size in addition to reduction of quantum confinement energy. The signals also showed the significant Stark shift when the device was under external electric field.

In chapter 8, the electronic state in $In_{0.1}Ga_{0.9}As/GaAs$ MQWs grown by MBE was investigated by photoluminescence spectroscopy. The sharp PL spectra due to the excitonic transition associated with the quantum wells are obviously observed. The well-defined PL spectra indicate high interfacial quality heterostructure between these two compounds. Their temperature dependency of this structure is thoroughly investigated and related parameters such as activation energy, electron-phonon interaction strength, and broadening mechanisms are achieved. The dependence of PL intensity on laser excitation intensity is also characterized. The experimental data showed that the PL intensity is linearly proportional to excitation intensity. The simple proposed model based on excitation and recombination processes is presented to explain the relationship between the excitation intensity and PL intensity.

King Mongkut's Institute of Technology Ladkrabang

This material is reserved for educational use only, not allowed for commercial use.
Forbidden to modify the content, and cite the document when use.